Femtosecond laser inscription of type A-based high index contrast waveguides and Bragg gratings

Laura Loi

THÈSE PRÉSENTÉE

POUR OBTENIR LE GRADE DE

DOCTEUR
DE L'UNIVERSITÉ DE BORDEAUX

ECOLE DOCTORALE SCIENCES PHYSIQUES ET DE L'INGÉNIEUR

LASERS, MATIÈRE ET NANOSCIENCES

Par **Laura LOI**

Femtosecond laser inscription of type A-based high refractive index contrast waveguides and Bragg gratings

Sous la direction de : **Lionel CANIONI**
Co-encadrant : **Yannick PETIT**

Soutenue le 17 novembre 2022

Membres du jury:

Prof. Matthieu LANCRY	ICMMO	Université Paris-Saclay	Rapporteur
Prof. Laurent GALLAIS	Institut Fresnel	École Centrale de Marseille	Rapporteur
Dr. Matthieu BELLEC	INPHYNI	Université Côte d'Azur	Examinateur
Prof. Eric CORMIER	LP2N	Université de Bordeaux	Président
Prof. Lionel CANIONI	CELIA	Université de Bordeaux	Directeur
Dr. Yannick PETIT	CELIA	Université de Bordeaux	Co-encadrant
Dr. Laura GEMINI	B.U. Procédés Lasers	ALPhANOV	Invitée

To my mother and my father.
To Irene.

A mia madre e a mio padre.
A Irene.

Introduction générale

Au cours des dernières décennies, depuis la première réalisation d'un laser dans les années 1960 et l'invention des fibres optiques plus tard dans les années 1980, la photonique a rapidement gagné un rôle clé dans de nombreux domaines de recherche, de la communication, de la médecine, de la fabrication et de la détection, au point que les technologies basées sur la photonique sont d'une importance fondamentale dans notre vie quotidienne.

Par exemple, les soins de santé ont largement bénéficié des innovations en photonique dans l'imagerie médicale, le diagnostic et le traitement des maladies, réduisant les coûts et offrant des procédures moins invasives.

De plus, alors que les lasers deviennent plus abordables, leur emploi dans l'industrie augmente en améliorant les technologies de fabrication telles que le soudage, le traitement des matériaux ou l'impression, en gagnant en flexibilité, en améliorant la qualité et en réduisant les déchets.

Néanmoins, c'est dans les télécommunications et le stockage, le traitement et le transfert de données que nous nous attendons à ce que la photonique joue un rôle stratégique pour répondre à la demande croissante de capacité de données et de bande passante, accélérer les réseaux et réduire la consommation globale d'énergie et l'empreinte environnementale.

En effet, les circuits photoniques intégrés permettent de réduire la taille des systèmes optiques volumineux et complexes, les intégrant dans des matériaux afin de minimiser l'interaction environnementale.

Parmi toutes les différentes techniques, Direct Laser Writing permet d'adresser directement la structuration 3D des matériaux par absorption multiphoton d'une source laser femtoseconde focalisée dans le voxel d'interaction.

Cette technique présente de nombreux avantages tels que la flexibilité et la fabrication en une seule étape par rapport, par exemple, à la structuration 2D par lithographie et des matériaux.

Cependant, l'efficacité des dispositifs optiques intégrés est directement liée à notre capacité à réduire les pertes. Vu que les guides d'ondes sont les composants de base des circuits optiques

intégrés, cela se traduit par une recherche optimisant la fabrication de guides d'ondes présentant de faibles pertes de propagation et une efficacité de couplage élevée.
Par ailleurs, l'amélioration de l'interaction laser-matière pour induire un contraste d'indice de réfraction élevé, est un autre axe de développement qui permet la miniaturisation des circuits optiques.
Bien que les verres à base de silice soient les matériaux les plus couramment utilisés pour les applications photoniques, les verres en général possèdent des propriétés structurelles et optiques uniques qui peuvent être adaptées en adaptant leur composition et leur processus de fabrication, par conséquent, la recherche en cours est axée sur le développement de nouveaux verres optiques pour atteindre de nouvelles fonctionnalités. Il n'est pas surprenant que le Conseil général de l'ONU ait déclaré cette année, en 2022, *l'Année internationale du verre*, en reconnaissant le rôle fondamental que les verres ont dans la société.

C'est dans ce cadre que les travaux rapportés dans ce manuscrit ont été réalisés.
Ce doctorat a été réalisé à l'Université de Bordeaux, au sein du groupe *Short-pulse Lasers : Applications & Materials* (SLAM) du laboratoire *Centre Lasers Intenses et Applications* (CELIA).
Le groupe possède une expertise internationalement reconnue en inscription laser femtoseconde de matériaux pour des applications photoniques. En particulier, grâce à des collaborations avec d'autres laboratoires et entreprises, en particulier l'*Institut de Chimie de la Matière Condensée de Bordeaux* (ICMCB).
Le groupe étudie l'inscription laser d'architectures photoniques à 3D dans le volume et en fibre, notamment des verres en phosphate photosensible contenant des ions argentés.
Les travaux de recherche antérieurs à cette thèse ont consisté à étudier la photochimie des ions d'argent induite dans l'interaction laser-matière et les propriétés optiques du changement d'indice de réfraction associé, qui n'est pas liée à des modifications structurelles, mais plutôt au mécanisme physicochimique activé dans l'absorption des impulsions laser.
De plus, cette étude a été menée parallèlement à une étude sur les matériaux pour comprendre l'influence de la structure des verres sur la photosensibilité des matériaux.
Les résultats prometteurs de ces études ont permis la fabrication de guides d'ondes liés à l'argent, de guides d'ondes à proximité de la surface et la réalisation d'un capteur d'indice de réfraction.

Par conséquent, les travaux développés au cours de cette thèse visaient à étudier davantage la formation d'impulsion-à-impulsion des agrégats d'argent induite dans l'interaction femtoseconde

pour l'exploiter pour la fabrication de guides d'ondes à base d'argent à fort contraste d'indice.
De plus, cette thèse vise à réaliser des composants optiques plus complexes basés sur les propriétés optiques de structures caractérisées par une modulation périodique de l'indice de réfraction.

Par conséquent, les travaux développés au cours de cette thèse visent à étudier la formation impulsions après impulsions des agrégats d'argent, induite dans l'interaction femtoseconde, pour l'exploiter dans la fabrication de guides d'ondes à fort contraste d'indice.
De plus, cette thèse vise à réaliser des composants optiques plus complexes basés sur les propriétés de structures optiques caractérisées par une modulation périodique de l'indice de réfraction.

Ce manuscrit est structuré comme suit.

Le premier chapitre traite des principes fondamentaux de l'interaction laser-matière.
La première partie est consacrée aux verres, à leurs propriétés structurelles et optiques et aux processus de fabrication.
Ensuite, les lasers ultrarapides sont introduits ainsi que les processus d'ionisation multiphoton produit par l'absorption des impulsions laser.
Enfin, les notions de base de l'optique guidée sont discutées pour introduire la théorie du guidage des ondes et les propriétés de la lumière se propageant dans les médias périodiques.

Le deuxième chapitre se concentre sur le Direct Laser Writing dans les verres.
Les modifications structurelles conduisant à une modification de l'indice de réfraction du verre sont étudiées.
En particulier, les propriétés des structures inscrites dans les régimes thermiques et athermiques sont présentées et différentes techniques de fabrication pour atteindre un contraste élevé de l'indice de réfraction induit sont discutées.
Ainsi, des verres contenant de l'argent et leur structuration par laser femtoseconde sont présentés.
Un bref état de l'art sur les structures d'indice de réfraction dues à l'argent et leurs propriétés optiques est réalisé et certains des principaux résultats obtenus par le groupe sont présentés.

Le troisième chapitre présente les résultats de l'inscription multiscan de verres contenant de

l'argent pour obtenir un changement élevé d'indice de réfraction.
La discussion est menée à la suite de l'étude sur trois différentes matrices vitreuses contenant de l'argent, analysant la dépendance impulsions après impulsions du contraste d'indice sur le nombre d'impulsions absorbées pendant toutes les inscriptions laser dans un régime athermique. Des résultats prometteurs concernant le contraste d'indice sont exploités pour la fabrication de guides d'ondes.

Le quatrième chapitre traite de la fabrication de structures dues à l'argent basées sur la modulation périodique de l'indice de réfraction.
La première partie présente les Waveguides Bragg Gratings, en discutant de leur procédé de fabrication, des caractéristiques géométriques et des propriétés optiques.
Ainsi, les spectres de transmission sont analysés pour étudier leur effet de filtrage. La deuxième partie rend compte des résultats préliminaires obtenus dans la fabrication des réseaux volumiques de Bragg.

Enfin, des conclusions sont tirées à partir des résultats rapportés et certaines perspectives sur les travaux futurs sont esquissées.

Résumé de la thèse

Les verres sont des matériaux amorphes fabriqués depuis des milliers d'années. Leurs processus de fabrication ont été optimisés au fil des ans afin qu'il soit possible de synthétiser des verres présentant des propriétés structurelles et optiques personnalisées. Différentes compositions sont examinées pour adapter les fenêtres de transmission et les indices de réfraction des verres optiques.
En particulier, le spectre d'absorption dans l'UV détermine la longueur d'onde de la source laser ultrarapide qui peut être absorbée par absorption multiphoton.
Un tel processus non linéaire permet de confiner l'interaction ultrarapide à l'intérieur d'un voxel avec des dimensions liées au paramétre géométrique du faisceau laser focalisé.
L'absorption multiphoton est liée à des processus de photoionisation qui peuvent conduire à une modification matérielle dans le voxel d'interaction.
Selon les propriétés du changement d'indice de réfraction associé, il est possible de guider la lumiére en utilisant les structures 3D induites par laser dans l'interaction d'une source femtoseconde et d'un verre.
La lumiére se propageant à l'intérieur d'un guide caractérisé par un changement d'indice de réfraction positif subit la réfraction interne totale aux bords du guide, les conditions limites établissent les solutions de l'équation de Helmholtz, connue sous le nom de modes, qui sont autorisés à se propager à l'intérieur de la structure de guidage, comme une fibre optique ou un guide d'onde.
Chaque mode est caractérisé par une constante de propagation et un changement d'indice de réfraction efficace.
Par ailleurs, connaissant le contraste d'indice induit entre la structure de guidage et le verre vierge et la dimension de la structure, il est possible de trouver le diamétre du champ du mode, qui donne des informations sur la fraction du mode qui est confiné sur la structure guidante.
Lorsque la lumiére se propage dans des milieux périodiques caractérisés par une modulation

périodique du changement d'indice de réfraction, elle subit plusieurs transmissions et réflexions aux interfaces entre différentes zones d'indice de réfraction. L'interférence entre les ondes transmises et réfléchies entraîne une augmentation de l'intensité de la lumiére transmise en correspondance avec la résonance de Bragg, liée à la périodicité de la structure. Le comportement de la lumiére qui se propage à l'intérieur des réseaux périodiques peut être simulé en modélisant la structure à l'aide de la matrice de transfert ou de la théorie des ondes couplées.

L'inscription femtoseconde dans les verres peut être réalisée en régime thermique ou athermique, en fonction du taux de répétition du laser ultrarapide utilisé.
En conséquence, les structures inscrites avec des sources de taux de répétition élevé présentent des dimensions plus grandes associées à la zone affectée thermiquement et des géométries symétriques.
L'ampleur de la variation induite de l'indice de réfraction est généralement plus élevée que celle obtenue dans un régime athermique. Néanmoins, l'amplitude du contraste des indices atteint avec Direct Laser Writing est beaucoup plus petite que ce qui est obtenu par d'autres méthodes de fabrication, telles que la lithographie.
Par conséquent, de nombreuses techniques ont été recherchées pour augmenter la variation d'indice, l'une d'entre elles étant l'inscription laser multiscan qui repose sur l'absorption de nombreuses impulsions lors de balayages laser consécutifs. Cependant, les effets thermiques se produisant dans l'absorption des impulsions laser rendent difficile l'augmentation du contraste d'indice induit en utilisant cette approche.
Le Direct Laser Writing dans des verres contenant de l'argent avec un laser à taux de répétition élevé permet d'induire la formation d'agrégats d'argent dans un régime athermique.
La photochimie des ions d'argent n'est activée que dans le voxel d'interaction, permettant la formation de structures pérennes dues à l'argent qui sont caractérisées par des éléments avec des dimensions plus petites que la limite de diffraction.
Par ailleurs, les espéces d'argent photoinduites montrent des propriétés de fluorescence et sont associées à un changement d'indice de réfraction positif, appelé Type A, qui n'est pas lié à la modification structurelle de la matrice de verre.
Un tel contraste d'indice positif s'est avéré utile pour les applications de guidage d'ondes, permettant la fabrication de guides d'ondes dues à l'argent, de guides d'ondes proches de la surface et d'un capteur d'indice de réfraction.
Par ailleurs, le réservoir d'argent constamment disponible de la matrice vitreuse permet de

réécrire dans ces matériaux.

En profitant du remarquable régime athermique de la formation des agrégats d'argent, l'approche multiscan est adoptée pour inscrire des modifications de Type A dans des verres contenant de l'argent visant à atteindre des changements d'indice de réfraction induits élevés.
Pour cette raison, plusieurs structures multiscan ont été inscrites à l'intérieur d'échantillons contenant de l'argent avec différentes matrices de verre en faisant varier les paramétres DLW, la vitesse de translation et l'intensité du laser, et le nombre de balayages laser.
Ainsi, l'indice de réfraction associé à chaque structure multiscan a été extrait des images de phase acquises au moyen du logiciel Sid4BIO et du capteur CCD basé sur la technique Quadri-wave Lateral Shearing Interferometry.
Les résultats ont été analysés en fonction du nombre d'impulsions cumulées absorbées pendant les acquisitions laser consécutives. Cette étude a permis de comprendre que le changement d'indice de réfraction induit dans un régime athermique suit des taux de croissance différents:

- lorsque le réservoir d'argent de la matrice de verre est plein, l'amplitude du changement d'indice de réfraction dépend directement du nombre d'impulsions cumulées absorbées. Le taux de variation de l'indice de réfraction est déterminé par l'intensité du laser puisque le nombre d'agrégats d'argent photoinduits dépend du nombre d'électrons libérés dans l'absorption de l'impulsion laser;

- lorsque le réservoir d'argent est presque vide, la quantité d'ions d'argent restant n'est pas suffisante pour créer un nombre d'agrégats d'argent déterminé par l'intensité du laser, donc le changement d'indice de réfraction sature. Finalement, l'épuisement du réservoir des ions d'argent au centre des structures inscrites peut conduire à un changement dans le processus d'absorption du verre et donc à des explosions.

Le contraste élevé de l'indice de réfraction en multiscan a été exploité pour la fabrication de guides d'ondes.
En fonction du nombre de balayages laser consécutifs, ces guides d'ondes dus à l'argent peuvent présenter un comportement monomode ou multimode à la même longueur d'onde. De plus, un traitement d'image des profils du mode du champ proche des guides d'ondes a permis d'estimer le diamétre du mode de champ de chaque structure en fonction du nombre de passages laser.
Cela a permis de démontrer que l'augmentation du nombre de passages laser entraîne une diminution du diamétre du mode des guides d'ondes, en conséquence une augmentation de l'indice de

réfraction. Néanmoins, cette augmentation du confinement du mode dans les guides d'ondes multiscan a été associée à une diminution des pertes de propagation mesurées.
Enfin, les guides d'ondes de Type A sont généralement caractérisés par un profil en mode double-elliptique, qui peut empêcher un couplage efficace avec, par exemple, des fibres optiques.
Par conséquent, en tirant parti de la capacité de réécriture des agrégats d'argent, des guides d'ondes multiscan ont été fabriqués pour remodeler la géométrie des guides d'ondes à contraste élevé et obtenir un profil de mode gaussien.

Un pas de plus dans la réalisation de dispositifs optiques pour les circuits photoniques intégrés est représenté par la fabrication de Waveguides Bragg Gratings.
Ces structures sont caractérisées par une modulation périodique de l'indice de réfraction du guide d'ondes pour obtenir la réflexion de la lumiére guidée à une longueur d'onde spécifique, connue sous le nom de longueur d'onde de Bragg.
La résonance de Bragg est déterminée par la période du réseau de Bragg et l'ampleur de l'indice de réfraction efficace ressentie par les modes guidés.
Ces types de structures sont utilisés dans de nombreux domaines de recherche pour les applications de détection et de filtrage du signal. Grâce à la particularité des modifications de Type A d'inscrire des éléments avec dimensions plus petite que la limite de diffraction, des Waveguides Bragg Gratings ont été fabriqués avec des périodicités d'environ plusieurs centaines de nm, afin de cibler la résonance de Bragg de premier ordre dans la gamme spectrale visible proche infrarouge, et avec différentes géométries, en particulier, le cas des réseaux hélicoïdaux est analysé.
Ces réseaux 3D permettent d'obtenir un coefficient de couplage élevé, environ deux ordres de grandeur plus élevés que ce qui est rapporté dans la littérature, pour des réseaux trés courts, avec longueur typique $L = 500$ μm.
Les spectres de réflexion des Waveguides Bragg Gratings collectés à la fois par couplage avec un circulateur monomode et en collectant la réflexion du guide d'ondes dans l'espace libre ont prouvé l'effet miroir des réseaux.
Une baisse de 99% de la transmission est présenté afin de démontrer le potentiel de tels guides d'ondes dans la réalisation de dispositifs optiques plus complexes, tels que des étalons Fabry-Perot.
Cependant, une étude sur l'évolution de l'efficacité de diffraction en fonction de la longueur du réseau a mis en évidence certains problémes d'instabilité pendant le processus de fabrication DLW.

Par ailleurs, un modéle basé sur la théorie des ondes couplées a permis de comprendre quels sont les principaux problémes impliqués dans le processus d'écriture, comme la dérive dans le repositionnement absolu des platines qui affecte la stabilité du processus d'écriture et ne permet pas de maintenir la périodicité du réseau fixe.
Enfin, les résultats des travaux préliminaires sur la fabrication des réseaux de Bragg volumiques à transmission due à l'argent sont présentés.
Des mesures de diffraction obtenus pour des réseaux monocouches démontrent l'existence de diffraction de Bragg pour la longueur d'onde de la sonde dans et hors de la bande d'absorption des agrégats d'argent.
Par ailleurs, dans chaque cas, un changement d'indice efficace élevé a été extrait en modélisant l'efficacité de diffraction à différents angles de diffraction par le modéle de Kogelnik basé sur la théorie des ondes couplées. Cependant, les réseaux monocouches présentent une faible efficacité de diffraction.
Pour cette raison, une série de réseaux de transmission multicouches a été inscrite pour analyser la dépendance de l'efficacité de diffraction avec l'épaisseur des réseaux volumiques.
Comme pour le cas de Waveguides Bragg Gratings, l'étude a souligné les questions d'instabilités affectant le processus d'écriture laser directe, qui a abouti à l'élargissement du pic de diffraction à l'angle de Bragg et en présence d'autres pics à différents angles.
Les positions des pics de diffraction supplémentaires ont permis de récupérer les périodicités effectives qui ont été involontairement inscrites et leur épaisseur effective.
Cependant, le gain de l'efficacité de diffraction, malgré les problémes d'instabilités, est un résultat prometteur qui suggére que des efficacités de diffraction élevées peuvent être atteintes par des réseaux basées sur des modifications de Type A une fois le processus d'inscription optimisé.

Conclusions générales et perspectives

Le projet á l'origine des travaux rapportés dans ce manuscrit visait á développer des guides d'ondes et des composants optiques pour circuits optiques intégrés par inscription laser femtoseconde dans des verres contenant de l'argent.

Il a été démontré que la DLW dans des verres contenant de l'argent avec une source laser de taux de répétition élevé et basse énergie d'impulsion, environ quelques dizaines de nJ, induit la formation d'agrégats d'argent dans un régime athermique.
Le regroupement des ions d'argent est associé á un changement d'indice de réfraction positif en conséquence d'un changement de la polarisabilité locale.
En 2017, il a été prouvé que le changement d'indice de réfraction positif permet de guider les applications, permettant la fabrication des premiers guides d'ondes soutenus par l'argent.
Ce nouveau type de changement d'indice de réfraction induit par laser a été nommé Type A, d'après *Argentum*.
Outre la capacité d'induire un contraste d'indice toujours positif, les agrégats d'argent photoinduites montrent d'autres caractéristiques particulières: les structures inscrites montrent de petits éléments avec dimensions en dessous de la limite de diffraction et le réservoir d'argent disponible dans le verre permet la réecriture.

Sur la base de ces résultats, ces travaux visaient á développer des guides d'ondes et des composants optiques basés sur la photochimie induite par laser des ions argentés pour des applications photoniques, telles que la fabrication de circuits intégrés optiques.

Pour cette raison, les effets de l'absorption cumulée des impulsions laser sur le changement induit de l'indice de réfraction dans l'inscription multiscan des modifications de Type A sont étudiées pour exploiter le régime athermique pour atteindre un contraste d'indice de réfraction

élevé.
Une telle étude a permis de démontrer qu'un élevé indice de réfraction de Type A jusqu'á 2×10^{-2} peut être obtenu. De plus, l'inscription athermique des modifications de Type A permet un contrôle fin du changement d'indice de réfraction d'impulsion á impulsion en ajustant soigneusement les paramètres de DLW.
Ce qui n'est pas possible dans l'inscription femtoseconde des modifications de Type 1 dans un régime de taux de répétition élevé en raison de l'accumulation de chaleur dans le voxel d'interaction.
En particulier, l'absence d'effet de saturation dans le cas de structures multiscan inscrites avec une irradiance laser modérée peut indiquer qu'un changement d'indice de réfraction encore plus élevé peut être obtenu en cumulant un nombre significatif d'impulsions.
Á cet égard, l'augmentation du nombre d'impulsions avec une source laser MHz entraînerait des temps de fabrication très longs, donc l'utilisation d'un laser avec un taux de répétition plus élevé (100 MHz) représente une perspective intéressante á considérer.
Par ailleurs, le changement élevé et contrôlé de l'indice de réfraction de Type A a été exploité dans la fabrication de guides d'ondes multiscan présentant des caractéristiques intéressantes.
Premièrement, en raison de la relation directe entre le nombre d'impulsions absorbées et l'amplitude de la variation de l'indice de réfraction, il a été possible de fabriquer des guides d'ondes présentant un fonctionnement monomode ou multimode á une longueur d'onde donnée en réglant le nombre d'acquisitions laser.
De plus, l'augmentation de l'indice de réfraction a permis de contrôler le confinement du mode guidé. En conséquence, les guides d'ondes ont montré des pertes de propagation réduites lors de l'augmentation du nombre de balayages laser.
Un tel résultat est prometteur pour la fabrication de guides d'ondes courbés avec un petit rayon de courbure, ce qui est une contrainte critique pour réduire les dimensions des circuits optiques intégrés sans augmenter les pertes.
Cette technique multiscan et la capacité de réécriture des agrégats d'argent ont permis la fabrication d'un guide d'ondes de type gaussien démontrant la capacité de remodeler le profil du mode guidé.
Cette technique serait très importante pour optimiser le couplage entre, par exemple, les guides d'ondes intégrés et les fibres optiques et pour réduire les pertes.

La fabrication de structures présentant une modulation périodique du changement d'indice

de réfraction, comme les Waveguides Bragg Gratings et Volume Bragg Gratings, permet de faire un pas en avant dans le développement de composants optiques. En effet, les réseaux de Bragg sont des dispositifs essentiels en photonique, ainsi que pour de nombreux autres domaines d'application, et ils sont largement utilisés dans les circuits optiques intégrés.
Profitant de la capacité de réécriture des agrégats d'argent et de la possibilité d'inscrire des éléments avec des dimensions inférieures á la limite de diffraction, des Waveguide Bragg Gratings avec une petite périodicité ont été inscrits en ciblant des résonances de Bragg de premier ordre dans la plage spectrale visible proche infrarouge.
Les spectres de transmission des WBGs ont démontré une grande efficacité de filtrage pour les réseaux très courts, généralement $L = 500$ μm, ce qui a donné lieu á des coefficients de couplage remarquablement élevés, environ deux ordres de grandeur plus élevés que ceux rapportés dans la littérature.
De plus, les spectres de réflexion ont prouvé le comportement de miroir des réseaux, ouvrant la voie á des configurations plus complexes, telles que les cavités de Fabry-Perot. Cependant, certaines instabilités dans le processus d'écriture se sont avérées affecter fortement l'efficacité des WBGs.
Á cet égard, il convient de prendre certaines précautions dans la procédure d'écriture: par exemple, au lieu d'inscrire un long réseau, il devrait être préférable d'inscrire plusieurs réseaux plus petits pour contourner la dérive du repositionnement absolu des platines de translation.
Étant donné que la nature de certains problèmes provoquant des fluctuations dans la périodicité des réseaux est inhérente á la méthode de modulated burst pour le DLW, une autre perspective intéressante prendrait en considération l'inscription des réseaux par la méthode du masque de phase.

Ces arguments sont toujours valables pour le cas de Volume Bragg Gratings basée sur les agrégats d'argent.
Les résultats des réseaux multicouches démontrent le potentiel des structures périodiques pour atteindre une efficacité de diffraction élevée avec des réseaux relativement fins, en jouant simplement sur le nombre de couches et le chevauchement entre elles.
En alternative á la méthode du masque de phase, ou façonner le faisceau laser en un faisceau, Bessel peut aider á améliorer le processus de fabrication, car il permettrait d'inscrire des structures plus épaisses et de réduire le nombre de couches á empiler.

Abstract

Direct Laser Writing (DLW) is a flexible and efficient technique to produce perennial material modifications in glasses, as well as many other materials. It is based on multiphoton absorption, a nonlinear process taking place in the voxel where the femtosecond laser is focused. Since the first demonstration in glasses in 1996, such a technique has allowed for the realization of waveguides and other more complex optical components for integrated photonics circuits. Besides the numerous advantages of the DLW technique, the induced refractive index change is still modest when compared to the one achieved in other techniques, such as lithography. Therefore, the achieving of higher index modification is a research axis that is currently being investigated since it will allow for the miniaturization of optical circuits. Different types of refractive index modifications have been achieved in glasses depending on the laser parameters and the glass composition. Among these, Type 1 is the only one suitable for waveguiding applications. However, in 2017, a new type of index modification has been demonstrated in silver-containing glasses, namely Type A. As a matter of fact, the femtosecond interaction enables the clustering of silver ions, leading to the inscription of silver-sustained structures with features overcoming the diffraction limit that are always associated with a positive refractive index change. Moreover, it has been demonstrated that the silver photochemestry is activated in an athermal regime, despite the use of a high repetition rate laser source. Nevertheless, Type A modifications have been exploited to fabricate waveguides, couplers, beam splitters and, recently, a refractive index sensor. The work reported in this manuscript has a twofold goal. On the one hand, the problem of achieving high refractive index change based on Type A modifications is addressed by adopting a multiscan approach. Such a technique allows for sensibly increasing the index contrast of waveguides induced by several repeated laser scans. However, in the high repetition rate regime, this technique is strongly limited by thermal effects. Thus, by exploiting the athermal regime in the inscription of Type A modification, this work demonstrated the achievement of remarkably high refractive index change up to 2×10^{-2}. Moreover, it is shown that fine control of the induced index change is obtained by simply adjusting the DLW parameters. Nevertheless, multiscan waveguides based on Type A modifications have been fabricated in silver-containing glasses showing both mode-confinement control and reduced propagation losses. On the other hand, this work reports on the fabrication of periodic gratings based on Type A refractive index change which have been exploited for the realization of Waveguides Bragg Gratings (WBGs) and transmission Volume Bragg Gratings (VBGs). The Type A WBGs demonstrated the ability of the silver-sustained structures to achieve first-order Bragg resonance in the VIS-NIR spectral

range. Moreover, high coupling coefficients, up to two orders of magnitude higher than what is reported in the literature, have been obtained for very short gratings, typically $L = 500$ μm. Finally, multilayer Type A VBGs have demonstrated that increasing diffraction efficiency is achieved by increasing the number of stacked layers: diffraction efficiency up to $\eta = 55\%$ is achieved for only 20 μm thick gratings. The results reported in this manuscript demonstrate the ability of Type A modifications to achieve high refractive index change and strong first-order Bragg resonances in the VIS-NIR range. Therefore, such interesting results highlight the potentiality of Type A modifications to fabricate efficient optical components for integrated photonics circuits, enabling a further step into the successful miniaturization of these.

Keywords Direct Laser Writing, femtosecond lasers, silver-containing glasses, silver clusters, Type A modifications, high refractive index change, waveguides, Volume Bragg Gratings, Waveguides Bragg Gratings.

Acknowledgements

This PhD thesis has been carried out in the Centre Lasers Intenses et Applications (CELIA) laboratory in Bordeaux. Therefore, I would like to thank the laboratory and its director Eric Mevel for accepting me and welcoming me in these three years.

I also want to thank Prof Matthieu Lancry, Prof. Laurent Gallais, Prof. Eric Cormier, Dr. Matthieu Bellec and Dr. Laura Gemini for accepting to be part of my PhD jury.

I am most thankful to my supervisors, Prof. Lionel Canioni and Dr. Yannick Petit, for proposing me this PhD and for following my work during these years.
I admire them professionally for their expertise and their extensive knowledge of physics and science in general.
In all our discussions and in their profuse explanations I have picked up the strong passion for their work. On my side, I have tried to behave like a sponge so as to retain every little information they have provided me, for as much as possible.
Particularly, I thank them for their guidance, their kindness and their help.
It was a pleasure to share coffee breaks with Lionel, to hear all the compelling stories and to learn about french expressions.
I have truly appreciated all the interesting conversations I had with Yannick and his funny *dad jokes*.

I am thankful to have worked with Prof. Thierry Cardinal and his group at the Institut de Chimie de la Matière Condensée de Bordeaux (ICMCB), it was instructive, as well as fun. In particular, I would like to thank: Sylvain Danto, Clément Strutynski, Théo Guérineau, Fouad Alassani, Florian Calzavara, Rayan Zaiter and George El Dib.
Particularly, I'm thankful to Théo and Fouad for providing me the glasses on which I have

conducted my work, for all the discussions and the friendly chats that made long experimental time fly by.

I am definitely grateful to have joined the SLAM group: Bruno Bousquet, Inka Manek-Hönninger, Romain Laberdesque, Alain Abou Khalil, Joyce Bou Sleiman, Wendwesen Gebremicheal, Julian Guézénoc, ChangHyun Park, Arthur Le Camus, Joelle Harb, Elise Clave, Raphael Hazem and all the *stagiaires*, especially Sabrina Benhamouche and Mathis Carpentier. I have shared with them such pleasant moments, great laughs and some bizarre situations that only the A4 building could provided.
In particular, I thank Bruno for his kindness, his help and his contagious laugh.

A PhD can be quite a challenging journey and sometimes it gets tough, especially if experiencing it during a pandemic.
Luckily, I had the support of the amazing people around me.

To Joyce, Linh, Jack and all the beautiful people I had the chance to meet here in Bordeaux, I am deeply thankful for their friendship, their support, for all the happy moments and the fun.

I owe so much to Alain for his help, his patience, his constant support in and outside work and for his good heart.

Beyond the Alps, I thank Alessandra, Daniela and Sara for their beautiful souls and their everlasting friendships. Your presence was tangible despite the distance.
Daniela, *ciccia*, thank you for always being there, in all the good or bad moments. I cherish all the cats videos and virtual hugs we shared.

My family has been the most supporting team one could ever wish for.

I am grateful from the bottom of my heart to my big big family, my aunts, uncles and cousins. In particular, I thank my dear *tate* zia Anna and zia Mimma and my cousins Ilaria and Giusy for their love and all the encouragements.
Ilaria, thank you for all the confidences and the advice, I hope one day I will finally convince you to take a flight and come visit me here with Diego and Dodo!

Finally, I thank my brother Emilio, who I look up to, my sister in law Luana and my sweet niece Irene for all the immense love and support.
I am most grateful to my parents.
They are my role models and I thank them for all the values they have instilled in me, for they have made me the person that I am and they have allowed me to achieve all my goals.
Thank you for everything.

Contents

List of Figures

List of Tables

Introduction

In the last decades, since the first realization of a laser in the 1960s and the invention of optical fibers later in the 1980s, photonics has rapidly gained a key role in many research fields from communication, medicine, manufacturing and sensing, to the point that photonics-based technologies are of fundamental importance in our everyday lives.
For instance, health care has largely benefited from photonics innovations in medical imaging, disease diagnostic and treatment, reducing the costs and providing less invasive procedures.
Moreover, while lasers become more affordable, their employment in the industry increases improving manufacturing technologies such as welding, material processing or printing, by gaining flexibility, enhancing the quality and reducing waste.
Nevertheless, it is in telecommunication and the data storing, processing and transferring that we expect photonics to play a strategic role in fulfilling the increasing demand for data capacity and bandwidth, speeding up networks and reducing the overall energy consumption and environmental footprint. Indeed, integrated photonics circuits allow for downsizing to chip scale bulky and complex optical systems, embedding them into materials to minimize environmental interaction. Among all the different techniques, Direct Laser Writing allows for directly addressing material 3D structuring by multiphoton absorption of a focused femtosecond laser source in the voxel of interaction. This technique exhibits many advantages such as flexibility and single-step fabrication with respect to, for instance, 2D structuring by lithography. However, the efficiency of integrated optical devices is directly related to the ability to reduce losses. Since waveguides are the basic components of integrated optical circuits, this translates into fabricating waveguides exhibiting low propagation losses and high coupling efficiency. Moreover, enhancing the laser-matter interaction to induce high refractive index contrast is an important research area that will allow for the miniaturization of optical circuits.
Although silica-based glasses are the most commonly used materials for photonics applications, glasses possess unique structural and optical properties which can be tailored by adapting their

composition and fabrication process, therefore ongoing research is focused on developing new optical glasses to achieve new functionalities. It does not surprise that the UN General Council has declared this year, 2022, the *International Year of Glass*, as to acknowledge the fundamental role that glass has in society.

It is in this framework that the work reported in this manuscript has been carried out.
This PhD has been performed at University of Bordeaux, inside the *Short-pulse Lasers: Applications & Materials* (SLAM) group from the *Centre Lasers Intenses et Applications* (CELIA) laboratory.
The group has internationally-recognized expertise in femtosecond laser inscription of materials for photonics applications. In particular, through collaborations with other laboratories and companies, especially the *Institut de Chimie de la Matière Condensée de Bordeaux* (ICMCB), the group investigates the laser inscription of 3D photonics architectures both in bulk and fibered samples, notably photosensitive phosphate glasses tailored with silver ions. Research work before this thesis consisted of investigating the photochemistry of the silver ions induced in the laser-matter interaction and the optical properties of the associated positive refractive index change, which is not related to structural modifications but rather to the physicochemical mechanism activated in the absorption of the laser pulses. Moreover, this investigation has been carried out alongside a material investigation to understand the influence of the glass structure on the photosensitivity of the material.
The promising results of these studies enabled the fabrication of silver-sustained waveguides, single-step near-surface waveguides and the realization of a refractive index sensor.

Therefore, the work developed during this thesis aimed at further investigating the pulse-to-pulse silver clusters formation induced in the femtosecond interaction to exploit it for the fabrication of high-contrast silver-based waveguides. Moreover, this thesis aims at realizing more complex optical components based on the optical properties of structures characterized by a periodic modulation of the refractive index.

This manuscript is structured as follows.

The first Chapter reports on the fundamentals of laser-matter interaction. The first part is dedicated to glasses, their structural and optical properties and fabrication processes. Then,

ultrafast lasers are introduced as well as the multiphoton ionization processes induced in the absorption of the laser pulses. Finally, basic notions of guided optics are discussed to introduce the waveguiding theory and properties of light propagating in periodic media.

The second Chapter focuses on Direct Laser Writing in glasses. The structural modifications leading to a change in the refractive index of the glass are investigated. In particular, the properties of structures inscribed in thermal and athermal regimes are presented and different fabrication techniques to achieve high induced refractive index contrast are discussed. Thus, silver-containing glasses and their femtosecond laser structuring are presented. A brief state of the art on silver-sustained structures and their optical properties is carried out and some of the major results achieved by the group are presented.

The third Chapter presents the results for the multiscan inscription of silver-containing glasses to achieve high induced refractive index change. The discussion is carried out following the investigation of three different silver-containing glass matrices, analyzing the pulse-to-pulse dependence of the induced index contrast on the number of pulses absorbed during the whole laser inscription in an athermal regime.
Hence, the promising results are exploited in the fabrication of high-contrast waveguides.

The fourth Chapter discusses the fabrication of silver-sustained structures based on periodical modulation of the refractive index. The first part introduces silver-sustained Waveguides Bragg Gratings, discussing their fabrication procedure, the geometrical characteristics and the optical properties. Thus, the transmission spectra are analyzed to investigate their filtering effect. The second part reports on the preliminary results achieved in the fabrication of silver-based transmission Volume Bragg Gratings.

Finally, conclusions are drawn based on the reported results and some perspectives on future works are outlined.

Chapter 1

Basics of glass and laser-matter interaction

Introduction to the chapter

Light-matter interaction is a wide research area in physics that finds many applications in several fields, such as telecommunication, sensing, biology and astrophotonics. The understanding of the phenomena involved in the interaction between an electromagnetic radiation and a medium is of crucial importance to exploit them and improve their photosensitivity. Indeed, the ability to permanently modify the optical properties of a medium, such as the refractive index, by light interaction depends on both the light and the material properties. Therefore, this chapter focuses on both aspects.

Glasses are amorphous materials that have been produced for thousands of years, they can show excellent optical properties depending on their composition and the atomic scale, and interesting thermo-mechanical properties that allow them for achieving high stability and homogeneity in the production process and to be drawn into fibers. For these reasons, glasses are highly suitable for photonics applications. Although the basics of glass production are known since Phoenicians times, the choice of materials and the fabrication process have evolved during the centuries to obtain glasses exhibiting sought optical and mechanical properties, depending on their applications. Nowadays, high-quality optical glasses are produced by several companies, among which Corning, Saint-Gobain and Pilinkgton might be mentioned.
For this reason, a brief overview of the history and the production techniques is given in the first

part of this chapter. Furthermore, the attention is focused on a specific class of inorganic glasses, the oxide glasses, given that this type of glasses have been adopted during the work reported in this manuscript. Moreover, the fabrication process of optical fibers is briefly discussed. To conclude the glass section, the optical properties of glasses are discussed.

The second part of this Chapter focuses on lasers, which have a much shorter history if compared with glasses.
However, in less than a century the development of lasers has deeply impacted research, paving the way to countless applications in several fields, notably medicine, telecommunication, industry and military. In particular, the achievement of ultrafast lasers has allowed for the improving of laser-matter interaction, enabling phenomena that otherwise would not have been achievable. Therefore, firstly the concepts behind laser operations are discussed. Secondly, the ultrafast lasers are introduced and explained to allow for the understanding of the ultrafast laser-matter interaction phenomena that are at the base of the work reported in this manuscript.

The Chapter ends with an introduction to guided optics. The basic notions recalled in this last part are of fundamental importance for the understanding of the main results achieved in this work.

1.1 Glasses

The history of glass is rooted in antiquity: the most ancient archeological finds, like beads and pendants, date the production of glass back to the late third millennium BC, while glass vessels on different scales seem to have been fabricated at the end of the Bronze Age, around the 16th century BC, in the area of Syria and Mesopotamia.

Indeed, the Roman author Pliny the Elder in his encyclopedic work *Naturalis Historia* documented the production of glass in the Roman empire using the sand coming from the mouth of the River Belus, an ancient river located in the Levantine area. The glass obtained adopting the *old* method, as defined by Pliny, using the Syro-Palestinian coastal sand was dull and opaque, therefore the author introduced the *new* method adopted by Romans:

> *Now, however, in Italy, too, a white sand which forms in the River Volturno is found along six miles of the seashore between Cuma and Literno. Wherever it is softest, it*

Figure 1.1: Some of the ancient glass finds from the collection of the Museum of Ancient Glass in Croatia.

> *is taken to be grinded in a mortar or mill. Then it is mixed with three parts soda, either by weight or measure, and after being fused is taken in its molten state to other furnaces. There it forms a lump known in Greek as "sand-soda" [hammonitrum]. This is again melted and forms a pure glass, and is indeed a lump of colorless glass. (Nat. Hist. XXXVI:194)*

Therefore, this production process involved the blending of soda and sand, which would have been subsequently melted in furnaces to obtain *hammonitrum* and then manufactured in the workshops to obtain, for instance, vessels.
From a chemical point of view, the glass produced in ancient history is based on silica SiO_2, like most modern glasses. Silica can be found naturally as quartz, whose melting point is reached around 1700 °C, therefore soda, sodium oxide Na_2O, was used as a flux to lower the melting temperature of silica. Because the silica-soda glass compounds can be easily affected by water, lime, calcium oxide CaO naturally found in limestone and shells, was used as a stabilizer in the glassmaking.
From ancient history to nowadays, the art of glassmaking has evolved and improved. The scientific process of glass formation has been deeply studied, allowing to control of the quality of the powdered materials, limiting the impurities contaminations and customizing the glass optical properties to meet specific constraints, depending on the purposes of the glass applications, leading to well-established industrialization processes on a wide scale.

1.1.1 Definition, formation and properties of oxide glasses

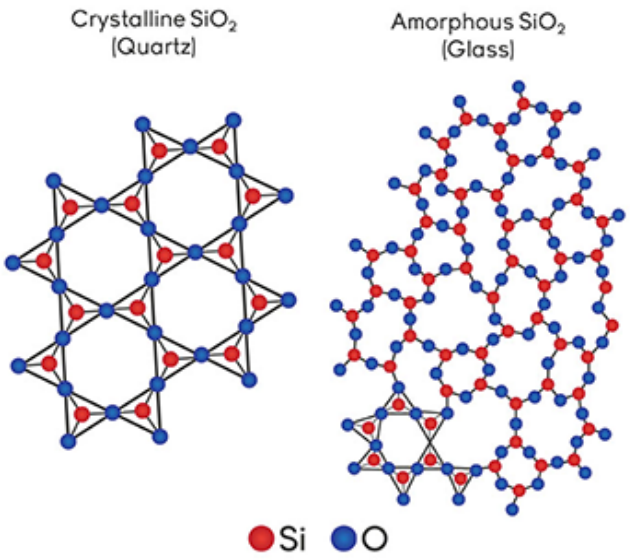

Figure 1.2: Difference in the structural arrangement of silica as (a) a crystal and (b) a glass.

Because of the disordered atomic structures, glasses are identified as amorphous materials that possess a liquid-like structure with no long range order at the molecular scale, though mechanically they behave like a solid.

Although many definitions have been given over the years, the one bringing together the scientific community is that: glass is a non-crystalline solid exhibiting the phenomenon of glass transition. The glass transition of a liquid to a solid state can be obtained by rapidly cooling a melt below its freezing point, causing a strong slowdown of the molecular motion and an increase in the relaxation time. During the cooling process, the rearrangement of the atomic structure is hampered by the viscosity that increases dramatically while the temperature of the liquid decreases. The crystallization phase can be avoided if the cooling process is sufficiently fast since the nucleation process is triggered at higher temperatures than the *glass transition temperature* T_g and for specific conditions of the melt's kinetic parameters and pressure.

In a narrow range around the T_g, a falling out of the equilibrium occurs for which the liquid's volume and enthalpy, both functions depending on the temperature, change abruptly but still continuously, as reported in Fig. 1.3a) and 1.3b).

The heat capacity C_p, reported in Fig. 1.3c), represents the slope of the enthalpy curve at

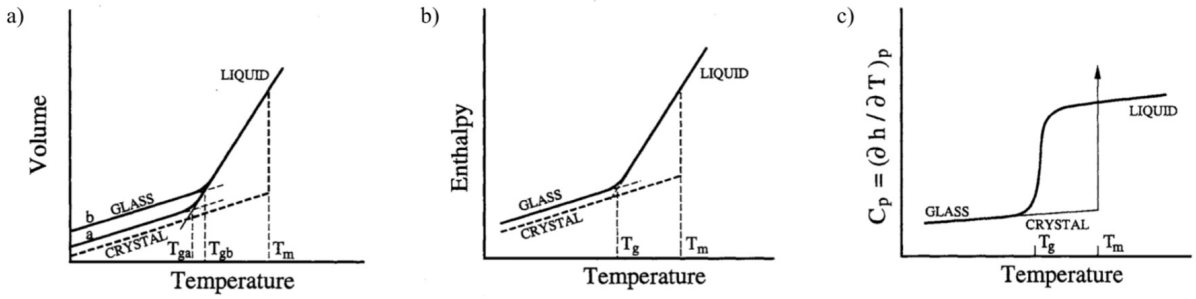

Figure 1.3: Isobaric relationships between (a) volume and temperature; (b) enthalpy and temperature for liquid, glass and solid states; (c) and heat capacity dependence on temperature during the glass transition. Image taken from [1]

constant pressure: when the glass phase is reached, only the vibrational contributions to the heat capacity remain, while the rotational and the vibrational are frozen.
Glasses can be classified in three major families: *metallic*, *organic* and *inorganic*. For the last category, namely the inorganic glasses, the classification is made on the type of anion forming the glass: in the case of *oxide* glasses the anions are oxygen elements, while *halide* and *chalcogenide* glasses are based on fluorine (or chlorine) and sulfur (or selenium or tellurium), respectively.
For the sake of brevity, only the oxide glasses will be discussed in this manuscript since the glasses employed in this work belong to this category.
The classification of oxide glasses follows the Zachariasen rules:

- glass formers, (SiO_2, P_2O_5, GeO_2, AsO_2 etc...) which are able to form the glass network and exhibit a high melting temperature;
- modifiers, which are added to reduce the structural cohesion and to modify the viscosity and the melting temperature, such as NaO_2, CaO and K_2O;
- intermediates, which can act as glass formers or modifiers but are not able to form the glass network by themselves (Al_2O_3, ZnO, Ga_2O_3 etc...).

1.1.2 Optical properties

In the making of glasses suitable for photonic applications it is desirable to control the optical properties of the material: for instance, it is desirable to control the refractive index as a function of the wavelength, which is achieved by adapting the glass composition.

An example of a dispersion curve, *i.e.* dependence of the refractive index on the wavelength,

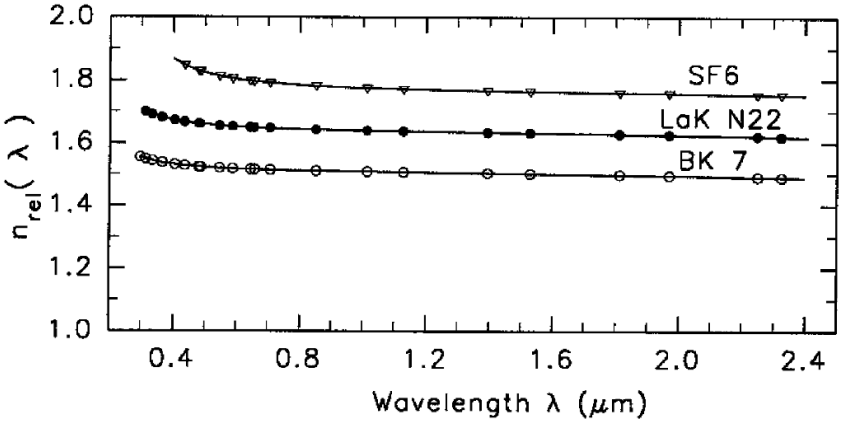

Figure 1.4: Examples of dispersion curves for different optical glasses, among which is reported the BK7 glass, one of the most common Borosilicate glasses used for producing high-quality optics. Image taken from [2].

of different optical glasses is given in Fig. 1.4.
One of the most common dispersion formulas is given by the *Sellmeier equation*:

$$n^2(\lambda) - 1 = \sum_{i=1}^{3} \frac{A_i \lambda^2}{\lambda^2 - B_i^2}, \tag{1.1}$$

where the three terms reported in the sum represent three harmonic oscillators with amplitudes A_i and resonance frequencies B_i, with $i = 1, 2, 3$. Two of the resonance wavelengths in the UV correspond to electronic transitions while the third one in the IR spectral range corresponds to ionic vibrations.
Moreover, the refractive index of the glass is critically dependent on the cooling process of the glass from the liquid to the solid state. Indeed, as reported in Fig. 1.5a, in most of the glasses a higher fictive temperature T_f, *i.e.* the temperature at which the liquid glass is frozen into the solid state, will result in higher volume and lower density glass, therefore lower refractive index.

However, this is not the case for silica glasses: Fig. 1.5b shows how higher density is exceptionally achieved with a fast cooling process. This anomalous behavior is at the base of the positive refractive index change induced by the femtosecond laser interaction in silica glasses. Figure 1.6 shows how a variation of the fictive temperature can influence the refractive index of the glass, in this case a GeO_2 glass.

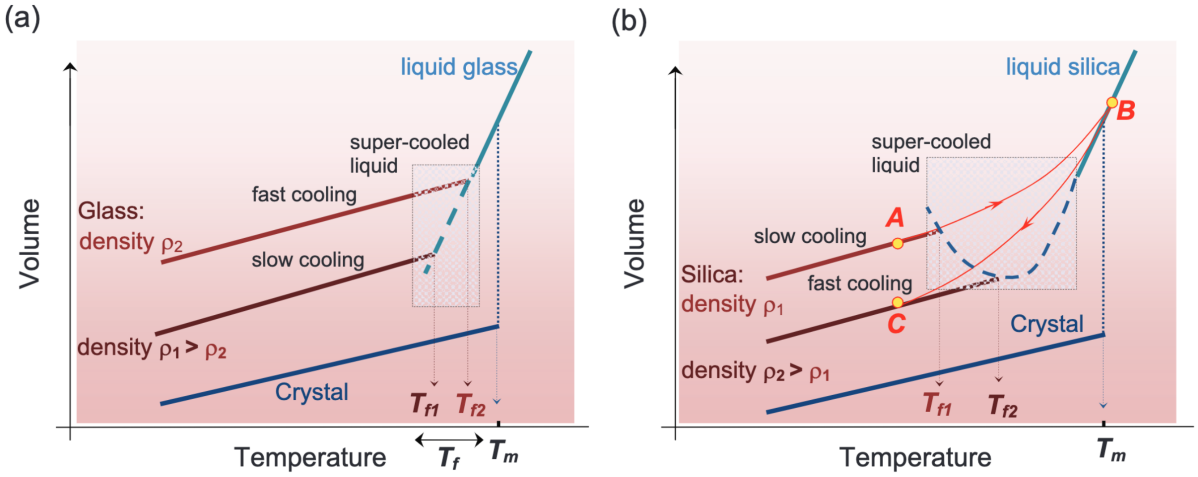

Figure 1.5: Temperature dependence of the glass volume during the glass transition for a) most of glasses and b) silica glasses: for the silica case, higher fictive temperature T_f results in a higher density glass, in contrast with the behavior of the majority of glasses. Image taken from [3].

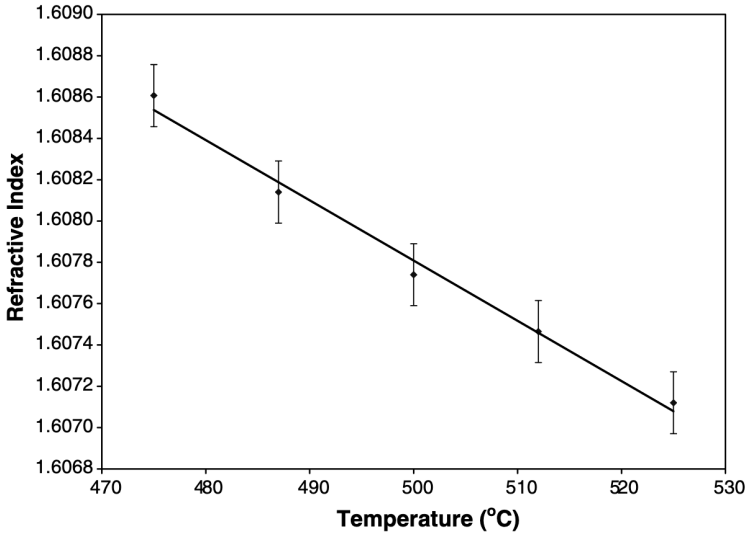

Figure 1.6: Refractive index dependence on the fictive temperature for a GeO_2 glass: the refractive index of the glass can be modified by $\delta n = 1.5 \times 10^{-3}$ by varying the fictive temperature of $\delta T = 50°C$. Image taken from [4].

Given a material, *e.g.* a glass, with refractive index n and an electromagnetic wave interacting with the medium, at the interface between air and the material the parallel $E_{\parallel}$ and perpendicular $E_{\perp}$ components of the incident electric field E_0 of the electromagnetic wave are partially reflected

following the ratios:

$$r_{\parallel} = \frac{E_{\parallel}}{E_0} = \frac{cos\theta_i - ncos\theta t}{cos\theta_i + ncos\theta_t} = -\frac{sin(\theta_i - \theta_t)}{sin(\theta_i - \theta_t)} \tag{1.2a}$$

$$r_{\perp} = \frac{E_{\perp}}{E_0} = \frac{-cos\theta_i - ncos\theta_t}{cos\theta_i + ncos\theta_t} = -\frac{tan(\theta_i - \theta_t)}{tan(\theta_i - \theta_t)} \tag{1.2b}$$

where θ_i and θ_t are the angle of incidence and transmittance, respectively. Thus, from the Eq. 1.2a) and Eq. 1.2b), the reflection coefficients for energy carried by the electromagnetic wave are obtained as $R_{\parallel} = |r_{\parallel}|^2$ and $R_{\perp} = |r_{\perp}|^2$. By interchanging the incidence and transmittance sides, one can obtain the **reflection coefficient** at normal incidence:

$$R = \frac{(n-1)^2}{(n+1)^2}. \tag{1.3}$$

However, Eq. 1.3 can be applied only in spectral regions where the absorbance is low. Indeed, in case of absorption, the refractive index can be written as a complex function $\tilde{n} = n + i\kappa$ where the complex part κ is known as *extinction coefficient*, which is related to the *absorption coefficient* α by $\alpha = \frac{2\kappa\omega}{c}$, where ω is the frequency of the considered electromagnetic wave and c is the speed of light.

In this case it is possible to obtain the *penetration depth* $d \propto 1/\alpha$ that describes the depth inside the material for which the intensity of the electromagnetic field falls to $1/e$ of the incident value. Therefore, the spectral transmittance is defined as the ratio between the transmitted intensity $I(\lambda)$ over the incident power $I_0(\lambda)$. Thus, in such a low signal regime, the **transmission** at a distance d inside the glass can be linked to the absorption coefficient α by the *Beer-Lambert* law:

$$T(\lambda) = \frac{I(\lambda)}{I_0(\lambda)} = e^{-\alpha d}. \tag{1.4}$$

As mentioned, the optical properties of a glass are strictly related to its composition and arrangement related to their thermal history: the transmission window of a glass, *i.e.* the spectral range in which the transmitted light is mostly unaffected, is limited by intrinsic mechanisms such as electronic transitions or excitations of ionic vibrations, commonly called phonons. For instance, silica glasses are transparent between around 180 nm and 3.5 μm, while they are considered as opaque in the extreme UV and in the far-IR: below 200 nm, strong absorption of the UV radiation is caused by the interaction with electrons of $Si-O$ bonds, with structural imperfections and points defects, such as OH. The position of the absorption edge in the UV depends on the presence of impurities resulting from the manufacturing process: for example, impurities such as Fe^{3+}, Cr^{3+} or Ti^{3+} would shift the absorption edge towards the visible.[55;56;57] In the infrared

part, absorption at $2.73-2.85$ μm, 3.5 μm, and 4.3 μm are related to the presence of OH groups, so that the magnitude of the absorption at these wavelengths is related to the concentrations of these groups, which can be regulated during the melting process.[55;56;58] Figure 1.7 reports on the transmission window of different glasses, such as silica, SiO_2, ZBLAN and Telluride.

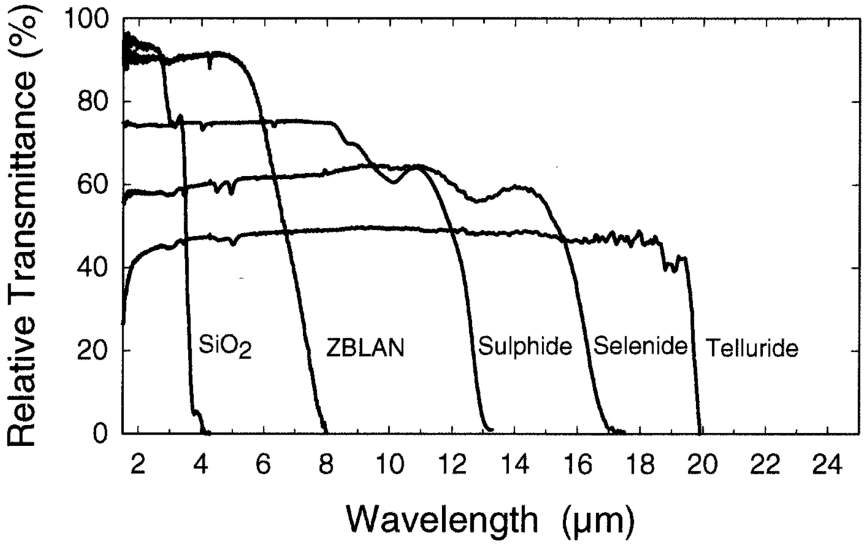

Figure 1.7: Example of the Fresnel-corrected transmission windows of different glasses with thickness around $2-3$ μm. Image taken from[5].

1.1.3 Glass production techniques

Many techniques exist for the fabrication of glasses: depending on the type of glass, its composition, the final structure that is targeted, and on the purpose of the final product, the glass can be synthesized by *chemical vapor deposition*, by *sol gel method* or by *melt-quenching method*. These methods are mostly preferred in laboratories for research applications while in the industry the most used technique is the *float glass method*.

Float glass method It has been introduced in the 1950s as a solution to the increased demand for flat glass production for automotive and architectural applications. The scheme reported in Fig. 1.8 gives an insight into the process followed in this method. A batch of raw materials is prepared and introduced into a horizontal furnace; the temperatures reached in this stage are around $\sim 1550-1600$°C to assure a good chemical homogeneity of the melt. Then, the glass is

brought in the foreheart to a lower temperature, around $\sim 1100 - 1200$°C, from which it flows over a channel over a refractory lipstone or spout on a tin bath. During the flow of the glass on the tin bath, the thickness of the glass sheet is controlled by regulating flow at the entry point and on the lateral sides of the bath. While the glass flows, the temperature of the melt is decreased and its viscosity increases. At the exit of the bath, the temperature of the glass is close to its transition temperature. Finally, once the glass is formed, it is annealed to eliminate the induced stress and the mechanical restraints. Thus, at the end of the process, the glass exhibits flat and polished surfaces due to the floating on the high-quality nonporous metal bath which has polishing nanoparticles of around $4 - 7$ nm.

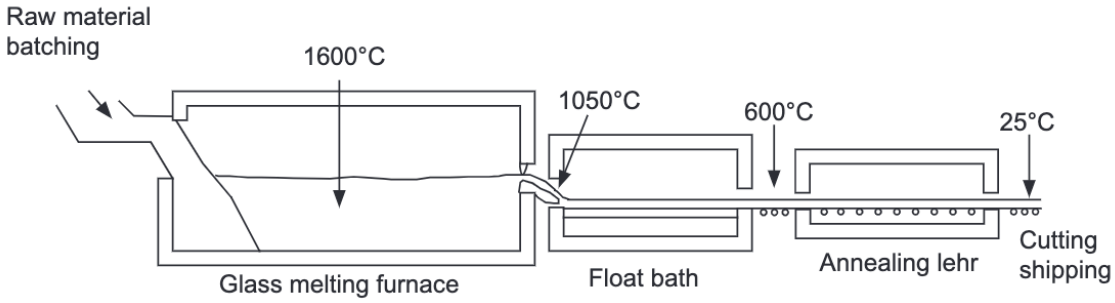

Figure 1.8: Schematic explanation of the float glass technique. Image taken from [6].

Melt-quenching method The technique adopted in the fabrication of the glasses investigated in this work is the melt-quenching method.

In this process, the materials are firstly grinded into powders by using a ball mill. The ground mixture is poured into a platinum crucible and then melted in a furnace, where it reaches a temperature of about 1200°C for several hours ($\sim$ 12 hours). Thus, the crucible is removed from the furnace and the glass is rapidly quenched to avoid the crystallization of the cooled liquid. Finally, as shown in Fig. 1.9, an annealing step below the glass transition is necessary in order to remove the induced mechanical stress. The cutting and the polishing of the produced glass are then performed in a second and third steps.

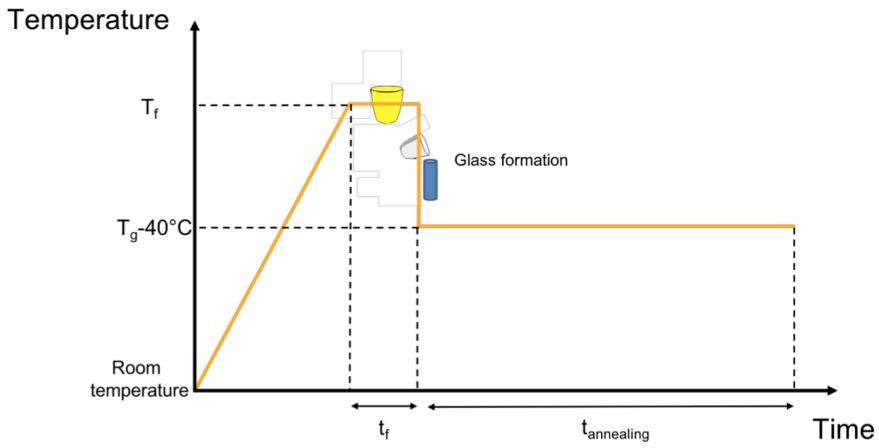

Figure 1.9: Schematic representation of the steps followed during the melt-quenching technique for glass fabrication. Image taken from [7].

1.1.4 Optical fibers fabrication

The fabrication process of optical fiber is now briefly discussed. Optical fibers are now considered of crucial interest for applications in many fields, such as telecommunications, computer networking, lasers, diagnostics and sensing.

Preform fabrication Optical fibers are typically fabricated by drawing a cylindrical preform that has, for instance for a simple fiber configuration, the same core-cladding structure sought in the optical fiber. There are many different methods for producing the preform, the most common is the *Modified Chemical Vapor Deposition* (MCVD), since it assures a very low level of contaminations, allowing for low-propagation losses. The MCVD method requires that the selected chemicals are deposited layer-by-layer onto a glass tube (or a substrate). The glass tube is placed horizontally and rotated on a glass-working lathe and heated uniformly with an oxy-hydrogen flame that is moved up and down along the tube axis. The mixing of the chemicals produces oxidizing reactions, resulting in numerous particles that are deposited on the glass tube. Finally, the deposited layers are sintered, collapsed under vacuum and condensed to form the core-cladding structure. A variant of this process is the *Plasma-activated Chemical Vapor Deposition* (PCVD) in which the glass tube is heated thanks to microwaves, which assures a very precise deposition of the layers, though the fabrication time is longer.

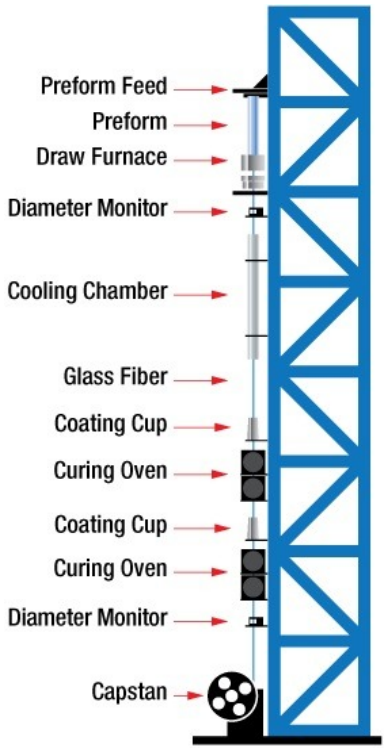

Figure 1.10: Schematic representation of a typical fiber draw tower: in this example, the fiber drawing process includes also the coating step. Image taken from CERSA MCI.

Draw tower Once the preform is ready, the fiber is drawn in a draw tower, depicted in Fig. 1.10. Firstly, the preform tip is heated in a furnace beyond its melting point while pure gasses are injected into the furnace to assure a clean and conductive temperature. Gravity then takes place, allowing for the free fall of the molten gob that stretches into a thin strand. The drawing process then starts from this point, while still keeping the preform heated at a suitable temperature to maintain the ideal drawing tension. The diameter of the fiber during the drawing process is monitored within a tolerance of about 1 μm by, typically, a laser-based diameter gauge. Eventually, the temperature of the fiber is cooled by a helium-filled tube before applying the coating, if necessary, and UV lamps are used to cure the coating layers.

1.2 Basics of the laser-matter interaction

In 1917 in his work *On the Quantum Theory of Radiation* Albert Einstein presented a novel derivation of Planck's formula, a distribution law describing the radiation emitted by blackbodies, in which he described the phenomena occurring in the interaction of photons with atoms, introducing the concept of *stimulated emission*.

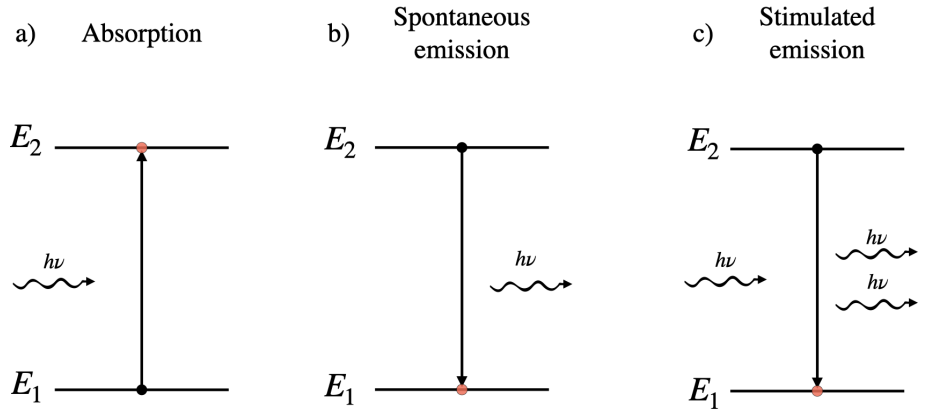

Figure 1.11: Processes occurring in the interaction of photons and atoms.

As discussed by Einstein, an atom with two energy levels E_1 and E_2 can interact with monochromatic radiation of energy $h\nu$ where $h\nu = E_1 - E_2$, i.e. the energy of the photons matches the atomic energy-level difference, resulting in three possible interaction processes: absorption, spontaneous emission and, as above mentioned, stimulated emission.
An absorption (Fig. 1.11a) is a phenomenon induced by a photon of energy $h\nu = E_1 - E_2$ which can promote an atom in the lower energy level E_1 to the excited energy level E_2 by an upward transition. From this excited energy level, the atom may decade spontaneously releasing a photon of energy $h\nu$ while returning to the lower energy level, resulting in a spontaneous emission (Fig. 1.11b). However, if the atom in the excited state interacts with an incident photon, a stimulated emission may occur: a new photon having the same phase, polarization and direction as the incident photon is emitted while the atom returns to the lower energy level (Fig. 1.11c). Such a process is the inverse of an absorption and results in the amplification of the interacting radiation, which is the phenomenon at the base of the operation of lasers.
A first application of the stimulated emission process for amplifying a radiation field resulted in the achievement of *MASER: Microwave Amplification by Stimulated Emission of Radiation*, which was developed independently in 1954 by Charles Townes and Jim Gordon at Columbia

university (USA) and by Nicolay Basov and Alexsander Prokhorov in Russia. Nowadays, masers are principally used as high-precision frequency references in atomic clocks and for low-noise microwave amplifiers in radio-telescopes.
The first studies on the principles of *LASERs*, where the generic term *Light-* is used to refer to any non-microwave amplifier device, were carried out between 1957 and 1959 notably by Arthur Schawlow and Charles Townes, introducing for the first time the concept of a resonator. The first functioning laser was achieved in 1960 by Theodore Maiman at the Hughes Research Laboratories and it was based on a synthetic ruby cube, therefore emitting coherent light in the red zone of the spectral range. In the following years, the development of gas lasers, primarily Helium-Neon lasers, paved the way for the amplification of infrared radiation.

1.2.1 Laser principles and Gaussian beams

A laser is an optical oscillator, that is a cavity composed of at least two mirrors, inside which an amplifier medium is placed and for which the laser oscillation can be described as a standing wave inside the cavity. The induced light emitted by the optical medium is proportional to the population of the excited state, therefore a necessary condition to obtain the lasing effect is the *population inversion* between the fundamental and the excited states. Such a condition is an out-of-equilibrium situation that is achieved by several methods, mostly: optical pumping, electron excitation, inelastic atom-atom collisions or chemical reactions. The minimum of the population difference required to start the amplification process is defined as the *gain condition*. Concerning the cavity, the simplest resonator configuration is composed of two flat, parallel and highly reflective mirrors (see Fig. 1.12a), and it is known as a Fabry-Perot resonator. In this configuration, in the ideal case of lossless mirrors the oscillating frequencies, known as longitudinal modes, are the solutions of the standing wave with appropriate boundary conditions given by the length of the cavity. The distance in frequency between each mode:

$$\Delta\nu = \nu_{n+1} - \nu_n = \frac{c}{2d}, \tag{1.5}$$

is known as *Free Spectral Range* F.S.R., where c is the speed of light and d is the length of the cavity.

Lasers can oscillate with a single longitudinal mode or several longitudinal modes at the same time, depending on the relation between the width of the gain curve and the F.S.R. (Fig 1.12b and Fig 1.12c). In a non-ideal situation, losses can be assumed inside the cavity, for example

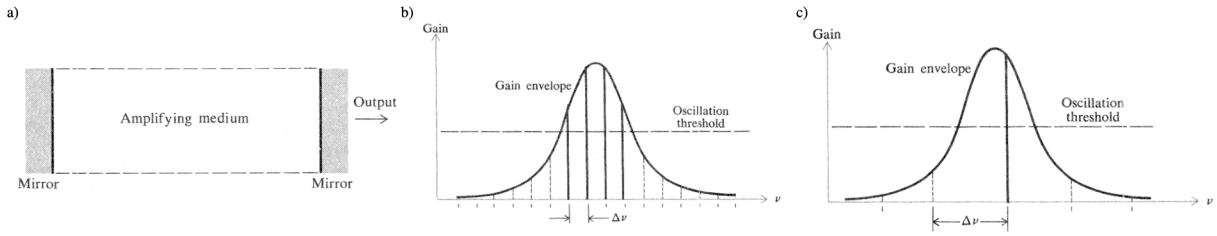

Figure 1.12: (a) Schematic representation of a laser cavity. Oscillation frequencies in the cavity: (b) many modes and (c) single mode. Image taken from [8].

because the reflectivity of the mirrors is less than the unity; in this regard, the quality of the cavity is described by the *Q factor*, which is defined as the ratio between the energy stored inside the cavity and the energy lost in one round-trip between the mirrors. In another way, the quality factor Q ca be found by:

$$Q = 2\pi\nu\tau_c, \tag{1.6}$$

where $\tau_c = d/c\gamma$ is the cavity photon lifetime, given by the transit time d/c of the beam inside the cavity and the cavity loss γ.

The simplest laser cavity configuration investigated so far, constituted by two planar and parallel mirrors, allows for obtaining at the output of the laser a planar wave propagating along the axis of the resonator. Such configuration, however, is non-stable and it is highly sensitive to misalignment. Therefore, laser resonators typically adopt spherical mirrors to achieve stable resonators in order to support the propagation of Gaussian beams.

The Gaussian beam

A Gaussian beam is a solution of the *Paraxial Wave Equation*

$$\frac{\partial^2 u}{\partial x^2} + \frac{\partial^2 u}{\partial y^2} - 2ik\frac{\partial u}{\partial z} = 0, \tag{1.7}$$

where u is a complex scalar wave amplitude describing the transverse profile of a beam propagating along the z axis. The Eq.1.7 is an approximation of the scalar wave equation

$$[\nabla^2 + k^2]E(x, y, z) = 0, \tag{1.8}$$

and it is used for describing the propagation of an electromagnetic field $E(x, y, z) = u(x, y, z)e^{ikz}$ whose transversal variation $u(x, y, z)$ along the propagation direction z is slow compared to the

plane wave e^{ikz} variation in the z direction.

At the propagation position related to its minimal dimension, the Gaussian beam is characterized by a spot size radius ω_0, known as the beam *waist*, and a planar wavefront with an infinite ray of curvature $R_0 = \infty$ in the transverse dimension. The associated reference plane is commonly taken at $z = 0$.

When getting far from the $z = 0$ plane, the beam diverges and the following parameters can be used to describe it:

$$\omega(z) = \omega_0 \sqrt{1 + \left(\frac{z}{z_R}\right)^2} \tag{1.9a}$$

$$R(z) = z + \frac{z_R^2}{z} \tag{1.9b}$$

$$\psi(z) = tan^{-1}\left(\frac{z}{z_R}\right) \tag{1.9c}$$

$$\omega_0 = \sqrt{\frac{\lambda z_R}{\pi}} \tag{1.9d}$$

where z_R is known as the *Rayleigh range* and defines the distance along z for which the width ω of the beam is $\omega = \sqrt{2}\omega_0$, while λ is the wavelength of the radiation in the considered propagation medium.

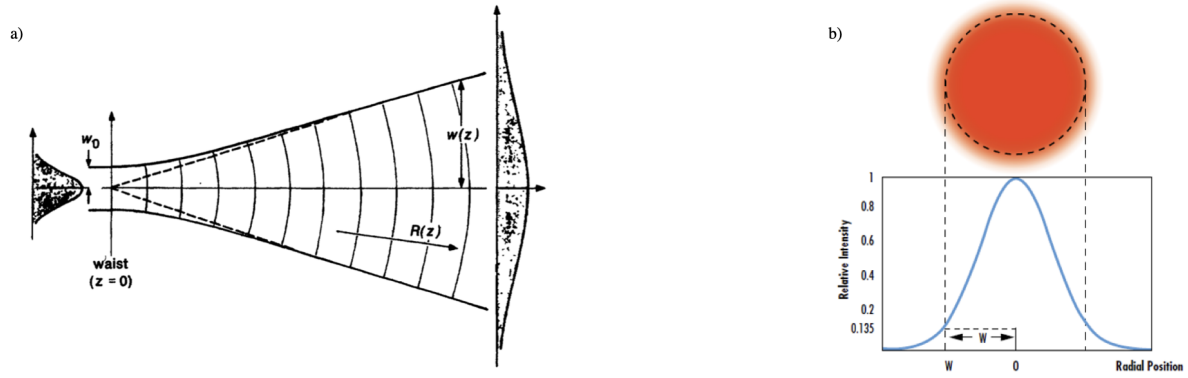

Figure 1.13: (a) Divergence of the Gaussian Beam away from the waist. Image taken from [9]. (b) Intensity profile of a Gaussian beam along the radial position. Image taken from Edmund Optics.

Typically, the quality of a laser beam is quantified by the *beam quality factor* M^2.[59] Such factor limits the degree to which the laser beam can be focused for a given beam divergence

angle:

$$\theta = M^2 \frac{\lambda}{\pi\omega_0}. \tag{1.10}$$

The Gaussian beam has $M^2 = 1$, which is the smallest value achievable for the M^2 factor due to diffraction law.

Figure 1.13(a) depicts the evolution of the Gaussian beam along z while diverging from its waist, while Fig. 1.13(b) shows the Gaussian profile of the beam intensity along the radial direction:

$$I(r) = \frac{2P}{\pi\omega} e^{-2r^2/\omega^2}, \tag{1.11}$$

where $P = \iint |u|^2 dA$ is the total power of the beam integrated over a cross-sectional area dA. Finally, an estimation of the collimated range of a Gaussian beam is given by the *confocal parameter* b given by:

$$b = 2z_R = \frac{2\pi\omega_0^2}{\lambda}. \tag{1.12}$$

Focusing a Gaussian beam

When a gaussian beam is focused using a microscope objective with a given N.A., the waist ω_0 of the laser beam at the wavelength λ in the focused spot can be found by the Airy diffraction pattern. A way to measure its dimension is given by the Rayleigh criterion:

$$\omega_0 = 0.61 \frac{\lambda}{N.A.}, \tag{1.13}$$

where the coefficient $\mathcal{C} = 0.61$ is found by measuring the distance between the maximum of the intensity distribution, described by a first-order Bessel function $\mathcal{J}$, and its first zero. However, this is not the only criterion: other ways to measure the focused beam spot derive from measuring the distance between the maximum of the intensity profile and its half (FWHM) or the position at which it drops to $1/e^2$ its value. In the case of high numerical aperture, $N.A. > 0.7$, the coefficients $\mathcal{C}$ given by the FWHM and the Rayleigh criteria almost coincide, while for $N.A. < 0.7$ the FWHM is only $\sim 85\%$ of the value, so $\mathcal{C} = 0.518$.[60]

However, the Airy function depicts the minimum spot achievable for an ideal optical system, free of aberrations that are generally introduced in complex lens systems such as microscope objectives. Moreover, it should be assumed that the back aperture of the microscope objective is uniformly illuminated, which is normally obtained by overfilling the objective's aperture. On the contrary, if the beam underfills the back aperture, the N.A. will be reduced and the focused beam spot will result larger than the predicted one, as depicted by Fig. 1.14.

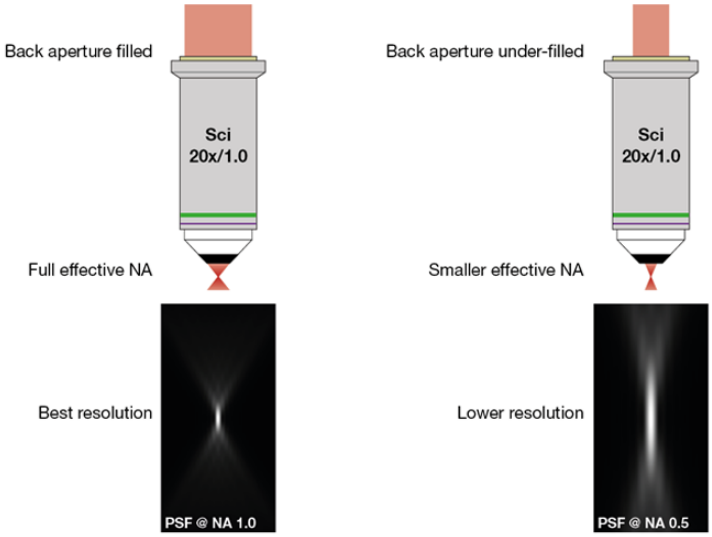

Figure 1.14: Overfilling the back aperture of a microscope objective is the way to fully exploit its numerical aperture. On the contrary, underfilling the back aperture results in reducing the numerical aperture and, thus, increasing the dimensions of the focused spot. Image taken from Scientifica.uk.com.

The Gaussian beam in a laser cavity

The wavefront of a gaussian beam is approximately planar near the beam waist while its curvature increases gradually while getting far from $z = 0$, until the wavefronts in both directions become spherical for distances much larger than the confocal parameters. Therefore, if the radius of curvature of a Gaussian beam and that of a spherical mirror coincide, the Gaussian beam reflected by the spherical mirror perfectly overlaps the incident beam. As a consequence, for the case of a Gaussian beam reflected inside a spherical resonator, *i.e.* a cavity constituted of two spherical mirrors separated by a distance d, for which the radius of curvature of the Gaussian beam at the same distance d matches that of both the spherical mirrors, the Gaussian beam is a solution to the Helmholtz equation with the boundary conditions imposed by the spherical mirrors. Finally, if the phase of the Gaussian beam after a round-trip inside the resonator satisfies:

$$2kd - 2\Delta\psi = 0 \text{ or } \pm 2\pi, \tag{1.14}$$

where $\Delta\psi = \psi(z_2) - \psi(z_1)$, z_1 and z_2 are the position of the two mirrors and ψ is defined as in the Eq. 1.9c, the Gaussian beam is defined as an Eigenmode of the resonator and the frequencies

$$\nu_q = q\Delta\nu + \frac{\Delta\psi}{\pi}\Delta\nu, \tag{1.15}$$

with $q = 0, \pm1, \pm2\ldots$ and $\Delta\nu$ the *Free Spectral Range*, introduced in Eq. 1.5, are the resonance frequencies of the Gaussian modes.

However, Gaussian beams are not the only solution, or *modes*, of the Helmholtz equation in the paraxial approximation inside the laser cavity. More generally, for these solutions the electric field profile is expressed as the product of a Gaussian function with a *Hermite* polynomial, therefore called *Hermite-Gaussian* modes. The Hermite-Gaussian modes are most generally called Transverse Electromagnetic Modes ($\text{TEM}_{n,m}$) and their intensity distribution, reported in Fig. 1.15, present n nodes in the horizontal direction and m nodes in the vertical direction, in addition to the asymptotic null amplitude far from the beam center. The Gaussian beam is depicted

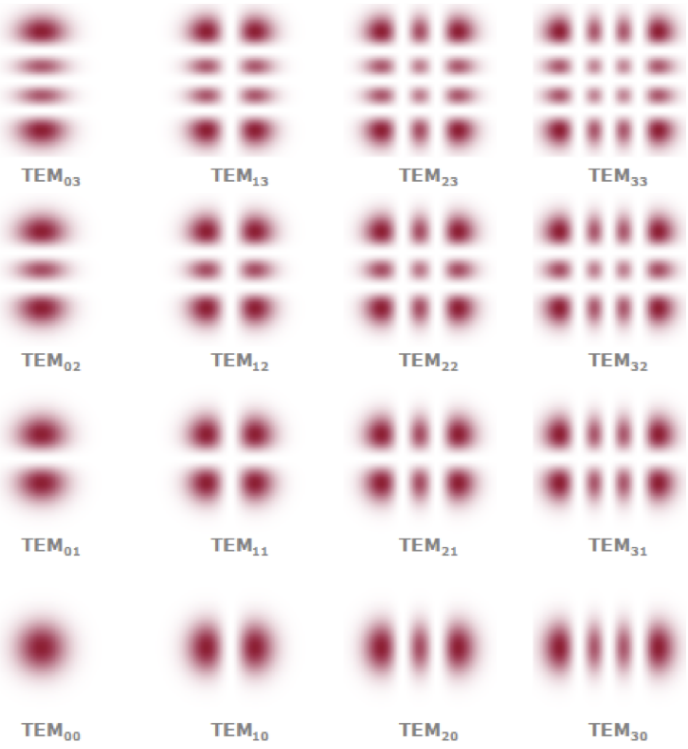

Figure 1.15: Intensity distribution of the Transverse Electromagnetic Modes ($\text{TEM}_{n,m}$). Image taken from RP-Photonics.

by the case of $n, m = 0$, therefore is also known as TEM_{00}. Both the amplitude distribution

and the wavefront profile of a Hermite-Gaussian beam with order (n, m) differ from those of a Gaussian beam. However, a laser cavity constructed to be resonant for a given Gaussian beam also allows for resonating all the Eigenfunctions of the associated Hermite-Gaussian basis set, independently on the values n, m. The resonance frequencies of these Hermite-Gaussian modes are then deducted from Eq. 1.15 as follows:

$$\nu_{n,m,q} = q\Delta\nu + (n + m + 1)\frac{\Delta\psi}{\pi}\Delta\nu. \tag{1.16}$$

These frequencies are known as longitudinal, or axial, modes and the distance between each frequency of a given transverse mode is given by the F.S.R. $\Delta\nu = c/2d$. The Hermite-Gaussian functions represent a complete set of solutions to the Helmholtz equation in the paraxial approximation, therefore any other solution can be obtained as a superposition of these functions. Other examples of complete sets are given by the *Laguerre-Gaussian* beams, which represent the Hermite-Gaussian beams in cylindrical coordinates, and by the *Bessel* beams, which describe beams with planar wavefronts but non-uniform intensity distribution in the transverse profile that is independent of the z position, leading thus to non-diverging beams over a given distance. Two or more transverse modes that do not overlap spatially can coexist inside the laser cavity, they may oscillate simultaneously due to the difference in the spatial distribution:

$$\nu_{n,m,q} - \nu_{n',m',q} = [(n + m) - (n' + m')]\frac{\Delta\psi}{\pi}\Delta\nu. \tag{1.17}$$

for two modes with n, m and n', m' orders. However, their contribution to the laser oscillation depends on the relation losses/gain for each transverse mode.

Laser cavities are generally designed in order to select only the TEM_{00} mode, since it is the one that can be focused to the smallest spot size. However, higher-modes oscillations with lower beam quality are suitable for generating larger optical powers than that of the ideal Gaussian beam.

Because of the difference in the spatial distribution, the selection of a specific transverse mode can be accomplished by placing an aperture of proper shape inside the laser cavity. Similarly, a single longitudinal mode can be selected by either sufficiently increasing the losses so that only the mode with the largest gain remains allowed to oscillate, or by increasing the longitudinal separation $\Delta\nu = c/2d$, so that such a spectral width becomes larger than the laser gain bandwidth, therefore by decreasing the length of the cavity.

As an example, single-mode selection can occur by inserting a short resonant cavity into the main laser cavity, so that the final longitudinal frequency must simultaneously undergo the two conditions of Eigenfrequencies of each of the two embedded cavities.

If many longitudinal modes are enabled to oscillate inside the laser cavity, under ordinary conditions, the phase of each mode has a random initial value, which corresponds to a random variation of the laser intensity (see Fig. 1.16a).

Pulse generation

Mode Locking However, if the phases are locked together by an external mean, then the modes can be coupled and form a Fourier-series of periodic functions with period $\tau_p = 1/\Delta\nu$, which constitutes a periodic pulse train. Each pulse has a duration $\Delta\tau_p = 1/\Delta\nu_L$, where $\Delta\nu_L = N\Delta\nu$ is the total oscillating bandwidth and N is the number of allowed longitudinal modes.

The Mode-Locking pulse generation can be achieved in two ways: **active mode locking**

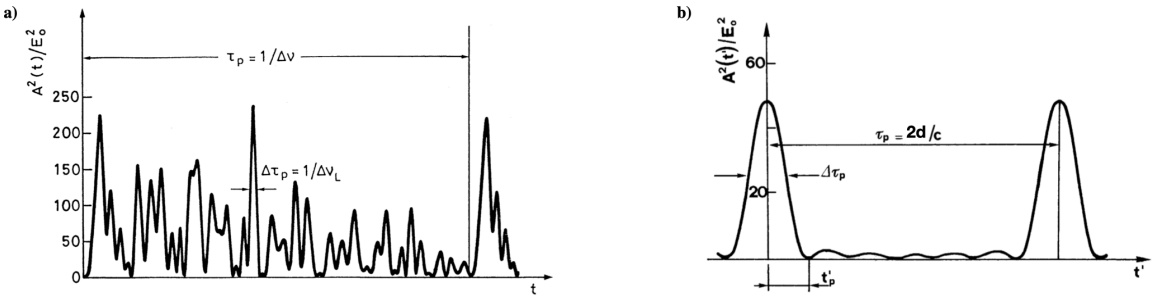

Figure 1.16: (a) Example of the time behavior of the squared amplitude of the electric field $|A(t)|^2$ of all the oscillating modes inside the cavity with same amplitude E_0 but random phases. (b) Example of the time behavior of the squared amplitude of the electric field $|A(t)|^2$ for the case of 7 oscillating modes with same amplitude E_0 and locked phases. Images taken from [8]

or **passive mode locking**. The first method requires the presence of an acousto-optic or electro-optic modulator placed inside the resonator that is synchronized with the oscillator's round trips so that the cavity losses are reduced right when the laser pulse is emitted and for the whole duration of the pulse.
The passive Mode-Locking is achieved using a saturable absorber, *i.e.* a medium whose absorption coefficient is dependent on the intensity of the light passing through it. Indeed, when the phases of N longitudinal modes oscillating inside the cavity with the same amplitude E_0 are locked together, the intensity of the resulting pulse is given by $N^2E_0^2$. For example, Fig. 1.16b

reports the time behavior of the intensity of seven oscillating modes with locked phases. In this case, the saturable absorber would be chosen so that its absorption is small or negligible at the intensity of the pulse train. An example of such a passive switch is the *SEmiconductor Saturable Absorber Mirror* (SESAM) which works in reflection, operating in a wide spectral range from 800 nm to 1600 nm, for pulse duration from fs to ns, at mean power at the mW level up to hundreds of W.

Other techniques to achieve laser pulse trains are: **gain switching**, **Q-switching** and **cavity dumping**.

Gain switching The gain switching method consists in turning on and off periodically the pump by just modulating its electric current. In this way, the lasing is achieved only during the on times, in which the gain coefficient exceeds the losses (see Fig. 1.17.

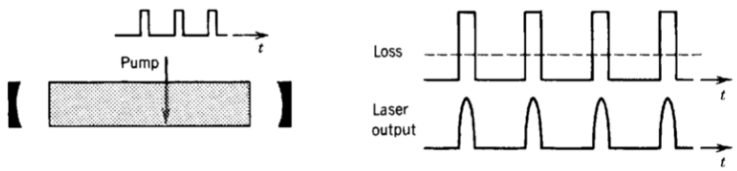

Figure 1.17: Schematic representations of gain switching with the time-dependence of the gain and losses inside the cavity and the associated laser output. Images taken from [10].

Q switching By acting on the Q cavity factor, introduced in Eq. 1.6, it is possible to act on the resonator losses by, for instance, introducing inside the cavity a modulated absorber. When the losses are increased, the energy constantly delivered by the pump is stored by the atoms so that when the losses are reduced an intense ultrashort pulse is emitted from the cavity, as shown in Fig. 1.18.

Cavity dumping The periodical dumping of the cavity is realized by temporally removing the transmitting mirror of the resonator, as depicted in Fig. 1.19, by just misaligning it for example. In this way during the off times, the transmittance of the cavity is reduced to storage the photons inside the resonator, while during the on times the transmittance is instantly increased to the maximum, resulting in an intense laser pulse emission.

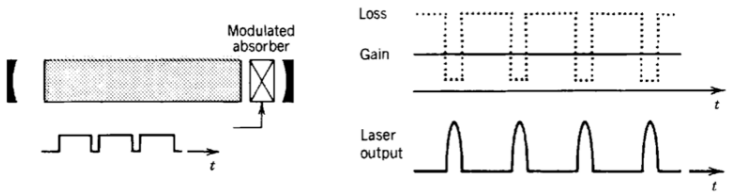

Figure 1.18: Schematic representations of Q switching with the time-dependence of the gain and losses inside the cavity and the associated laser output. Images taken from [10].

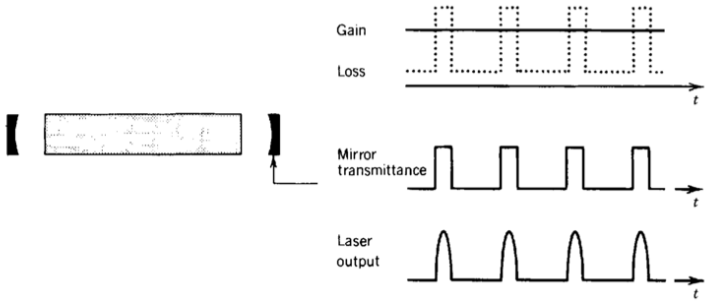

Figure 1.19: Schematic representations of cavity dumping methods for pulse generation: the time-dependence of the mirror transmittance allows for tuning the gain/loss ratio. Images taken from [10],

1.2.2 Ultrafast pulsed lasers

Between the end of the 60's and the beginning of the 70's much interest has been paid to the production of dye-based lasers which could enable the generation of sub-picosecond pulses by passive mode-locking or self-mode locking. [61;62] The properties of the pulsed dye lasers depend on both the choice of the dye and the wavelength of the source used for the pumping: the emission spectrum could be varied continuously in the range 350 nm to 1 μm, with a spectral bandwidth that could be narrowed down to 1 pm in commercial dye lasers. Wavelengths below 350 nm can be obtained by second harmonic generation due to the high peak power that could be reached in a single pulse. Flash-lamps or laser systems like copper vapors lasers or Nd:YAG lasers can be used as pumps, in this way it is possible to achieve pulsed dye lasers with repetition rates of 10 Hz up to 1 MHz. Dye lasers in the configuration of Colliding Pulse Mode-Locked (CPM) were the first laser systems able to produce short pulses below 100 fs in 1980; the use of prisms in this configuration to compensate normal dispersions allowed to shorten the pulses down to 27 fs. [63] Moreover, external pulse compression resulted in achieving short laser pulses

of 6 fs in 1987, as reported in Fig. 1.20a.[64]

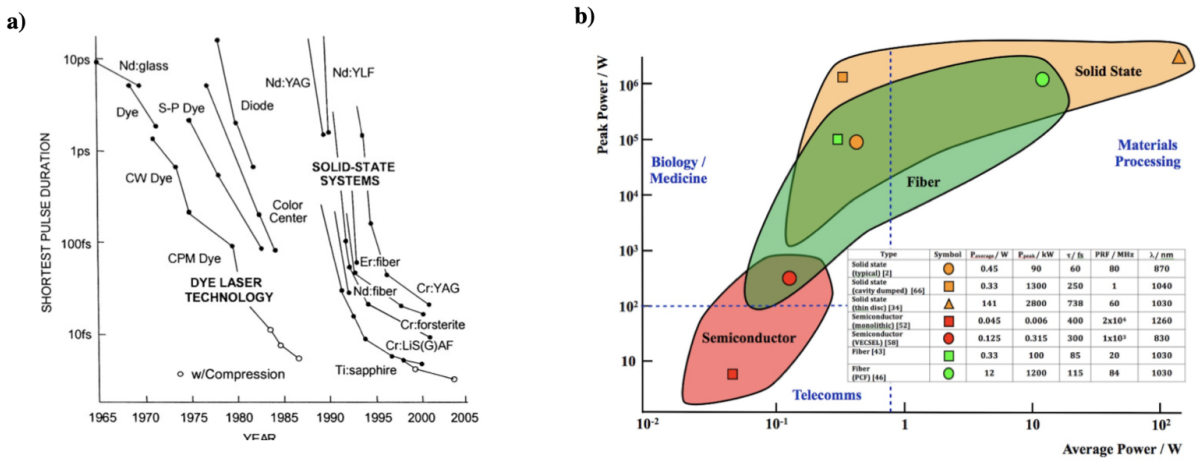

Figure 1.20: (a) History of ultrashort pulse duration. Image taken from[11]. (b) Peak power versus average power for different types of ultrashort pulse lasers. Image taken from[12].

However, it is the pioneering work of Sibbett *et al*[65] in 1991 to be recognized as a key point for the fabrication of femtosecond lasers systems. The laser system produced by this group was based on a self-mode-locked Titanium:Sapphire solid state laser in which the nonlinearity of the crystal was used to lock in phase a considerably large number of longitudinal modes to generate sub-100 fs pulses. Indeed, this work proposed the novel *Kerr Lens Mode Lock* (KLM) technique: an artificial saturable absorber based on the *Kerr effect* was successively used to passively achieve the mode-locking of the laser. The Kerr effect is a nonlinear effect producing a change in the refractive index of a material that is dependent on the intensity:

$$n = n_0 + 2n_2 < E^2 >, \tag{1.18}$$

where n_0 is the value of the refractive index under a weak field and the nonlinear index n_2 represents the increase of the refractive index depending on the intensity $< E^2 >$, where the brackets imply a time average.[13] When considering most common cases where n_2 is positive, the Kerr effect is also known as *self-focusing* effect. Therefore, a transient Kerr lens leads to an additional focusing optical element in the resonator mode when considering high enough intensities. If an aperture is placed inside the cavity, the Kerr lens can lead to a change in the gain/loss ratio in two ways: a) by shrinking the beam at the position of the aperture (*Hard-aperture KLM*), therefore reducing the diffraction losses, or by increasing the overlap between the laser and the pump beams (*Soft-aperture KLM*), therefore achieving a higher gain than that at low intensity.

By exploiting this technique it was possible to achieve ultrafast pulse Ti:Sa lasers with pulse width down to 5 fs.[66] Figure 1.20a reports on the historical developments of ultrashort pulse lasers: it can be highlighted that Ti:Sa lasers were the first to achieve short pulse width below 10 ps without the need for an extra-cavity amplification and pulse-compression process.
Since the first demonstration of KLM Ti:Sa lasers, the development of ultrafast lasers has involved the research of new gain media resulting in a wide and versatile range of ultrafast lasers sources.

Solid-state lasers Solid-state lasers can be classified in: rare-earth-doped (Yb^{3+}, Er^{+3}, Nd^{3+}, Tm^{3+}, Ho^{3+}) and transition-metal-doped (Cr^{2+}, Cr^{+3}, Cr^{4+}, Ti^{3+}, Ni^{2+}, Co^{2+}). For the case of rare-earth-doped lasers, $4f$-electrons are responsible for the laser transition, which are shielded from the crystal host, as a consequence the gain bandwidth is limited and the pulse duration can be of few hundreds of fs. Shorter pulses can be achieved in rare-earth-doped lasers in glass hosts, for instance phosphate or silicate glasses doped with Nd^{3+} or Yb^{3+}, possibly leading to pulse durations down to $\sim$ 60 fs, but the average power is limited by the glass thermal conductivity.[67;68] In recent years, the rapid growth in the production of InGaAs-based pump laser diodes has facilitated the spreading of low-cost, efficient and compact Yb-based fs lasers at 1 μm. For instance, SESAM mode-locked Yb^{3+}:KGW lasers have been produced achieving $\sim$ 70 fs pulses, same pulse duration was achieved by Kerr-lens mode-locked Yb^{3+}:KYW lasers, while external compression for a mode-locked Yb:YCOB laser allowed for 35 fs pulses.[69;70;71] Transition-metal-doped lasers have a broader amplification bandwidth than rare-earth-doped lasers, this allows for shortening the pulse duration below 0.5 ps. In this case, $3d$-electrons are responsible for laser transition but the shielding effect from the host crystal is not as strong as for the rare-earth-doped counterpart, therefore these lasers are phono-broadened and can support much shorter pulses. For instance, Ti^{3+}:sapphire lasers can generate down to 6 fs long pulses when pumped with frequency-doubled solid-state laser.[66] Moreover, these lasers can operate in mid-IR range: for instance, C^{4+}-doped Mg_2SiO_4 (known as Forsterite) or $Y_3Al_5O_{12}$ (YAG) lasers can generate sub-50 fs pulses around 1.3 μm and 1.55 μm, which are interesting regions for biological applications, while C^{2+}-doped chalcogenide materials, such as Cr:ZnS can emit around 2.4 μm, making them suitable for high-resolution molecular spectroscopy.[72;73]

Fiber lasers Fiber lasers represent a versatile and practical alternative to solid-state lasers. Generally, fiber lasers are based on Yb-, Er- and Tm-doped gain media, therefore operating

in the NIR spectral range. Most of the fiber lasers generating high average output power are fabricated in the *Master Oscillator Power Amplifier* (MOPA) configuration: the master oscillator provides low-power/energy pulses, which are carefully engineered so to achieve low noise, high compactness, and extreme robustness. A subsequent fiber amplifier can increase the average power by several orders of magnitude. In the MOPA configuration, the mode lock is achieved by a saturable absorber.Using the Chirped-Pulse Amplification (CPA) process, such as for solid-state lasers, it is possible to achieve more than MW peak power.[74] Since the cavity dispersion may affect the evolution of the laser pulse in a single pass inside the cavity, Photonics Crystal Fibers (PCFs) and chirped Fiber Bragg Gratings (cFBGs) are used in order to compensate for this problem. Concerning the achievable repetition rates, several-meters-long fiber can operate at tens of MHz. Oppositely, in order to achieve repetition rates above 200 MHz, the length of the cavity must be reduced to a few tens of centimeters, requiring a high doping level to provide sufficient gain.[75;12]

Ultrafast lasers provide high peak intensity and broad optical spectrum and can be used to probe the dynamics of physical systems that have a very short timescale. Indeed, these lasers find many applications in a wide range of research fields such as material processing, metrology, medicine, nonlinear optics and telecommunication.
Nevertheless, many advantages of using focused ultrafast laser sources come from the **Multi-photon absorption** (MPA), which is a nonlinear process triggered during the interaction of such lasers and the media.

1.2.3 Multiphoton absorption

As introduced at the beginning of Sec. 1.2, the (linear) absorption reported in Fig. 1.11a is a process involving a single photon that can excite an atom in the fundamental state E_1 to the excited state E_2, if this transition is allowed by selection rules. However, if this transition is forbidden or if specific conditions are met, multiphoton absorption can occur: in this case a number N of photons is simultaneously absorbed, each photon allowing the transition to a virtual state, as depicted in Fig. 1.21; the number N of photons depends on the energy of the photons and the difference between the two atomic states (or the bandgap) E_g, so that $N\hbar\omega \geq E_g$. The MPA process is highly dependent on the field intensity I, therefore the rate of

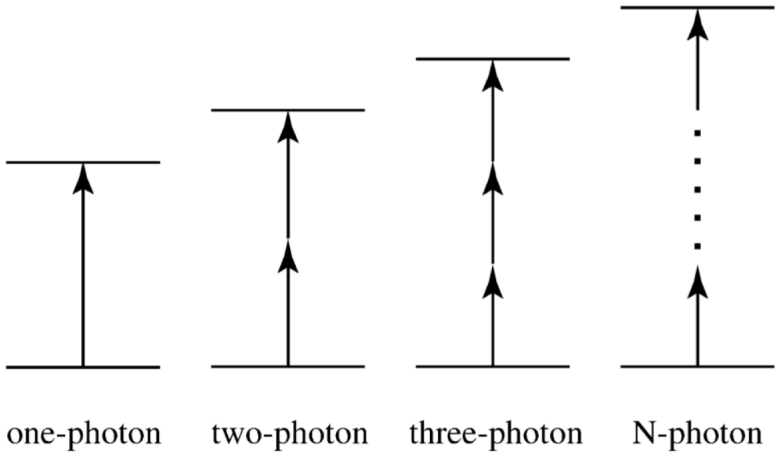

Figure 1.21: Examples of linear and multiphoton absorption for different numbers of photons N. Image taken from [13].

this process can be written as:

$$R(I) = \sigma^{(N)} I^N \tag{1.19}$$

where $\sigma^{(N)}$ represents the N-photon cross-section.

However, the MPA process depicted in Fig. 1.22a, in which an electron of the valence band is promoted to the conduction band by the simultaneous absorption of two or more photons, is not the only pathway to achieve photoionization. Indeed, a competitive process is represented by the **tunneling ionization**, depicted in Fig. 1.22b, in which the intense laser field can modify and depress the Columbian potential that bonds the electrons to the atoms enough to allow the tunneling of the electrons out of the potential well.

These two channels of photoionization can be achieved in the weak- or strong-field regimes, respectively for multiphoton and tunneling ionization. The transition between these two regimes is expressed by Keldysh's parameter [76]

$$\gamma = \omega \frac{\sqrt{2 m_e I_p}}{e E_0} \tag{1.20}$$

where m_e and e are the mass and the charge of the electron, I_p is the ionization potential of the atom and ω and E_o are the frequency and the electric field amplitude of the laser source. The tunneling ionization is possible only when the mean tunneling time τ_t of an electron traveling

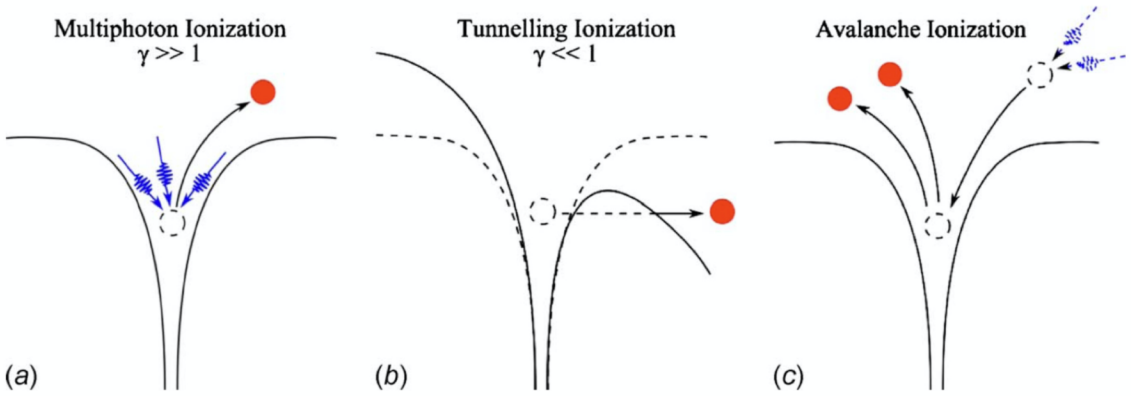

Figure 1.22: Schematic representation of the release of an electron from the valence band during the photoionization processes: (a) multiphoton ionization, (b) tunneling ionization (b) and (c) avalanche ionization. Image taken from [14].

with a mean velocity $< v >= (2I_p/m_e)^{1/2}$ (by the Virial theorem) [77]:

$$\tau_t = \frac{l}{< v >} = \frac{\sqrt{I_p m_e}}{\sqrt{2} e E_0}, \tag{1.21}$$

where $l = I_p/eE_0$ is the length of the barrier the electron has to cross, is shorter than half of the laser period, when the ionization rate is at its maximum,

$$\tau_t \ll \tau_0/2 = 1/2\omega \implies \gamma \ll 1 \tag{1.22}$$

Hence, for $\gamma \gg 1$ the dominant photoionization process is the multiphoton absorption.
For the case of the work reported in this manuscript the Keldysh's parameter is $\gamma \sim 1.3$: although it is not very far from the boundary condition, the main process taking place is considered as to be the multiphoton absorption.

The multiphoton ionization can create enough electrons to transform the medium into a *plasma*, *i.e.* a partial or fully ionized gas. The plasma formation is described by [13]:

$$\frac{dN_e}{dt} = \frac{dN_i}{dt} = (N_T - N_i)\sigma^{(N)} I^N - r N_e N_i, \tag{1.23}$$

where N_e and N_i are the volume number density of generated free electrons and ions, respectively, N_T is the concentration of elements (namely the total amount of ionized and unionized atoms), r is the electron-ion recombination rate and $\sigma^{(N)}$ is the $N-$photon cross-section reported in the

Eq. 1.19. The dielectric constant of the plasma differs from the one of dielectric media and it's defined by:

$$\epsilon(\omega) = 1 - \frac{\omega_p^2}{\omega^2}, \tag{1.24}$$

where $\omega_p = \sqrt{4\pi N e^2/m_e}$ is known as *plasma frequency*.

Finally, in the case of high intensity of the laser field, the free electrons produced during the photoionization process can be accelerated by the intense laser field to the point they acquire enough kinetic energy to free other electrons from the valence band in the collision with the surrounding atoms. These newly released electrons can in turn produce additional free electrons; this process, known as **avalanche ionization**, is depicted in Fig.1.22c. When the number of free electrons is critical, it creates a high-density plasma for which the plasma frequency is equal to the one of the laser source. In these conditions the medium becomes highly absorbing - a phenomenon known as *inverse Bremsstrahlung* absorption - resulting in the deposition of high heat energy and in the breaking of chemical bonds, leading to a breakdown of the optical material.

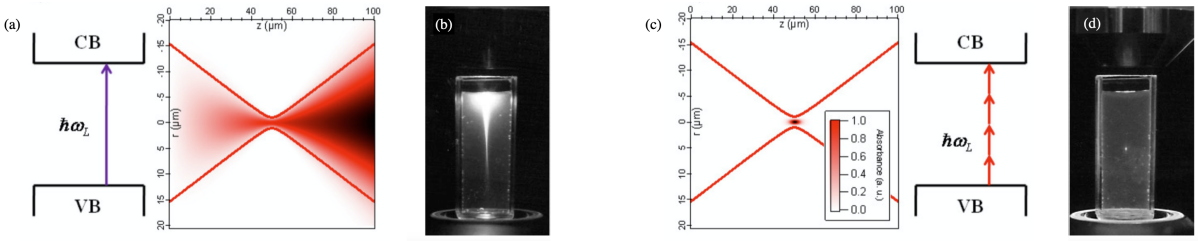

Figure 1.23: Interaction zones for the case of linear absorption (figures (a) and (b)) and multiphoton absorption (figures (c) and (d)). In particular, images in (b) and (d) show the fluorescence of a dye solution under laser excitation, proving that the interaction in the case of multiphoton absorption occurs only in the focal volume. Images taken from [13;15]

The importance of the multiphoton absorption lies in its nonlinear dependence on the field intensity I, as described in Eq. 1.19. As a consequence, for the case of a focused laser beam, the MPA process will take place only in the focal volume, where the focused intensity is higher. Figure 1.23 shows indeed the difference in the interaction zone between linear (Fig. 1.23a and Fig. 1.23b) and multiphoton absorption (Fig. 1.23c and Fig. 1.23d).

In particular, the images reported in Fig. 1.23b and Fig. 1.23d show the fluorescence emitted by the excitation of a dye solution in interaction with a laser source in the two above-mentioned cases: for the case of multiphoton absorption, the excitation is achieved only in the focal volume.

For this reason, multiphoton absorption is a technique widely adopted in serval research fields. For instance, *two-photon absorption microscopy* is largely used in the fluorescence imaging of cells or thick biological samples due to the several advantages that this technique has compared to confocal microscopy. Indeed, when operating with an near-IR source, the penetration depth inside the specimen is higher than what achieved in classical fluorescence microscopy; in addition, higher wavelengths lead to less photobleaching and thus less photo-damaging of the sample. Moreover, since the excitation occurs in the focal volume, this technique strongly allows for reducing the background noise.
Nonetheless, MPA is a very important technique adopted for the nonlinear spectroscopy of optical and electronic properties of crystals, especially for the cases in which specific transitions are forbidden by selection rules for linear absorption. Finally, MPA plays a relevant role in the fabrication of 2D and 3D structures for photonics applications, which can be achieved by modifying the optical properties of the photosensitive media (extensively discussed in the next section) or by inducing chemical changes in the material by multiphoton lithography, for example.
The changes induced by adopting this lithography method are localized in a very small volume and depend on the chemical nonlinearity of the photodeposition process, which does not occur below a certain exposure threshold.
Moreover, one of the greatest benefits of this method is represented by the high resolution achieved during the fabrication of the above-mentioned structures. Indeed, the *Point-Spread Function* (SPF) for the MPA process is smaller than the one for linear absorption at the same wavelength.[78;79] Figure 1.24 reports the images of high-resolution structures fabricated by multiphoton absorption polymerization; in particular, Fig. 1.24b) reports the image of the word "HAIR" fabricated on a human hair.

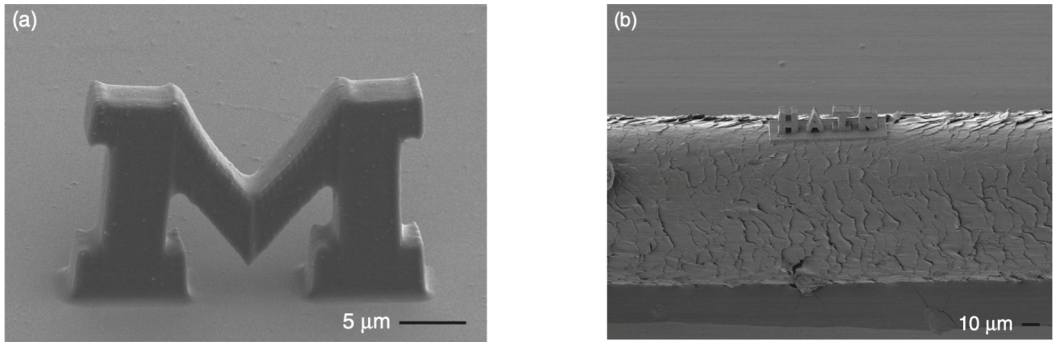

Figure 1.24: Example of 3D structures with high resolution achieved by multiphoton absorption polymerization. Images taken from[16]. It should be noticed that the word "HAIR" is fabricated on an actual human hair.

1.2.4 Material modifications and optical properties

The focusing of an ultrafast laser source in the bulk of photosensitive media enables directly addressing material modifications in a voxel whose dimensions depend on the focal volume and the laser parameters.
In order to understand the mechanism leading to a perennial modification of the material it is important to keep in mind the phenomena involved during the ultrafast laser-matter interaction. As discussed in the previous section, free electrons are produced in the absorption of the ultrafast laser pulses in the first few fs. The diffusion of the released electrons will result in the transfer of their kinetic energy to the phonons over a ps timescale. When a plasma is created by avalanche ionization, the heat deposition in the highly ionized medium occurs in a very short timescale with a speed much higher than the sound speed inside the plasma region. Therefore, at high intensity a shock wave may be produced in the surrounding gas within a couple of ns. Finally, the thermal energy is diffused out of the focal volume on a μs scale, allowing for ion diffusions, consequently enabling chemical reactions. In the end, if the temperature in the interaction voxel overpasses the melting temperature of the material during the pulse absorption, a faster localized melting occurs followed by a resolidification process within the μs scale. This timeline is reported in Fig. 1.25.

However at high laser fluency, as the plasma density increases also its energy increases, reducing the ionic shielding and causing Coulomb repulsion between ions. This can lead to void formations, also known as explosions. For long-enough laser pulses, it has been observed that

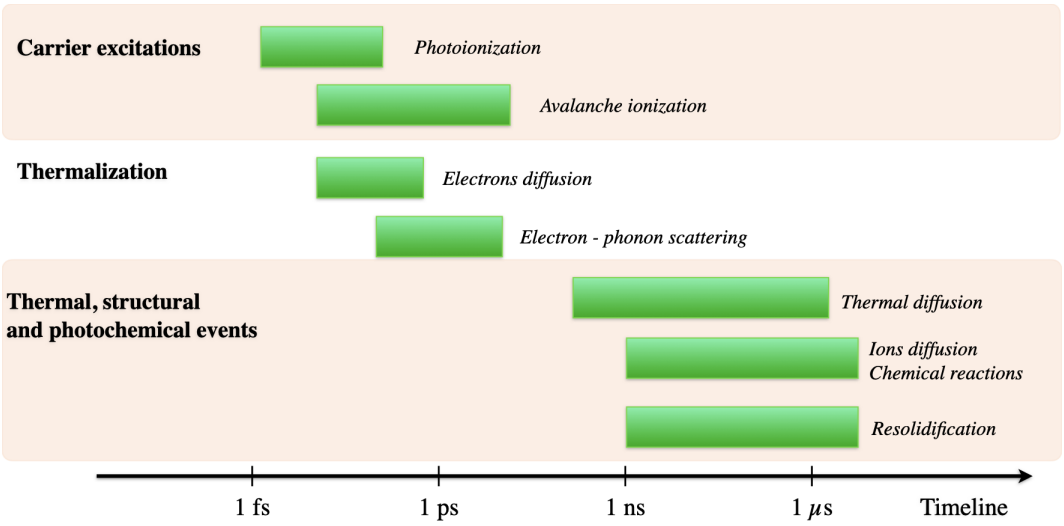

Figure 1.25: Timeline of the processes involved during the focusing of a femtosecond source in the bulk of photosensitive media. Adapted from [17]

the laser intensity required to produce damages evolves as $\tau_p^{-1/2}$, where τ_p is the duration of the laser pulse, for τ_p from 10 ps to 10 ns. Such dependence can be explained by noticing that the heat produced during avalanche photoionization is diffused in the voxel of interaction following the heat transportation equation:

$$(\rho C)\frac{\partial T}{\partial t} - \kappa_T \nabla^2 T = N(1-f)P, \tag{1.25}$$

in which T represents the temperature distribution $T(\mathbf{r}, t)$, (ρC) is the heat capacity per volume unit, κ_T is the thermal conductivity and the term on the right side represents a source term that involves the concentration of free electrons N and the absorbed power P, while f is a factor that takes into consideration only the part of the absorbed power that contributes to the ionization process. Thus, if the source term is neglected, the equation Eq. 1.25 describes the heat diffusing in an area of dimension L over the time τ_p, connecting the two scales by:

$$L \propto \tau_p^{1/2}. \tag{1.26}$$

As a consequence, also the damage threshold will follow the same dependence on the laser pulse duration.

However, for pulse duration below the picosecond range, the electrons are excited in a timescale that is smaller than the time required for electron-phonon scattering (which is about 1 ps, see Fig. 1.25. Therefore, the heat diffusion outside the voxel of interaction is minimized, so that

the damage threshold becomes independent of the ultrashort pulse duration.

During the absorption of the femtosecond pulses and the plasma generation, electronic excitons - properly speaking, electrons bonded to holes by Coulomb attraction - are created. The relaxation processes of the lattice can be localized or not-localized: in transparent materials and wide-bandgap dielectrics, the main relaxation mechanism is localized and allows for the creation of *Self-Trapped Excitons* (STE). Generally, STE result from the interactions between excitons and carriers localized on a lattice site for which the potential well has been distorted. In the same way, holes can be trapped in the lattice deformation and form STE by interacting with electrons. The formation of STE during the femtosecond laser-matter interaction can provide sufficient energy that allows for generating intrinsic defects, such as vacancy-interstitial pairs.[80;81;82;23]

The creation of STE may also open a channel for damage formation, as a consequence of a large production of intrinsic defects. Other mechanisms leading to damage formation and optical breakdown in the femtosecond interaction might be local melting or vaporization of the solid due to strong phonon emissions, or Coulomb explosions.

Indeed, in the last two decades the focusing of a femtosecond laser source has been adopted to

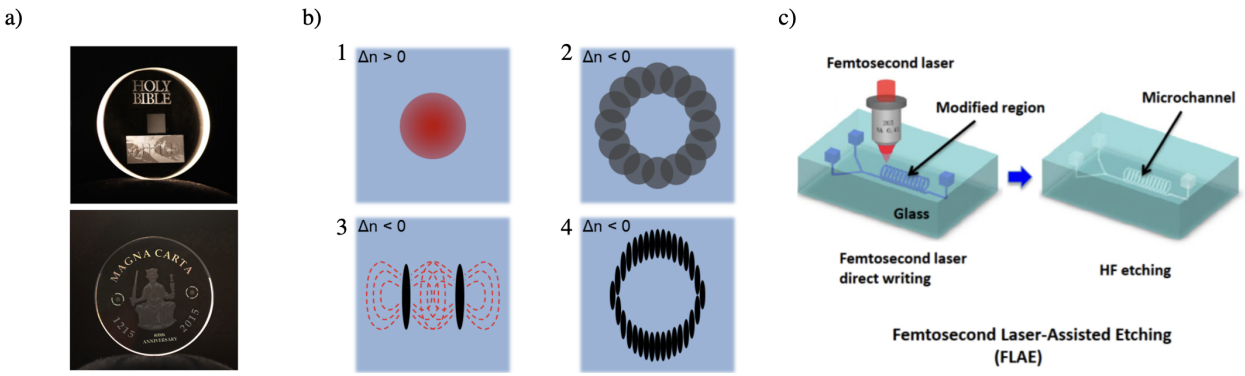

Figure 1.26: (a) Example of the functionalization of materials: femtosecond imprinting of (top) *King James Bible* and (bottom) the *Magna Carta* in glass (Images taken from[18]), (b) fabrication of waveguides in crystal and glass with different 3D arrangement, depending on the induced refractive index change Δn (image taken from[19]) and (c) a schematic explanation of one of the methods to achieve microfluidics channels by femtosecond irradiation (image taken from[20]).

locally modify glasses, crystals, polymers and other materials to functionalize them. The femtosecond laser machining can indeed create vacancies that can give rise to photoluminescence in transparent materials and wide bandgap semiconductors such as diamonds. Moreover, color

centers can be produced in the femtosecond interaction; such deep-level defects can be created in the bandgap for example to obtain single-photon sources. Femtosecond lasers can also induce the creation of metallic nanoparticles or nanostructures that can be exploited for instance for surface-enhanced Raman spectroscopy (SERS).[83]
Furthermore, the local material rearrangement occurring during the absorption of the laser pulses is associated with a local change in the refractive index.
These perennial material modifications and associated refractive index changes can be exploited to achieve high-density perennial optical memory storing, up to 5D optical memory storage, or to fabricate photonics devices, such as components for Photonic Integrated Circuits (PICs), volumetric gratings, microfluidics devices and sensors.[84;85;86] Some examples are reported in Fig. 1.26.
This topic is thoroughly addressed in the next chapter of this manuscript.

1.3 Basics of guided optics

Some basic notions on guided optics are introduced in this section since they are going to be essential for the understanding of the topics of the next Chapters.

1.3.1 Waveguiding theory and propagation constants

In the interface between two media with different refractive indexes, n_1 and n_2, there exists a critical angle of incidence from the first to the second medium for which the propagating light is not refracted but totally reflected. Therefore, for the case of $n_2 < n_1$, the critical angle is defined by the Snell law as:

$$\theta_c = arcsin\left(\frac{n_2}{n_1}\right) \tag{1.27}$$

so that if $\theta > \theta_c$, the propagating light is reflected back into the n_1 medium.
This condition, known as *total internal reflection*, is at the base of the optical fibers functioning.

Fibers Optical fibers are dielectric waveguiding structures fabricated with low loss materials, most-commonly silica-based glasses, that can transport light for remarkably long distances, a few tens of kilometers for telecommunication fibers, thanks to the total internal reflection. On a basic level, the fiber is composed of a *core* defined by its radius a and its refractive index n_{core} and a *cladding* with refractive index n_{clad} so as $n_{core} > n_{clad}$ and thus $\theta_c = arcsin(n_{core}/n_{clad})$.

If the core index is kept constant along the diameter of the core region, the fiber is known as *step index* and at the boundary between the cladding and the core the refractive index changes abruptly. Otherwise, the core index can change gradually from the n_{clad} at the edges of the core region to reaching the maximum at the center of the core, such as in gradient fibers. The difference in the refractive index between the core and the cladding defines the *Numerical Aperture* (N.A.) of the fiber, which describes the *acceptance cone* of the fiber, *i.e.* the set of angles of the incoming light that undergoes the total internal reflection inside the core and, therefore, leading to propagated light along the whole fiber length.
Indeed, the N.A. is found to be:

$$N.A. = sin\alpha = \sqrt{n_{core}^2 - n_{clad}^2}; \tag{1.28}$$

since large N.A. can collect more light than small N.A., the acceptance angle α is a fundamental parameter in the design of an optical fiber.

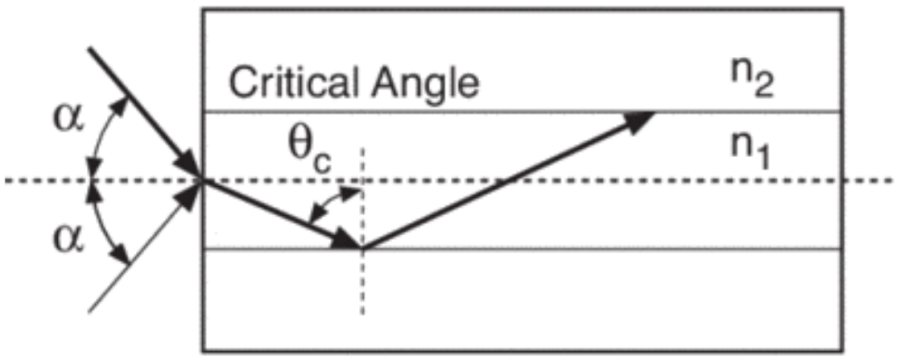

Figure 1.27: Schematic representation of an optical fiber with $n_{core} = n_1$, $n_{clad} = n_2$ and the acceptance angle α defining the Numerical Aperture. Image taken from Newport.

For a monochromatic light traveling along the fiber length, the component of the propagation constant along the z direction β has to satisfy the following condition:

$$n_2 k < \beta < n_1 k, \tag{1.29}$$

where $k = 2\pi/\lambda$, with λ the wavelength in the vacuum of the considered radiation. Thus, the boundary conditions between the core and the cladding of a fiber define the solutions of the

Helmholtz equations that are allowed to propagate inside the fiber. Such solutions are called Eigenmodes, or simply *modes*.

1.3.2 Guided modes

In the weakly guiding regime for a step-index fiber, the difference Δn in the refractive index between the core and the cladding is low, like in the case of silica fibers for telecommunication where $\Delta n < 10^{-1}$ so:

$$N.A. \approx \sqrt{2n_{core}\Delta n} \tag{1.30}$$

and the guided light propagates mostly parallel to the fiber axis. In this case, the transverse components of both the electric and magnetic fields of the guided modes are much stronger than the longitudinal components; the linear polarizations along the x and y directions will then form a complete set of orthogonal solutions for the polarization state. The functions are known as **Linearly Polarized** ($LP_{l,m}$) modes and can be mathematically written using Bessels functions.

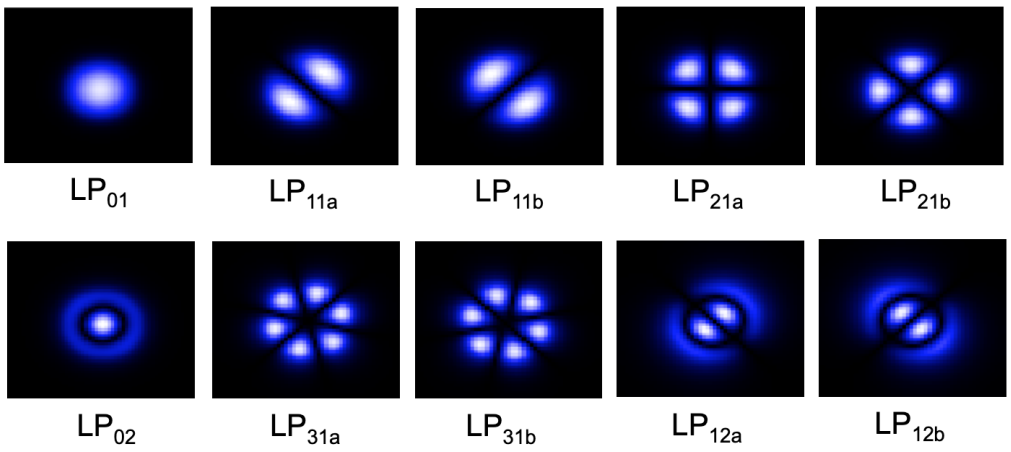

Figure 1.28: Spatial intensity profile of some of the Linearly Polarized $LP_{l,m}$ modes inside a fiber. Image taken from [21].

The lowest-order mode LP01 is always guided inside the dielectric fiber and has an intensity profile that is roughly similar to that of a Gaussian beam, as depicted in Fig. 1.28.
The number of modes that can propagate inside the fiber is determined by the V number:

$$V = \frac{2a\pi}{\lambda}\sqrt{n_{core}^2 - n_{clad}^2}, \tag{1.31}$$

where a is the radius of the core region and λ is the wavelength in the vacuum of the propagating light: if $V < 2.405$ then only the lowest-order mode LP_{01} can propagate along the fiber and therefore the fiber is called *singlemode* at the considered wavelength. Otherwise, higher orders are allowed to propagate and the fiber becomes *multimode*. Each mode is described by the β_m parameter, which is dependent on the mode effective index n_{eff_m} by $\beta_m = \frac{2\pi}{\lambda n_{eff_m}}$, therefore it is possible to represent the number of guided modes using the *normalized propagation constant* b

$$b = \frac{(\beta/k)^2 - n_{clad}^2}{n_{core}^2 - n_{clad}^2} \approx \frac{(\beta/k) - n_{clad}}{n_{core} - n_{clad}} \tag{1.32}$$

which can be then linked to the V number.
Figure 1.29 shows the dispersion curve $b(V)$ with the different $\mathrm{LP}_{l,m}$ modes. At $V = 2.405$, the step from single mode to multimode regime is then highlighted.

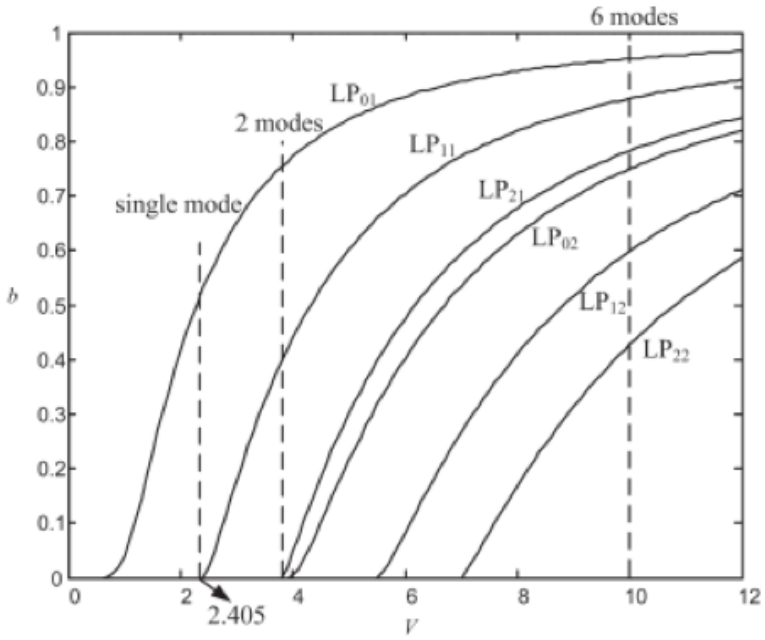

Figure 1.29: Dispersion curve for the normalized propagation constant b as a function of the V number: the passage from single mode to multimode operation is highlighted at $V = 2.405$.

Moreover, for each mode the *effective index* $n_{eff}(V)$ can be found by:

$$n_{eff}(V) = \frac{\beta(V)}{k_0} = \sqrt{n_{clad}^2 - b(V)(n_{core}^2 - n_{clad}^2)}. \tag{1.33}$$

When the V number increases, also the effective index increases from the cladding index, $n_{eff} = n_{clad}$, to the core index, $n_{eff} = n_{core}$, when $V \to \infty$: this means that when the V is low, the

guided mode extends inside the cladding, while for V that increases, the mode shrinks to be mostly confined inside the core.
The extension of the guided mode inside the fiber can be then quantified by the *Mode Field Diameter* (MFD).

Mode Field Diameter For a step-index fiber, the Mode Field Radius w can be estimated knowing the core radius a and the V number by *Marcuse's equation*:

$$\frac{w}{a} \approx 0.65 + \frac{1.619}{V^{3/2}} + \frac{2.897}{V^6}, \tag{1.34}$$

therefore, the MFD is given by $2w$. Figure 1.30 reports the behavior of the LP_{01} mode radius depending on the dimension of the core, for step-index fibers with different N.A..

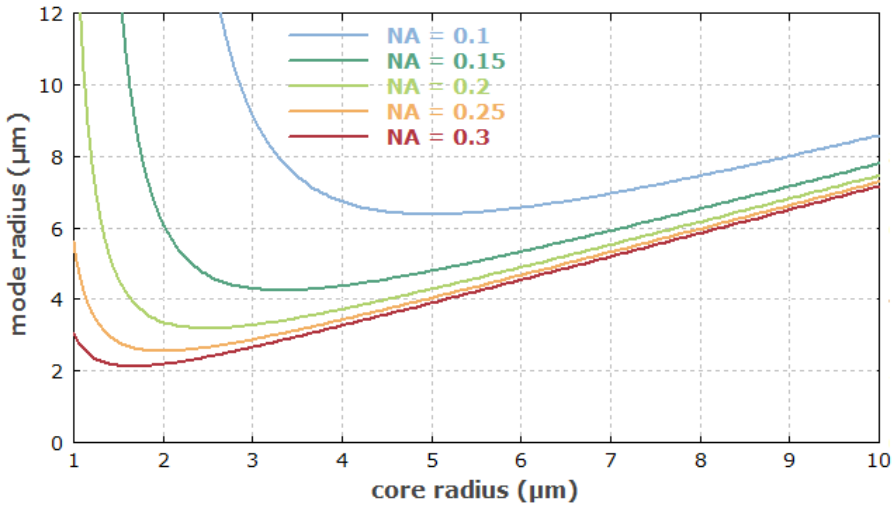

Figure 1.30: LP_{01} mode radius dependence on the core radius dimension of step-index fibers with different N.A. for $\lambda = 1550$ nm. Image taken from RP-Photonics.

The formula shows that for a given core radius a, the MFD decreases when decreasing the wavelength λ of the propagating light.
The MFD is an important parameter for the conception of the fiber since it describes the intensity distribution of the mode inside the fiber: typically, the MFD is defined at the radial position where the intensity drops to $e^{-2}I_{peak}$, where I_{peak} is the peak intensity. Indeed, to maximize the coupling of an incoming beam inside the fiber it is necessary that the injected beam profile matches the intensity mode profile given by the MFD.

1.3.3 Light propagating in multilayered media

Finally, this last section introduces the concept of multilayered media, such as *Bragg Gratings* and *Photonic Crystals*, and analyzes the effect of a periodic variation of the refractive index on the propagating light.

Bragg Gratings A Bragg Grating consists of a series of periodic multilayers with a modulated refractive index. Therefore, light propagating in the transverse direction will overcome multiple reflections and transmissions at the interfaces between the gratings layer and the medium in which the gratings are placed. The combined effects of the multilayers can then enhance the reflection wave up to achieve the total reflection under specific conditions.
If the Bragg Grating has a constant refractive index n_2 and period Λ, the discretization in a series of N identical multilayer structures allows for a simple calculation of the forward and backward waves using the *Transfer Matrix* approach. Considering a gratings of period Λ, like reported in Fig. 1.31, composed of N equally-spaced segments, the single multilayer structure with n_1 and n_2 indexes is described by a wave-transfer matrix $\mathbf{M}_0$:

$$\mathbf{M}_0 = \begin{bmatrix} 1/t^* & r/t \\ r^*/t^* & 1/t \end{bmatrix} \tag{1.35}$$

where r and t are the complex reflectance and transmittance, respectively, so that $|r^2| + |t^2| = 1$, and the $(^*)$ stands for the complex conjugate.

The unimodular matrix $\mathbf{M}_0$ is then applied N times for all the multilayered segments of the gratings, each time taking into consideration that the output parameters calculated for the n^{th} segment represent the input parameters for the calculation of the intensity $|r^2|$ and $|t^2|$ for the $n^{th} + 1$ segment. Therefore, the wave-transfer matrix $\mathbf{M}$ for the whole gratings is given by:

$$\mathbf{M} = \mathbf{M}_0^N = \Psi_N \mathbf{M}_0 - \Psi_{N-1}\mathbf{I}, \tag{1.36}$$

where

$$\Psi_N = \frac{sin(N\Phi)}{sin\Phi}, \tag{1.37a}$$

$$cos\Phi = Re\{1/t\}, \tag{1.37b}$$

and $\mathbf{I}$ is the identity matrix. The interference factor Ψ_N is a function of the number N of periodic structures and of $\Phi = cos^{-1}(Re\{1/t\})$, which is then related to the transmittance. Thus, two different regimes are defined:

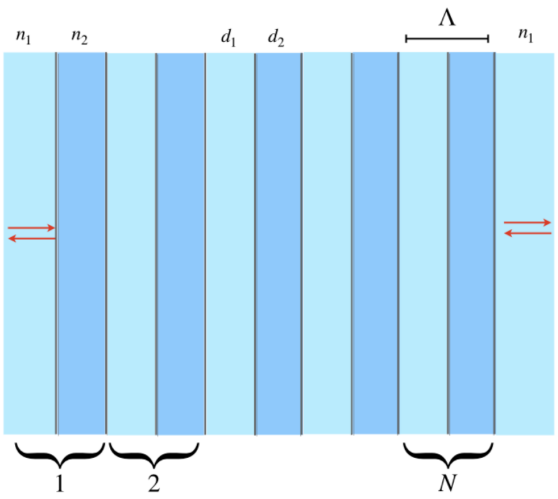

Figure 1.31: Schematic representation of a grating composed of $N = 10$ multilayer segments with n_1, d_1 and n_2, d_2 parameters, so that $d_1 + d_2 = \Lambda$ period of the grating. Image adapted from [10]

- $|Re\{1/t\}| \leqslant 1$ implies a partial or zero-reflection regime
- $|Re\{1/t\}| > 1$, therefore Φ is complex and a total-reflection regime appears.

Since Ψ is a function of the frequencies ν, the total-reflection regimes appear for specific ν_B frequencies that are given by the *Bragg condition*:

$$\nu_B = \frac{c}{2\Lambda}. \tag{1.38}$$

as reported in Fig. 1.32.

Moreover, for such Bragg Gratings configuration, the spectral dependence of the intensity reflectance $\mathcal{R}$ can be described by:

$$\varphi_1 + \varphi_2 = k_0(n_1 d_1 + n_2 d_2) = \frac{\pi\nu}{\nu_B}, \tag{1.39}$$

where φ_1 and φ_2 are the phases introduced by the layers with n_1 and n_2. The Transfer Matrix approach allows for easily simulating the reflection and transmission characteristics for different types of Bragg Gratings, such as chirped, lossy or tilted gratings. However, it is quite complex to deduce the parameters of the grating from reflections and transmission measurements. For this reason, another approach based on the **Coupled-wave theory**, particularly indicated for the

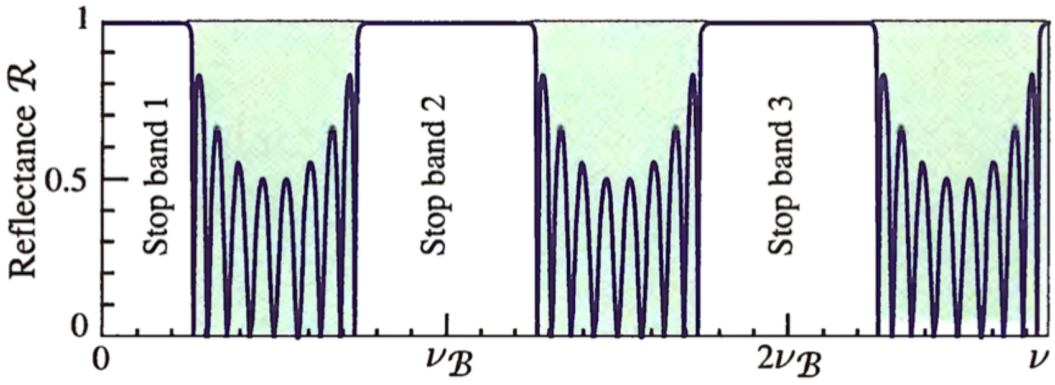

Figure 1.32: Spectral dependence of the intensity Reflectance $\mathcal{R}$: the total-reflection regime is highlighted by the Stop Bands that are centered at the frequency $\nu_B = \frac{c}{2\Lambda}$. Image taken from [10].

case of Gratings fabricated with $n_2 = n_1 + \Delta n$, where Δn is small modulation of the refractive index, will be discussed in Chapter 4 and taken into account for characterizing the fabricated Waveguides Bragg Gratings and Volume Bragg Gratings.

Photonic Crystals A fascinating recent development in optics is represented by Photonic Crystals: these multilayer media are generally composed of nanostructures with a periodic modulation of the refractive index for which the period is comparable with the wavelength λ of the propagating light.

The interest of these structured materials lies in the similarity of their behavior with the periodic lattice in crystals, which results in the existence of electronic band gaps and thus prohibited regions in the Brillouin zone for the electronic energy states.
Indeed, in the same way the Bloch functions describe the electronic wave functions in a periodic lattice, the *Bloch modes* describe an optical wave that has the characteristic of a standing wave in the periodic structure.
By using the same Transfer Matrix approach used for the Bragg Gratings, it is possible to simplify the N periodic structure by writing the wave-transfer matrix $\mathbf{M}_0$ of the single multilayer segment at the position $m\Lambda$ and applying it to the complex amplitudes $\{U_m^{(\pm)}\}$ of the forward $(^+)$ and

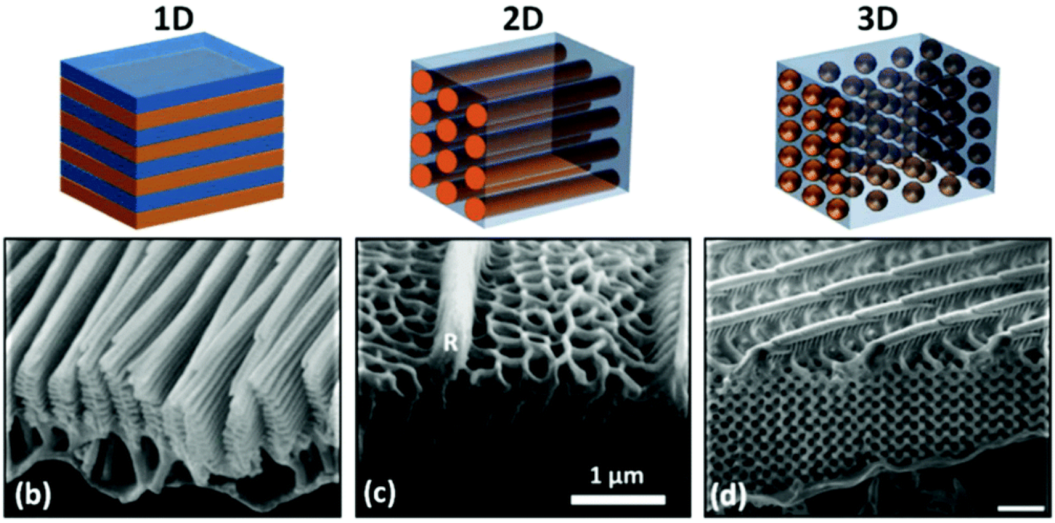

Figure 1.33: Examples of 1D, 2D and 3D Photonic Crystals and their corresponding arrangements on a biotemplate. Image taken from [22].

backward ($^-$) waves, so that:

$$\begin{bmatrix} U_{m+1}^{(+)} \\ U_{m+1}^{(-)} \end{bmatrix} = \mathbf{M}_0 \begin{bmatrix} U_m^{(+)} \\ U_m^{(-)} \end{bmatrix}, \tag{1.40}$$

Since the solutions of the periodic structure, *i.e.* the modes, are self-reproducing waves, the Eq. 1.40 can be rewritten in the form:

$$\begin{bmatrix} U_{m+1}^{(+)} \\ U_{m+1}^{(-)} \end{bmatrix} = e^{-j\Phi} \begin{bmatrix} U_m^{(+)} \\ U_m^{(-)} \end{bmatrix}, m = 1, 2, ... \tag{1.41}$$

which describes a wave with an unmodified magnitude that has acquired a phase Φ after a distance Λ. The Φ phase is called *Bloch phase* and it is related to the *Block wavenumber* K by:

$$\Phi = K\Lambda \tag{1.42}$$

The relation in Eq. 1.37b obtained for the Bragg Gratings case is still valid.
However, in this case:

$$cos(\Phi) = cos(2\pi\frac{K}{g}) = Re\left\{\frac{1}{t(\omega)}\right\} \tag{1.43}$$

where $cos(2\pi\frac{K}{g})$ is a periodic function of K with period $g = 2\pi/\Lambda$.

Therefore, as depicted in Fig. 1.34, it is possible to observe two regimes for the dispersion relation with multiple spectral bands:

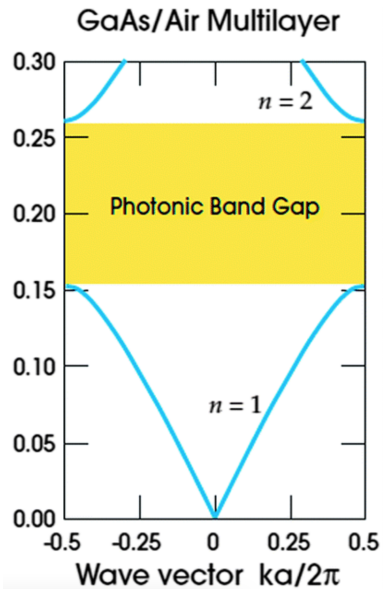

Figure 1.34: Example of dispersion diagram for a Photonic Crystal where the Photonic Bandgaps are highlighted. Image taken from [10].

- a propagation regime for spectral bands with K real, defining the propagating modes;
- a Photonic Bandgap regime for K complex defining spectral bands corresponding to evanescent waves that are rapidly attenuated while there are no existing propagating modes.

Conclusions on the chapter

The chapter focuses on the concepts behind the phenomena involved in the laser-matter interaction.
The importance of understanding such phenomena is crucial for improving the photosensitivity of materials processing with an ultrafast laser source.

For this purpose, the optical and material properties of glasses, in particular oxide glasses, are discussed. Moreover, both industrial and non- production processes are presented and the optical fiber drawing process is briefly introduced.

Furthermore, a brief insight into the laser history and the theory of lasing operation is given.

Indeed, the laser cavity is introduced as well as the concepts of modes, namely the allowed oscillating frequencies. Further, the Gaussian beam and its geometrical and physical properties are discussed.
Finally, the overview of lasers concludes with a discussion on the achievement of pulsed lasers, their typologies and their applications.
Successively, the discussion is focused on the interaction between an ultrafast laser and a medium. Therefore, much attention is paid to the explanation of the photoionization processes, in particular of the multiphoton absorption process.
As discussed, such a nonlinear process occurs in a time scale that is comparable with the one of the phenomena in the voxel of interaction. As a consequence, the ultrafast laser-matter interaction enables material modifications over a volume that is dependent on the voxel of interaction. Such material modifications are going to be discussed in the next Chapters, especially in Chapter 2.

Finally, some basic notions on guided optics have been introduced in the last part of this Chapter.
The basic concept of waveguiding inside fibers has been discussed, together with an overview of Linearly Polarized (LP) modes and the related Mode Field Diameter (MFD). To conclude, multilayer media are discussed; specifically, Bragg Gratings (BGs) and Photonics Crystals (PCs) are briefly introduced. The insight in this last part is of interest for the following Chapter and it is of importance for the understanding of Chapter 4.

Chapter 2

Direct Laser Writing in glasses

Introduction to the chapter

Ultrafast lasers have paved the way for new and improved laser processing of glasses, thanks to the fine control of the localized pulse-to-pulse energy deposition. In this Chapter, the attention is focused on the optical properties arising from the physicochemical modifications induced in the femtosecond laser-glass interaction. Such optical properties can be affected by the glass composition.

Therefore, the first part of the Chapter deals with the Direct Laser Writing of glasses, mostly silica-based, and the associated refractive index changes depending on the glass composition and the laser parameters. Moreover, the thermal management in the voxel of interaction is discussed in the two cases of the high and low repetition rate of the femtosecond laser to distinguish between the thermal and athermal regime of inscription, highlighting both the advantages and flaws. Thus, some applications of the different types of induced refractive index change are presented, focusing attention on embedded waveguides. In the fabrication of optical waveguides achieving high refractive index change is of critical importance to enable the downsizing of integrated optical circuits. For this reason, few techniques to accomplish such a goal are presented.

The second part of the Chapter introduces silver-containing phosphate glasses. Such an interesting type of tailored oxide glasses allows for obtaining particular optical properties associated with the formation of new silver species during femtosecond irradiation. Indeed, the physicochemical modification of the glass matrix leading to the formation of the silver clusters under

laser inscription is detailed in order to explain the appearance of a new type of refractive index change that has been only recently observed. Such a new type of refractive index change occurs in an athermal regime and it has proved to be suitable for waveguides inscription. Some properties of the silver-sustained structures fabricated during the femtosecond irradiation are then discussed to relate the induced refractive index change to the Direct Laser Writing parameters.

2.1 State of the art of DLW in glasses

Direct Laser Writing (DLW) is a widely spread technique in the femtosecond laser inscription to easily address perennial 3D material structuring. As a matter of fact, the DLW consists of focusing an ultrafast laser source in the bulk of photosensitive media. Due to multiphoton absorption, the dimensions of the interaction voxel are directly related to the geometrical parameters of the focused laser beam, which have been discussed in Sec. 1.2.1. Therefore, the dimensions of the focused laser spot in the plane transversal to laser beam propagation direction are given by Eq. 1.13, while the dimension along the beam propagation direction is related to the confocal parameter $b = 2z_R$, introduced in Eq. 1.12.
By simply translating the material under the femtosecond irradiation it is possible to obtain 3D patterns by locally inducing the material modifications introduced in Section 1.2.4 of the previous Chapter.
The DLW can be performed in two different configurations, mostly for the case of waveguides inscription, which is reported in Fig. 2.1.

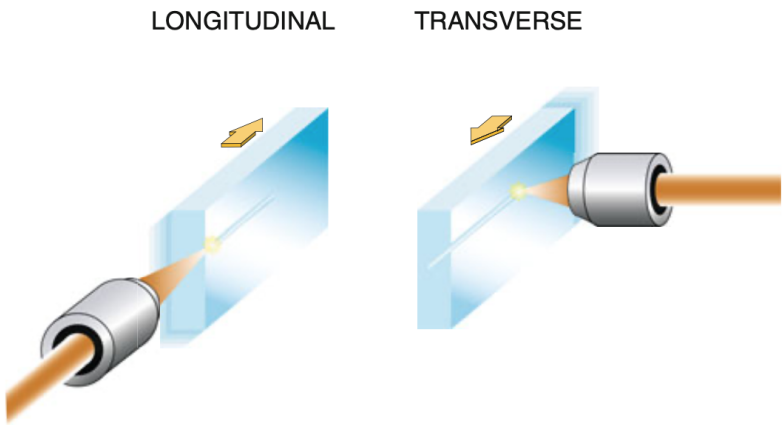

Figure 2.1: Representation of the two different configurations used for the DLW, in particular for the inscription of waveguides. Image taken from [23]

Longitudinal configuration The sample is translated in a direction parallel to the one of the beam propagation, either towards or away from the incident laser spot. On the one hand, the structures will be characterized by a cylindrical geometry due to the circular shape of the Gaussian beam at the focus plane. On the other hand, the length of the inscription inside the glass is limited by the working distance of the microscope objective used for focusing the femtosecond laser and by aberrations.

Transversal configuration In this case, the sample is moved in a direction that is perpendicular to the one of the beam propagation. As a result, there is no restriction to the length of the structures that can be inscribed at a depth varying from hundreds of μm inside the sample, depending on the working distance of the microscope objective, up to the surface of the sample. However, writing on the surface of a media has some limitations: for instance, since most of the microscope objectives are fabricated to work at a specific depth inside the sample, where the aberrations are eliminated, or at least reduced, or immersion oils with matching indices should be used. Moreover, the quality of the surface could highly affect the writing process, resulting in damages and explosions for instance. Nevertheless, the structures will be characterized by an asymmetrical geometry, with an ellipticity that increases when lowering the N.A. of the microscope objective. Therefore, in the inscription of waveguides in this configuration, it is preferable to work with higher N.A. or to use cylindrical lenses in order to spatially shape the laser beam so as to efficiently couple the waveguides to optical fibers.

2.1.1 The refractive index change Δn

The origin of the refractive index change induced in the femtosecond interaction has been investigated during the years and it is close to be fully understood. Indeed there have been many studies that tried to link the local modification of the refractive index to laser-induced material rearrangements. Much attention has been paid to investigating these phenomena in silica-based glasses, since these are the most commonly used glass so far.
For instance, the work of Hirao *et al.* in 1998[87] was one of the first linking both the densification and the creation of color centers to the change in the refractive index of the glass. Using an *Atomic Force Microscope* (AFM), the group observed an increase in the densification during the writing of waveguides in the bulk of the silica glass, while *Electron Spin Resonance* (ESR) spectroscopic measurements pointed out the formation of defects and color centers in the femtosecond irradiated areas. Indeed it has been observed that one of the relaxation mechanisms of

femtosecond-induced STEs in silica glasses is the breaking of $Si-O$ bondings. As a consequence, the glass matrix undergoes a structural and electronic rearrangement that leads, for instance, to the formation of Non-Bridging-Oxygen-Holes-Centers (NBOHC) and E' centers. The formation of such defects can improve the glass absorption during laser irradiation, resulting in a smooth refractive index change.
Furthermore, in the work of Chan *et al.*[88] in 2001 it has been hypothesized that thermal accumulation resulting from the absorption of subsequent pulses in the interaction voxel leads to glass densification and thus to the appearance of a Δn. Indeed, by performing Raman spectroscopy it was observed an increase in the intensity of the peaks at 490 cm^{-1} and 605 cm^{-1} related to the breathing of modes from $3-$ and $4-$membered rings in the silica network, which translates in a decrease of the overall bond angle, leading to an increase of the glass density.
However, in the work of Streltsov *et al.* in 2002[25] an annealing post-treatment of the irradiated sample showed that the refractive index change remained while the color centers disappeared, proving that defects creation and densification do not fully explain the appearance of refractive index change, but rather they contribute to it.

While the debate on the origin of the Δn is still ongoing, it is well known how the local modifications of the refractive index depend on the femtosecond inscription parameters.
Generally, three types of induced refractive index changes have been classified in glasses depending on the laser intensity.[80]

Type 1 For moderate laser intensity, the induced refractive index change is smooth and isotropic. In this case, the glass composition will affect the threshold for DLW as well as the amplitude of such induced Δn, which could be positive or negative. Type 1 refractive index change is mainly exploited in the fabrication of waveguides for photonics applications.

Type 2 When increasing the laser intensity, an anisotropic refractive index change may appear depending on the orientation of the polarization of the focused laser beam. Such type of refractive index change is related to the formation of nanostructures arising from the modification of the chemical composition of the glass matrix. Due to the anisotropy of Δn, the laser-induced Type 2 structures show birefringence effects. This type of material modification is used in the fabrication of nanogratings.

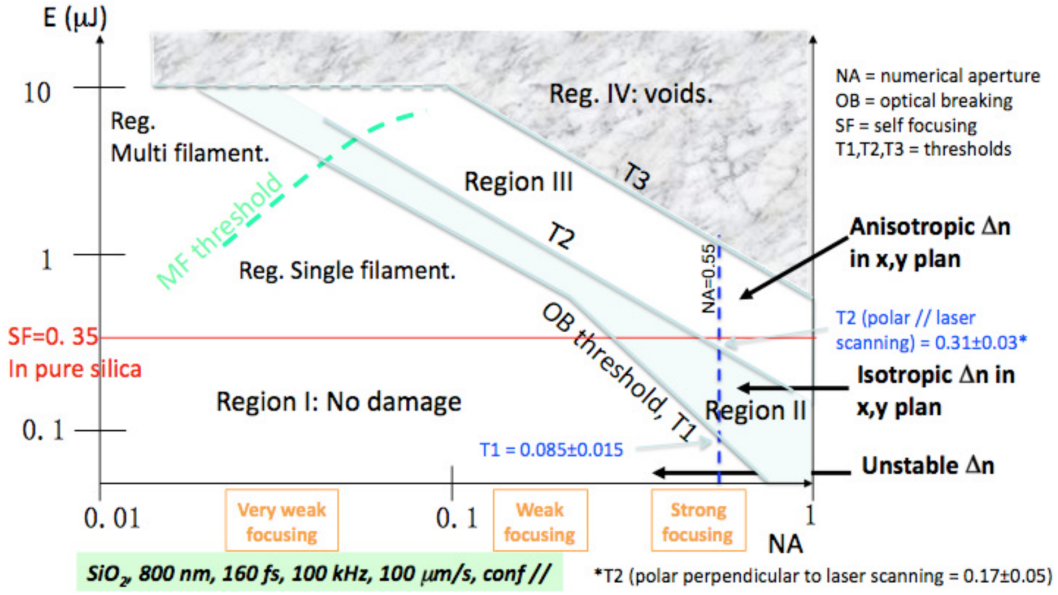

Figure 2.2: Evolution of the different types of refractive index change Δn in the DLW on Silica glass, depending on the pulse energy E and the numerical aperture $N.A.$ of the microscope objective used to focus the femtosecond laser (represented on a log-log scale). The red horizontal line individuates the self-focusing threshold for silica, which depicts the critical optical power leading to damage. Image taken from [24]

Type 3 Finally, at high intensity voids and damages are created in the interaction between the femtosecond laser and the glass matrix as a result of critically-dense plasma production and subsequent Coulomb explosions, as explained in Section 1.2.4 of the previous Chapter.
Such a type of refractive index change is not useful for the fabrication of waveguides since it is related to the creation of scattering centers, leading to high propagation losses. However, it might be used for optical storing and the fabrication of photonic bandgap materials. [89;90;91]

Figure 2.2 shows the different regions in which the Type 1, 2 and 3 material modifications occur for a silica glass during the interaction with a femtosecond source, depending on the pulse energy E and the numerical aperture N.A. of the microscope objective used during the DLW process. The laser system adopted in the work of Lancry *et al.* [24], from which the figure is taken, is a femtosecond laser with pulse duration τ_p of 160 fs, repetition rate f_{rep} 100 kHz operating at the wavelength 800 nm, while the DLW has been performed at 100 μm/s.

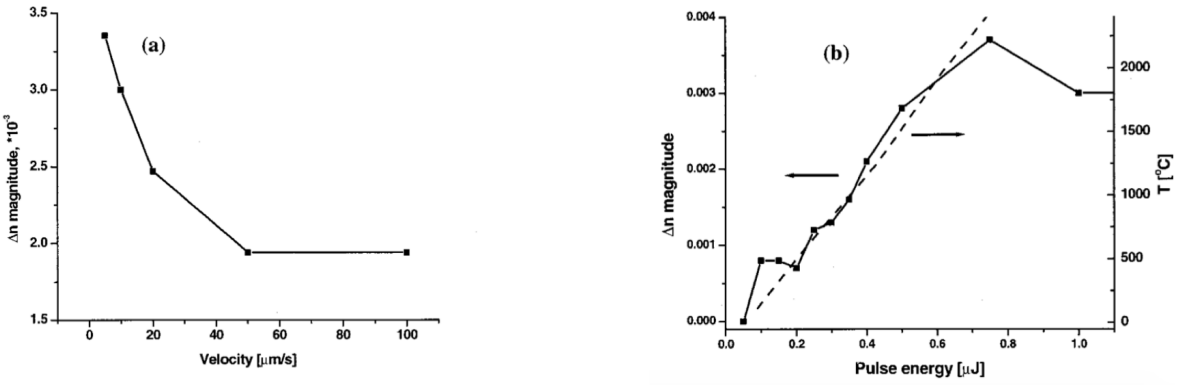

Figure 2.3: Evolution of the magnitude of the Δn depending on: (a) the DLW speed and (b) the pulse energy for a silica glass irradiated using a 800 nm femtosecond source with τ_p 40 fs and r_{rep} 20 kHz. The temperature reported on the graphs refers to the estimated temperature reached by the lattice during the inscription. Images taken from [25]. It should be noticed that the highest reached value of Δn in silica is less than 4×10^{-3}.

Moreover, the magnitude of the induced Δn decreases with increasing the writing speed, *i.e* the sample's translation speed, as reported in Fig. 2.3a, and increases with increasing the pulse energy, as shown in Fig. 2.3b.
Nevertheless, the laser-induced material modifications and related refractive index changes are highly affected by the repetition rate f_{rep} of the femtosecond laser source. Indeed, two different regimes for DLW are observed depending on the f_{rep} since this parameter will highly affect the heat accumulation and the thermal management in the interaction voxel. [19;92;26;93;94;95;96;29]

Athermal regime For low repetition rate, $f_{rep} < 250$ kHz, and for low pulse energy, the time between two consecutive pulses is long enough to allow for the diffusion of the heat accumulated during the pulse absorption out of the interaction voxel. As a consequence, the material modification will occur in a volume whose dimensions are related to the size of the interaction voxel. The magnitude of the Δn achieved in this regime is moderate: for instance in silica glass is about $3 - 4 \times 10^{-3}$, as reported also in Fig. 2.3. Moreover, the geometry of the inscribed structures is affected by asymmetry due to the focusing parameters, *e.g.* the numerical aperture N.A. of the microscope objective used during the writing. Overall, the DLW in this regime is suitable for fabricating Type 1 modifications with smooth positive or negative refractive index

changes. Indeed, as discussed in the previous Chapter, melting of the glass occurs in the voxel of interaction due to the absorption of laser pulses then, depending on the fictive temperature T_f, lower or higher density can be achieved by fast or slow cooling.

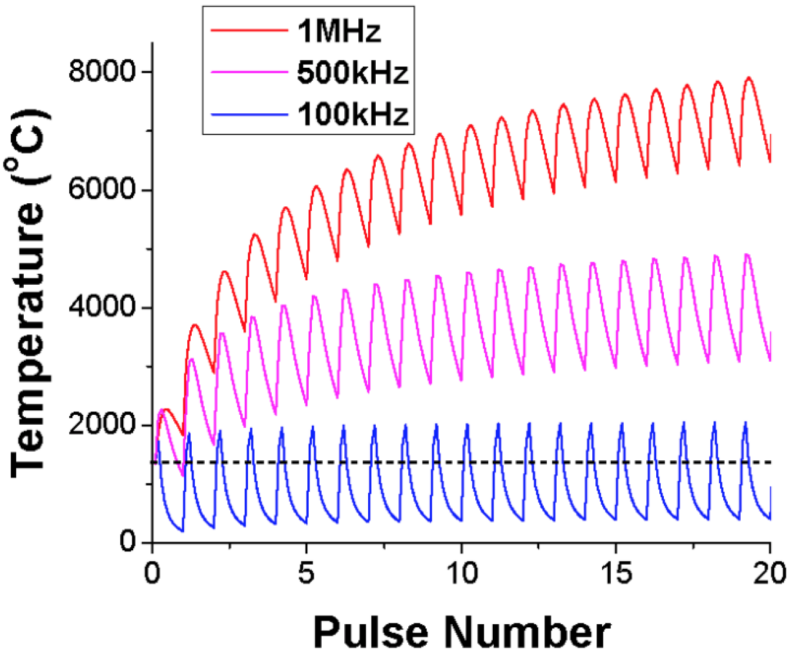

Figure 2.4: Numerical simulation of the evolution of the temperature in the interaction voxel during the absorption of subsequent pulses for the case of different repetition rates. Image taken from[26] It is possible to observe the transition from the athermal regime (case of $f_{rep} = 100$ kHz) and the thermal regime which is highly affected by heat accumulation.

Thermal regime When the repetition rate of the femtosecond source is sufficiently high, $f_{rep} > 1$ MHz, the subsequent pulses are so close in time that the cumulative effect of the many-pulses absorption leads to heat accumulation in the interaction voxel. Thus, the local temperature builds up while each pulse is absorbed to the point it overcomes the glass transition temperature T_g, causing the melting and quick quenching of the glass. As a result, a rearrangement of the glass matrix will occur in the interaction voxel. The magnitude of the induced refractive index change may be higher than what it achieved in the athermal regime, still it can be positive, negative or show both behaviors.[97;36] Moreover, the DLW process should be adapted to the glass thermal properties, for instance to its thermal conductivity κ_T, in order to manage heat accumulation and to avoid damages formation and Coulomb explosions. Therefore,

the DLW in this regime is generally performed at high speed, from hundreds of μm/s to few mm/s, which is an advantage with respect to the limiting speed required in the athermal regime to achieve high Δn. Finally, the induced material modifications present a symmetrical geometry as a result of the heat diffusion from the interaction voxel to the surrounding glass, and their volume is dependent on the heat-affected zone, which is inevitably larger than the size of the focused laser beam.

Figure 2.4 shows the evolution of the temperature during the absorption of subsequent pulses for the DLW performed with different repetition rates, obtained by numerical simulation by Zhang *et al.* in 2005.[26] In the athermal regime, depicted in the graph by the case of $f_{rep} = 100$ kHz, the overall temperature remains below the melting point of the AF45 glass simulated. However, in the case of the thermal regime, the building up of the temperature follows a slope that increases with the increase of the repetition rate f_{rep}.

2.1.2 Applications

Nanogratings formation and applications

The femtosecond inscription of self-assembled nanostructures with a periodic arrangement was first observed by Kazansky's group in 2003.[98] Further studies confirmed that the femtosecond inscription of Type 2 modifications results in the fabrication of nanogratings for which the direction of the array is always perpendicular to the polarization of the laser beam. Also, it has been observed that the periodic array is resulting from a periodic variation of the concentration of specific elements: for the case of silica glasses, a lower refractive index is associated with the areas showing a lack of oxygen concentration. Therefore, the creation of nanogratings results in the fabrication of nanostructures showing a periodic modulation of the refractive index; the intensity of the induced birefringence is then dependent on the direction of the polarization with respect to the writing direction. The period Λ of the gratings is tightly related to the wavelength λ of the laser by

$$\Lambda = \lambda/2n, \tag{2.1}$$

where n is the refractive index of the glass, as shown in Fig. 2.5a. Since the Type 2 modifications appear in a narrow window of DLW parameters that varies depending on the glass composition, it is of crucial importance to adapt the laser parameters, such as the repetition rate and the pulse energy, to the material properties.[28] Indeed, Fig. 2.5b shows the influence of the laser

parameters on the production of nanogratings.

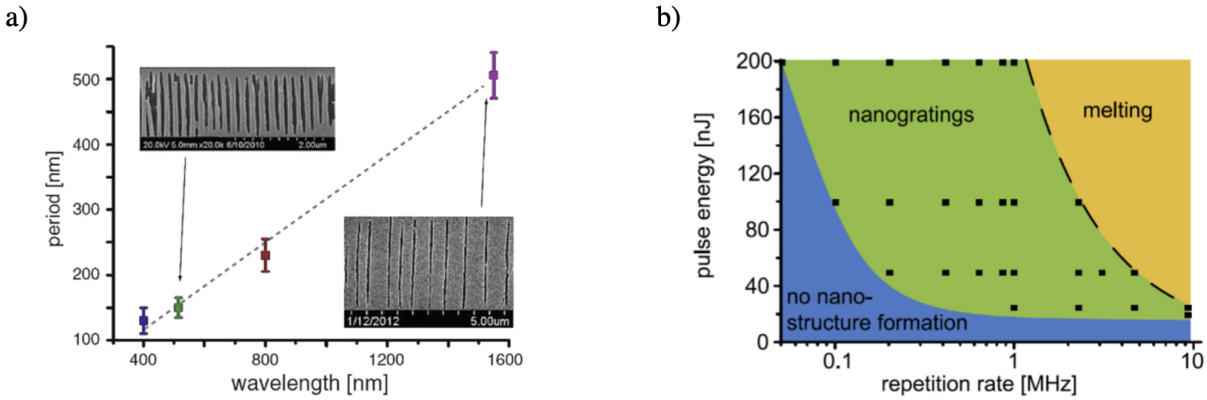

Figure 2.5: (a) Dependence of the periodicity of the nanogratings on the wavelength of the laser.[27] (b) Window inscription of Type 2 modifications in silica glass, depending on the laser parameters. Images taken from[28]

One of the primary advantages of nanogratings is their tunable birefringence, which makes them suitable for polarization control applications, such as the realization of waveplates.[99;100;101] For instance, in the work of Lammers *et al.* in 2019[102] nanogratings have been embedded in waveguides fabricated by DLW in fused silica. The work aimed at realizing waveplates for which the strength of the birefringence effect was modulated by changing the pulse energy, while the orientation of the optical axis was set by rotating the laser polarization during the inscription of the nanogratings.
Moreover, it has been demonstrated that etch selectivity is related to the orientation of self-organized nanogratings induced by femtosecond irradiation.[103;104] Therefore, microchannels for microfluidics application have been obtained from the inscription of Type 2 modifications using a chemical treatment, such as etching.[105;106]

Waveguides

Since the pioneering work of Davis *et al.*[107] in 1996, the femtosecond laser inscription of waveguides in glass has been an extensively studied research field, not only in silica-based glasses but also in phosphate, chalcogenide glasses and other more exotic glass compositions. Waveguides represent the basic device necessary to develop integrated photonic circuits, therefore the fabrication of efficient waveguides becomes of fundamental importance.

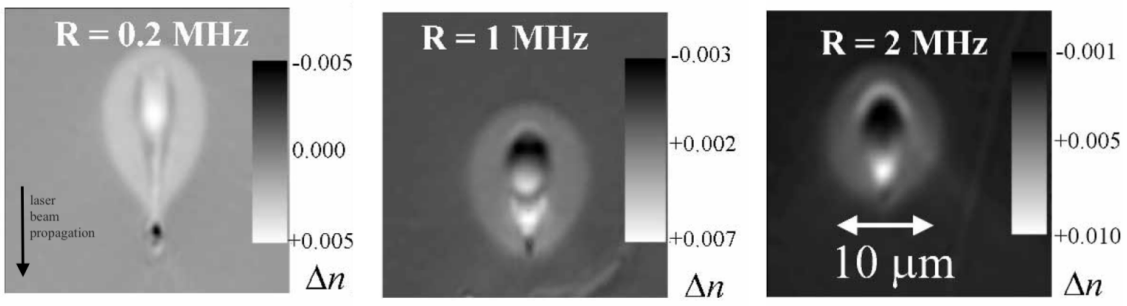

Figure 2.6: Evolution of the cross-section geometries and associated refractive index changes Δn for waveguides embedded in silica glass while changing the repetition rates. The black arrow individuates the laser beam propagation direction. Images adapted from [29]

The study of Eaton *et al.* from 2008 highlighted the evolution of the geometry of waveguides embedded in a silica glass sample depending on the thermal or athermal regime of inscription. Figure 2.6 reports the cases documented in this work for 2 kHz, 1 MHZ and 2 MHz: besides the enlarging of the heat-affected areas for increasing repetition rate, it is possible to notice that also the Δn is changing as a consequence of the transition from the athermal to the thermal regime.

As a matter of fact, the sign of the refractive index change, its magnitude and the propagation losses of the waveguide are important parameters that play a role in the efficiency of the inscribed waveguide.
Concerning the first parameter, *i.e.* the sign of the induced smooth Δn, as explained in Section 1.3 of the previous Chapter, only positive refractive index change can guide light. Therefore, when negative refractive index change is obtained in the femtosecond inscription, as for the works of Fletcher *et al.* [40] and Lancaster et al. [30], there are several hacks and escamotages that could be used in order to exploit such Δn to create waveguides. One of these is the fabrication of *Depressed cladding waveguides*. Such a complex structure requires the inscription of several waveguides displaced on a ring shape around a pristine glass circular area, allowing the formation of a central core with positive Δn, surrounded by a cladding with negative Δn, as shown in Fig. 2.7.

The magnitude of the induced Δn is an important parameter for the miniaturization of optical integrated components: indeed, high refractive index change allows for higher confinement of

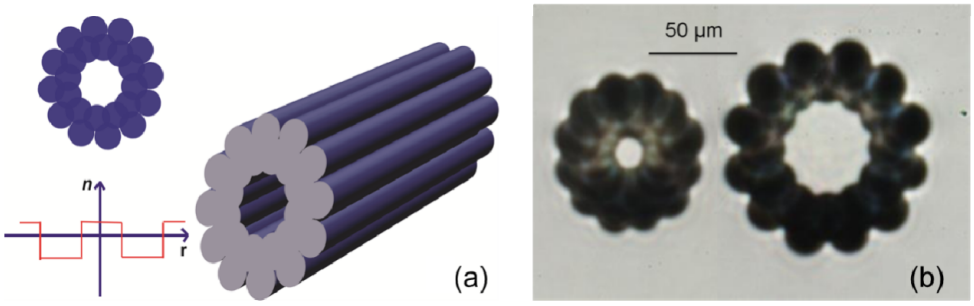

Figure 2.7: Example of Depressed cladding waveguides: (a) schematic representation of the waveguide structure and plot of the idealized refractive index versus the radius of the waveguide; (b) microscope image of two of these complex waveguides in ZBLAN glass (for both structure the cladding is composed of 24 overlapping waveguides with negative Δn). Images taken from [30]

the guided mode on the waveguiding structure. Therefore, in the fabrication of bent waveguides it is important to achieve a high smooth refractive index change that would allow for a smaller radius of curvature, and thus, a more compact photonic device.
Many techniques exist for increasing the induced Δn in Type 1 modifications for both thermal and athermal regimes, some of these will be discussed in the next Section.

Finally, an important parameter to quantify the efficiency of the inscribed waveguides is given by the Propagation Losses (PL). Indeed, light guided in a material can experience losses due to intrinsic or extrinsic causes: depending on the wavelength, the optical power guided in the structure could be absorbed or, for instance, scattered by defects. Therefore, normally the PL are quantified by a coefficient α expressed in dB/length unit. Due to the high dependence of the PL on the material, it is desirable to perform the DLW in materials that have low absorption at the wavelengths for which the waveguide is supposed to work. For instance, Barium-Gallium-Germanate (BGG) glasses are characterized by a large transparency window up to $\lambda \sim 5$ μm, enabling the inscription of waveguides with propagation losses down to 0.5 dB/cm. [108] However, silica glasses are preferred for waveguiding applications in the NIR, indeed propagation losses down to 0.05 dB/cm at 1.5 μm have been achieved for the inscription of waveguides in the athermal regime [109;110]. Nevertheless, very low propagation losses can be achieved in the DLW of microstructured waveguides in BK7 glasses using a high repetition rate laser source, achieving a low loss coefficient of 0.062 dB/cm at 1.155 μm. [111]

Couplers Couplers represent a useful device in integrated circuits to allow for splitting and combining of optical signals, enabling the fabrication for instance of power splitting, optical switchers and multiplexers. Moreover, it is possible to realize couplers that are sensitive to light polarization, enabling the inscription of rotated waveplates and birefringence retarders in the bulk of glasses.[112;113;114;115;116;117]

Figure 2.8a reports the case of a directional coupler (DC): such device, based on the coupled-mode theory, is composed of two evanescently-coupled waveguides that allow for transferring the optical power from one waveguide to the other depending on the overlap between the guided mode of one of the waveguides on the other structure. The amount of the overlapped field is controlled by tuning the *coupling length* L and the distance d between the two waveguides. Moreover, DL are strongly sensitive to the wavelength, due to the intrinsic dependence of the interference process on the wavelength and to modal dispersion.

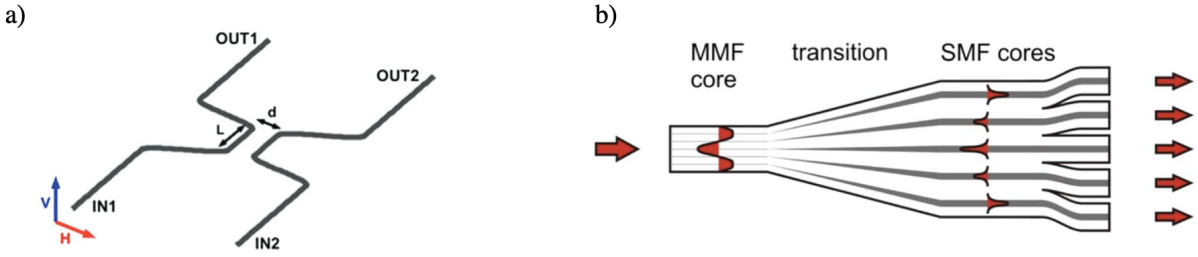

Figure 2.8: Schematic representation of a) Directional Coupler (DC) characterized by the coupling length L and the distance d (Image taken from[31]) and b) Photonic Lanterns with the multimode waveguide converted into several single mode waveguides (Image taken from[32]).

Photonic lanterns A further step into the application of embedded waveguides for photonics applications is the fabrication of Photonic Lanterns. Such devices are composed of a large multimode waveguide that is connected to several single mode (or few-mode) core waveguides. Figure 2.8b shows a schematic representation of a Photonic Lantern: the transition region between the highly multimode waveguide and the smaller single-mode waveguides is engineered in order to achieve gradual and smooth conversion of light between the two systems, thus reducing the optical losses. These optical devices find applications in several research fields, mostly in astrophotonics. For instance, the light imaged from a telescope can be collected and filtered by just embedding tailored *Bragg Gratings* into the single mode waveguides in order to select specific

wavelengths in each waveguide, which can be finally connected to spectrographs. [118;119;120]

Fiber Bragg Gratings Fiber Bragg Gratings (FBGs) represent one of the most widely used optical sensors thanks to their high sensitivity and compactness. Such a device is obtained by periodically modulating the refractive index of a fiber core. As introduced in Sec. 1.3.3, thanks to the coupling of the forward and backward propagating modes it is possible to achieve high narrow-band Bragg reflection at the wavelength:

$$\lambda_B = \frac{2n_{eff}\Lambda}{p}; \tag{2.2}$$

where Λ is the period of the refractive index modulation, n_{eff} is the *effective* refractive index experienced by the propagating modes and p is the diffraction order.
Several techniques exist to obtain the periodic modulation of the core index, such as the adoption of a *phase mask* or by *laser holographic interferometry*, which will be discussed in Chapter 4. However, femtosecond laser inscription of FBGs has quickly gained interest thanks to its flexibility and for easily achieving highly efficient FBGs even in non-photosensitive fibers.
Two methods are generally adopted in this technique to inscribe Type 1 modulations of the fiber core index: *Point by Point* (PbP) and *Line by Line* (LbL).
In the first case, the laser is focused in the fiber core and the fiber is translated along its axis, allowing for inscribing BGs with period $\Lambda = v/f$, where v is the translation speed and f is the repetition rate of the femtosecond source. Although this method enables fast fabrication of mm long FBGs, the inscribed point structures may behave as scatters for the propagating modes, resulting in increasing the propagation losses. Figure 2.9a reports a schematic representation of the PbP inscription method, while Fig. 2.9c, shows a top view image of the inscribed PbP gratings where it is possible to observe that the dimension of the periodic structures is smaller than the dimensions of the core, therefore the efficiency of such structures is highly dependent on the positioning of the focused beam inside the fiber.

The LBL method is instead achieved by translating the fiber in a direction perpendicular to the fiber axis, as reported in the schematic representation in Fig. 2.9b. This method allows for better control of the overlap of the Type 1 modulations in the fiber core. Moreover, the periodic modulation is achieved by finely controlling the on and off modulation of the femtosecond sources by adopting, for example, an AOM or a chopper.
The fabrication of *Waveguides Bragg Gratings* (WBGs), similar to FBGs, will be deeply discussed in Chapter 4 of this manuscript.

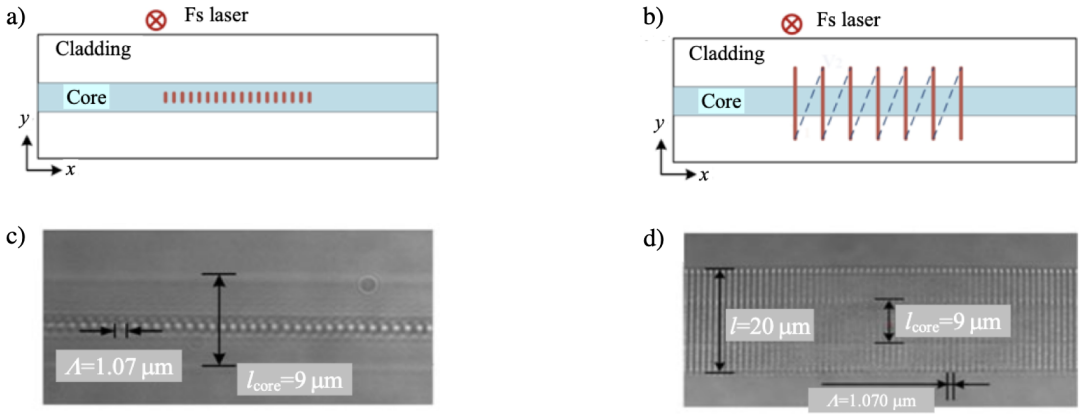

Figure 2.9: Femtosecond inscription of FBGs by different methods: a) and b) schematic representation of the fabrication process by PbP and LbL methods, respectively. Pictures in c) and d) report top views of the inscribed BGs, to be noticed that with LbL method the BGs inscription occurs also in the cladding of the fiber. (Images taken from [33]).

Finally, thermally stable FBGs can be achieved with the inscription of Type 3 refractive index changes by PbP methods. Indeed, while Type 1 modulations can be erased at high temperatures, above 500°C, the FBGs fabricated by voids creation can remain stable at temperatures higher than 1000°C. However, such FBGs are characterized by high propagation losses and poor spectral selectivity, as a result for instance of strong coupling into cladding modes due to non-uniform refractive index change along the core. [121;122]

2.1.3 Techniques to increase the refractive index change

The down-sizing of integrated optical circuits is limited by the bend losses, *i.e.* the losses induced by the presence of curvature in the waveguides, which are directly related to the *radius* of curvature. [123] A way to reduce the bend losses is to increase the refractive index change Δn associated with the guiding structures.

However, the induced refractive index change in the femtosecond inscribed waveguides is rather weak if compared to the one associated with, for instance, wafer waveguides in *Silicon on insulator* (SiO) configuration or by photolithography, thus many solutions have been found to increase the Δn associated with Type 1 modifications.

H_2 loading, UV hypersyntatization, OH-flooding In the post-fabrication process it is possible to increase the photosensitivity of the glass or the fiber by hydrogen H_2 loading at high pressure (> 100 bars) and room temperature (< 50°C) in order to diffuse the hydrogen molecules into the glass network. Such a method is mainly used in the fabrication of *Bragg Gratings* (BGs) on fibers.[33] Furthermore, it has been demonstrated that improved photosensitivity is obtained by short exposure of the H_2 loaded samples to UV light - this method is known as UV hypersensytatization. The absorption of the UV light in the silica glasses leads to an increase in densification, which, as already discussed in the previous section, is one of the causes leading to Δn formation. Finally, H_2 loaded samples can also undergo a post-thermal treatment above 1000°C for a very short time, less than 1 s, to increase the hydroxyl concentration, thus, the defects concentration, which leads to an improvement of photosensitivity; such method is known as OH-flooding.[124;125]

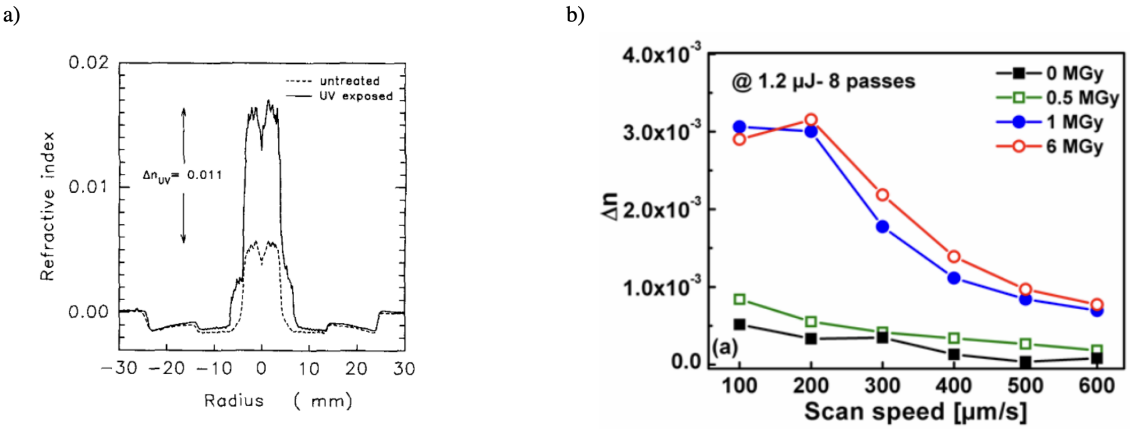

Figure 2.10: Increase of the induced refractive index change Δn by: a) UV exposition of H_2 loaded GeO_2 doped optical fibres (image taken from[34]) and b) X-ray pretreatment of silica based glasses with different irradiation doses (image taken from[35]).

***X*-ray preconditioning** The work of Royon *et al*[35] investigates the role of X-ray pretreatment in silica glasses in the increase of the femtosecond laser photosensitivity by precursors formation.

In this work it is demonstrated that silica glasses exposed to X-rays irradiation show an inhomogeneous formation of NBOHC defects and densification which are dependent on the penetration depth and the dose of the X-rays. As a consequence, it is observed an improvement in the photosensitivity of the pretreated silica glasses under femtosecond irradiation, leading to an increase

of the induced refractive index change Δn, as shown in Fig. 2.10b. The increase in the Δn results in the fabrication in the pretreated samples of more efficient waveguides, with improved mode confinement, although the high dose of X-rays may affect the transmission of the glass.

Frequency doubling Depending on the optical properties of the glass, an interesting solution to achieve high absorption and subsequent high refractive index change consist of doubling the frequency of the femtosecond source, which results in reducing the order of the multiphoton absorption. For instance, in the work of Shah *et al.*[96], an amplified Yb-fiber laser at 1045 nm has been frequency-doubled using a BBO nonlinear crystal to obtain its second harmonic at 522 nm with high repetition rate, 1 MHz, and $\tau_p \lesssim 500$ fs. With this configuration, Shah's group has fabricated waveguides by tuning different pulse energies and translation speeds. The characterization of the near-field profiles of the guided modes enabled to estimate of a high positive refractive index change up to $\Delta n = 1 \times 10^{-2}$ in fused silica.

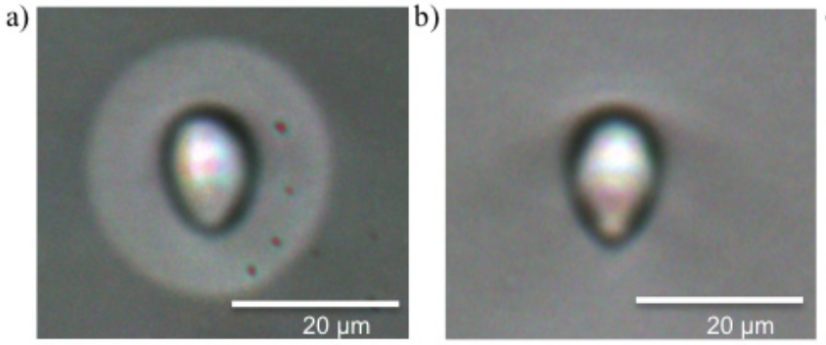

Figure 2.11: Bright field images of the femtosecond laser-induced waveguides in alkaline earth boro-aluminosilicate glass showing a complex refractive index Δn: a) the presence of the outer ring with positive Δn result in the multimode operation of the waveguides with related high propagation losses. (b) After a post-annealing process, the outer ring is removed, enabling the single mode operation. Images taken from[36].

Thermal post-treatment Femtosecond inscriptions at a high repetition rate in multicomponent silicate glasses may produce a complex refractive index change Δn, *i.e.* composed of both positive and negative profiles, because of the heat accumulation and consequent thermal effects. In this case it is possible to apply a thermal post-treatment to adjust the Δn complex profile, as reported by Arriola *et al.*[36] in 2013. In this work, multimode waveguides have been inscribed in an alkaline earth boro-aluminosilicate glass, showing multiple areas with different values of positive or negative induced Δn, as shown in Fig. 2.11a. Subsequently, a slow annealing treatment is applied to the sample: the glass is heated at a temperature higher than the glass transition temperature T_g to start an erasure process, then slowly cooled down to remove the stress and birefringence. Figure 2.11b shows the bright field image of the post-treated waveguides. As a result, the inscribed waveguides showed single mode operation and reduced propagation losses, which makes them suitable for bent configurations.

The multiscan approach Finally, a method to increase the femtosecond induced Δn that does not require any pre- or post-treatment of the glass sample and could be adopted in both low and high repetition rate regimes exploits the *multiscan* inscriptions. As suggested by the name, the laser passages are repeated *in loco*, or with a small translation in one of the inscription directions, to modify either the geometry of the structures and the associated refractive index change. Such a method is based on the shot-to-shot memory of the glass matrix in the absorption of the laser pulses when the subsequent laser passages overlap one on the other.[126] In the work of Lapointe *et al.*[37] in 2020, this method has been exploited in a silica glass irradiated with a low repetition rate femtosecond source in order to achieve high refractive index change, up to 9×10^{-3} after 500 laser scans (see Fig. 2.12a). Moreover, this work shows that the tuning of the refractive index by selecting the number of laser scans allows for the fabrication of waveguides showing either single mode or multimode operation at the same wavelength, as reported in Fig. 2.12b.

However, the author demonstrated that the same approach in a high repetition rate regime does not allow for achieving such good results. The main problem in this regime is related to the heat accumulation and subsequent thermal effects in the heat-affected zone. Indeed, as shown in the work of Graf *et al.*[38], the DLW window in a high repetition rate regime is limited and by increasing the pulse energy it is possible to observe a particular pearl-shaped structure, as reported in pictures on the left in Fig. 2.13, as a consequence of critical thermal effects.

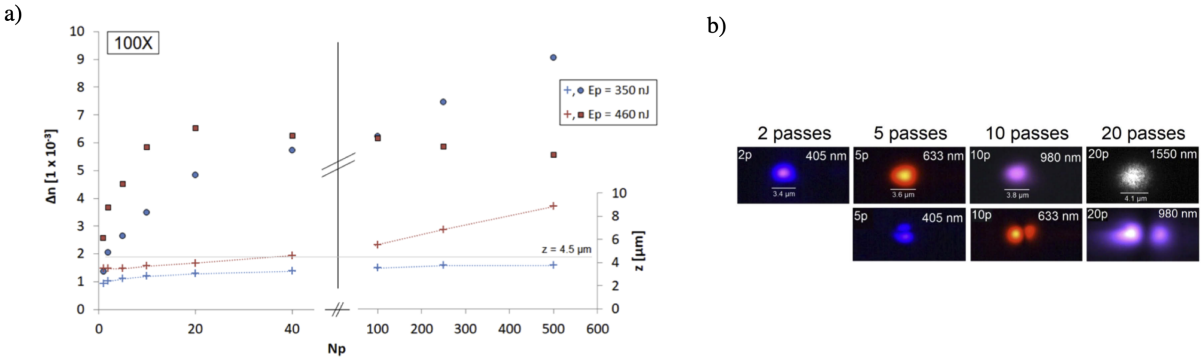

Figure 2.12: Multiscan approach in the low repetition rate regime in silica glass: a) increase of the induced refractive index changes Δn from following laser scans, up to 9×10^{-3} after 500 passages. b) The high refractive index change has been then exploited to fabricate waveguides showing single mode or multimode operation at the same wavelength depending on the number of laser scans. Images taken from [37].

A possible explanation for these peculiar structures may come from the strong increase of the temperature in the heat-affected zone, where the glass is melted and the material is partially dissociated in a gas and plasma mixture, then, the high variation of pressure in the laser-affected spot will then lead to void creations, resulting the in the pearl-chained structures. Once the pearl is formed, the focused radiation is scattered by the surface of the structures and the beam is deformed; moreover, the laser pulses can not affect anymore the area where the pearl-shaped structure is formed because the material is already highly dense.
Regardless of the high refractive index change Δn associated with the pear-chained waveguides, such sharp structures do not allow for efficient guiding application because of high propagation losses.

Finally, the multiscan inscriptions can be exploited for shaping the waveguides in a different geometry. Such approach has been firstly introduced by Liu *et al.* [127] in 2004 and subsequently adopted by Martinez *et al.* [39] in 2015 in order to fabricate in fused silica substrate step-index high contrast waveguides, $\Delta n/n_{core}$ up to 7×10^{-2}, enabling guiding applications around 3.5 μm. The waveguides inscribed with the multiscan approach reported in the pictures on the right of Fig. 2.13 show different areas with Type 1 (areas I and I^*) and Type 2 (area II) modifications. In particular, the luminescent 2D micro mapping of the waveguide reported in d) picture of Fig. 2.13 shows the location of the laser-induced defects, mostly produced in the core I area.

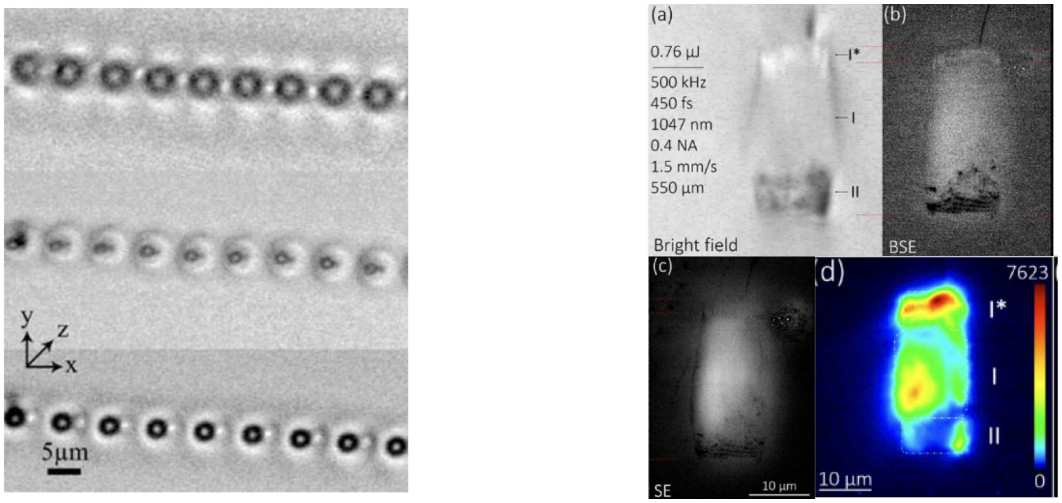

Figure 2.13: (Left) Formation of pearl-chained waveguides in the multiscan laser inscription of a fused silica sample in the high repetition rate regime, 10 MHz (Images taken from [38]). (Right) Multiscan inscription of a step-index waveguide in fused silica substrate to allow for guiding application at 3.5 μm with low propagation losses: a) bright field image, b) and c) back-scattered and secondary electrons images, respectively and d) luminescent 2D micro mapping of the fabricated waveguide revealing the disposition of femtosecond induced defects (Images taken from [39]).

Overall, the multiscan approach proved its efficiency in the increase of the induced refractive index change in both high and low repetition rate regimes. However, the key point to achieving high Type 1 refractive index change with this method is to limit the heat accumulation when performing DLW with high repetition rate sources.

2.2 State of the art of DLW in silver-containing glasses

Silver-containing glasses are developed in the framework of fabricating materials that can lead to an improvement of the photosensitivity during the femtosecond irradiation and new optical properties.

The glasses adopted in this work belong all to the same family, *i.e.* phosphate glasses. The interest in these glasses comes from the ability of such oxide glasses to allow for a high concentration of rare-earth ions or transition metal ions, like silver, while remaining amorphous. [128;129]

2.2.1 The silver-containing phosphate glasses

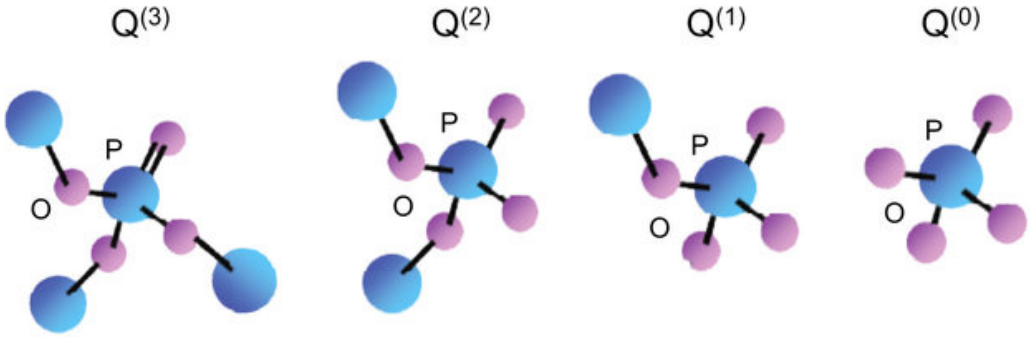

Figure 2.14: Examples of tetrahedra PO_4 (represented as blue spheres) with a different number of bridging oxygen (represented as pink spheres) for the case of $\mathcal{Q}^3$, $\mathcal{Q}^2$, $\mathcal{Q}^1$ and $\mathcal{Q}^0$ entities. Image taken from [40].

The PO_4 tetrahedron is the basic structural unit in the phosphate glass matrix for which the $\mathcal{Q}^n$ notation is used to describe the number n of bridging oxygen, *i.e.* oxygen linking neighboring phosphate tetrahedra, see Fig. 2.14. The acting of glass modifiers (introduced in Sec. 1.1.1) in the phosphate glass matrix is to depolymerize the long phosphate chains, which increases the ratio $\frac{[O]}{[P]}$ between oxygen and phosphate quantities. Therefore, the $\mathcal{Q}^n$ notation is generally used to classify phosphate glasses depending on the length of the phosphate chains and, thus, on the ratio $\frac{[O]}{[P]}$ as following: [41]

- *Ultra*-phosphate, for which $\frac{[O]}{[P]} < 3$,, characterized by long phosphate chains and a glass matrix having a reticular structure;

- *Poly*-phosphate, for which $\frac{[O]}{[P]} \geq 3$, characterized by long phosphate chains without interconnections. In the particular case of $\frac{[O]}{[P]} = 3$, the matrix is defined as *Meta*-phosphate, for which the phosphate chains are, theoretically, infinitely long;

- *Pyro*-phosphate, for which $3.25 < \frac{[O]}{[P]} < 3.75$, characterized by shorter phosphate chains composed majorly of dimeric entities;

- *Ortho*-phosphate, for which $\frac{[O]}{[P]} > 3.75$, that is finally composed of monomeric entities, principally, that are connected thanks to other glass formers, such as the Al_2O_3 oxide, functioning as intermediates.

The introduction of glass modifiers, like ZnO or Ga_2O_3, can have an impact on the chemical and water durability of the phosphate glasses. Indeed, the sensitivity of the glass matrix to humidity is mainly linked to the presence of the pentavalent phosphorus, therefore the shortening of the phosphate chains, and thus the increase in the number of non-bridging oxygen (NBO), results in the diminishing of the pentavalent phosphorus entities.
The glasses adopted in the experimental work reported in these Chapters are mainly belonging to two types of phosphate glasses:

- Zinc-phosphate glasses (**PZn**), where Ga_2O_3 oxide is added in a small percentage to the $58Zn - 43P_2O_5$ glass matrix to improve its chemical durability;
- Sodium-gallium phosphate glasses (**GPN**), where the glass matrix is composed of sodium metaphosphate $NaPO_3$ to which the Ga_2O_3 oxide is added in percentages higher than those used for the zinc-phosphate glasses.

Finally, the insertion of silver ions in the phosphate matrix allows for the presence of large absorption bands in the UV, typically between $200 - 300$ nm.

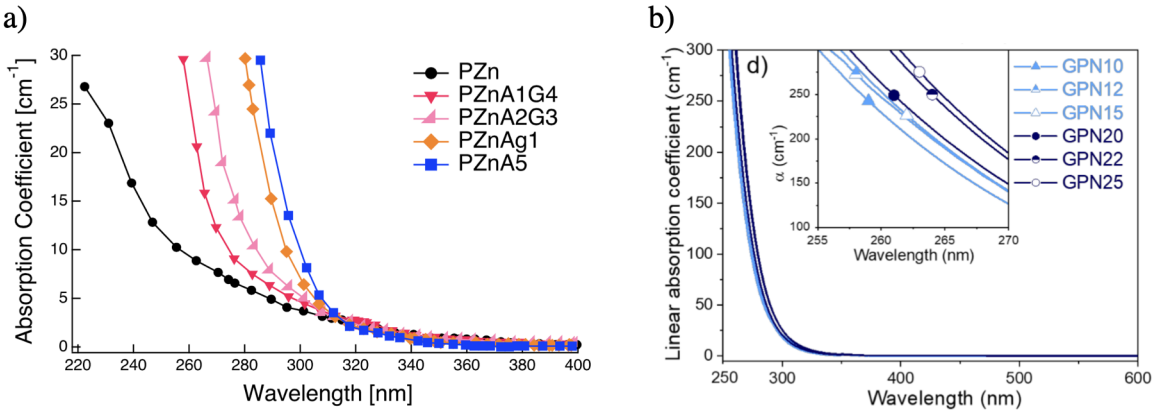

Figure 2.15: Absorption spectra in UV and visible of a) Zinc-phosphate glasses (PZn) with and without (black curve) silver addition (image taken from [7]) and b) silver-containing Sodium-gallium phosphate glasses (image taken from [41]).

Indeed, the silver-containing phosphate glasses are characterized by a typical absorption spectrum like the one reported in Fig. 2.15 for the two families, PZn and GPN.
Additionally, Fig. 2.15a compares the absorption spectrum of the PZn samples with and without the addition of silver: it is possible to observe that the adding of silver ions into the glass

matrix extends the UV absorption of the glass to longer wavelengths.

2.2.2 The femtosecond irradiation

Femtosecond irradiation of a silver-containing glass at 1030 nm leads to a 4-photon absorption due to the presence of Ag^+-Ag^+ pairs, which exhibit an excitation band at 260 nm.[42] The ratio between the concentration of silver ions and silver pairs depends on the glass matrix structure: evolving from poly-, to pyro,- to ortho-phosphates the concentration of silver pairs increases with respect to the one of the silver ions. Therefore, the photosensitivity of silver-containing phosphate glasses is dependent on the glass matrix structure, as reported in the work of Guérineau *et al.* in 2018[130] and shown in Fig. 2.16.

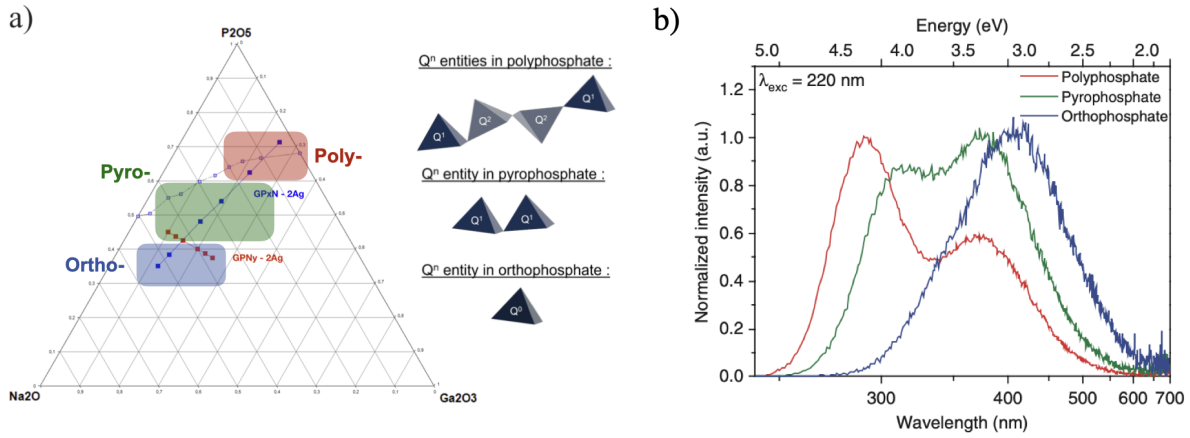

Figure 2.16: a) $P_2O_5 - Ga_2O_3 - Na_2O$ ternary diagram of the GPN series investigated by Guerineau *et al.*, highlighting the different class of phosphate glasses, for each of them is reported on the right a schematic representation of the corresponding phosphate chains by means of $\mathcal{Q}^n$ notation. b) Emission spectra of the same GPN glasses showing the redshift of the emission curve due to the increasing concentration of silver pairs for glasses evolving from poly- to ortho-phosphate configuration. Images adapted from[42;41].

Silver clusters formation

When operating with a high repetition rate femtosecond source, and while keeping low pulse energy (few tens of nJ) the absorption of the single laser pulse activates the clustering of the silver ions. Such a process involves three different entities: the silver ions Ag^+ of the glass

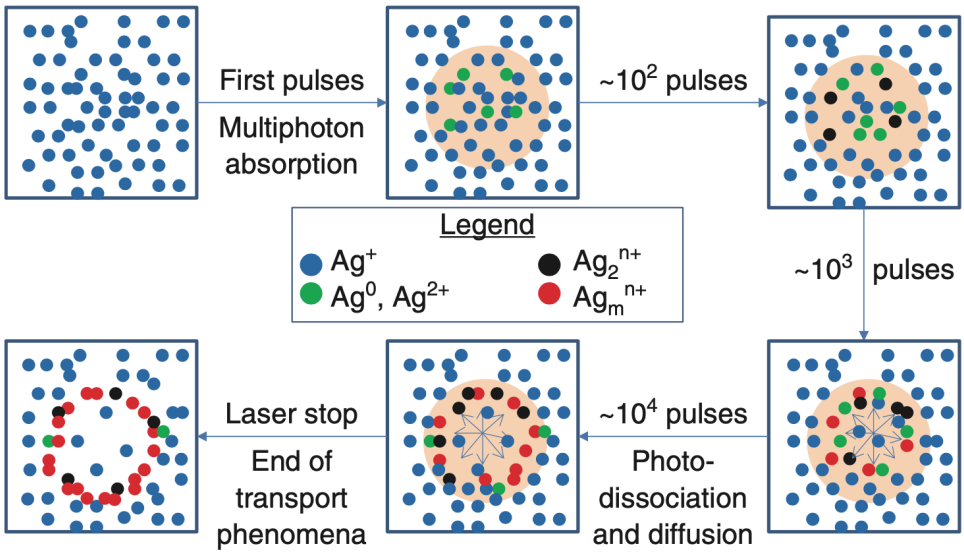

Figure 2.17: Schematic representation of the physical processes involved in the silver cluster formation during the many-pulse absorption of a focused femtosecond source. Image taken from [42]

matrix and the e^- electrons and h^+ holes produced during the absorption of each femtosecond pulse.

The released electrons will enable the formation of Ag^0 species by the reaction:

$$Ag^+ + e^- \rightarrow Ag^0, \tag{2.3}$$

where Ag^0 should be considered more like an electron localized near a silver ion, rather than a silver ion itself. The reaction in Eq. 2.3 ends when there are no more available electrons, therefore the concentration of Ag^0 is related to the number of electrons produced during the absorption of each pulse.

At the same time, the holes h^+ can be trapped by the Ag^+ silver ions producing

$$h^+ + Ag^+ \rightarrow Ag^{2+}, \tag{2.4}$$

where Ag^{2+} are considered to have no mobility, and recombination mechanisms

$$e^- + Ag^{2+} \rightarrow Ag^+ \tag{2.5a}$$

$$h^+ + Ag^0 \rightarrow Ag^+ \tag{2.5b}$$

$$e^- + h^+ \tag{2.5c}$$

are carried out in competition with the production of Ag^0 and Ag^{2+}.

Thus, the mobility of Ag^0 species is activated allowing them to diffuse at the edge of the voxel of interaction; the trapping of Ag^0 by the silver ions leads to the first stage of the formation of the clusters:

$$Ag^0 + Ag^+ \rightarrow Ag_2^+, \tag{2.6}$$

therefore the concentration of first-step silver clusters is directly related to the quantity of Ag^0 species.
Finally, the absorption of the following laser pulses will lead, on the one hand, to further growth of larger silver clusters Ag_m^{x+} with no mobility and, on the other hand, to the photodissociation of the previously-induced silver clusters in the center of the interaction voxel, as a consequence of the high laser intensity and the existence of absorption bands for the clusters in the UV.

Thermal management during the silver cluster formation

A theoretical model for simulating the evolution of the temperature during the femtosecond irradiation elaborated by Smetanina *et al.*[43] in 2016 concluded that the increase of temperature in the interaction voxel is only a few tens of °C, as reported in Fig. 2.18. Such an increase in the temperature is sufficient to enable the diffusion of silver ions but insufficient to locally melt the glass matrix, resulting in no modifications or re-arrangement of the glass structure. Therefore, the silver clustering in silver-containing glasses during the femtosecond irradiation occurs in an **athermal regime**, despite the use of a high repetition rate laser.

Indeed, the small increase of the local temperature is the consequence of a very low nonlinear absorption, typically below 0.1% per pulse, as observed by Bellec *et al.*[45] in 2009, and the threshold for achieving silver clusters is reached after a considerable amount of pulses, above 10^2 pulses.

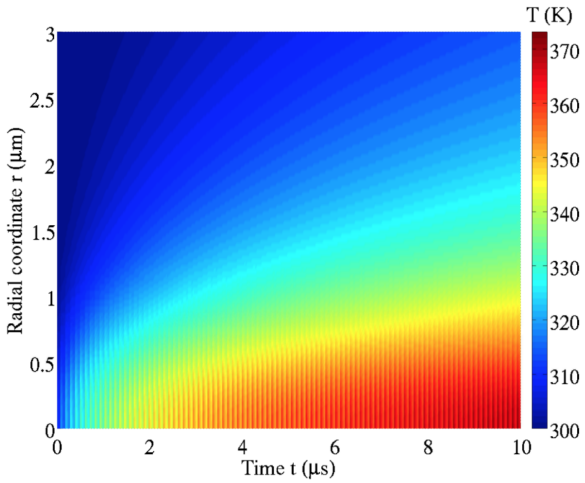

Figure 2.18: Simulation of the evolution of the local temperature in the voxel of interaction during the many-pulse absorption. Image taken from [43]

Geometry of the silver sustained structures

After stationary femtosecond irradiation on a single spot, the silver clusters arrange in a circular shape on the plan xy perpendicular to the laser beam propagation direction with a diameter $\phi = 2\omega_0 = 1.2\frac{\lambda}{N.A.}$ related to the N.A. of the microscope objective used to focalize the laser, as depicted in Fig. 2.19a. In the z direction, instead, the silver sustained structure presents a thickness that is comparable with the b confocal parameter of the laser-focused inside the glass. Notably, the image in Fig. 2.19a shows that the silver-induced structures present features that overcome the diffraction limit. Indeed, the profile obtained by *High Resolution Scanning Electron Microscope* (HRSEM) imaging of the structure reported in Fig. 2.19a along the dashed line shows a sub-micron (~ 80 nm) thickness of the silver sustained structure.

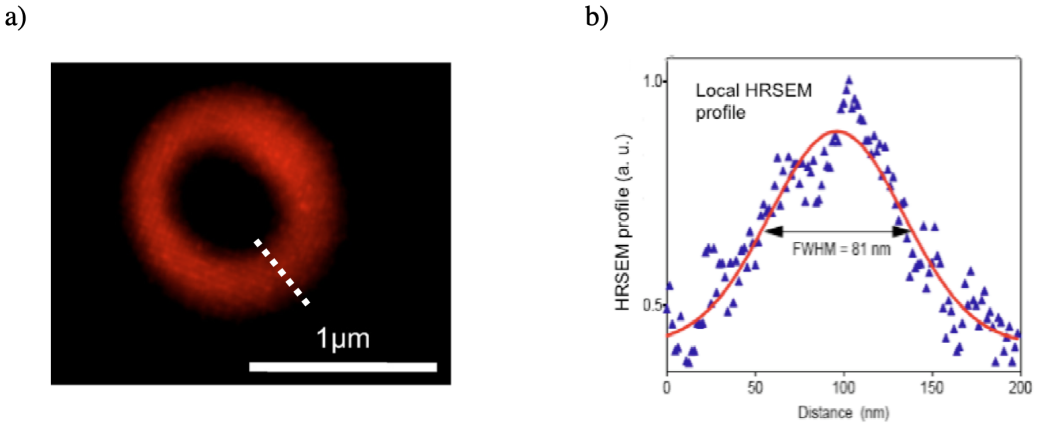

Figure 2.19: a) Fluorescence confocal image of the laser-induced silver clusters on the plane perpendicular to the laser beam direction ($\lambda_{exc} = 405$ nm). Image taken from [44]. b) Profile of the structure in a) along the dashed line obtained by HRSEM imaging, showing a thickness of around 80 nm, well below the diffraction limit. Image taken from [45]

Fluorescence

The silver clusters present two main absorption bands in the UV peak around 290 nm and 345 nm which extend to the visible, while the fluorescent emission covers the whole visible range.[131;45;46] In 2010 Bellec *et al.* demonstrated that the fluorescence intensity of the silver clusters is dependent on the repetition rate of the laser: the fluorescence intensity decreases when decreasing the repetition rate of the laser, although it is still present at 100 kHz for 10^7 number of pulses. Indeed, the fluorescence of the clusters is tightly dependent on the number of pulses and the laser intensity, since the quantity of photoinduced clusters is also dependent on these two parameters.

The dependence of the fluorescence intensity on the number of pulses, the irradiance and on the repetition rate is reported in Fig. 2.20.

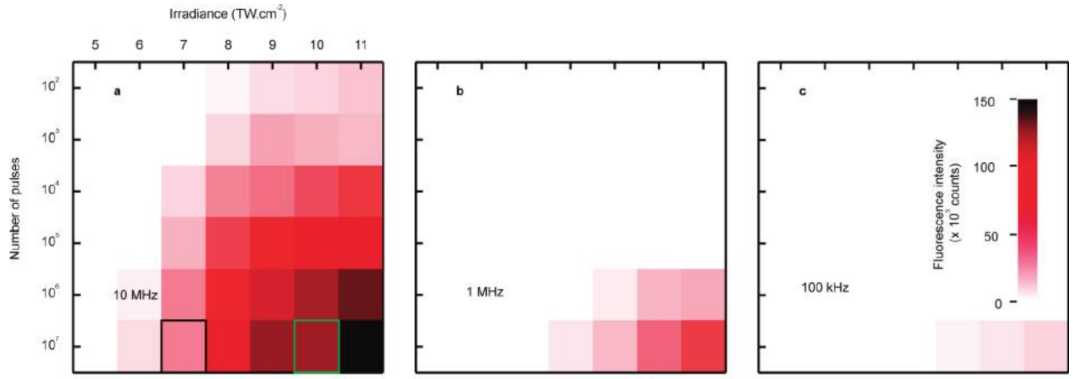

Figure 2.20: Dependence of the fluorescence intensity on the number of pulses and the irradiance for different repetition rates: a) 10 MHz, b) 1 MHz and c) 100 kHz. Image taken from [46]

2.2.3 The Type A refractive index change

In 2017, Abou Khalil *et al.* [47] discovered that a new type of refractive index change is associated with the silver clusters formation. This variation of the refractive index of the glass is no more related to glass matrix modifications but it is instead originated from the creation of new silver species with enlarged molecular polarizability, which increases the electric susceptibility.
Such new type of induced Δn has been denominated *Type A* after *Argentum*.
Moreover, in the same work it has been demonstrated that the novel Type A refractive index change is always positive and located at the position where the silver clusters are photoinduced.

Figure 2.21a reports the fluorescence image of a series of serpentine silver-sustained structures inscribed 160 μm below the surface of a PZn sample, each of them is achieved at different DLW parameters by changing the irradiance and the translation speed of the sample, *i.e.* the number of pulses. The phase image reported in Fig. 2.21b is obtained thanks to the Sid4Bio software and camera by Phasics company. Such device is based on the *Quadriwave Lateral Shearing Interferometry* (QWLSI) in order to reconstruct both the intensity and the phase from the diffraction pattern given by 4 replicas of a (coherent or not) beam passing through the sample and diffracted by a *Modified Hartmann Mask* (MHM) before reaching the sensor CCD camera. [132] The refractive index change associated with the inscription of the serpentine structures is obtained from the Optical Path Difference (OPD) extracted from the phase image

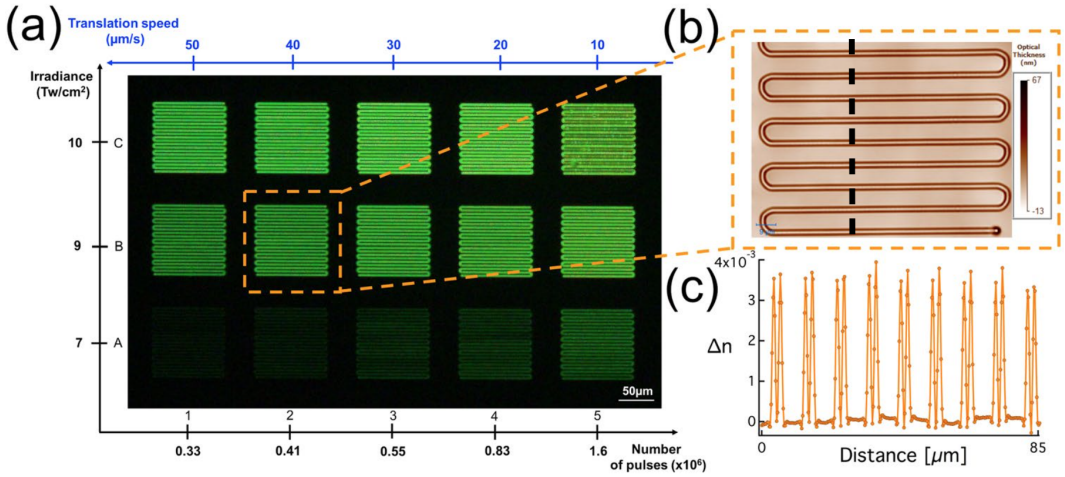

Figure 2.21: Demonstration of the positive Δn associated with the inscription of Type A modifications: a) white fluorescence image of a series of serpentine structures inscribed in a PZn sample while varying the DLW parameters ($\lambda_{exc} = 480$ nm), b) phase image of one of the silver-sustained structures and c) profile of the induced Δn obtained from the phase image along the black dashed line in b). Image adapted from [47]

and the thickness e of the structure by simply:

$$\Delta n = \frac{OPD}{e}, \tag{2.7}$$

for optically-thin samples. On the contrary, the way to quantify the refractive index change in optically-thick sample is more complex and the interested reader is referred to the work of Abou Khalil *et al.* [133] for a detailed description.
Thus, Fig. 2.21c reports the profile of the induced Δn along the black dashed line in Fig. 2.21b.

Similarly to the fluorescence, also the refractive index change Δn is dependent on the number of pulses and the irradiance, as reported in Fig. 2.22, as to remark the link between these two properties and the number of photoinduced clusters.

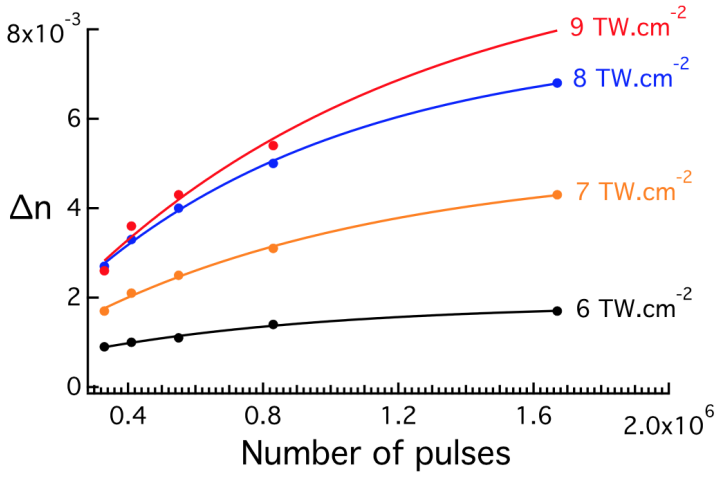

Figure 2.22: Dependence of the Δn associated with Type A modifications on the number of pulses and the irradiance. Image taken from [47]

Waveguides

Such positive refractive index change is suitable for waveguiding applications.
As reported by Abou Khalil *et al.* [47], the inscription of a waveguide based on photoinduced silver clusters results in the fabrication of a double-track structure for which each fluorescent track acts like a single waveguide. Therefore, the guided mode at the output of the waveguide presents a peculiar double-gaussian profile, as reported in Fig. 2.23.

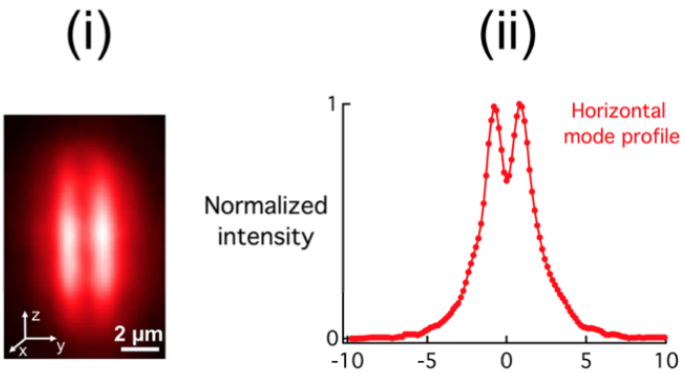

Figure 2.23: i) Near-field images of the guided mode at the output of a waveguide based on Type A modifications, while the picture in ii) reproduced the guided mode profile along the horizontal direction. Images taken from [47]

Furthermore, it is noteworthy to highlight that Type A refractive index modifications enabled the fabrication of beam splitters, Y-junctions, couples and, more recently, a refractive index sensor based on near-surface waveguides.[134] Particularly, the inscription of the near-surface waveguides has been achieved requiring no additional processing, as instead necessary in the case of Type 1 near-surface waveguides.
The interested reader will find an insightful comparison between Type A and Type 1 modifications in literature.[135]
Nevertheless, it is of interest to point out that it is still possible to achieve Type 1, 2 and 3 modifications in silver-containing glasses.

Rewriting ability

Finally, a peculiarity related to the Type A modifications is the rewriting ability of the silver clusters: when the laser spot invests a pre-existing silver-sustained structure, a photodissociation of the silver clusters on the overlapped area will occur, allowing for the inscription of a new double structure.

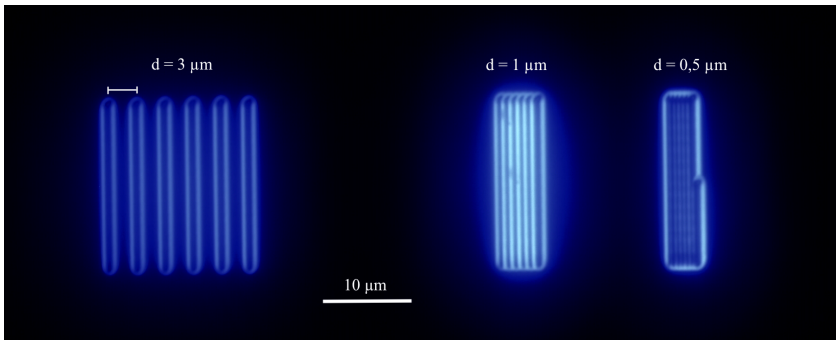

Figure 2.24: Fluorescence image ($\lambda_{exc} = 365$ nm)of three structures composed of a series of lines (20 μm long) separated by $d = 3$, 1 and 0.5 μm, showing the rewriting ability of the Type A modifications. The structures have been inscribed 160 μm below the surface of a PZn sample using a microscope objective with N.A. 0.75 and imaged on a fluorescence microscope with a 60× N.A. 0.7 microscope objective.

Indeed, as reported in Fig. 2.24, by approaching the lines of a distance smaller than laser spot diameter $\phi = 2\omega_0 = 1.2\frac{\lambda}{N.A.}$, the previously-induced double-track is converted into a single-track structure.

The fluorescence image in Fig. 2.24 reports different structures for which the distance between consecutive laser scans is $d = 3, 1$ and 0.5 μm, respectively. Remarkably, it is still possible to observe fluorescence at the center of the structure with an interline distance of 0.5 μm. Moreover, the modulation of the fluorescence is associated with a modulation of the refractive index change, as reported in Fig. 2.25.

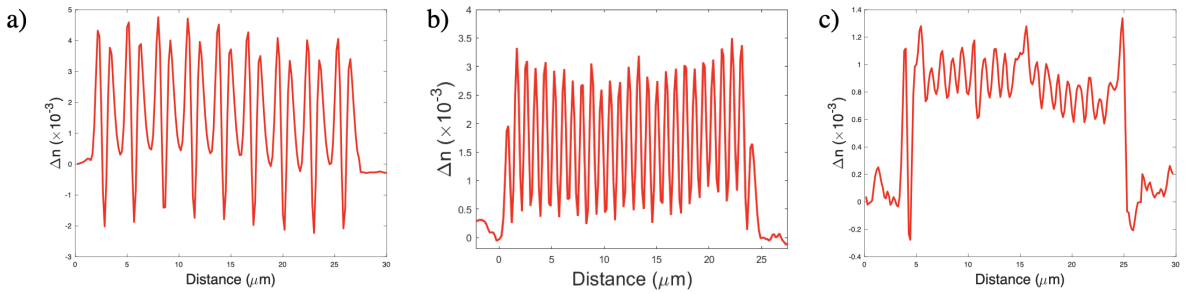

Figure 2.25: Refractive index Δn profiles for periodic structures with interline distances: a) $d = 3$, b) 1 and c) 0.5 μm. The profiles have been extracted from phase images acquired using the SID4Bio software from Phasics company and a $100\times$ microscope objective with N.A. 1.3 (index matching oil $n = 1.518$).

The refractive index profiles reported in Figure 2.25 are obtained from phase images acquired with the SID4Bio software using a $100\times$ microscope objective with N.A. 1.3, enabling spatial sampling down to ~ 300 nm for each pixel of the CDD camera. Such a spatial sampling allow for fully resolving features 1 μm distant but has strong limitations when the distance decreases to 500 nm. Figure 2.25a reports the case of 3 μm separation between consecutive laser scans: since the structure has been inscribed using a microscope objective with N.A. 0.75, the beam diameter at the focal plane is 1.6 μm, thus smaller than the interline separation d. Indeed, the refractive index profile shows the positive Δn associated with the double-line structures and a negative Δn associated with the depletion of silver in the center of the laser spot. However, when the separation d is smaller than the beam diameter, the rewriting ability of the silver sustained structures allows for producing a modulation of the Δn that has a positive D.C. component, while its magnitude and the magnitude of the A.C. component depend on the separation between the laser scans and, thus, on the overlap between the positive Δn of the remaining single-tracks. Therefore, given the resolution of the CDD sensor, it is possible to fully resolve the periodic structure with $d = 1$ μm, as reported in Fig. 2.25b, while for $d = 0.5$ μm only the positive

D.C. component of the Δn is measured in Fig. 2.25c. However, the A.C. component of the induced refractive index change can be retrieved, for instance, by diffraction measurements of the periodic structure, as will be discussed in Chaper 4.

Indeed, such interesting ability of Type A modifications to write periodic structures with very small periodicities has been exploited for the inscription of Bragg Gratings with very short periodicity, well below the diffraction limit, which will be discussed in Chapter 4.

Conclusions on the chapter

The Chapter deals with the processes involved in the DLW of glasses using a femtosecond laser source.

In the first part of the Chapter, the DLW technique is discussed, highlighting the phenomena involved in the femtosecond irradiation of glasses that are associated with the appearance of a refractive index change and stressing the importance of the DLW parameters on the magnitude and the different types of Δn obtained.
In particular, the cases of DLW with high and low repetition rate laser sources are discussed in order to distinguish between laser inscription in thermal and athermal regimes, reporting specifically the effects of both regimes on the inscription of Type 1 refractive index modifications. Indeed, such type of induced Δn is the only one allowing for the inscription of embedded waveguides.
Therefore, the fabrication of waveguides in different glass compositions is briefly reviewed and some techniques adopted to increase the associated refractive index change are discussed, pointing out the importance of high Δn for enabling the miniaturization of integrated optical circuits.

The second part of the Chapter focuses on silver-containing phosphate glasses.
Firstly, the optical properties of pristine silver-containing phosphate glasses are examined. Afterward, the physicochemical mechanisms involved in the femtosecond irradiation of such glasses are discussed, analyzing the reactions that lead to the silver clustering during the absorption of each laser pulse. Thus, a discussion on the thermal management of the glass matrix in the interaction voxel during the silver cluster formation is carried out to highlight that the inscription of silver-sustained structures occurs, remarkably, in an athermal regime, despite the use of a high repetition rate laser source.

The innovative Type A refractive index change is, thus, introduced and a discussion on its dependence on DLW parameters is carried out.
Moreover, some properties of the silver-sustained structures, such as fluorescence, under-diffraction-limited features and rewriting ability, are discussed.

Chapter 3

Laser inscription of Type A modifications with a multiscan approach

Introduction to the chapter

Based on the discussions carried out in the previous Chapter, this Chapter investigates the effects of the multiscan technique on the inscription of the Type laser modifications in an athermal regime.

For this purpose, multiscan structures have been performed in three silver-containing glasses with different compositions. Thus, the results are presented and discussed to provide a phenomenological explanation of the high refractive index associated with the multiscan silver-sustained structures.

In the second part of the Chapter, the promising high refractive index change is exploited in the fabrication of multiscan waveguides.
A study on the evolution of the Mode Field Diameter and the propagation losses of the multiscan waveguides, together with the exploitation of the silver-clusters rewriting ability, shows the potentiality of such waveguiding structures for applications in integrated optical circuits.

3.1 Experimental setup, DLW and characterization procedures for the multiscan Type A structures

The multiscan inscriptions have been performed using a prototype fs fiber laser at 1030 nm, with repetition rate 9.25 MHz, pulse duration 400 fs and average output power 5 W.
The samples investigated in this work are:

- a commercial silver-containing zinc-phosphate glass, hereinafter referred to as *AG01*, from Argolight company;
- a silver-containing super-ortho gallo-phosphate glass, hereinafter referred to as *GPN*, elaborated at the ICMCB laboratory in Bordeaux;
- a commercial silver-containing magnesium-phosphate glass, hereinafter referred to as *AG03*, from Argolight company.

The positioning of the samples during the laser inscription was assured within a precision of 30 nm by motorized 3-axis stages from Newport (XMS100 - VP5ZA). For each sample, a series of serpentine structures of length $L = 50$ μm and interline distance of 10 μm has been inscribed using a 40$\times$ microscope objective with N.A. 0.75 at a depth of 160 μm below the sample's surface, to prevent aberrations.
For each structure, the DLW parameters, the speed $v = 10, 20, 35, 50$ and 100 μm/s and the laser intensity, have been changed to create a matrix of irradiances. Each matrix of irradiances has been repeated *in loco* a number of times given by $N_{scan} = 1, 2, 3, 5, 7, 10$ and 20. The laser intensity has been varied for each sample from the DLW threshold to the explosion threshold, therefore for AG01 $I = 4 - 11$ TW/cm^2 (equivalent to pulse energy $E_p = 18 - 50$ nJ), for GPN $I = 4 - 8.7$ TW/cm^2 ($E_p = 18 - 38.5$ nJ) and for AG03 $I = 12 - 23$ TW/cm^2 ($E_p = 56.5 - 103$ nJ).

Figure 3.1 reports the fluorescence images of the matrices of irradiance inscribed with $N_{scans} = 1$ and 10 in the AG01 sample. The fluorescence intensity of the 10-scans serpentine structures appears higher than the one of the single-scan structures, especially for high speed and low intensity (see green dashed lines), suggesting that more silver clusters are induced when repeating the inscription several times.

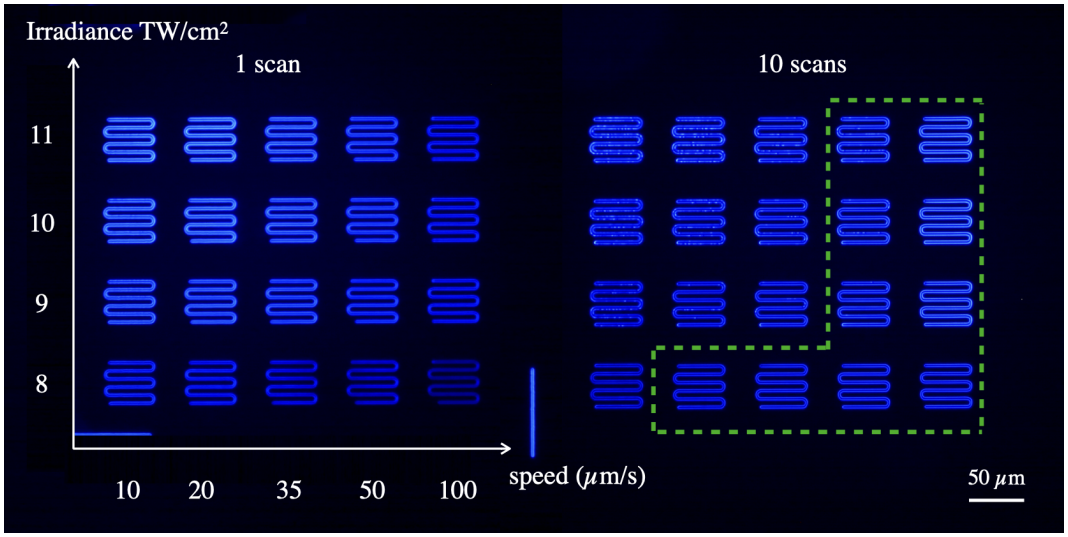

Figure 3.1: Fluorescence images of the irradiance matrices for $N_{scan} = 1$ and 10 for the AG01 sample. The green dashed lines highlight the area where the fluorescence of the 10-scans structures is higher than the one observed for single-scan structures. Images have been acquired using a 60× microscope objective with N.A. 0.7 with excitation $\lambda_{exc} = 365nm$.

After the inscription, each serpentine structure has been imaged with the Sid4BIO software to quantify the Optical Path Difference OPD associated with the inscribed structures. The processing of more than 600 phase images acquired from multiscan structures has been carried out using a homemade mask approach to remove the background noise and eventual glass inhomogeneity and to average the OPD measurements along all the branches of the serpentines. For sake of clarity, the mask approach is discussed in Appendix.
In order to retrieve the thickness e of the multiscan structures, multiscan lines have been inscribed at the edges of the sample with the same DLW parameters. By polishing the lateral surfaces it was then possible to bring the multiscan lines on the surfaces and image them on a microscope using white light. Figure 3.2 shows the growing thickness of the multiscan structures when increasing the number of scans (as highlighted by the black arrows), given a constant laser irradiance, in this case $I = 14$ TW/cm^2, for the AG03 sample.

Finally, the refractive index change Δn associated with each multiscan structure has been calculated by Eq. 2.7.

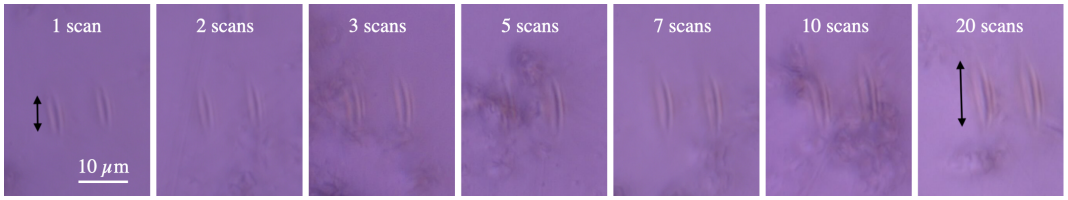

Figure 3.2: Evolution of the thickness of the multiscan structures for the AG03 sample: a series of two multiscan lines inscribed with the same DLW parameters, $v = 10$ μm/s and $I = 14$ TW/cm^2 in this case. Black arrows highlight the growing thickness of the multiscan structures when increasing the number of laser passages. Images acquired in white light after polishing the lateral surface in order to bring the structures on the surface.

3.2 Results and comparison between different glasses

The results from the refractive index measurements Δn of the multiscan structures will now be presented and discussed singularly for each sample. Thus, the results for all the samples will be compared in order to discuss the phenomena involved in the multiscan inscription of Type A modifications for different glass matrices.

In order to link the evolution of the refractive index changes Δn to the increase of the laser scans, the cumulative number of absorbed pulses has been calculated for each inscription from:

$$N_{pulses} = \frac{N_{scans}\,\phi\,f_{rep}}{v}, \tag{3.1}$$

where f_{rep} is the repetition rate of the fiber laser, $\phi = 1.2\frac{\lambda}{N.A.}$ is the diameter of the focused laser spot, N_{scans} is the number of repetition and v is the DLW speed.

3.2.1 AG01

Figure 3.3 reports the induced Δn associated with the multiscan structures in the AG01 sample versus the cumulative number of absorbed pulses.

The data reported in Fig. 3.3 show that there is a dependence of the induced Δn on the cumulative number of absorbed pulses and the DLW intensity. Indeed, it is possible to distinguish between results achieved at high and low DLW intensity. At high intensity, for $I \geq 8$ TW/cm^2, the Δn associated with the multiscan structures rapidly increases to 1×10^{-2} after

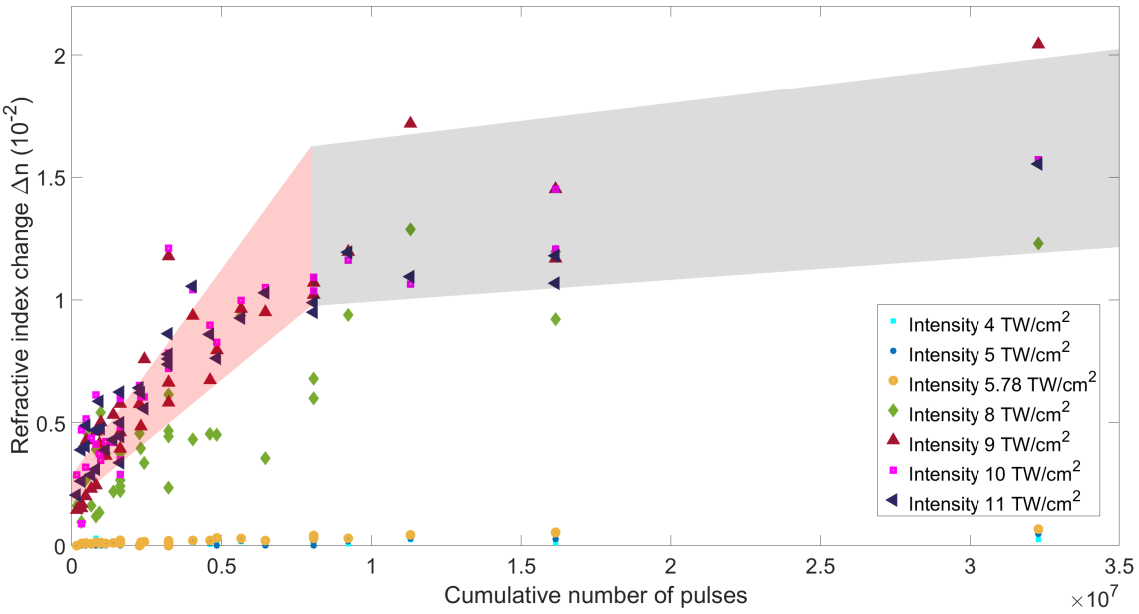

Figure 3.3: Refractive index change Δn associated with each inscribed multiscan structure in AG01 depending on the number of cumulative absorbed pulses, *i.e.* the total number of pulses absorbed in the N_{scan}, for a given laser irradiance. Remarkably, high refractive index change up to 2×10^{-2} is achieved after 3×10^7 pulses. The colored areas individuate two different regimes of inscription: the area in red highlights a linear increase of the refractive index change Δn associated with the multiscan structures with the number of cumulative absorbed pulses, while a flat growth is highlighted in grey, suggesting a saturation regime.

$N_{pulses} = 0.5 \times 10^7$ and it remarkably achieves 2×10^{-2} after $N_{pulses} = 3 \times 10^7$ at $I = 9$ TW/cm^2. It should be noted that the error bars have been omitted in the graph reported in Fig. 3.3 since the errors on the Δn measurements arises from the quality of the reference images of pristine areas of the sample used to acquire the phase images: such error is estimated typically on the order of 1.5×10^{-3}, which is negligible when compared with the values of Δn achieved at high intensity and high number of cumulative absorbed pulses.
However, such error is significant for Δn measurements at low intensity and low N_{pulses} and may smooth the results for $I = 8$ TW/cm^2 reported in green in Fig. 3.3.
Moreover, two areas have been shaded in red and gray colors in Fig. 3.3 for the Δn data at high intensity:

- red area: the fast growth of the induced Δn points out a direct dependence of the refrac-

tive index change, *i.e.* of the number of induced silver clusters, on the cumulative number of pulses absorbed during the N_{scans} laser inscription. On a first phenomenological description, such dependence can be approximated with a linear increase of the Δn with the N_{pulses} which corroborates the argument that the process of silver clusters formation occurs in an athermal regime.

- gray area: the growth of the refractive index change Δn slows down and the Δn seems to settle to a constant value, which can be described as a saturation effect.

The linear dependence of the induced Δn on the N_{pulses} is supported by the iso-Δn curves reported in Fig. 3.4.

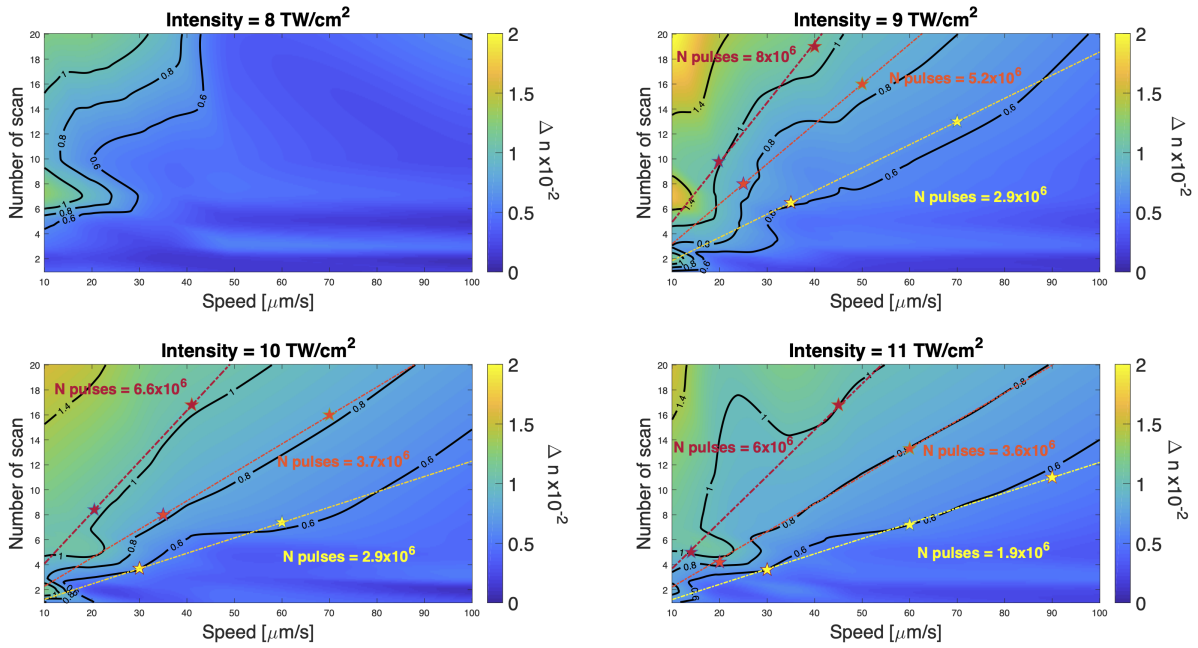

Figure 3.4: Iso-Δn curves for each laser irradiance for the AG01 sample: the black lines individuate the curves where the induced Δn is constant while changing the number of laser scans and DLW speed. The dashed colored lines identify the iso-N_{pulses} curves for $\Delta n = 0.6, 0.8$ and 1×10^{-2} for the cases of $I = 9, 10$ and 11 TW/cm^2: the number of cumulative absorbed pulses N_{pulses} necessary to achieve the specific Δn magnitude is reported, accordingly, with the same color.

The 2D graphs report the magnitude of the Δn versus both the number of laser scans and

the DLW speed for a given high DLW intensity: for each plot, the increase of the induced Δn follows the increase of the cumulative number of pulses, which is obtained by reducing the DLW speed and increasing the number of repetitions (as defined in Eq. 3.1).
Moreover, the black lines individuate the curves with constant Δn obtained with different inscription parameters: indeed, the iso-Δn curves confirm that the magnitude of the induced Δn is dependent only on the number of pulses absorbed, which is a direct consequence of the athermal regime. Finally, the slope of the iso-Δn curves determines the associated N_{pulses}, therefore some of the experiments having the same number of N_{pulses} have been identified by the starred marks, highlighting the iso-N_{pulses} line with the same color: for instance, at $I = 11$ TW/cm^2, $\Delta n = 0.6$ and 0.8×10^{-2} are achieved with $N_{pulses} = 1.9$ and 3.6×10^6, respectively.

At low intensity, no saturation of the induced Δn is observed in Fig. 3.3. Although its magnitude is quite low, it is still possible to individuate a linear increase of the induced Δn with respect to the N_{pulses}. Moreover, the slow increase of the refractive index contrast associated with the multiscan structures enables for fine-tuning of the Δn magnitude which in the end allows for good control of such value.
As a matter of fact, it can be supposed that fine-tuning of very high refractive index change can be achieved by firstly inscribing the Type A modifications at high intensity, in order to rapidly obtain high induced Δn, then its magnitude can be slowly increased by lowering the laser intensity for the following laser scans.

3.2.2 GPN

Similar results have been obtained for the GPN sample.
Figure 3.5 reports the induced Δn for all the multiscan structures versus the cumulative number of absorbed pulses, for each laser intensity.

High refractive index change up to 1.3×10^{-2} is achieved in the GPN sample after 3×10^7 pulses at high DLW intensity, $I = 7.3$ TW/cm^2. Also in this case there is a clear dependence of the refractive index contrast associated with the silver-sustained multiscan structures to the cumulative number of pulses absorbed during all the repetitions.
Moreover, the shaded colored areas individuate the linear growth of the Δn with the N_{pulses}: from the data, it is clear that the slope of the Δn increase is dependent on the DLW intensity, as already observed by Abou Khalil *et al.* in 2017.[47]
Nevertheless, as already observed for the AG01 sample, no saturation occurred at low DLW

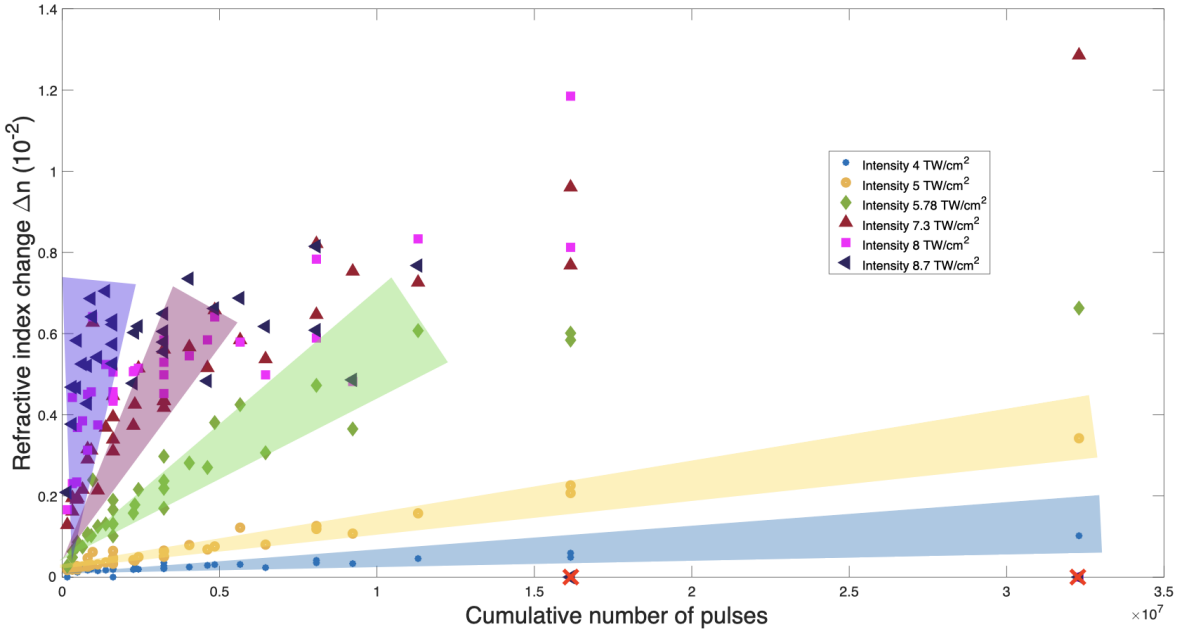

Figure 3.5: Refractive index change Δn of each inscribed multiscan structure in GPN depending on the number of cumulative absorbed pulses, *i.e.* the total number of pulses absorbed in the N_{scan}, for a given laser irradiance. High refractive index change Δn up to 1.3×10^{-2} is achieved after 3×10^7 pulses. The colored areas individuate the linear increases of the Δn for each irradiance: it is noteworthy to mention that the slope of the Δn increase is dependent on the irradiance, therefore at high irradiance high Δn is achieved with a smaller number of cumulative absorbed pulses. Two red crosses individuate the explosions that occurred at high irradiance and high number of cumulative pulses: in this case, the associated refractive index change has been imposed $\Delta n_{exp} = 0$.

intensity in the GPN sample, however, the saturation threshold is reached at lower N_{pulses} when increasing the DLW intensity. Indeed, for the case of $I = 8.7$ TW/cm^2, the Δn saturates around $0.7 - 0.8 \times 10^{-2}$ after only 0.4×10^7 cumulative absorbed pulses.
Additionally, after 1.5×10^7 pulses at $I = 8.7$ TW/cm^2, explosions occurred for the multiscan structures inscribed with 10 μm/s and 20 laser scans ($N_{pulses} = 3.16 \times 10^2$), and for 10 μm/s and 10 laser scans and 20 μm/s and 20 laser scans ($N_{pulses} = 1.56 \times 10^2$). For these cases, the induced Δn has been imposed equal to 0 since only Type A refractive index changes are of interest in this work. The experiments for which explosions occurred have been marked with

red crosses in Fig. 3.5.

Iso-Δn curves for the GPN sample are reported in Fig. 3.6.

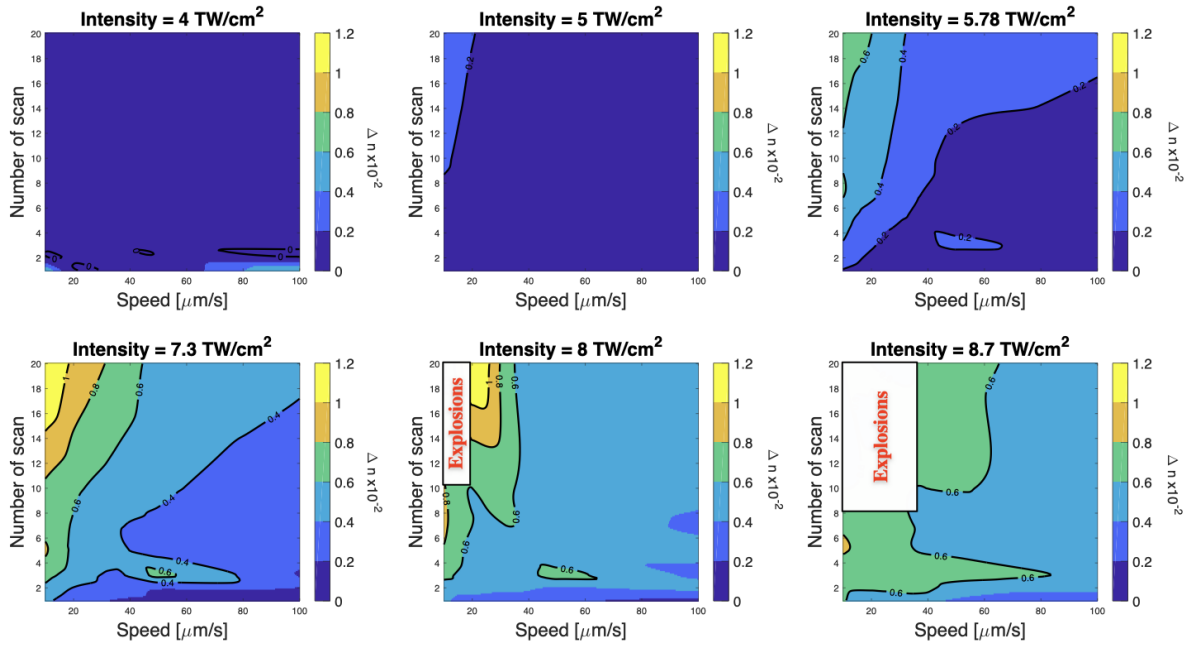

Figure 3.6: Iso-Δn curves for each laser irradiance for the GPN sample: the curves at constant Δn are individuated by the black lines. It is possible to observe that for each irradiance case higher Δn is achieved at low DLW speed and high number of laser scans, therefore at higher number of cumulative pulses. Explosions occurring at high number of cumulative pulses and high laser irradiance are highlighted for the cases of $I = 8$ and 8.7 TW/cm^2.

The 2D plots for each DLW intensity validate the results achieved for the AG01 sample:

- the magnitude of the refractive index change associated with the multiscan silver-sustained structures increases with the cumulative number of absorbed pulses;
- constant Δn is obtained at fixed N_{pulses}, as depicted from the black curves;
- the slope of the iso-Δn curves follows the increase of the N_{pulses}.

3.2.3 AG03

Finally, Fig. 3.7 reports the experimental data for the Δn associated with the multiscan structures inscribed in the AG03 sample depending on the cumulative number of absorbed pulses.

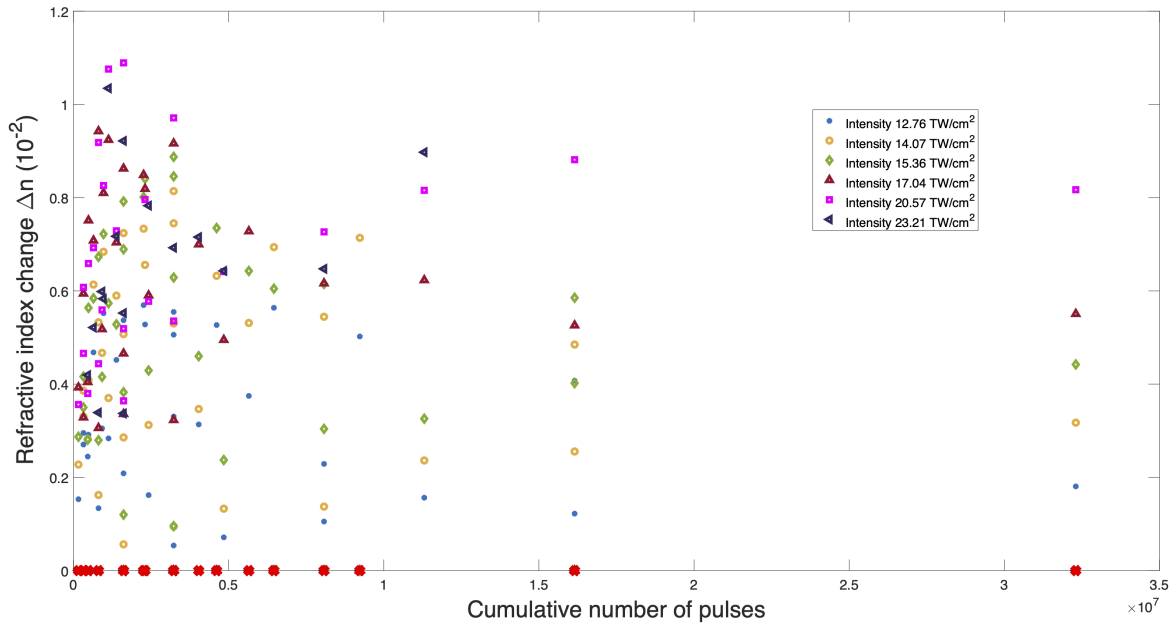

Figure 3.7: Refractive index change Δn of each inscribed multiscan structure in GPN depending on the number of cumulative absorbed pulses, *i.e.* the total number of pulses absorbed in the N_{scan}, for a given laser irradiance. High refractive index change up to 1.1×10^{-2} can be achieved at high irradiance, however, there is no more dependence of the Δn on the number of cumulative pulses. Explosions have been marked with red crosses and the associated refractive index change has been imposed $\Delta n_{exp} = 0$.

Although high Type A refractive index contrast up to 1.1×10^{-2} is achieved also in this silver-containing glass, it is clear that no more correlation exists between the induced Δn and the cumulative number of pulses absorbed after N_{scans} repetitions.
Moreover, many explosions occurred during the multiscan inscriptions, which have been marked by the red crosses at the $\Delta n = 0$ level. It is interesting to point out that the explosions occurred at high N_{pulses}, as well as at low N_{pulses}.

A clearer picture of the situation is given by the iso-Δn graphs in Fig. 3.8.

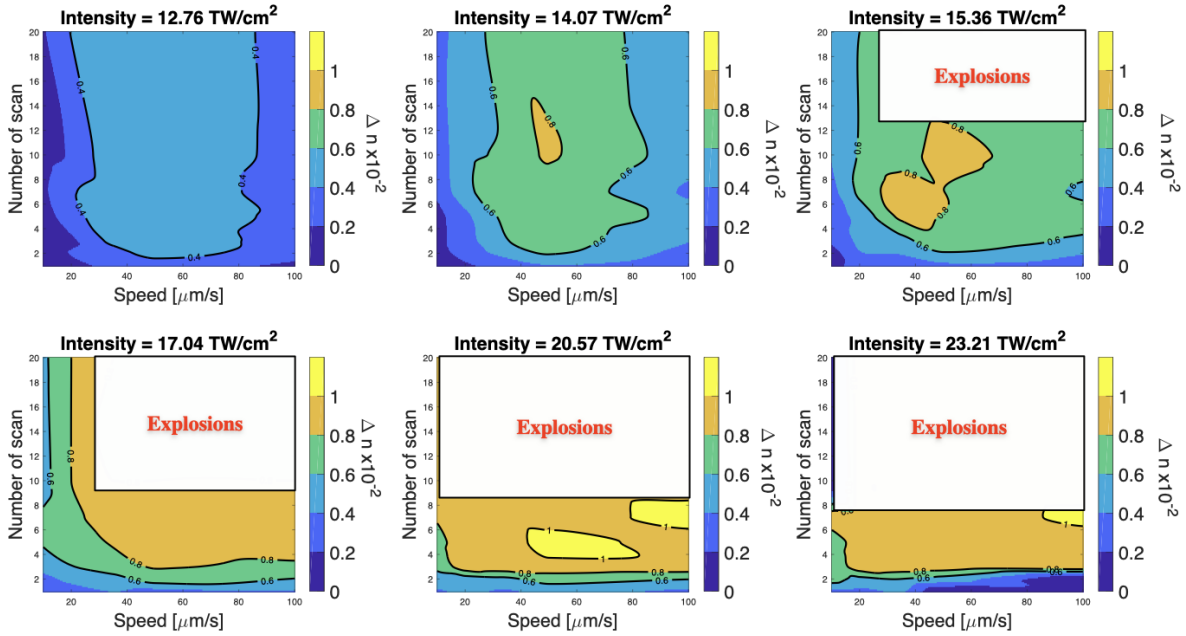

Figure 3.8: Iso-Δn curves for each laser irradiance for the AG03 sample: the curves at constant Δn are individuated by the black lines. Remarkably, high Δ is not more achieved at a high number of cumulative absorbed pulses, moreover, it is independent of the number of laser scans. Many explosions have occurred at high laser intensity for high DLW speed and high number of laser scans.

As already observed for the AG01 and the GPN samples, also for the case of the AG03 sample higher Δn is achieved by increasing the DLW intensity.
However, for each intensity, the highest Δn is no more found in the correspondence of the highest N_{pulses}, instead, it is located at the center of the 2D plot.

Indeed, as shown for instance in the case of $I = 14.07$ TW/cm^2 reported in Fig. 3.9, the yellow arrows identify the directions in which the induced Δn increases. Contrarily to the previous cases of AG01 and GPN samples, the iso-Δn curves are parallel to the vertical axis, showing that there is no improvement of the Δn with the number of laser repetitions.
Therefore, it is not possible to identify the athermal regime in this context for the AG03 sample.

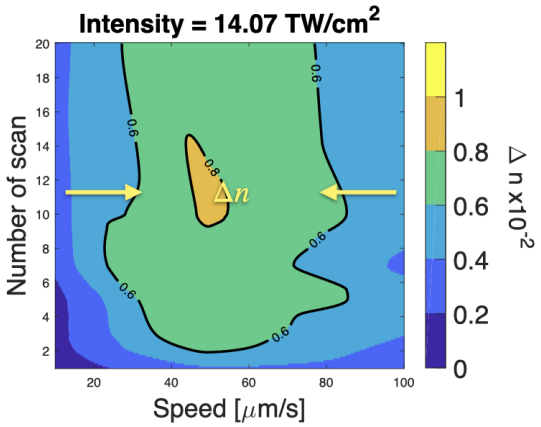

Figure 3.9: Iso-Δn plot for laser intensity $I = 14.07$ TW/cm^2 from the AG03 sample: the yellow arrows individuate the directions in which the magnitude of the induced Δn increases.

Finally, it is interesting to notice that explosions do not originate in correspondence of the highest N_{pulses}, as for the case of the GPN sample, instead, they occur at high speed after several laser scans.

3.2.4 Discussion on the high Type A Δn with the multiscan approach

The results reported so far for the silver-containing glasses confirm that the multiscan technique is effective for increasing the induced refractive index change Δn even in the case of high repetition rate regime. In particular, the results reported in Fig. 3.3 and Fig. 3.5 for the samples AG01 and GPN, respectively, recall the results reported in the work of Lapointe *et al.* for the case of low repetition rate and athermal regime.

Nevertheless, the mechanisms leading to Type A modifications differ from those originating Type 1 modifications. Indeed, the evolution of Type A Δn associated with the multiscan inscriptions can be explained in terms of the evolution of the silver reservoir in the matrix of the silver-containing glasses.

As a matter of fact, the absorption of each laser pulse depletes the available silver reservoir, which is only a portion of the total silver reservoir in the glass matrix: the quantity of silver ions removed from the available reservoir is directly related to the number of free electrons produced in the laser pulse absorption, as discussed in the previous Chapter and reported in Eq. 2.3, thus it is dependent on the DLW intensity.

Indeed, as shown in Fig. 3.5, the slope of the Δn growth is dependent on the DLW intensity.

Such a growth of the induced Δn is sustainable for the glass matrix as long as the silver amount in the available silver reservoir is enough.
However, when this constraint is not met, the induced Δn saturates at a constant value since no more silver clusters can be formed in that specific voxel.

The depletion of the silver reservoir leads to a change in the absorption of the glass matrix in the areas where the silver is missing. As a result, when the Δn has saturated and no silver cluster can be formed anymore, the absorption of the following laser pulses leads to explosions. Such behavior is corroborated by the experimental results in Fig. 3.6 for the cases $I = 8$ and 8.7 TW/cm^2 for the GPN sample.

In support of this argumentation, Fig 3.10 reports the OPD profiles extracted from the three different silver containing glasses for the highest cumulative number of absorbed pulses obtained for $N_{scans} = 20$ and $v = 10$ μm/s with $I = 10$ TW/cm^2 for AG01, with $I = 7.3$ TW/cm^2 for AG01 and with $I = 20.57$ TW/cm^2 for AG03.

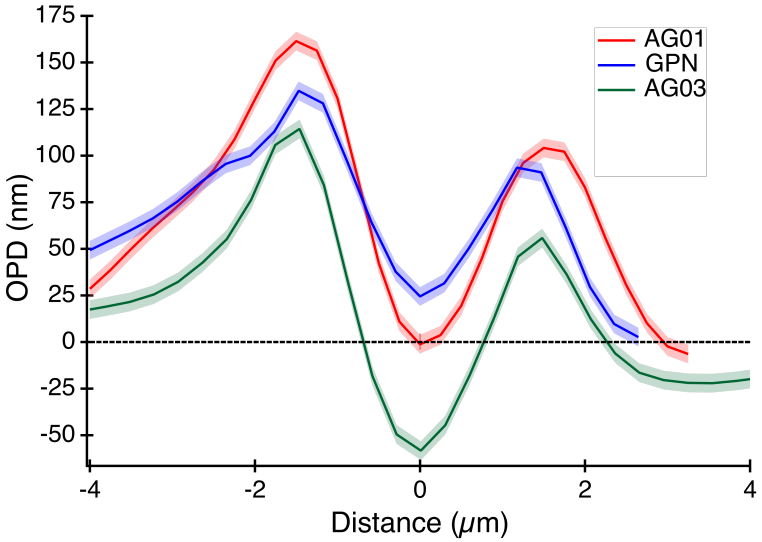

Figure 3.10: Optical Path Difference profiles of the multiscan silver-sustained structures for $N_{scans} = 20$, $v = 10$ μm/s and: $I = 10$ TW/cm^2 for AG01 (in red); $I = 7.3$ TW/cm^2 for GPN (in blue); $I = 20.57$ TW/cm^2 for AG03 (in green). Zero OPD value is highlighted by the black dashed line.

All the profiles show that the positive Δn is located at the edge of the laser track, as a consequence of the accumulation of the silver clusters.
However, for the case of AG03, the building up of positive Δn at the edges of the structure is carried out parallel to a strong depletion of the silver ions in the center of the laser track. Indeed, the depletion of the silver at the center of the Type A modifications is associated to a lower refractive index change; moreover, thermal effects can lead to local melting of the glass and rearrangement of the matrix with lower density (see Fig. 1.5).[136]

It is reasonable to suppose that such a strong depletion is one of the causes explaining the high number of explosions that occurred in the multiscan inscription of the AG03 sample with respect to the inscription of the AG01 and GPN samples.
Nevertheless, the occurrence of explosions in multiscan inscriptions performed with a laser source with high repetition rate regimes stems from the thermal effects, as already discussed in Sec. 2.1.3 and reported by Graf *et al.*.[38]
Indeed, in the case of the AG03 sample, the explosions occurring at high speed before low speed may result from a less effective thermal management of the glass matrix at high DLW speed.

Furthermore, the two-regimes description proposed for modeling the Δn dependence on the cumulative number of pulses is surely a simplified phenomenological representation of the depletion mechanisms of the silver reservoir involved in the laser inscription of Type A modifications. Detailed numerical modeling should take into consideration the nonlinear energy deposition, diffusion processes and chemical reactivity taking place at the microscopical level. Moreover, such a meaningful model should deal with a pulse-to-pulse memory effect, providing for instance a description of the pulse-to-pulse evolution of the silver species distribution, as proposed by Smetanina *et al.* in 2016.[43]

3.3 Multiscan waveguides

In order to exploit the promising results from the multiscan inscription of high Type A refractive index change, multiscan waveguides have been inscribed in the AG01 sample using the above-mentioned fiber laser setup.
The multiscan waveguides have been inscribed 160 μm below the sample surface using a 40$\times$ microscope objective with N.A. 0.75 choosing a DLW irradiance of 6.2 TW/cm^2, so as to prevent any saturation effect with the cumulative pulses, and DLW speed $v = 10$ μm/s, varying the number of repetitions $N_{scans} = 1, 2, 3, 5, 10, 20$ and 30, therefore realizing 7 multiscan waveguides.
The lateral faces of the sample have been polished to bring the waveguides to the surface.

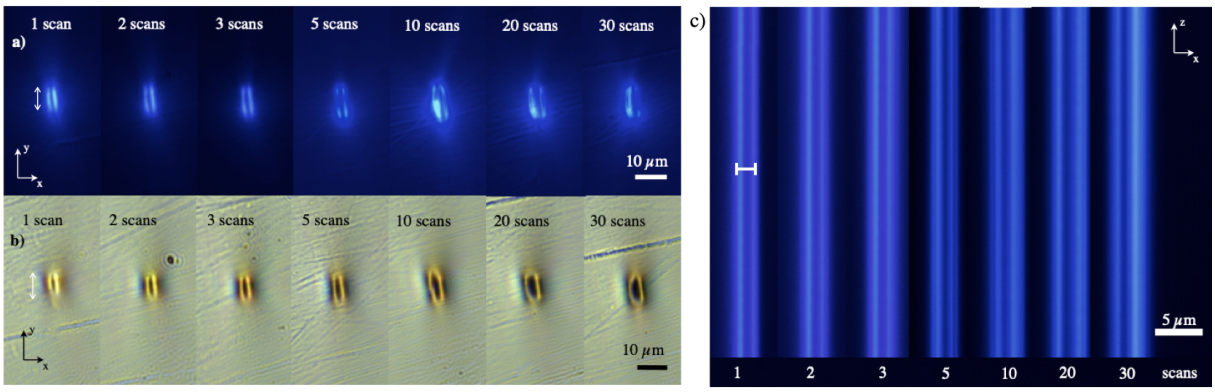

Figure 3.11: a) Fluorescence and b) white light imaging of the lateral surface, after polishing, of the AG01 sample showing the thickness of the multiscan waveguides (highlighted by the white arrows). c) Fluorescence images of the top view of the multiscan waveguides showing the width of the multiscan waveguides (highlighted in white). The pictures have been acquired using a 60× microscope objective with N.A. 0.7, for the fluorescence images $\lambda_{exc} = 365$ nm.

Therefore, their thickness has been measured by imaging the polished lateral face of the sample under white light. Figure 3.11a and Fig. 3.11b report the fluorescence and white light images, respectively, of the lateral surfaces of the sample, showing the thickness of waveguides along the y direction.
The width of the multiscan waveguides, *i.e.* the separation between the tracks of the double-line silver-sustained structure, has been measured instead by imaging the structures from the top, as reported in Fig. 3.11c and highlighted by the white segment.
Table 3.1 reports the measurements for the thickness and the width of the mulstican waveguides depending on the number of laser scans.

N scans	1	2	3	5	10	20	30
thickness (μm)	6.2	6.2	6.8	7.2	7.8	8.7	9
width (μm)	1.6	1.66	1.82	2.6	2.08	2.5	2.7

Table 3.1: Measured values of thickness and width for the multiscan waveguides in AG01 depending on the number of lasers scans N_{scans}.

3.3.1 Improved mode confinement

The multiscan waveguides have been injected at different wavelengths: 750 nm, 900 nm and 1030 nm using a tunable Ti:Sapphire laser from Coherent (repetition rate 80 MHz and output power $>$ 2.9 W at 800 nm), and 1550 nm using a butterfly diode laser from Thorlabs (ASE power 40 mW at 1550 nm).
The injection of the Ti:Sapphire laser has been carried out in free space using a 20$\times$ microscope objective with N.A. 0.5, while for the collection of the output of the multiscan waveguides a 100$\times$ microscope objective with N.A. 0.9 has been used. Thus, the near-field mode profiles have been imaged using a 12 bit camera beam profiler from Thorlabs.
The injection of the fiber diode laser has been optimized using a 6-axis fiber positioner FPR2-C1A from Newport, while the output of the waveguides has been collected in the near-field using a 100$\times$ microscope objective with N.A. 0.7 and imaged on a 16 bit InGaAs camera from Hamamatsu.

The near-field images of the guided modes at different wavelengths are reported in Fig. 3.12. Due to the high refractive index change associated with the multiscan inscription of Type A modifications, the waveguides can exhibit single mode (SM) or multimode (MM) operation at the same wavelength depending on the number of laser scans. Therefore, in Fig. 3.12 the SM and MM operation is highlighted in different colors.

It is noteworthy to mention that for the MM waveguides it is always possible to excite only the fundamental mode.
Moreover, all the waveguides at 1550 nm exhibit only SM operation.

In order to demonstrate the improvement in the mode confinement of the multiscan waveguides when increasing the number of laser scans, the Mode Field Diameter (MFD) of each waveguide has been investigated.
Since the Type A waveguides show a peculiar double-elliptical mode profile, as already observed in the work of Abou Khalil *et al.*[47] in 2017, the MFD has been extracted from the near-field images along the x and y directions.

The processing of the near-field images required the calculation of the first two statistical moments. The first statistical moment allowed for retrieving the x_0 and y_0 central positions of

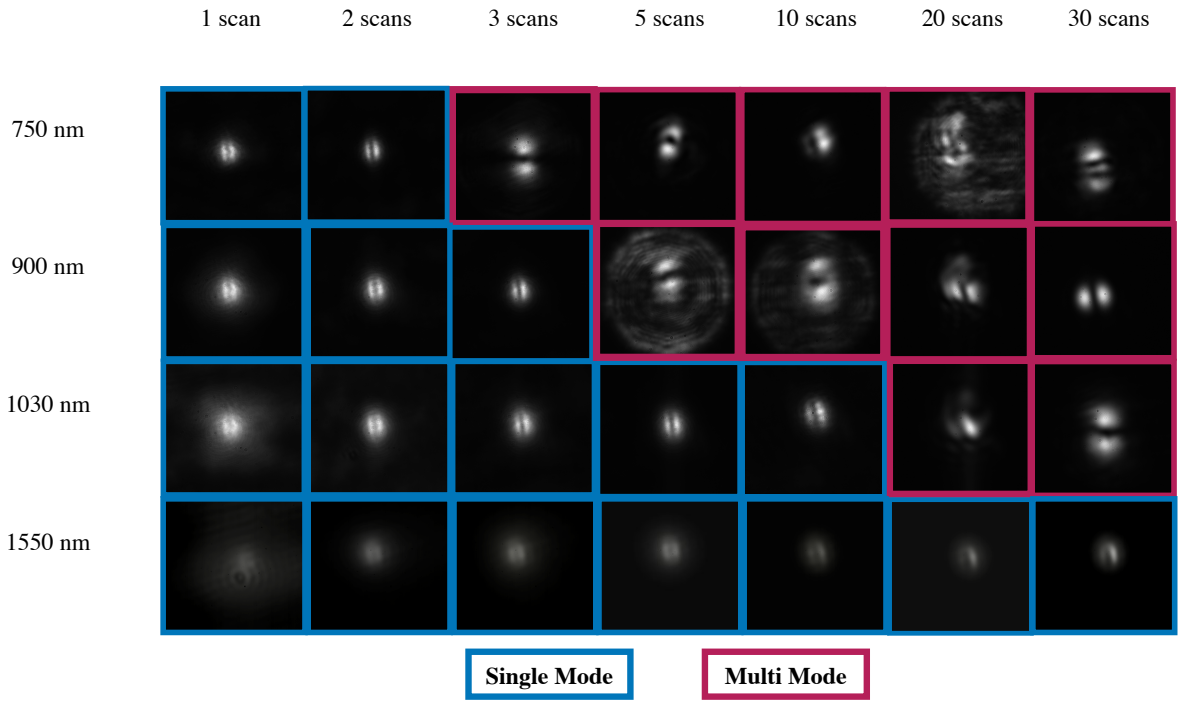

Figure 3.12: Near-field images of the mode profile of each multiscan waveguide at different wavelengths. Depending on the number of laser scans, the waveguides can exhibit single mode or multimode operation at the same wavelength. A colored edge individuates single mode and multimode behavior in blue and magenta, respectively.

the intensity distributions I along the x and y directions from:

$$s_0 =< \bar{s} >= \frac{\int s \cdot I(s) ds}{\int I(s) ds}, \tag{3.2}$$

where s is the statistical variable x or y and $I(s)$ has been obtained by applying a binning of the 2D profile along the opposite direction, therefore y or x.
After centering the intensity distribution, the second statistical moment

$$< \bar{s}^2 >= \frac{\int (s - s_0)^2 \cdot I(s) ds}{\int I(s) ds}, \tag{3.3}$$

allowed to estimate the MFD along the x and y directions. Indeed, the width of a Gaussian intensity profile can be found by measuring the positions at which the intensity drops to $1/e^2$ its maximum value (as reported in the ISO-11146), however, for non-Gaussian profiles the D4σ method should be applied, therefore the width is found at the $4\sigma_{x,y}$ positions, where $\sigma_{x,y}$ is the

standard deviation of the distributions along x and y directions.[59]

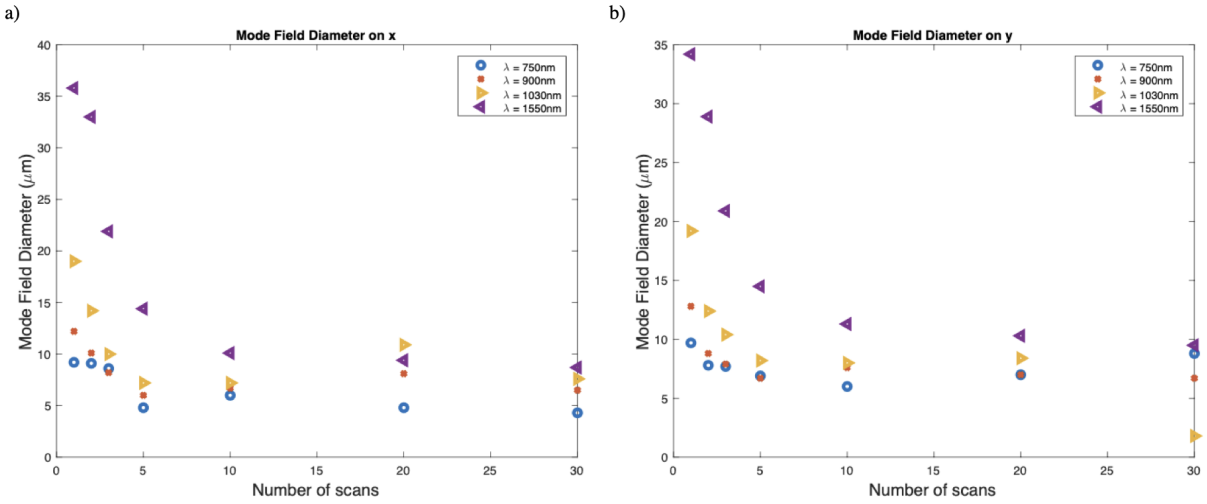

Figure 3.13: Mode Field Diameters of the fundamental guided mode for the multiscan waveguides at different wavelengths along the a) x and b) y directions, respectively.

Figure 3.13a reports the evolution of the MFD along the two directions for all the multiscan waveguides at different wavelengths, evidencing the improved confinement of the fundamental guided mode when passing from $N_{scans} = 1$ to $N_{scans} = 30$ laser scans repetitions.
An evident case of mode shrinking is reported in Fig. 3.14 by the near-field images of the mode profile at 1030 nm for the multiscan waveguides inscribed with $N_{scans} = 1$ and 10 laser scans as a consequence of the increase of associated Δn. The red dashed lines identify the ellipse having the axis equal to the MFDs along the x and y directions for the two waveguides reported in Fig. 3.13.

Finally, the propagation losses of the multiscan waveguides have been estimated while injecting the fundamental mode at 750 nm, 900 nm and 1030 nm. The transmission of the waveguides collected at the output of the $L = 9.4$ mm long waveguides has been corrected by taking into account the transmission of the injecting and collecting objectives, the Fresnel reflections at the input and output faces of the sample and the coupling efficiency η between the focused injected laser beam and the waveguides.
The η parameter has been estimated accordingly[137]:

$$\eta = \frac{|\int E_1^* E_2 dA|^2}{\int |E_1|^2 dA \cdot \int |E_2|^2 dA}, \tag{3.4}$$

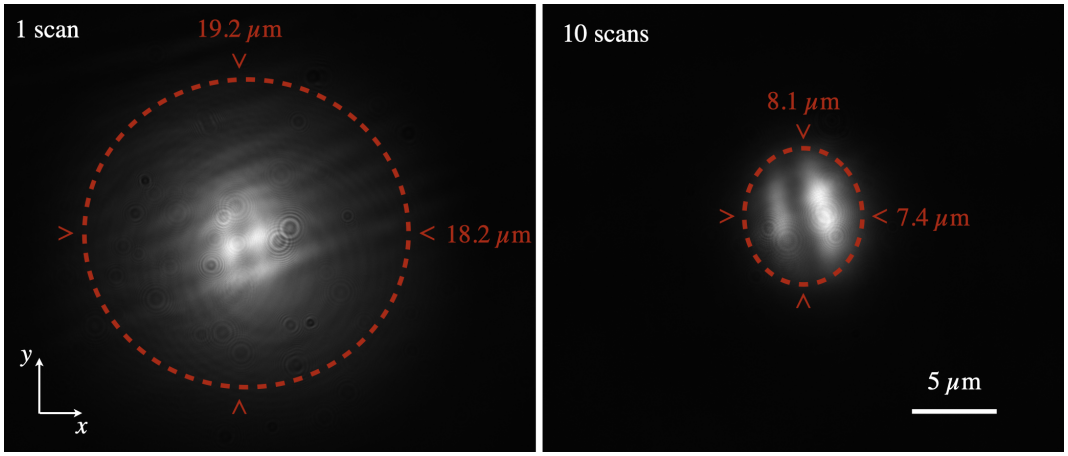

Figure 3.14: Examples of two processed near-field images of the guided modes at 1030 nm: on the left, 1 laser scan, on the right, 10 laser scans. The red dashed lines in the two pictures identify the estimated ellipse with axes on x and y equal to the Mode Field Diameters in the corresponding directions. The shrinking of the MFDs of the multiscan waveguides from 1 laser scan to 10 laser scans is evident.

where E_1^* and E_2 are the (conjugate) electric fields of the focused laser beam and the propagating fundamental mode, respectively, for each multiscan waveguide at a given wavelength, while the dA is a surface element accounting for the integration of the whole profile.
In order to retrieve the near-field profile of the injected light at a different wavelength, the laser beam has been focused directly on the CCD sensor of the beam profiler (once the sample was removed).
Table 3.2 reports the values obtained for the propagation loss coefficient α (measured in dB/cm) at different wavelengths for the different multiscan waveguides.

α (dB/cm)	1 scan	2 scans	3 scans	5 scans	10 scans	20 scans	30 scans
750 nm	0.35	0.33	0.41	0.5	0.34	0.29	0.26
900 nm	0.35	0.32	0.39	0.42	0.27	0.26	0.29
1030 nm	0.38	0.34	0.37	0.38	0.39	0.29	0.24

Table 3.2: Propagation loss coefficient α for the multiscan waveguide at different wavelengths. The increase of the refractive index change Δn along the different waveguides for a given wavelength is associated with a decrease of the propagation loss coefficient of 25%, on average.

It is of interest to point out that the propagation losses decrease by about 25% when increasing the number of laser scans from $N_{scans} = 1$ to $N_{scans} = 30$: for instance, the α coefficient is estimated 0.38 dB/cm at 1030 for a single-scan waveguide, while it decreases to 0.24 dB/cm when the laser scans are 30.
It can be supposed that the shrinking of the guided mode might positively affect the propagation losses since this will result in a lower interaction between the propagating mode and the pristine glass surrounding the waveguides.

3.3.2 Reshaping of the mode profile

As already discussed in Sec. 2.2.3, one of the peculiarities of the Type A modifications is the rewriting ability, shown in Fig. 2.24. Thus, it is interesting to exploit this ability in the case of the multiscan waveguides.
Indeed, Type A waveguides show a typical double-elliptical mode profile that much differs from the gaussian LP_{01} profile of the fundamental guided mode in fibers. Such a difference in the mode profile may highly affect the coupling between fibers and Type A waveguides, precluding the possibility of fully exploiting the Type A waveguides, especially the multiscan waveguides, for integrated optical circuits.
Therefore, here is discussed a multiscan approach to reshape the multiscan Type A waveguides in order to obtain a gaussian-like profile for the guided mode.

An engineered multiscan waveguide has been inscribed by 10 laser scans separated by 500 nm, achieving an overlap of 70% between consecutive laser scans, in order to fabricate a square structure of side $L = 6$ μm. Moreover, the multiscan waveguide has been repeated 6 times at the same position but alternating the directions of the laser spot displacement, this allows for obtaining an homogeneously written structure. The DLW parameters for the multiscan inscription, laser irradiance $I = 6.12$ TW/cm^2 and DLW speed $v = 100$ μm/s, have been selected in order to avoid saturating the Δn associated with the engineered multiscan waveguide.

Figure 3.15a shows a schematic representation of the procedure followed for the inscription of the reshaped waveguide, while Fig. 3.15b and Fig. 3.15c reports the side-view and top-view phase images, respectively, of the waveguide, demonstrating the homogeneous repartition of the refractive index contrast in the center of the structure. The reshaped waveguide has been

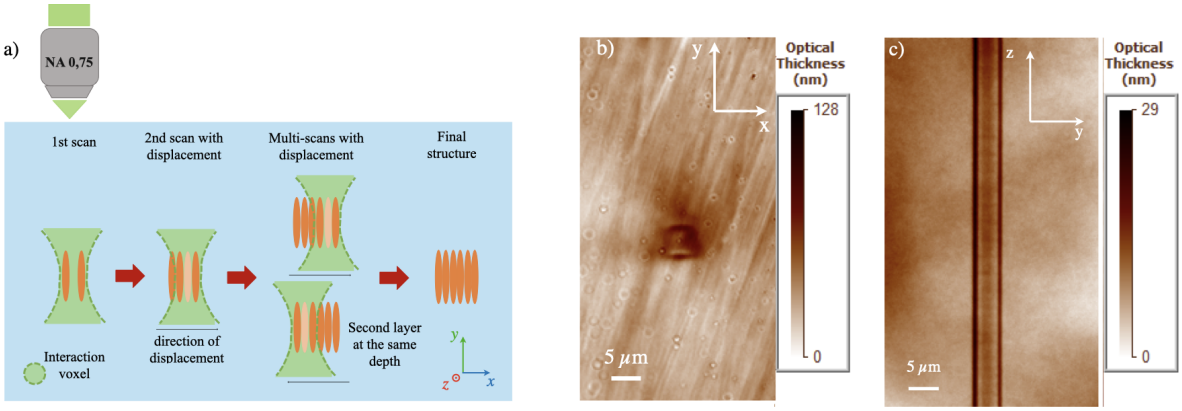

Figure 3.15: a) Schematic explanation of the procedure followed for the inscription of the engineered multiscan Type A waveguide. b) Side-view and c) top-view phase images of the reshaped waveguide acquired by the Sid4Bio software using a 100× microscope objective with N.A. 1.3 and index matching oil $n = 1.518$. It should be noted that surface quality highly affects the phase image of the reshaped waveguide in b), while c) appears homogeneous since it is acquired 160 μm below the surface.

injected at 1030 nm using the same abovementioned setup, exhibiting single mode operation at such a wavelength. The near-field image of the guided mode, reported in Fig. 3.16, has been acquired using a 16-bit Sony αIII camera.
Figure 3.16 clearly shows that it is possible to obtain a gaussian-like profile by reshaping a Type A waveguide using the multiscan technique, thanks to the remarkable rewriting ability of the silver clusters. The gaussian profiles of the engineered multiscan waveguide along the x and y directions have been plotted in blue and red, respectively, on the near-field image in Fig. 3.16.

Conclusions on the chapter

The Chapter is focused on applying the multiscan technique to the laser inscription of Type A modifications in order to analyze the benefits of such a method for increasing the laser-induced refractive index change in the case of DLW in an athermal regime with a high repetition rate laser source.

For this purpose, a series of multiscan structures have been realized in silver-containing phosphate glasses with different compositions.

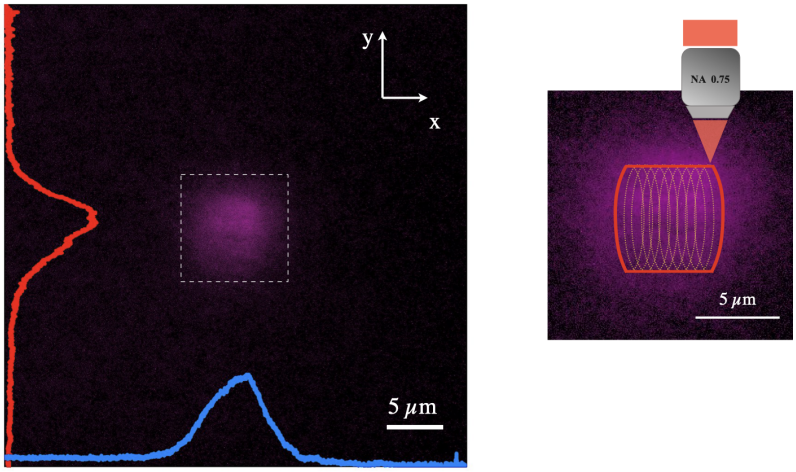

Figure 3.16: Near-field image of the gaussian-like mode profile of the engineered multiscan waveguide at 1030 nm. The blue and red curves depict the profiles along the x and y directions, respectively. A zoom of the mode profile selected by the white dashed line has been reported on the right. A schematic representation of the inscription procedure for the multiscan structure has been reproduced, showing the overlap of consecutive laser scans, while a bold red line highlights the perimetry of the final obtained structure.

The multiscan structures have been characterized in order to quantify the associated refractive index change. Thus, the induced index contrast has been analyzed for each sample and laser irradiance with respect to the cumulative number of pulses absorbed during the consecutive laser scans.

This inscription method enabled for achieving remarkably high refractive index change: more than 1×10^{-2} in all the samples and up to 2×10^{-2} for the AG01 sample.

Moreover, such a study demonstrated that the athermal laser inscription of Type modifications allows for direct linking of the magnitude of the induced refractive index change to the total number of laser pulses absorbed when the silver reservoir of the glass matrix is sufficiently filled. Indeed, such behavior is confirmed by the $2D$ isoΔn curves for the cases of the AG01 and GPN samples.

However, when the available reservoir is partially empty, the refractive index's growth slows down until it settles to a constant value when there is no more silver available for the formation of silver clusters.

The local depletion of silver ions in the glass matrix is confirmed by the appearance of a negative refractive index change in the center of the double-track structure in the AG03 sample.

The absence of silver may produce explosions as a result of the change in the absorption of the glass matrix, right at the position where the focused laser beam is more intense, as reported for the GPN sample.
Finally, the case represented by the AG03 sample demonstrates that the multiscan inscription of Type A modifications in a thermal regime may be strongly affected by the thermal accumulation at high laser irradiance.

However, the results reported in the first part of this Chapter demonstrate that laser inscription of Type A modifications with a multiscan approach enables fine control of the positive refractive index change associated with the cluster formation by tuning the DLW parameters.
Such a promising technique is exploited in the fabrication of multiscan waveguides, discussed in the second part of the Chapter.
These waveguides show single mode and multimode operation at the same wavelength, depending on the number of laser scans, and demonstrate the ability to control the confinement of the guided mode, as a consequence of the tunable high refractive index change associated with these structures.
The improved mode confinement allowed for reducing the propagation losses of the multiscan waveguides. This important result is very promising for the application of Type A modifications in the fabrication of bent waveguides with a high radius of curvature since it would enable the miniaturization of the integrated optical circuits.
Nevertheless, the multiscan technique in combination with the peculiar rewriting ability of the silver clusters allowed for the fabrication of an engineered multiscan waveguide, exhibiting single mode operation at 1030 nm, which showed a reshaped gaussian-like profile of the guided mode. Reshaping the double-elliptical mode profile, typical of the Type A waveguides, into a gaussian-like profile will optimize the coupling between the embedded Type A waveguides and, for instance, optical fibers.

Chapter 4

Laser inscription of silver-sustained Waveguides Bragg Gratings and Volume Bragg Gratings

Introduction to the chapter

The Chapter deals with the femtosecond laser inscription of periodic structures based on Type A modifications in silver-containing glasses.

The first part of the Chapter is dedicated to Waveguides Bragg Gratings.
Firstly, the state of the art on such waveguides is briefly discussed, providing an overview of the different fabrication processes. Moreover, theoretical modeling of the Waveguides Bragg Gratings based on the Coupled Wave Theory is presented.
Thus, the Type A Waveguide Bragg Gratings are introduced, presenting the DLW process, the inscribed geometry, in particular for helicoidal gratings, and the associated periodic modulation of the refractive index. Finally, the transmission and reflection spectra are analyzed and a numerical solution for the Coupled Wave model is proposed in order to extract the effective gratings parameters.

Fs laser inscription of Type A Volume Bragg Gratings is discussed in the second part of the Chapter.
The case of a single-layer periodic grating is presented and analyzed while, in the last part of the

Chapter, the promising results for a series of multi-layers Volume Bragg Gratings are discussed.

4.1 State of the art of Waveguides Bragg Gratings

Waveguides Bragg Gratings (WBGs) are fabricated by periodically modifying the refractive index change of a waveguide in order to obtain a 1D photonic bandgap which will allow for optical filtering of the light propagating into the waveguide.
Conceptually, WBGs are equivalent to Fiber Bragg Gratings (FBGs) which correspond to narrowband mirrors integrated into optical fibers. FBGs have been firstly achieved in 1978 by Hill *et al.*[138] in SiO_2 based fibers by coupling highly intense contradirectional beams: the standing waves produced by the counterpropagating beams induced a periodic variation of the refractive index of the core, which resulted in the fabrication of narrowband reflectors.
Since this first achievement, FBGs, and later WBGs, have quickly gained interest since such devices find many applications in a wide range of research fields such as telecommunications, sensing, astrophysics and medicine.
Indeed, different typologies of FBGs and WBGs can be fabricated to target specific applications: for instance, chirped gratings can be used for dispersion compensation in optical communication systems and laser systems while phase shifted gratings can be used to obtain temporal differentiation and filtering in narrow bandwidths.
Particularly, WBGs and FBGs have specific importance in sensing since the resonant wavelength can be affected by external parameters, such as temperature or induced stress or strain.
Photolithography is one of the most common techniques used for fabricating planar lightwave circuits, however such a method is time-consuming since it requires normally several steps, among which: UV exposure, selective chemical or plasma etching, and doping or ion diffusion in a clean environment.[139;140]
Therefore, other fabrication methods have been investigated over the years, such as holographic interferometry, the use of phase masks or femtosecond laser inscription; in particular, the latter provides flexibility in the selection of the geometry of the grating as well as in the shaping of the laser beam, allowing to select specific spectral properties and the range of processable glasses.[141;142;143;144;145]

4.1.1 Techniques for fabricating FBGs and WBGs

Three main methods exist for the fabrication of FBGs and WBGs: the first one is the holographic interference of two identical beams, the second one takes advantage of densification increase thanks to UV exposure, while the last one is based on material modifications due to the interaction of a femtosecond laser source.

Holographic interferometry

An incident laser beam is divided into two equal beams by a 50% beam splitter (or a reflection grating) and the reflected and transmitted beams are then brought together on the fiber with an angle θ between them, as reported in Fig. 4.1.

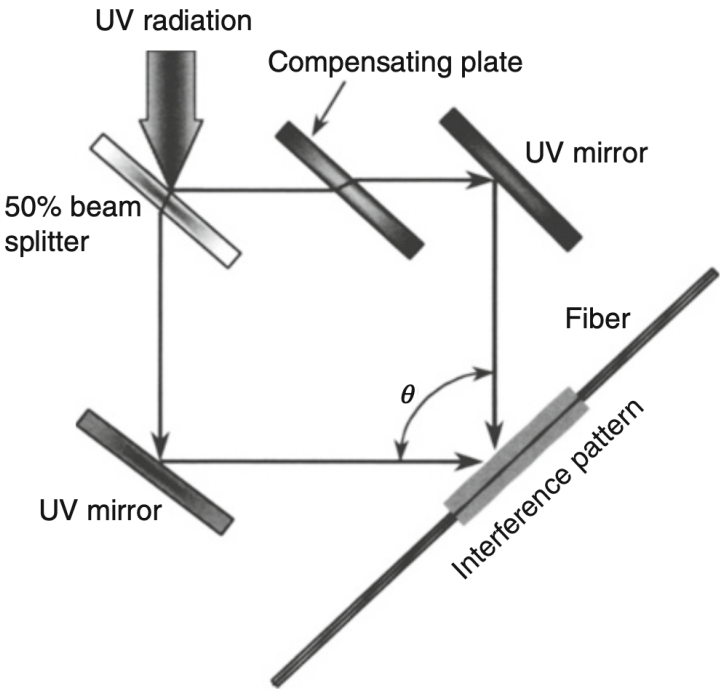

Figure 4.1: Schematic representation of the holographic interferometry method for achieving Bragg Gratings in fiber. Image taken from [48].

The period of the interferometric pattern on the fiber will lead to a Bragg diffraction at the λ_B given by:

$$\lambda_B = \frac{n_{eff}\lambda}{n(\lambda)sin(\frac{\theta}{2})}, \tag{4.1}$$

where n_{eff} is the effective refractive index that is experienced by the mode, λ is the wavelength of the laser beam and $n(\lambda)$ is the refractive index of the fiber at the laser wavelength. It is clear that the period of the interferometric pattern is selected by tuning the mutual angle θ. However, when the holographic pattern is created by means of an UV radiation, for instance 240 nm, is it possible to make θ vary between 0° and 180°: since the n_{eff} is very close to the $n(\lambda)$, this allows for achieving λ_B from almost the wavelength of the UV beam to infinity (when θ is approaching 0°).
When a low-coherence beam is adopted, a compensating plate can be placed in the interferometer in order to compensate for the unbalance in the path introduced by the beam splitter: this method allows for achieving long gratings once provided constant path length.

Phase Mask

This method adopts a diffractive optical device to modulate the incident beam, typically UV radiation. The diffractive grating may be obtained by interferometric pattern or, more commonly, by electron beam lithography; in the latter case, it is possible to produce more complicated patterns, like for instance quadratic chirps.
The transmission grating allows for diffracting the incident beam into several orders $m = 0, \pm 1, \pm 2 \ldots$ which follow the diffraction equation:

$$\Lambda_{pm} = m \frac{\lambda}{sin\theta_{m/2} - sin\theta_i}; \tag{4.2}$$

where Λ_{pm} is the period of the phase mask, λ is the wavelength of the incident beam and $\theta_{m/2}$ and θ_i are the angles of the diffracted m order and of the incident beam, respectively. Figure 4.2 reports a schematic representation of the phase mask method.

The interference between the different orders of diffraction creates a fringe pattern that forms the Bragg gratings. Normally, phase masks are optimized by equally diffracting and maximizing the first positive and negative orders $m = \pm 1$, or the zero order and the minus first one $m = 0, -1$, therefore higher orders are suppressed when possible. In this case, the periodicities of the fringes for the interference of two orders become:

$$\Lambda_{fringes} = \frac{\Lambda_{pm}}{2}. \tag{4.3}$$

The use of a Phase Mask is a robust way to produce efficient Bragg Gratings in fibers and on waveguides. Long Phase Masks, for instance 120 mm, can be achieved with the lithography

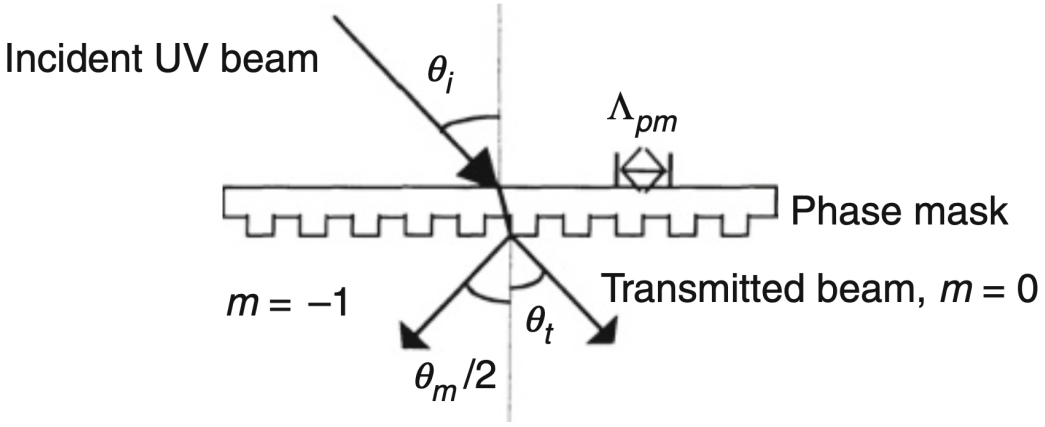

Figure 4.2: Schematic representation of the functioning of a phase mask for the fabrication of a FBG. Image taken from [48].

method. The quality of the produced BGs depends on the uniformity of the phase mask, therefore the absolute position accuracy of the electron beam has to be reduced to around 5 nm. [146]

Femtosecond inscription

One of the many advantages of using an ultrafast laser is achieving material modifications by multiphoton absorption, therefore this technique allows for inscribing Bragg Gratings in all glasses, not only the photosensitive ones used in the case of UV radiation discussed before.
The previous methods can be adopted also when using a femtosecond source, however some precautions need to be taken into account. Concerning the holographic method, a femtosecond laser source can be split and recombined in the bulk of glass or on fiber in order to create an interferometric pattern, as reported in Fig. 4.3a. However, the lengths of the two interferometric arms have to match to within the overlap of the femtosecond pulse. For a 100 fs laser, the error on the path length has to be inferior to 3 μm. Therefore, a transmission grating is used to divide the laser instead of a beam splitter. [147;148]

The use of a Phase Mask solves the problem of overlapping the split beams within the envelope of the short pulse. The inscribed sinusoidal interference path will be associated with a Type 1 refractive index modulation for which the selected λ_B will be given by:

$$m\lambda_B = 2n_{eff}\Lambda_G, \tag{4.4}$$

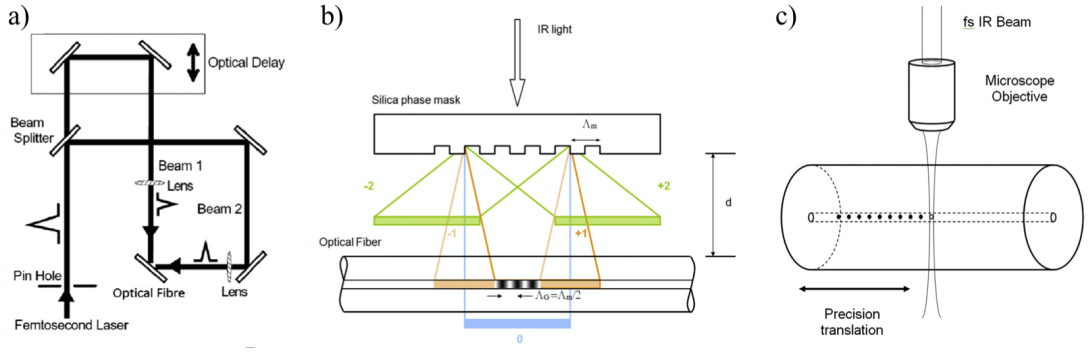

Figure 4.3: Schematic representation of the techniques used in the fabrication of BGs using a femtosecond laser source: a) holographic interferometry, b) Phase Mask and c) DLW. Image taken from [49].

where n_{eff} is the effective mode index, m is the order of diffraction of the inscribed Bragg gratings and Λ_G is the gratings period. However, the diffraction of a femtosecond laser by the Phase Mask has a particular behavior: while the diffracting pulses propagate away from the mask, the pulse fronts of pulses belonging to different orders of diffractions will remain parallel to the mask but not anymore to the phase fronts, *i.e.* their fronts will be tilted with respect to the propagation direction, except for the zero order. This implies that different orders of diffraction will interfere at different distances from the Phase Mask, since the interference path made by two different orders m and $m+1$ will disappear when the separation of their pulse fronts overcomes the coherence length of the femtosecond pulse, as reported in Fig. 4.3b. [149;150;151] When such effect occurs the interference of the $m = \pm 1$ orders enables for achieving $\Lambda_G = \Lambda_{pm}/2$, as for the case reported in Eq. 4.3 of UV laser fabrication of BGs. Highly-efficient FBGs can be achieved with this method, although quite a high energy pulse is needed to enable laser-induced modifications. [152]

However, femtosecond laser inscription of BGs on fiber or waveguides has recently gained interest due to the inherent flexibility of this technique for which each modulation of the refractive index is finely controlled.
As already mentioned in Sec. 2.1.2, two different techniques exist for the DLW of FBGs and WBGs: Point by Point and Line by Line.

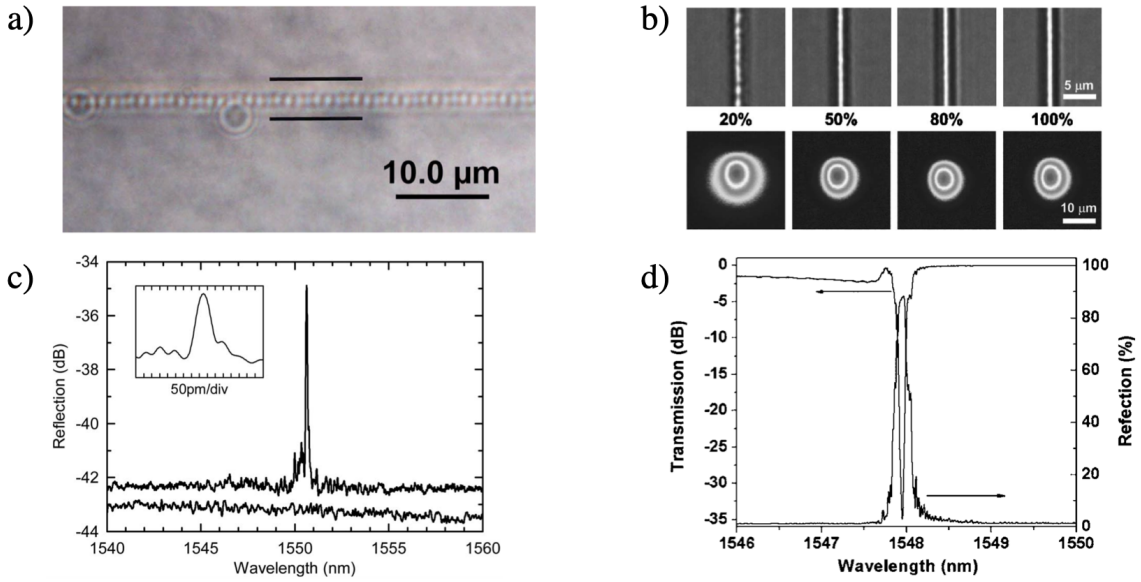

Figure 4.4: White light pictures of WBGs inscribed with the a) single-pulse and b) modulated burst methods; moreover, b) shows the near-field mode profiles of the different WBGs fabricated with different duty cycles. Reflection spectra of the WBGs achieved with c) single-pulse method and d) modulated burst method and 60% duty cycle. Images a) and c) taken from [50]. Image taken b) and d) from [51]

Single pulse inscription Marshall *et al.* proposed for the first time the PbP method for the inscription of BGs on waveguides previously inscribed inside the bulk of a fused silica sample: the two-step process allowed for the inscription of a weak BGs in the core of a strong waveguide. [50] As reported in Fig. 4.4a, the periodic material modifications are fully embedded in the core of the waveguide, therefore, thanks to fine control of the focused laser positioning it is possible to tune the BGs parameters: the period and the phase are determined by the position along the axis of the waveguide, while the transverse positioning plays on the coupling strength between the BGs and the waveguide. For this reason, this method allows for easy fabrication of complex gratings, such as chirped or phase-shifted gratings. [153;154;155;156] Moreover, Jovanovic *et al.* [157] in 2009 demonstrated that PbP refractive index modulations can produce BGs showing birefringence effects: indeed, due to the geometrical asymmetry of the induced material modifications, the group showed how the size, the ellipticity and the transverse positioning of the PbP structures would affect the birefringence of the gratings and the transmission spectra for two orthogonally polarized modes.

Since typically BGs inscribed with the PbP method are based on Type 3 refractive index modifications, which are associated with negative index change resulting in high propagation losses. However, by optimizing the inscription parameter, it is possible to fabricate efficient BGs with narrow bandwidth selection, as reported in Fig. 4.4c.[50] Moreover, shaping the laser beam into a Bessel beam can increase the efficiency of the BGs, as demonstrated by Zhang *et al.*[158]: the thigh confinement of the Bessel beam assures the inscription of a uniform and one-dimensional void structure, enhancing the precision in the spectral selection of the BGs.
Overall, the PbP is a fast method that allows for achieving efficient BGs even by the absorption of a single pulse, although the inscription of negative Type 3 refractive index change may introduce high losses and some precautions need to be taken into account to enhance the coupling between the gratings and the waveguide.

Modulated bursts inscription The benefit of inscribing BGs by modulating the bursts of an ultrafast laser comes from the fact that thanks to the many-pulse absorption it is possible to control the energy deposition in the voxel of interaction and, thus, to tune each single refractive index modulation. Moreover, this method enables the control of the dimension and the positioning of each refractive index voxel forming the periodic structure. As a result, this method allows for the fabrication of efficient BGs with small periodicities that can select the λ_B in a very narrow spectral range: sub-μm periodicities can be achieved by partially overlapping the induced refractive index voxels.[51;156;159;160] The modulation of the ultrafast laser is achieved in many ways, among these AOM, choppers and Pockels cells can be cited. For instance, Fig. 4.4b reports the microscope images and near-field mode profiles of WBGs written in a fused silica sample for which an AOM has been used to modulate the ultrafast beam with different duty cycles ($20\% - 50\% - 80\% - 100\%$) for a given period of the gratings $\Lambda = v/f$, where f is the modulation frequency of the laser burst and v is the scan speed. The shrinking of the near-field profile from the 20% to 100% duty cycles highlights the increase of the induced refractive index change when cumulating many pulses. Such WBGs showed a strong reflection peak and narrow bandwidth when the duty cycle was settled at 60%, as reported in Fig. 4.4d.
The LbL method allows for enhancing the coupling between the BGs and the waveguides, moreover, the positioning of the periodic structure can be adjusted in order to further optimize the efficiency of the BGs.[161;162] Nevertheless, complex gratings can be obtained by modulated bursts inscription, such as chirped BGs and phase-shifted, while apodized BGs can be inscribed in order to suppress the sidelobes appearing in the spectrum right on the side of the λ_B.[163;164;160;165] Finally, the inscription of LbL periodic gratings in the thermal regime using a

high repetition rate laser led to the inscription of a WBG showing sub-μm periodic structures, with periodicity 512 nm, based on Type 3 modifications induced by heat accumulation: the modulation of the laser burst by using Pocket cells allowed for the simultaneous inscription of both the periodic nanovoids and the waveguide, which has been produced by thermal diffusion, thus has the dimension of the heat affected zone.[166] Such a method allows for inscription of WBGs at high speed.

4.1.2 Coupled Wave Theory

The *Coupled Wave Theory* (CWT) is a powerful formalism adopted to explain and simulate many physics or engineering phenomena. In particular, the CWT has been widely adopted in integrated optics for analyzing the case of guided-wave optics for dielectric waveguides.[167;168;169] Nevertheless, such formalism is suitable for describing the phase matching conditions of propagating waves by periodic perturbation of the refractive index, and thus the dielectric constant, of a waveguide. Therefore the CTW is a useful tool for the designing of FBGs and WBGs and, especially, for their quantitative characterization by calculating their diffraction efficiency and spectral dependence.

The Bragg gratings inside the FBGs and WBGs act as reflection gratings for which the coupling occurs between the propagating and the contra-propagating modes in the core. The constructive interference will take place when:

$$\beta_2 = \beta_1 + m\frac{2\pi}{\Lambda}, \tag{4.5}$$

where $\beta_{1,2} = \frac{2\pi}{\lambda n_{eff_{1,2}}}$ are the mode propagation constants, introduced in Sec. 1.3, $n_{eff_{1,2}}$ are the effective refractive indices reported in Eq. 1.33, Λ is the period of the gratings and m is the order of diffraction. The condition in Eq. 4.5 can be rewritten stating that $\beta_2 < 0$ for the reflection at the order $m = -1$, therefore:

$$\lambda = (n_{eff_1} + n_{eff_2})\Lambda, \tag{4.6}$$

which will give the known Bragg condition for the reflection $\lambda = 2n_{eff}\Lambda \equiv \lambda_B$ when the two modes coincide.

A periodic modulation of the refractive index of the waveguide can be described by:

$$\delta n_{eff}^{AC}(z) = \delta n_{eff}^{DC}\left\{1 + v\, cos\left[\frac{2\pi}{\Lambda}z + \phi(z)\right]\right\} \tag{4.7}$$

where δn_{eff}^{DC} is the "DC" component of the modulation averaged over a grating period, v is the fringes visibility of the refractive index modulation and $\phi(z)$ is an eventual chirp of the grating

period. Given two waves propagating in the forward and back-forward direction in the single mode waveguide with periodic perturbation of the n_{eff} of the guided modes, the CWT will link the amplitudes of the two waves as:

$$\frac{dR}{dz} = i\hat{\sigma}R(z) + i\kappa S(z) \tag{4.8a}$$

$$\frac{dS}{dz} = -i\hat{\sigma}S(z) - i\kappa^* R(z) \tag{4.8b}$$

where the amplitudes of the the forward R and back-forward S waves are $R(z) \equiv A(z)exp(i\delta z - \phi/2)$ and $S(z) \equiv B(z)exp(i\delta z + \phi/2)$, respectively. The boundary conditions for the two waves are:

$$R(-L/2) = 1, \quad S(L/2) = 0; \tag{4.9}$$

The κ term represents the coupling coefficient of the BGs and can be written as:

$$\kappa = \frac{\pi}{\lambda} v\, \delta n_{eff}^{DC}, \tag{4.10}$$

while $\hat{\sigma}$ is a self-coupling coefficient defined as:

$$\hat{\sigma} \equiv \delta + \sigma - \frac{1}{2}\frac{d\phi}{dz}, \tag{4.11}$$

where δ represents a detuning from the λ_B condition:

$$\delta \equiv \beta - \frac{\pi}{\Lambda} = \beta - \beta_B = 2\pi n_{eff}\big(\frac{1}{\lambda} - \frac{1}{\lambda_B}\big), \tag{4.12}$$

and $\sigma = \frac{2\pi}{\lambda}\delta n_{eff}^{DC}$ is the period-averaged coupling coefficient.
If the grating is uniform along the z direction, $d\phi/dz = 0$ and the DC component of the refractive index modulation δn_{eff}^{DC} and the coupling coefficients κ, σ (therefore $\hat{\sigma}$) are constant. In this case, the reflection coefficient ρ of such a grating with length L can be found by[170]:

$$\rho = \frac{-\kappa\, sinh(\sqrt{\kappa^2 - \hat{\sigma}^2}L)}{\hat{\sigma} sinh(\sqrt{\kappa^2 - \hat{\sigma}^2}L) + i\sqrt{\kappa^2 - \hat{\sigma}^2} cosh(\sqrt{\kappa^2 - \hat{\sigma}^2}L)}, \tag{4.13}$$

while the reflectivity of the gratings is then found as $R = \rho\rho^*$, therefore:

$$R = \frac{sinh^2(\sqrt{\kappa^2 - \hat{\sigma}^2}L)}{cosh^2(\sqrt{\kappa^2 - \hat{\sigma}^2}L) - \frac{\hat{\sigma}^2}{\kappa}}. \tag{4.14}$$

It is worth noticing that the Eq.4.14 has its maximum

$$R_{max} = tanh^2(\kappa L) \tag{4.15}$$

when $\hat{\sigma} = 0$, which is found at the wavelength $\lambda_{max} = \left(1 + \frac{n_{eff}^{DC}}{n_{eff}}\right)\lambda_B$, therefore not at the exact designed wavelength for the gratings, which can be thus tuned.
The bandwidth of the uniform BGs can be calculated from the first two zeros of the reflectivity in Eq. 4.14, therefore taking into consideration the values for $\hat{\sigma}$ from zero to those for which the numerator in Eq. 4.14 goes to zero:

$$\frac{\Delta\lambda^0}{\lambda} = \frac{v\,\delta n_{eff}^{DC}}{n_{eff}}\sqrt{1 + \left(\frac{\lambda_B}{v\,\delta n_{eff}^{DC} L}\right)^2}, \tag{4.16}$$

where $\Delta\lambda^0$ is the bandwidth measured from the zeros of the R function. If the perturbation of the refractive index n_{eff} is small, the BGs behaves in the *weak-grating limit*, so $v\,\delta n_{eff}^{DC} \ll \frac{\lambda_B}{L}$ and $\frac{\Delta\lambda_0}{\lambda} \to \frac{\lambda_B}{n_{eff}L}$, while for *strong* gratings $v\,\delta n_{eff}^{DC} \gg \frac{\lambda_B}{L}$ and $\frac{\Delta\lambda_0}{\lambda} \to \frac{v\,\delta n_{eff}^{DC}}{n_{eff}}$.
Finally, this formalism allows for describing more complex gratings, for instance a chirp in the periodicity of the grating can be described by the term $\phi(z)$.

4.2 WBGs in silver-containing glasses

4.2.1 Concept, experimental setup, procedure (LbL, helix)

In the work reported in this Chapter, several WBGs have been inscribed, primarily on AG01 samples from Argolight company in Bordeaux.

The setups

Two setups have been used to inscribe the WBGs, depending on the type of the BGs. For the classical **LbL** BGs it has been adopted the same prototype fiber laser setup used for the inscription of the multiscan structures in the previous Chapter.

For the inscription of the helicoidal WBGs, a KGW:Yb femtosecond oscillator (up to 2.8 W, 9.8 MHz, 390 fs FWHM at 1030 nm) was used. The control of the power has been achieved by an AOM, while an SLM was used in order to correct for spherical aberrations (LCOS; X10468-03, Hamamatsu Photonics). The positioning of the sample is obtained thanks to 3D translation stages XMS-50 with resolution down to 50 nm.

Different microscope objectives have been used for the inscription of the different WBGs, depending on the sought periodicity of the gratings. However, the results reported in this

Chapter have been all achieved with a 100× microscope objective with N.A. 1.3 (Olympus) and index matching oil $n = 1.518$.
The inscription of the WBGs is a two-step process. The first step is the fabrication of the waveguide, the geometry of the waveguide is directly dependent on the microscope objective used to focalize the laser beam, as discussed in Chapter 2: for the case of N.A. 1.3, the double-track waveguide has a diameter ϕ of 0.8 μm on the x, y plan and a thickness of about 3 μm on z at a physical depth of 170 μm below the surface of the sample.
The second step is the inscription of the BGs. For the case of the LBL gratings, a series of lines of 40 μm width equally spaced of Λ_{BG} is inscribed always in the same direction, crossing the waveguide exactly at the middle of the width.

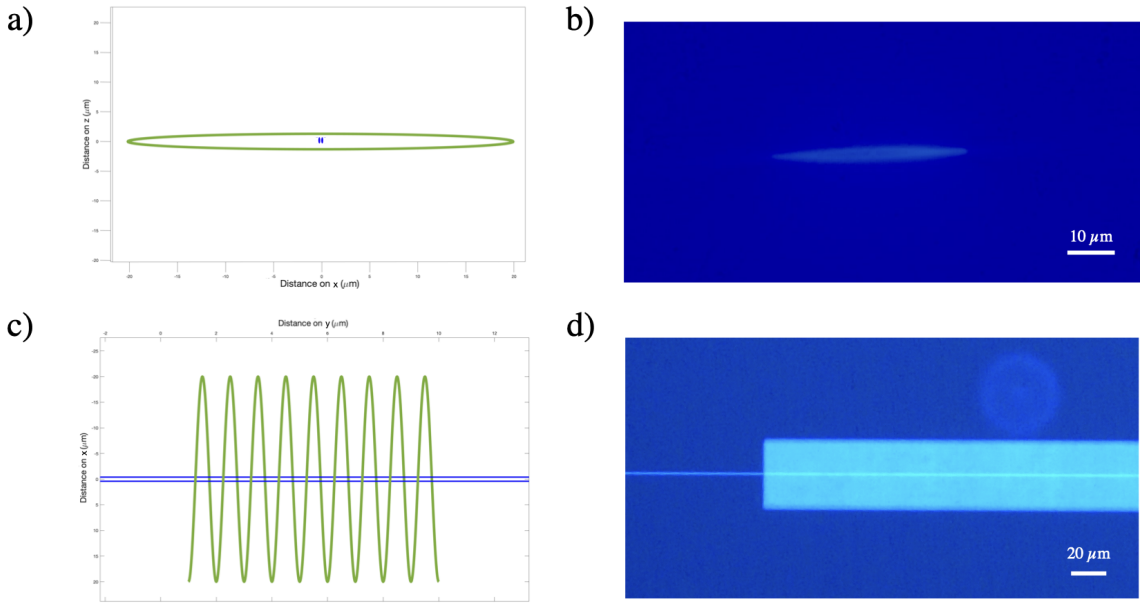

Figure 4.5: Geometrical characteristics of the helix: a) drawing and b) fluorescence image of the front view and c) drawing and d) fluorescence image of the top view of helicoidal WBGs. Fluorescence images were collected with a 60× microscope objective with N.A. 0.7 with excitation light at $\lambda_{exc} = 365$ nm.

For the case of the helix BGs, a helicoidal $3D$ Spline trajectory is created with a given period Λ_{helix}, semi-minor axis of 1.5 μm in the z direction and semi-major axis of 20 μm in the direction orthogonal to the axis of the waveguide; thus, the grating is inscribed around the waveguide, which occupies the center of the elliptical projection of the gratings. It is noteworthy to mention

that the height of the helix matches the thickness of the silver-sustained structure: in this way, the bottom edge of the top arch and the top edge of the bottom arch of the helicoidal structures lay always on the same plan, which is exactly at the center of the waveguide, as reported in Fig. 4.5a and Fig. 4.5b. Moreover, it is possible to observe that even if the BGs are added to the waveguide on a second step, the fluorescence of the waveguide is still present, due to the re-writing ability of the silver clusters.

The waveguides were written at a writing speed of 20 μm/s with peak intensity in the range $8 - 17$ TW/cm^2, while the BGs have been written at the writing speed of 100 μm/s, to both reduce the number of cumulative pulses, and with a peak intensity slightly lower than the one used for the writing of the waveguide, assuring the writing of the grating as a perturbation of the waveguide.

4.2.2 Characterization

Refractive index change

The refractive index change associated with both the waveguide and the Bragg gratings has been measured thanks to the, already mentioned, Sid4BIO software from Phasics company.
Although the periodicity of the gratings is well below the resolution of the CDD sensor, it is still possible to observe the DC component of the refractive index modulation associated with the grating, as reported in Fig. 4.6.

Moreover, the Δn profile reported in the same picture clearly shows that the waveguide is still present at the center of the BGs, even though the inscription of the waveguide is prior to the one of the gratings. Nevertheless, this represents a further confirmation of the rewriting ability of the silver clusters and their inscription memory, which allows for the building up of the induced Δn by just cumulating a larger number of pulses when still below the saturation threshold imposed by the finite amount of available silver in the glass matrix.

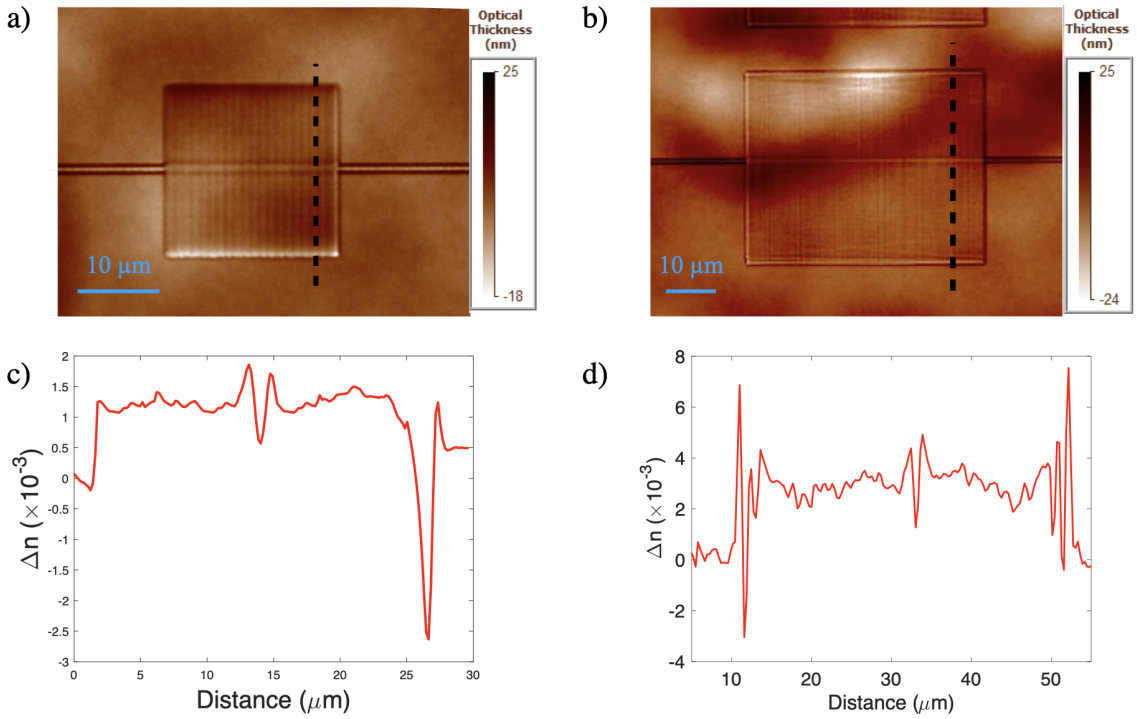

Figure 4.6: Phase images of a) a test LBL gratings with $L = 20$ μm, width 20 μm and periodicity $\Lambda = 500$ nm, and b) an helicoidal gratings with $L = 50$ μm, width 40 μm and periodicity $\Lambda = 250$ nm. Profiles in plots c) and d) report the refractive index changes induced by the LBL and the helicoidal gratings, respectively, along the two black, dashed lines in a) and b) pictures. It should be noted that negative Δn is observed at the starting points of the LBL structure in a) and at the edges of the helix in b) as a consequence of the cumulation of many pulses.

Setup

The WBGs were tested on the same setup used to inject the multiscan waveguides in Chapter 3, using the same sources used for characterizing such waveguides:

- a tunable Ti:Sa laser;
- a butterfly diode laser at 1550 nm.

The Ti:Sa laser injection was achieved both in free space, with a 20× microscope objective with N.A. 0.5. The transmission of the WBGs injected with the TI:Sa laser was collected in free space with a 100× microscope objective with N.A. 0.9, the output of the waveguide was selected with a pinhole, then focused on the surface of a SM fiber by a 20× microscope objective with

N.A. 0.5. The alignment of the fiber was achieved with a 6-axis fiber positioner from Newport company.
The injection of the diode laser at 1500 nm and the collection of the transmission of the WBGs were achieved by butt-coupling the fibers to the sample and optimized by two 6-axis fiber positioners.
The transmission of the WBGs was then observed on an Optical Spectrum Analyzer (OSA) AQ6370D from YOKOGAWA company, allowing for analysis in a spectral range of $600 - 1700$ nm with a resolution down to 0.02 nm.

Transmission

The acquired transmission spectra have been processed in order to reconstruct the transmission curves of the guiding structures out of the Bragg resonances. Thus, the acquired data have been normalized to the reconstructed curves in order to obtain the normalized transmission curves.
The normalized transmission spectra of helicoidal WBGs with periodicity $\Lambda_{helix} = 490$ nm and remarkably short length of $L = 500$ μm and $L = 750$ μm are reported respectively in Fig. 4.7a and Fig. 4.7b. Since $\lambda_B = \frac{2\pi n_{eff}\Lambda_{BG}}{m}$, the selected λ_B when the Bragg gratings periodicity is exactly the $\Lambda_{helix} = 490$ nm for the first order of diffraction $m = 1$ is $\lambda_B \sim 1.560$ μm, given $n_{eff} = 1.59$ at 1550 nm, as reported in Fig. 4.7b. However, the same helicoidal structure gives a strong Bragg signature at $\lambda_B = 786$ nm.

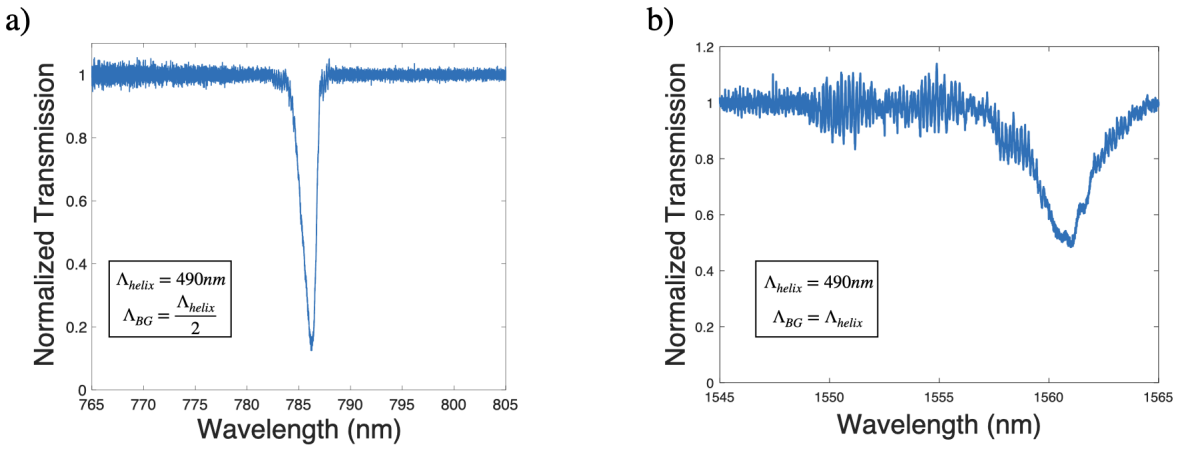

Figure 4.7: Normalized transmission spectra of helicoidal WBGs with periodicity $\Lambda_{helix} = 490$ nm and length a) $L = 500$ μm and b) $L = 750$ μm: the periodicities of the gratings associated with the two WBGs are a) $\Lambda_{BG} = \frac{\Lambda_{helix}}{2}$ and b) $\Lambda_{BG} = \Lambda_{helix}$.

Not ruling out that the Bragg signature at the short wavelength may result from the second order of diffraction $m = 2$, although the very high drop in transmission might be excluded, it is hypothesized that the inscription of such a flat helicoidal structure, with the top and bottom edges intersecting the waveguide, may lead to a periodic pattern with periodicity $\Lambda_{BG} = \frac{\Lambda_{helix}}{2}$, resulting in a non-zero-Fourier component at $2\nu_B$.
Indeed, Fig. 4.8a shows a schematic representation of the helicoidal BGs inscription: the image reports both the periodicity of the inscribed helix Λ_{helix} and the periodicity at $\frac{\Lambda_{helix}}{2}$ resulting from the modulation of the refractive index of the waveguide when inscribing the top and the bottom of the helicoidal gratings. Moreover, Fig. 4.8b shows the cases of more confined (top) and less confined (bottom) guided modes: in the first case, the mode is mostly in interaction with the gratings with $\Lambda_{BG} = \frac{\Lambda_{helix}}{2}$, while in the other case the extension of the mode allows for the interaction with the gratings having $\Lambda_{BG} = \Lambda_{helix}$.

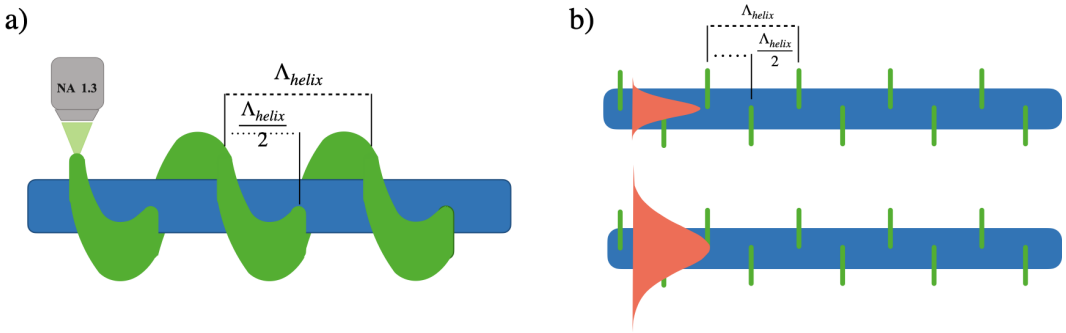

Figure 4.8: a) Schematic representation procedure for the DLW of the helicoidal BGs on the waveguide: both the Λ_{helix} and the $\frac{\Lambda_{helix}}{2}$ are highlighted. b) On top, a confined mode propagates inside the waveguide interacting with the gratings having $\Lambda_{BG} = \frac{\Lambda_{helix}}{2}$, while on the bottom, the extension of the mode allows it to interact with the gatings having $\Lambda_{BG} = \Lambda_{helix}$.

Such behavior of the helicoidal gratings has been observed in other WBGs at different wavelengths. For instance, Fig. 4.9 reports the normalized transmission spectra of three WBGs targeting different wavelengths in the VIS-NIR, showing on the one side that the silver-sustained WBGs can efficiently work in a broad spectral range from VIS to telecommunications (as demonstrated in Fig. 4.7b), and on the other side they can allow for the inscription of very short periodicity, as shown by the orange spectrum in Fig. 4.9 obtained from a helicoidal WBGs with $\Lambda_{helix} = 280$ nm.

Moreover, a transmission drop of more than 99% was remarkably achieved at $\lambda_B = 1.007$

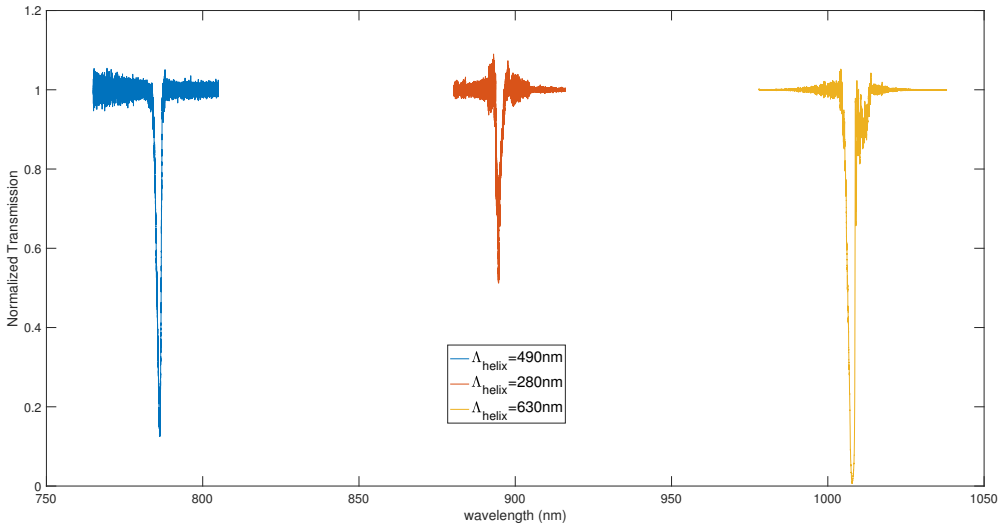

Figure 4.9: Accordability of WBGs functioning at different wavelengths. WBGs normalized transmission spectra with: in blue, $\lambda_B = 786$ nm for $\Lambda_{BG} = \frac{\Lambda_{helix}}{2}$ and length $L = 500$ μm; in orange, $\lambda_B = 895$ nm for $\Lambda_{BG} = \Lambda_{helix}$ and length $L = 500$ μm; in yellow $\lambda_B = 1.007$ μm for $\Lambda_{BG} = \frac{\Lambda_{helix}}{2}$ and $L = 500$ μm.

μm for an helicoidal WBG with period $\Lambda_{helix} = 630$ nm and length $L = 500$ μm, as reported in Fig. 4.10. Such strong filtering behavior could have interesting outcomes once proved that the WBGs do not only filter at the designed λ_B, but also reflect.

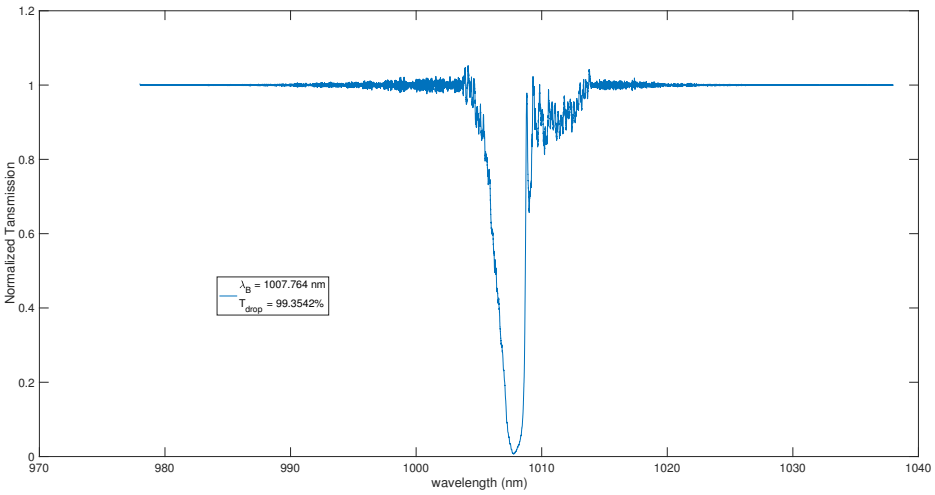

Figure 4.10: Normalized transmission spectra showing a remarkable drop in transmission, more than 99%, achieved at $\lambda_B = 1.007$ μm, for an helicoidal WBGs with periodicity $\Lambda_{helix} = 630$nm and length $L = 500$ μm, for which $\Lambda_{BG} = \frac{\Lambda_{helix}}{2}$.

Reflection

The reflection spectra of the WBGs have been collected both in free space and in fiber, then observed at the OSA. Two of the collected reflection spectra are reported in Fig. 4.11.

The collection of the reflection spectrum at $\lambda = 1.550$ μm in Fig. 4.11a has been acquired by connecting the butterfly diode to port 1 of a SM 6015-3-APC circulator from Thorlabs company, the port 2 was butt-coupled to the sample and the port 3 was injected into the OSA.
The collection of the reflection spectrum at $\lambda = 786$ nm reported in Fig. 4.11b nm was obtained by collecting the reflection from the waveguide in free space thanks to a $50\% - 50\%$ beam splitter placed before the microscope objective used to inject the WBGs. The reflection was then collected by a $20\times$ microscope objective with N.A. 0.26 and injected into a SM fiber connected to the OSA.

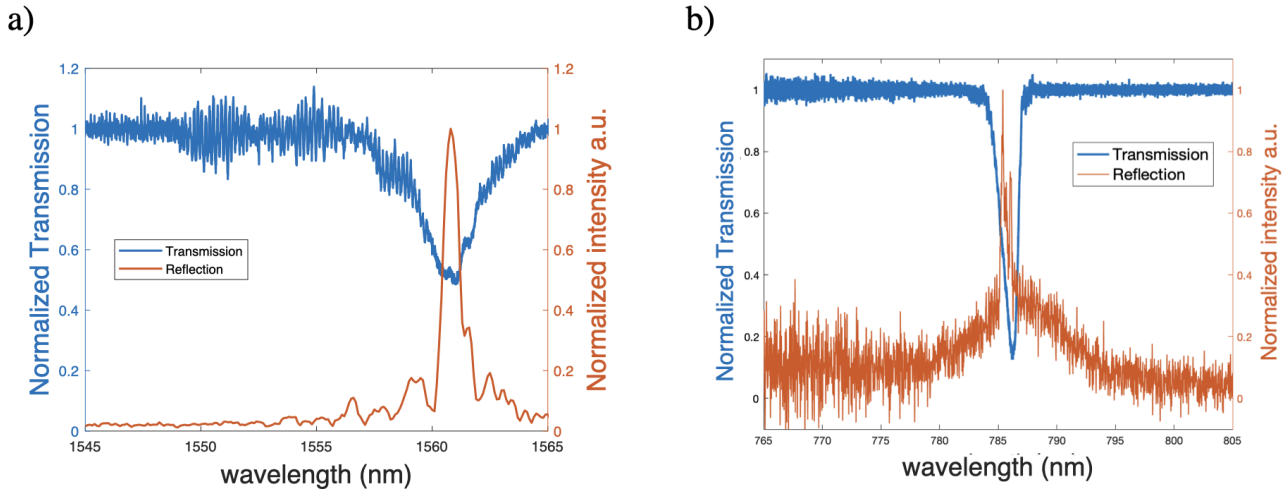

Figure 4.11: Reflection and transmission curves at a) $\Lambda_B = 1560$ nm and b) $\lambda_B = 786$ nm for helicoidal WBGs with $\Lambda_{helix} = 490$ nm and a) $L = 750$ μm, b) $L = 500$ μm. The reflection spectrum in a) has been collected using a SM circulator butt-coupled to the entrance of the WBG, while the reflection spectrum in b) has been collected from the WBG in free space and focused on a SM fiber connected to an OSA.

BGs parameters and simulation

The CWT allows for further characterization of the silver-sustained WBGs by a quantitative measure of their strength, the κ coupling coefficient and the bandwidth $\Delta\lambda$. The coupling coefficient κ has been calculated from Eq. 4.15, where R_{max} was calculated from the transmission spectrum as:

$$R_{max} = 1 - 10^{-(T/10)}, \tag{4.17}$$

where T is measured in dB.[156] Very high values of κ have been obtained. For instance, for low-efficient WBGs with $T_{drop} \sim 50\%$, like for the case reported in Fig. 4.7b and Fig. 4.9, the evaluated experimental κ have been found:

- $\kappa_{exp} = 1.21$ mm^{-1}, for the WBGs targeting $\lambda_B = 1.56$ μm with $L = 750$ μm;
- $\kappa_{exp} = 1.73$ mm^{-1}, for the WBGs targeting $\lambda_B = 895$ nm with $L = 500$ μm.

However, when the efficiency of the Bragg gratings increases, also the coupling coefficient κ increases: for a T_{drop} of 88% at $\lambda_B = 786$ nm achieved in a WBGs with $L_{BG} = 500$ μm, and reported in Fig. 4.7a, the experimental coupling coefficient is $\kappa_{exp} = 3.4$ mm^{-1}.

Finally, for the best WBG, reported in Fig. 4.10, a T_{drop} of 99.3% was achieved in only $L = 500$ μm long gratings, leading to a **remarkably high** $\kappa_{exp} = 6.42$ **mm**$^{-1}$.

Such high values of the coupling coefficient can be compared to the values reported in literature[156]: for first order $m = 1$ at $\lambda_B \sim 1.55$ μm, the coupling coefficient κ was found to be 1.457 mm^{-1} for a 4 mm long WBG obtained by modulated burst in silicate glass, and $\kappa = 1.23$ mm^{-1} for a 1 mm long WBG achieved by multi-scan inscription in $LiNbO_3$ sample.[156;171]. Moreover, for first order $m = 1$ for $\lambda_B = 725$ nm, a 4 mm long WBG inscribed by modulated burst in silicate glass showed $\kappa = 0.696$ mm$^{\cdot 1}$.[156] Finally, for first-order WBGs at $\lambda_B \sim 1.03$ μm, 4 mm long grating in silicate glass gave the coupling coefficient $\kappa = 0.634$ mm^{-1}, while in a borosilicate glass 5.3 mm long WBGs showed a coupling coefficient of $\kappa = 0.848$ mm^{-1}.[156;172]. For sake of clarity, Tab. 4.1 recaps all the values discussed so far.

λ_B (nm)	order	length L (mm)	$\kappa_{literature}$ (mm^{-1})	$\kappa_{manuscript}$ (mm^{-1})
725	$m = 1$	4	0.696	–
786	$\mathbf{m = 1}$ for $\mathbf{\Lambda_{BG} = \frac{\Lambda_{helix}}{2}}$	**0.5**	–	**3.4**
1007	$\mathbf{m = 1}$ for $\mathbf{\Lambda_{BG} = \frac{\Lambda_{helix}}{2}}$	**0.5**	–	**6.42**
1030	$m = 1$	4	0.634	–
1030	$m = 1$	5.3	0.848	–
1540	$m = 1$	1	1.23	–
1545	$m = 1$	1	1.457	–
1560	$\mathbf{m = 1}$ for $\mathbf{\Lambda_{BG} = \Lambda_{helix}}$	**0.75**	–	**1.21**

Table 4.1: Comparison between the experimental data and the results reported in literature: the results obtained in this work have been highlighted in bold font.

Moreover, the coupling coefficient κ is directly related to the n_{eff}^{DC}, as shown in Eq. 4.10, which is dependent on the DLW intensity, as discussed in the previous Chapter.
Therefore, a series of helicoidal WBGs with $\Lambda_{helix} = 630$ nm, length $L = 500$ μm was inscribed with different DLW intensity in order to observe the dependence of the coupling coefficient κ to the refractive index change. The resulting κ coefficients are reported in Fig. 4.12. It should be noted that the reflection efficiencies reported in Fig. 4.12 have been calculated following the Eq. 4.17, while the κ values have been calculated from Eq. 4.15.

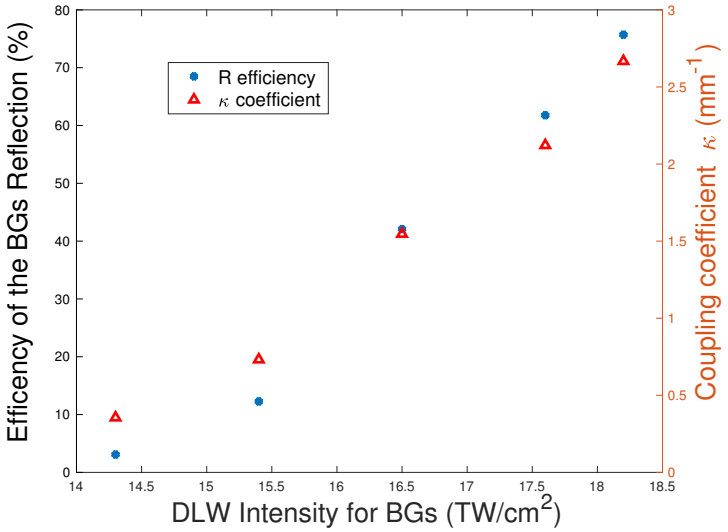

Figure 4.12: Dependence of the coupling coefficient κ and the BGs reflection efficiency on the DLW intensity for a series of helicoidal WBGs inscribed fixing the periodicity $\Lambda_{helix} = 630$ nm and the length $L = 500$ μm. It should be noted that the reflection efficiency is calculated from the transmission spectra following the Eq. 4.17.

Nevertheless, an increase of the n_{eff}^{DC} results in both the increase of the κ parameter and a red-shift of the λ_B, since $\lambda_B \propto n_{eff}$.
However, this was not the case for the intensity series reported in Fig. 4.12. Indeed, by taken the cases of $I = 17.6$ TW/cm^2 and $I = 18.2$ TW/cm^2, the κ coefficients are found to be 2.12 mm^{-1} and 2.66 mm^{-1}, respectively, however the position of the λ_B is 1005.7 nm and 1005.3 nm, respectively.

Finally, a numerical simulation has been used to model the normalized transmission spectrum in Fig. 4.10 in order to extract the effective length of the gratings and recalculate the κ parameter.
The simulation, based on the same CWT model presented by Kogelnik in 1975 [169] and reported by Erdogan in 1997 [170], allowed to retrieve a numerical solution for the reflection coefficient ρ by Mathematica software:

$$\rho = \frac{-\delta + i\sqrt{(\kappa-\delta)(\kappa+\delta)}\, tanh\left[L\sqrt{(\kappa-\delta)(\kappa+\delta)} - i\, arctanh\left(\frac{\delta}{\sqrt{\kappa^2-\delta^2}}\right)\right]}{\kappa}, \tag{4.18}$$

where $\delta = \beta - K/2$ is the detuning and $\beta = \frac{2\pi}{\lambda}$ and $K = \frac{2\pi n_{eff}}{\Lambda_{BG}}$ are the propagation and gratings constants, respectively.

It should be noted that the solution reported in Eq. 4.18 has been found without making any approximation, with the only assumptions and boundary conditions imposed in the work of Kogelnik. Therefore, the two Eq. 4.13 and Eq. 4.18 for the reflection coefficient ρ should be considered completely similar. Nevertheless, Eq. 4.18 can be seen as more general description of the ρ coefficient.

Figure. 4.13 reports the normalized transmission spectrum for the WBGs at $\lambda_B = 1.007$ μm with inscribed length $L = 500$ μm, for which $\kappa = 6.42$ mm^{-1} has been calculated, and the numerical simulation from which an effective length of $L_{eff} = 498$ μm and $\kappa_{sim} = 7.85$ mm^{-1} have been extracted.

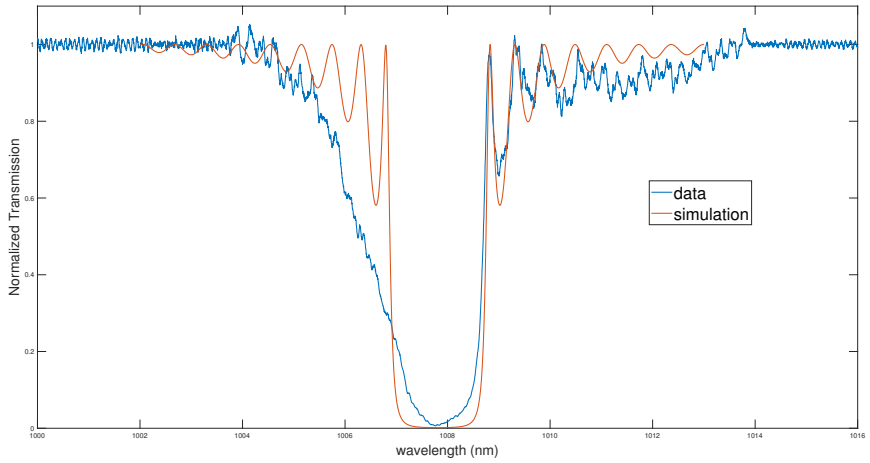

Figure 4.13: Experimental normalized transmission spectrum, in blue, of the helicoidal WBG with $\Lambda_{helix} = 630$ nm and $L = 500$ μm with $T_{drop} > 99\%$ at $\lambda_B = 1007$ nm, giving $\kappa_{exp} = 6.42$ mm^{-1} and simulation curve, in orange, obtained from Eq. 4.18 with $\kappa_{sim} = 7.85$ mm^{-1} and $L_{eff} = 498$ mm^{-1}. It can be noted that the simulation well fits the range $\lambda > \lambda_B$, in particular the sidelobe, while the asymmetry of the experimental spectrum does not allow for a good fit in the range $\lambda < \lambda_B$.

By observing the two curves in Fig. 4.13, it can be noticed that the model well fits the data for long wavelength $\lambda > \lambda_B$, for instance, in particular the fit well individuates the sidelobe. However, for short wavelengths $\lambda < \lambda_B$, the experimental data and the simulation do not over-

lap. Indeed the experimental transmission curve is not symmetric, as it should be theoretically. Moreover, the width of the experimental curve is much larger than the one simulated. These problems could arise from inhomogeneity of the refractive index change along the z direction.

Indeed, the experimental bandwidths of the silver-sustained WBGs have been measured from the first zeros of the normalized transmission curves and have been compared to the theoretical bandwidths reported in Eq. 4.16, which at λ_B can be rewritten as:

$$\Delta\lambda_{theo} = \frac{\lambda_B^2}{n_{eff}}\sqrt{\frac{\kappa^2}{\pi^2} + \frac{1}{L^2}}. \tag{4.19}$$

The results have been reported in Tab. 4.2: the experimental bandwidth is around $3\times$, or more, larger than the theoretical bandwidth. Such a great disparity between the theoretical and the experimental width of the Bragg signature points to presence of some issues in the fabrication of the WBGs, like the existence of a chirp, for instance.

λ_B (nm)	κ_{exp} (mm^{-1})	L_{exp} (mm)	$\Delta\lambda_{exp}$ (nm)	$\Delta\lambda_{theo}$ (nm)
786	3.4	0.5	4.5	0.87
895	1.73	0.5	3.5	1.03
1007	6.42	0.5	4.3	1.81
1560	1.21	0.75	6.1	2.1

Table 4.2: Comparison between the experimental bandwidth, measured from the first zeros of the transmission spectra, and the theoretical bandwidth, calculated from Eq. 4.19 of helicoidal WBGs highlighting the broadening of the curves at the Bragg resonances.

Moreover, by modeling the transmission curves of the DLW intensity series reported in Fig. 4.12, it was possible to retrieve not only the real κ coefficients and the effective lengths of the WBGs, but also the associated Bragg gratings periodicities. From the results, reported in Tab. 4.3, it is possible to observe that: on the one hand, the effective length does not match the inscribed length of the gratings for many of the WBGs, and on the other hand, there is a non-negligible difference in the inscribed periodicities.

Such a result raises a question on the stability of the WBGs inscription process.
Therefore, in order to have a better picture of the problem, two series of WBGs have been

Intensity (TW/cm^2)	κ_{sim} (mm^{-1})	L_{eff} (mm)	$\lambda_{B_{eff}}$ (nm)
14.3	0.1	0.5	0.3141
15.4	0.25	0.5	0.31425
16.5	0.58	0.39	0.31405
17.6	1.9	0.43	0.31433
18.2	2.39	0.22	0.31418

Table 4.3: WBGs parameters extracted from the simulations using Eq. 4.18 for the series of the helicoidal WBGs with fix $\Lambda_{helix} = 630$ nm, resulting in $\lambda_{BG} = \frac{\Lambda_{helix}}{2} = 315$ nm, and length $L = 500$ μm. The values here reported show that both the $\Lambda_{B_{eff}}$ and the L_{eff} are not fixed, in particular the latter is highly affected by the instability of the inscription process.

written by changing the length L of the gratings. The two sets of WBGs have been inscribed both as helicoidal gratings and by LBL method, with $\Lambda_{helix} = 630$ nm and $\Lambda_{LbL} = 315$ nm, in order to achieve the same Λ_{BG}. The results of the two series have been reported in Fig. 4.14.

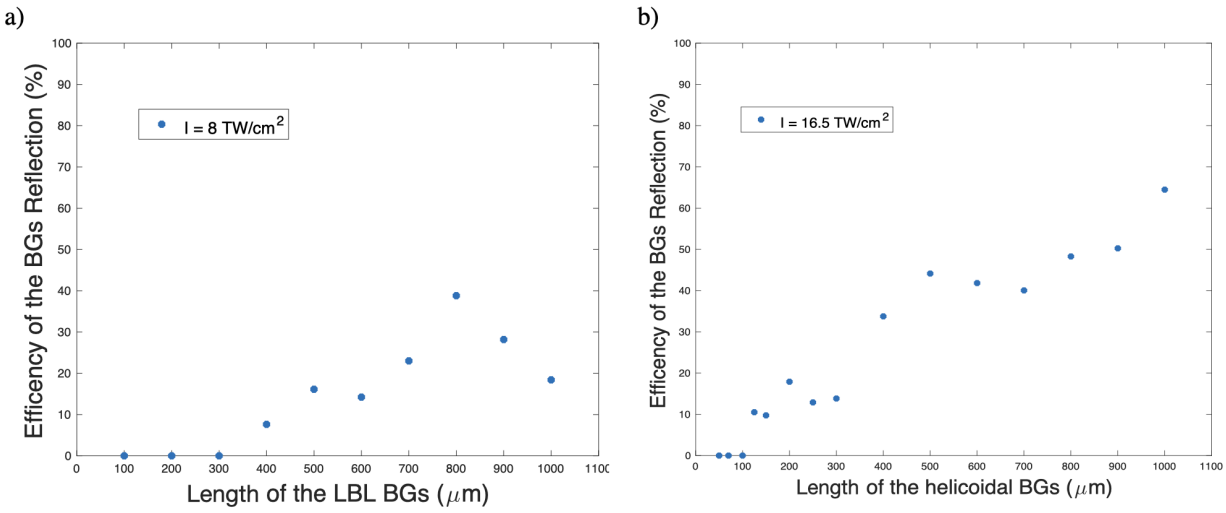

Figure 4.14: Reflection efficiency for two series of a) LBL b) helicoidal WBGs with different length L of the BGs but same $\Lambda_{BG} = 315$ nm, in particular for a) $\Lambda_{BG} = \Lambda_{LbL}$ while for b) $\Lambda_{BG} = \frac{\Lambda_{helix}}{2}$. The reflection efficiency is calculated from the transmission spectra following Eq. 4.17. It is noteworthy to highlight that the reflection efficiency in a) surprisingly decreases after $L = 800$ μm.

Problematics encountered in the writing of the WBGs

Some assumptions have been made on the cause, or the causes, leading to an instability of the silver-sustained WBGs fabrication process.
From the dependences of the reflection efficiency on the length of the Bragg gratings, reported in Fig. 4.14, it can be assumed that the inscription of long gratings (length $L > 800$ μm for the helix method and $L > 500$ μm for the LbL method) is not stable. Two main reasons can be addressed:

- a random fluctuation of the absolute positioning of the stages that results in a random variation of the periodicity of the grating;
- a drift in the absolute repositioning of the stages, especially for the case of the inscription of LBL gratings. Even if the distance between two lines of the gratings is kept constant to the sought Λ_{BG}, there might be a trend in the placement of each period. Such a drift becomes more important when the length of the gratings increases, as reported in Fig. 4.14a, meaning that it has to be related to the number of steps, *i.e.* the number of periods in the gratings; therefore the drift will result in a chirp of the periodicity of the grating which is more critical at small periodicities. Indeed, the broadening of the Bragg resonance bandwidths $\Delta\lambda_{exp}$ suggests the presence of such a chirp. The asymmetry of the normalized transmission curves may point out the presence of a quadratic chirp.

However, the instabilities in the absolute repositioning of the stages might not be the only source of errors in the inscription of the WBGs.
For instance, the fluctuations in the laser intensity and the motion speed, therefore the number of absorbed pulses, may strongly affect the size of the inscribed structures, as reported by Bellec *et al.* in 2010.[46]

A variation of the laser intensity $I' = I + \delta I$ results in a variation of the irradiance:

$$\delta I_{peak} = \frac{\delta I \, T_{obj}}{f_{rep} \, \omega_0 \sqrt{\pi \tau_p^2 / 2}}; \tag{4.20}$$

thus, for instance, a 10% variation in the laser intensity can result in a variation up to 20% on the radius of the silver structures, beside a variation of the refractive index change. Such a modification of the structures dimensions is equal to a variation of 80 nm on the size the laser spot focused with a microscope objective with N.A. 1.3, as reported in the case of the WBGs here, when the laser irradiance is about 10 TW/cm^2.

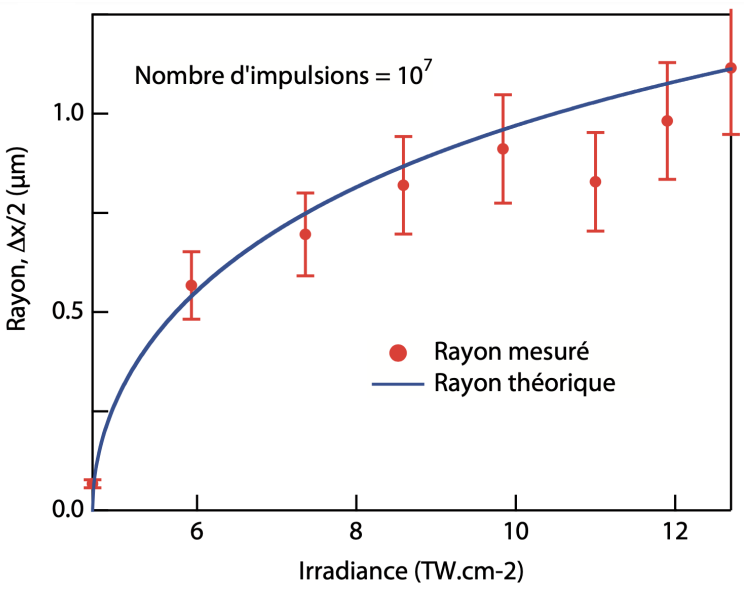

Figure 4.15: Variation of the radius of the laser-induced silver structures depending on the laser irradiance. Image adapted from [52]

Finally, if the direction of the laser output changes in time, also the position of the focused spot changes. Typically, the variation in the direction of the laser output are stabilized around the μrad; however, during the writing of the helicoidal gratings with the KGW:Yb femtosecond oscillator, the direction of the laser may have changed of larger angles. For instance, if the laser direction tilts of 1 mrad, equivalent to 0.057°, the position of the laser spot, focused by the 100× microscope objective with N.A. 1.3 with focal length $f = 1.8$ mm used for the inscription of the WBGs, is translated of 180 nm from the original position. Such a huge displacement of the laser spot may compromise the inscription of gratings with periodicities as small as the ones inscribed in this work.

In conclusion, the inscription of Type A WBGs in silver-containing glasses has demonstrated to achieve high coupling coefficient for very short gratings and to select Bragg resonances at the first order in the VIS-NIR spectral range, due to the ability of silver-sustained structures to obtain sub-λ features. Moreover, the fabrication of helicoidal gratings allows for inscribing gratings with periodicities twice smaller the ones of the helices. However, some instability issues have been highlighted, meaning that some precautions are necessary for the successful fabrication of WBGs based on Type A modifications.

4.3 Volume Bragg Gratings

As suggested by the name, Volume Bragg Gratings (VBGs) are thick periodic gratings fabricated in the bulk of media.

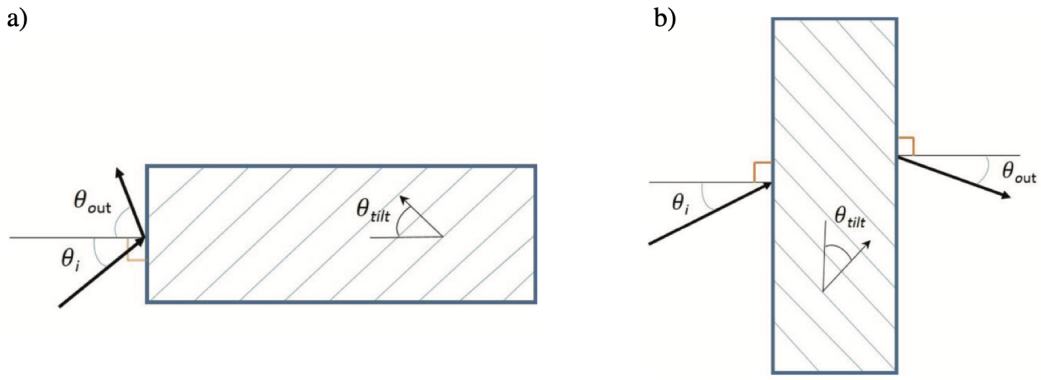

Figure 4.16: Volume Bragg Gratings: a) reflection gratings, for which the Bragg resonance is achieved at $\lambda_B = 2\Lambda\, cos(\theta_i + \theta_{tilt})$, and b) transmission gratings, for which the Bragg resonance is achieved at $\lambda_B = 2\Lambda\, sin(\theta_i + \theta_{tilt})$. Image taken from [53]

Such gratings are distinguished in two categories, depending on their behavior at the Bragg resonance:

- *reflection* gratings: the incoming light satisfying the Bragg condition $\lambda_B = 2\Lambda\, cos(\theta_i + \theta_{tilt})$ will be reflected from the gratings, as depicted in Fig. 4.16a;
- *transmission* gratings: the incoming light satisfying the Bragg condition $\lambda_B = 2\Lambda\, sin(\theta_i + \theta_{tilt})$ will be diffracted and transmitted by gratings, as depicted in Fig. 4.16b;

where Λ is the gratings period and θ_{tilt} is the tilt angle of the gratings.

VBGs can be fabricated in the bulk of photosensitive media by UV holographic interferometry, like for silica-based glasses containing dopants, by adopting phase masks or by femtosecond laser inscription. In the latter case, high-energy pulses are necessary for achieving the material modifications at the base of the refractive index modulation for non-photosensitive media.
Reflection or transmission bulk gratings can be used for many applications, such as notch filters, wavelength stabilizers in laser systems or diodes, due to their narrowband filtering characteristic, or for spectral beam combining and wavelength division multiplexing. [173;174;175;176;177]

4.3.1 Kogelnik's model

In 1969 Kogelnik proposed a model based on the CWT to simulate the diffraction efficiency of a light incident of thick holograms near to the Bragg condition. For dielectric lossless gratings, Kogelnik's model derives the gratings diffraction efficiency η as:

$$\eta = \frac{sin^2(\sqrt{\nu^2 + \xi^2})}{1 + \xi^2/\nu^2}, \tag{4.21}$$

where the function ν represents the phase incursion and describes the strength of the BG at the maximum of its diffraction efficiency, while ξ represents a dephasing function describing the deviation from the Bragg condition. The two functions are expressed as:

$$\nu = \frac{\pi \Delta n \, d}{\lambda \sqrt{c_s c_r}}, \tag{4.22a}$$

$$\xi = \frac{d}{2c_s}\left(Kcos(\phi - \theta_i) - \frac{K^2\lambda}{4\pi}\right), \tag{4.22b}$$

where d, ϕ and Δn are the thickness, the tilt angle, and the modulation of the refractive index of the gratings, respectively, $K = 2\pi/\Lambda$ is the gratings vector, λ and θ are the wavelengths and the incident angle of the incoming light, respectively, and c_r and c_s are found from propagation vectors of the incoming, ρ and diffracted δ beams, respectively, which are related to the K vector by:

$$\delta = \rho - K. \tag{4.23}$$

Figure 4.17a depicts the geometrical relationship between the K, ρ and δ vectors, while Fig. 4.17b reports the vector diagram for the conservation of the momentum at the Bragg condition:

$$cos(\phi - \theta_i) = \frac{K}{2\beta}, \tag{4.24}$$

where $\beta = 2\pi/\lambda n$ is the free propagation constant.
Therefore, the c_r and c_s terms in the formulations of ν and ξ are expressed as:

$$c_r = cos\theta_i, \tag{4.25a}$$

$$c_s = cos\theta_i - \frac{K}{\beta}cos\phi. \tag{4.25b}$$

4.3.2 Single-layer transmission Bragg gratings

A single-layer Volume Bragg grating has been inscribed inside a silver-containing zinc-phosphate glass using 40× microscope objective with N.A. 0.75. The laser system is the same one used for

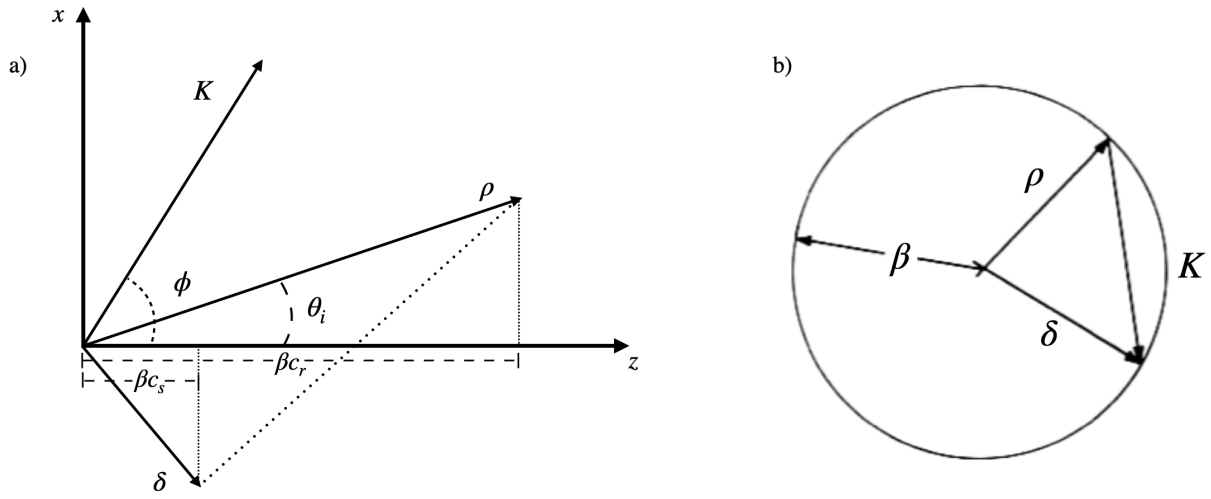

Figure 4.17: a) Vectorial representations of the propagation vectors δ and ρ of the incident and diffracted beams, respectively, giving an incident angle θ_i and tilt gratings with tilt angle ϕ and gratings vector K. b) Vectorial diagram at the Bragg condition $cos(\phi - \theta_i) = \frac{K}{2\beta}$ for which $\delta = \rho - K$. Images adapted from [54]

the fabrication of the multiscan waveguides, with DLW intensity and writing speed respectively of 11 TW/cm^2 and 50 μm/s. The gratings periodicity has been fixed to $\Lambda = 800$ nm, which is exactly half of the beam diameter $2\omega_0 = 1.6$ μm at the depth of 160 μm below the surface of the sample at which the microscope objective is optimized to prevent aberrations. The 8 μm thickness of the inscribed gratings has been measured by imaging the structure on the lateral polished side of the sample on a fluorescence microscope under UV light ($\lambda_{exc} = 365$ nm).
After the DLW, the sample has been positioned on a 5-axis translation stages to measure the reflection efficiency of the gratings: 3 micrometer stages have been coupled to move the sample in x, y and z, while a motorized 2-axis goniometer stage from Optics Focus company has been used to adjust the tilt of the grating by aligning the back reflection from the sample surface to the direction of the incoming beam and to rotate the gratings around the gratings axis.
The incoming light has been focused on the gratings using a lens, the gratings groves have been oriented in the direction perpendicular to the polarization of the incoming beam and the diffraction efficiency has been calculated by measuring the diffraction efficiency of the $m = 0, 1$ orders, P^0 and P', as follow:

$$\eta_{exp} = \frac{P'}{P^0 + P'}. \tag{4.26}$$

Figure 4.18 reports a geometrical representation of the diffraction of an incoming beam with incident angle θ into the zero, P^0, and first P' orders by thick transmission gratings with thickness d, period of the refractive index change (represented by green bands) Λ, and tilt angle ϕ.

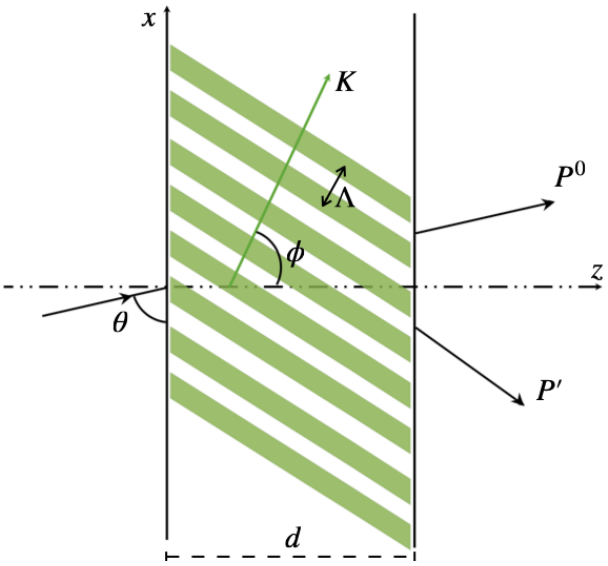

Figure 4.18: Diffraction of the zero-order P^0 and first order P' of an incident beam with incident angle θ_i by a transmission VBG characterized by gratings vector $K = \frac{2\pi}{\Lambda}$, where Λ is the periodicity of the refractive index modulation here represented by the green slanted bands, tilt angleϕ and thickness d along the z direction. Image adapted from [54]

The diffraction measurements have been repeated with a different light source in order to extract the diffraction efficiency, and thus the refractive index change associated with the inscribed structure, at different wavelengths: 375 nm, 405 nm and 632 nm. It is important to note that the UV probes are resonant to the absorption bands of the silver clusters.
Finally, a theoretical diffraction efficiency has been retrieved from fitting the experimental measurements with Kogelnik's model reported in Eq. 4.21 in order to extract the modulation of the refractive index associated with the gratings at different wavelengths.

Figure 4.19 shows the experimental data and the modelling, while Table 4.4 reports the experimental and theoretical values.

The experimental data and the simulations are in good agreement, however the diffraction

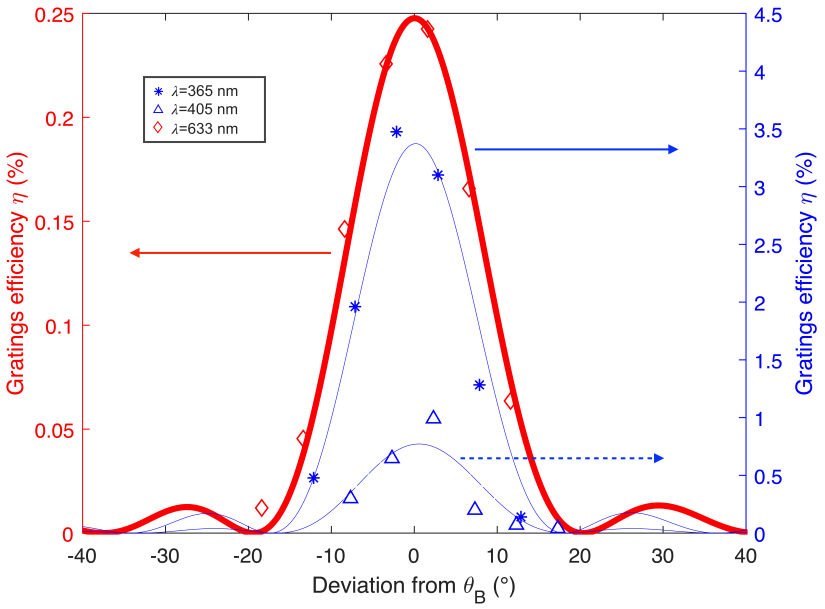

Figure 4.19: Experimental data and simulation using Kogelnik's model of the first order diffraction from a single-layer silver-sustained VBG with period $\Lambda = 800$ nm and thickness $d = 8$ μm. The transmission gratings have been probed at different wavelengths, $\lambda_{probe} = 375, 405$ and 633 nm to observe the dependence of the diffraction efficiency in and out of the absorption bands of the silver clusters and to extract the effective thickness d_{eff} and associated refractive index modulation Δn for each wavelength. The extracted values are reported in Tab. 4.4.

Probe wavelength λ (nm)	Effective thickness d_{eff} (μm)	Effective index modulation Δn_{eff}
375	7.5	3.2×10^{-3}
405	8.7	1.5×10^{-3}
633	3.5	2.75×10^{-3}

Table 4.4: Effective thickness d_{eff} and refractive index modulation Δn_{eff} values extracted from fitting experimental diffraction measurements of the single-layer silver VBG with the simulations based on Kogelnik's model. It is interesting to notice that even when λ_{probe} is outside the absorption band of the silver clusters, the Δn_{eff} is still rather high (on the order of a few 10^{-3}).

efficiency of the single-layer gratings is quite poor, as shown in Fig. 4.19.
Therefore, a series of transmission VBGs has been inscribed with different thicknesses aiming for improving the gratings diffraction efficiency.

4.3.3 Multi-layers transmission Bragg gratings

A series of VBGs with periodicity $\Lambda = 750$ nm and different number of layers has been inscribed in an AG01 sample for Argolight company. The transmission gratings have been inscribed using a 100× microscope objective with N.A. 1.3 (in combination with a matching index oil with $n = 1.518$) using the above-mentioned fiber laser setup. The structures have been realized 100 μm below the surface of the silver-containing sample choosing a DLW intensity of 11 TW/cm^2 and a DLW speed of 50 μm/s. A schematic representation of the inscription process and the structure geometries is found in Fig. 4.20.

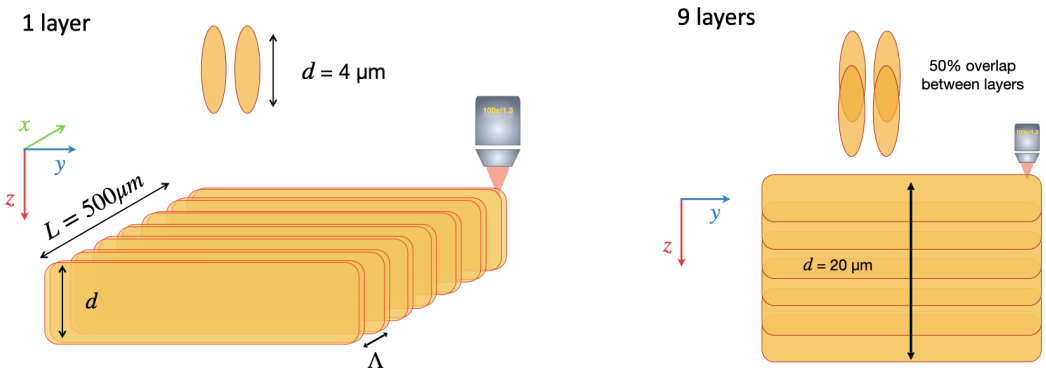

Figure 4.20: Schematic representation of the inscription process for the fabrication of the multi-layers VBGs: a) the inscription of single-layer gratings with period Λ and $L = 500$ μm results in the fabrication of a $d = 4$ μm thick gratings, while a thicker multi-layers grating is achieved by stacking several single-layer gratings on top of each other with an overlap of 50% between different plans. Figure b) reports the case of the 9-layers gratings with achieved $d = 20$ μm thickness.

Four squared gratings of length $L = 500$ μm have been obtained with different thicknesses achieved by increasing the number of layers, $N = 1, 3, 6$ and 9, with fix overlap of 50% between each layer: the silver-sustained structures inscribed using the N.A. 1.3 and $I = 11$ TW/cm^2 have an estimated thickness of 4 μm, therefore each grating has been estimated to be $4, 8, 14$

and 20 μm thick.

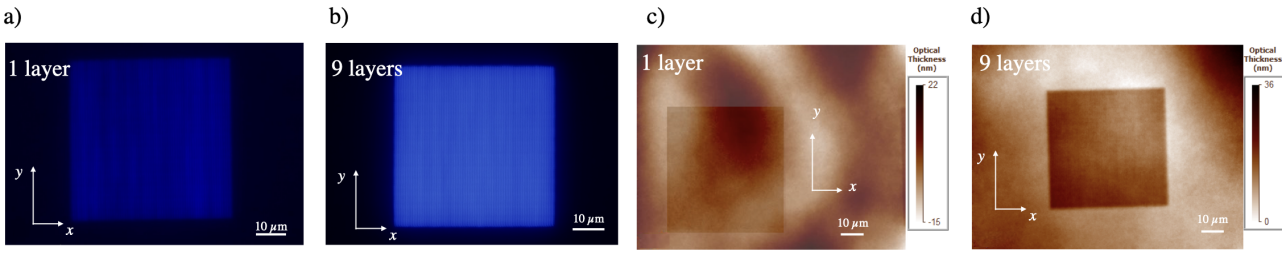

Figure 4.21: a) and b) Fluorescence and c) and d) phase images of multi-layers silver-sustained VBGs with $N = 1$ and $N = 9$ layers and length $L = 50$ μm. Fluorescence images have been acquired on a fluorescence microscope using a 60× microscope objective with N.A. 0.7 at $\lambda_{exc} = 365$ nm. Phase images have obtained using a 100× microscope objective with N.A. 1.3, index matching oil ($n = 1.518$), and the Sid4BIO software.

Figure 4.21 reports the fluorescence, pictures a) and b), and the phase images, pictures c) and d), of $L = 50$ μm multi-layers gratings with $N = 1$, and $N = 9$ number of layers for which the estimated thicknesses are 4 and 20 μm, respectively.
The experimental diffraction efficiencies of the inscribed multi-layers gratings probed with a UV source at $\lambda = 405$ nm have been measured by Eq. 4.26, as already discussed for the single-layer case, from which the refractive index modulation Δn associated with each multi-layers gratings has been extracted. Figure 4.22 reports the results for both the experimental diffraction efficiency η and the refractive index change Δn obtained from the thick gratings.

The results of the diffraction measurements are of two-fold importance.
On the one hand, it gives the confirmation that the diffraction efficiency of the silver-sustained VBGs increases with increasing the thickness of the transmission gratings, while still keeping an overall constant modulation of the refractive index Δn.
On the other hand, the results demonstrate the potentiality of the silver-sustained VBGs in achieving high diffraction efficiency for remarkably thin gratings. Indeed, as reported in Fig. 4.22, diffraction efficiency of $\sim 55\%$ has been obtained for a 20 μm thick gratings.

Finally, the diffraction measurements have also highlighted the weaknesses of the DLW inscription of stacked Bragg gratings. For the sake of brevity, only the diffraction measurements

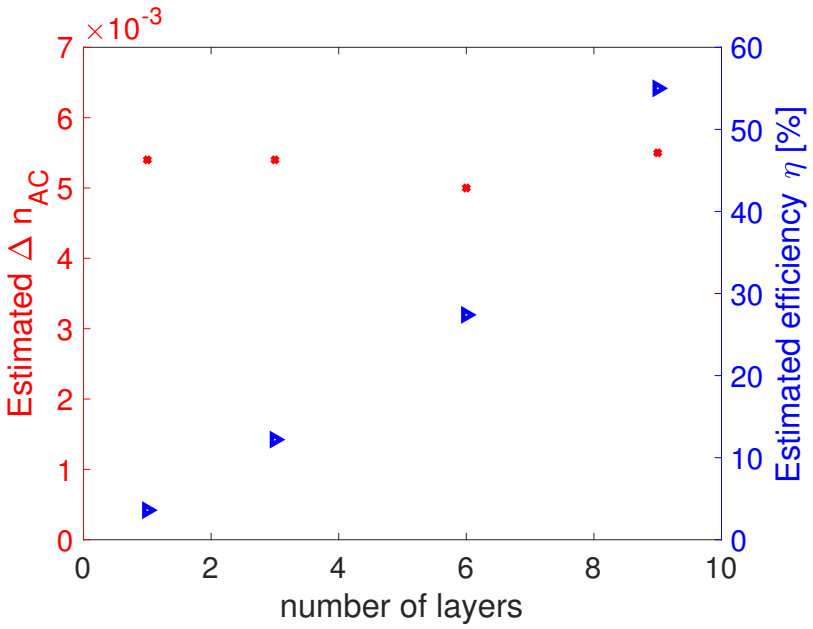

Figure 4.22: Dependence of the experimental diffraction efficiency η and the refractive index modulation Δn_{AC} on the number N of layers for the series of multi-layers silver sustained VBGs. The graph demonstrates that it is possible to achieve high diffraction efficiency, up to 55%, for only 20 μm thick gratings.

collected from the 9−layers grating are here analyzed and reported in Fig. 4.23.

Besides the broad diffraction peak at the expected Bragg angle θ_B, the data show the existence of other resonances at positions different from the Bragg angle θ_B.
The positions of the additional diffraction peaks determine the periodicities of the associated thick gratings from which these peaks originated: the result suggested that those peaks correspond to the second order diffraction by gratings with periodicities different from the sought one at $\Lambda = 750$ nm.
Thus, Kogelnik's model has been adopted to simulate the first-order diffraction of gratings with all the different periodicities, retrieving for each of the effective thickness and induced index modulation. The simulated grating efficiency is reported in Fig. 4.23 in red, taking into account all the contributions from the different inscribed gratings.

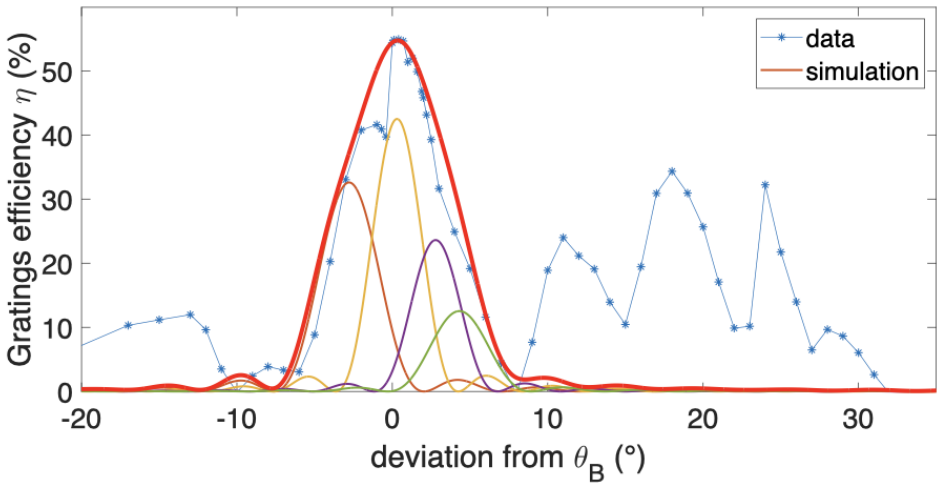

Figure 4.23: The experimental data show a broad diffraction peak centered at the Bragg angle θ_B. Moreover, other diffraction peaks are evident far from the Bragg resonance. By assuming that these are second-order diffractions due to periodicities unintentionally inscribed, it is possible to apply the Kogelnik model and obtain the simulated diffraction efficiency η by taking into consideration all the contributions of the different, which is reported in red.

Conclusions on the chapter

The Chapter deals with the femtosecond laser inscription of waveguides Bragg gratings and transmission volume Bragg gratings based on Type A modifications in silver-containing glasses.

Firstly, a brief overview of the production of WBGs in glasses is carried out, discussing several fabrication techniques, in particular stressing the advantages deriving from the femtosecond laser inscription of the periodic gratings.
Thus, the fabrication process, the geometrical characteristics and the optical properties of the silver-sustained WBGs are presented. In this regard, phase images of the Type A WBGs demonstrate that the laser inscription of the periodic silver-sustained structures is associated with a positive periodic modulation of the refractive index change. This result is in agreement with what has been discussed in the previous Chapter. Indeed, if the silver reservoir of the glass matrix is still sufficiently available, subsequent laser inscription will contribute to increasing the induced refractive index change.
Thus, the transmission spectra of some of the fabricated WBGs are reported, demonstrating the filtering ability of the periodic gratings in the selection of the proper Bragg resonance.

In particular, the particular case of helicoidal WBGs is discussed. The geometrical features of the helicoidal gratings allow for achieving a Bragg resonance simultaneously at the periodicity of the helix and half of it. Moreover, such a WBG allows for obtaining a high coupling coefficient between the guided mode and the helicoidal gratings. As a result, strong transmission drop at the Bragg resonance, up to more than 99%, have been reported for very short gratings, $L = 500$ μm typically.
As to confirm the proper functioning of the Type A WBGs, the reflection spectra of some of the WBGs are reported, demonstrating the mirroring behavior of the silver-sustained gratings.
However, instability issues in the inscription of the periodicity of the grating have been encountered. In particular, simulations based on CWT highlighted the broadening of the resonance bandwidth and the mismatch between the inscribed length of the gratings and the one contributing to the Bragg resonance.

The second part of the Chapter presents the results obtained for the fabrication of transmission volume Bragg gratings based on Type A modifications.
Firstly, the diffraction measurements for a single-layer silver-sustained VBG are discussed: although the diffraction efficiency is quite poor, the measurements demonstrated that the gratings can work at wavelengths resonant and not with the absorption band of the clusters, showing still a significant effective refractive index change, about few 10^{-3}.
Moreover, the inscription of a series of multi-layers VBGs with different thicknesses demonstrates the potentiality of the silver-sustained VBGs for achieving very high diffraction efficiency for thicknesses smaller than those reported in the literature.
However, the absolute repositioning of the stages during the DLW inscription is a critical parameter for the successful fabrication of efficient gratings, as already observed in the case of the waveguides Bragg gratings. The case of the 9-layer VBG well illustrates this instability problem.

General conclusions and perspectives

The project behind the work reported in this manuscript aimed at developing waveguides and optical components for integrated optical circuits by femtosecond laser inscription in silver-containing glasses.

It has been demonstrated that the DLW in silver-containing glasses with a high repetition rate source and low energy pulse, about a few tens of nJ, induced the formation of silver clusters in an athermal regime. The clustering of silver ions is associated with a positive refractive index change as a consequence of a change in the local polarizability. In 2017 it was proved that the positive refractive index change allows for guiding applications, enabling the fabrication of the first silver-sustained waveguides. This novel type of laser-induced refractive index change has been named Type A, after *Argentum*.
Besides the ability to induce always positive index contrast, the photoinduced silver clusters show other peculiar characteristics: the inscribed structures show small features overcoming the diffraction limit and the available silver reservoir allows for rewriting ability.

Based on these results, this work aimed at developing waveguides and optical components based on the laser-induced photochemistry of silver ions for photonics applications, such as the fabrication of optical integrated circuits.

For this reason, the effects of cumulative absorption of laser pulses on the induced refractive index change in the multiscan inscription of Type modifications are investigated to exploit the unusual athermal regime for achieving high refractive index contrast. Such a study allowed for demonstrating that high Type A refractive index change up to 2×10^{-2} can be achieved in silver-containing glasses. Moreover, the athermal inscription of Type A modifications allows for fine control of the pulse-to-pulse refractive index change by carefully tuning the DLW parameters,

which is not possible in the femtosecond inscription of Type 1 modifications in a high repetition rate regime due to the heat accumulation in the voxel of interaction. In particular, the absence of saturation effect for the case of multiscan structures inscribed with moderate laser irradiance may indicate that even higher refractive index change can be achieved by cumulating a significant number of pulses. In this regard, increasing the number of pulses with a MHz laser source would entail very long fabrication times, therefore the use of a laser with a higher repetition rate (100 MHz) represents an interesting perspective to be considered.
In addition, the high and controlled Type A refractive index change has been exploited in the fabrication of multiscan waveguides showing interesting characteristics.
Firstly, due to the direct relationship between the number of absorbed pulses and the magnitude of the refractive index change, it was possible to fabricate waveguides exhibiting singlemode or multimode operation at a given wavelength by tuning the number of laser scans. Moreover, the increase in the induced refractive index of the waveguides allowed for controlling the confinement of the guided mode. As a result, the waveguides showed reduced propagation losses when increasing the number of laser scans. Such a result is promising for the fabrication of bent waveguides with a small radius of curvature, which is a critical constraint for downsizing integrated optical circuits without increasing the losses.
Nevertheless, the multiscan technique together with the rewriting ability of the silver clusters enabled the fabrication of an engineered Type waveguide demonstrating the capability of reshaping the profile of the guided mode. This technique would be very important for optimizing the coupling between, for instance, the embedded waveguides and optical fibers and for reducing the losses.

The fabrication of structures showing a periodic modulation of the refractive index change, like Waveguides Bragg Gratings and Volume Bragg Gratings, allows for taking a step forward in the development of optical components. Indeed, Bragg gratings are essential devices in photonics, as well as for many other application fields, widely used in integrated optical circuits.
Taking advantage of the rewriting ability of the silver clusters and the possibility to inscribe features with dimensions below the diffraction limit, Waveguide Bragg Gratings with small periodicity have been inscribed targeting first-order Bragg resonances in the VIS-NIR spectral range.
The transmission spectra of the silver-sustained WBGs demonstrated high filtering efficiency for very short gratings, typically 500 μm long, resulting in remarkably high coupling coefficients,

about orders of magnitude higher than those reported in the literature. Moreover, the reflection spectra proved the mirroring behavior of the gratings, paving the way for more complex configurations, such as Fabry-Perot cavities. However, some instabilities in the writing process have proved to highly affect the efficiency of the WBGs. In this regard, some precautions in the writing procedure should be taken: for instance, instead of inscribing a long grating, it should be preferable to inscribe several smaller gratings to bypass the drifting of the absolute repositioning of the stages. Since the nature of some of the problematics causing fluctuations in the periodicity of the gratings is inherent to the modulated burst method, another interesting perspective would take into consideration the inscription of silver-sustained gratings by the phase mask method.

These argumentations are still valid for the case of silver-sustained Volume Bragg Gratings. The results of the multilayers gratings demonstrate the potentiality of the periodic silver-sustained structures to achieve high diffraction efficiency with relatively thin gratings, by just playing on the number of layers and the overlap between them. Alternatively to the phase mask method, the shaping of the laser beam into a Bessel beam may help improve the fabrication process since it would allow for inscribing thicker structures and for reducing the number of layers to stack.

Appendix A

Mask method for processing phase images

The procedure followed to process the phase images of the multiscan structures introduced in Chapter 2 is now presented for the case of a test phase image. The phase image of the multiscan structure inscribed in the AG01 sample with $N_{scans} = 10$, DLW speed $v = 50$ μm/s and laser intensity $I = 9$ TW/cm^2 has been used for the example.

The Sid4BIO software allows for quantifying the Optical Path Difference introduced by the femtosecond inscribed structures with respect to a reference area of the pristine glass. Therefore, the acquired phase image contains informations about both the inscribed structure and the background noise, deriving from the pristine glass.

The test phase image acquired with the Sid4BIO software using a 100× microscope objective with N.A. 1.3 (and index matching oil $n = 1.518$) is shown in Fig. A.1 on the left side, while the $3D$ plot of the phase image showing the OPD values recorded for each pixel of the phase images is reported in Fig. A.1 on the right side.
The relevant OPD values relative to the inscribed structures lay on the surface formed by the background noise, therefore is of crucial importance to correct the OPD values for the background noise when processing the phase images.
The method here proposed creates a *mask* from the original phase image by selecting an OPD

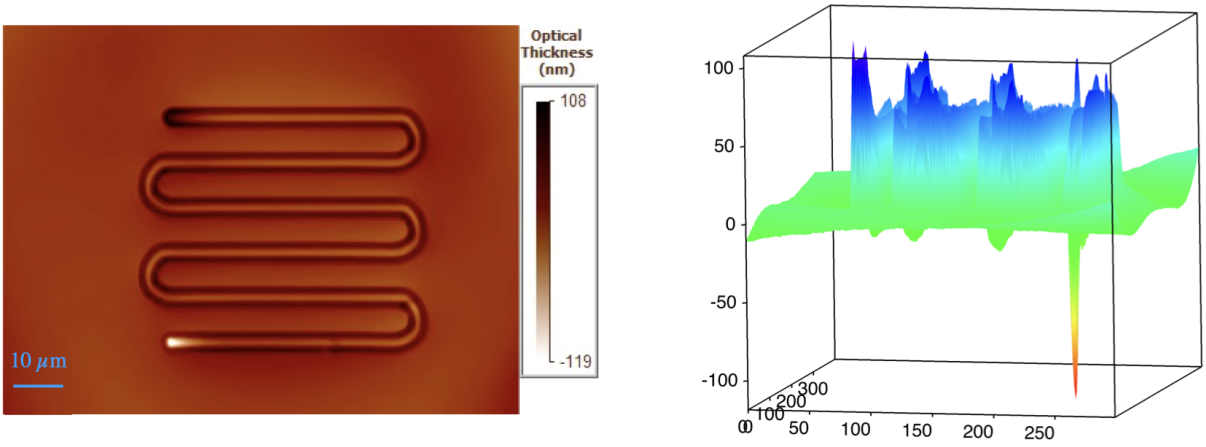

Figure A.1: Test phase image: on the left the phase image acquired with the Sid4Bio software, the structure is inscribed with $N_{scans} = 10$, DLW speed $v = 50$ μm/s and laser intensity $I = 9$ TW/cm^2 in the AG01 sample. On the right, a 3D plotting of the same phase image showing the background level, the positive *walls* of the silver-sustained structure and the intense negative spot at the starting point of the structure.

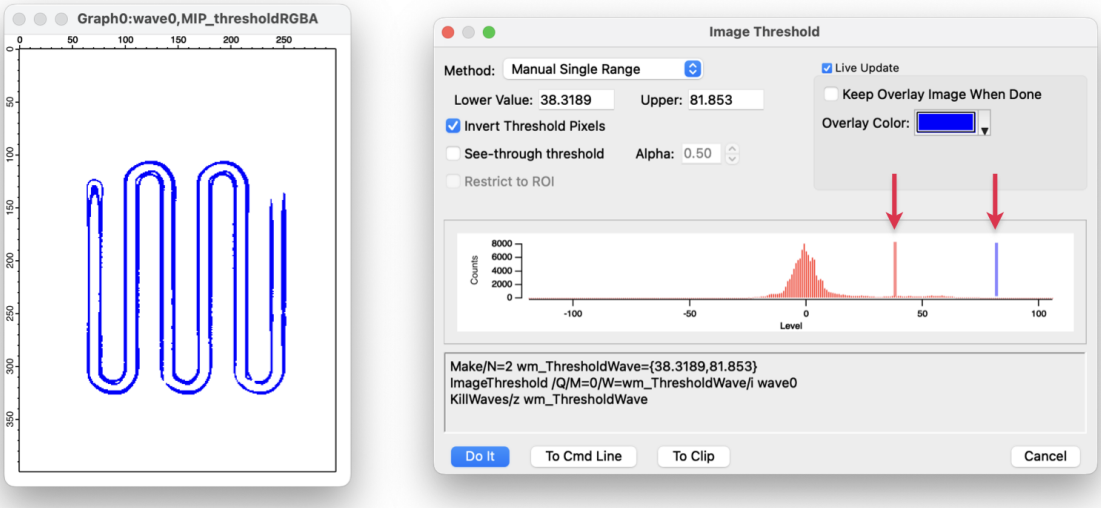

Figure A.2: Threshold manual selection: the threshold image on the left is obtained by manually tuning the range of OPD values outlining the double-track of the serpentine structure. On the right, two red arrows highlight the two sliders limiting the OPD range.

range in which only the pixels belonging to double-track structure of the inscribed serpentine are selected.
The manual setting of the OPD range, depicted in Fig. A.2 by a threshold selection, allows to safely exclude any defect or inhomogeneity of the pristine glass and DLW inscription.

The mask is then obtained from the threshold selection by assigning value 1 to all the pixels forming the serpentine structure and value 0 to all the remaining pixels, and by convolving the filter with a gaussian function to smooth the edges of the mask.
Thus a fitting process is launched for minimizing the distance between the original phase image and the mask multiplied by a coefficient a:

$$fit(Image, a) = Image - a * mask \tag{A.1}$$

where the coefficient $a > 0$ varies inside a range of reasonable OPD values. The fit function returns the standard deviation σ for each a coefficient in the OPD range: for test phase image, Fig. A.3 reports the extracted σ values.

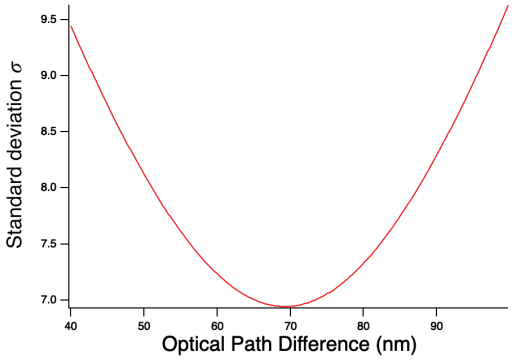

Figure A.3: Standard deviations σ extracted from the fit function for each a value of Optical Path Difference for the case of the test phase image.

The range of OPD values can be freely chosen in order to fine tune the a coefficient.
Finally, the true value of the averaged OPD associated to the inscribed structure is obtained by finding the minimum value among all the σ values: for the test phase image $OPD = 69$ nm.

Bibliography

[1] P.G. Debenedetti and L. Brewer. *Metastable Liquids: Concepts and Principles. Physical Chemistry: Science and Engineering.* Princeton University Press, 1996.

[2] H.-J. Hoffmann. Optical glasses. In *Reference Module in Materials Science and Materials Engineering*. Elsevier, 2017.

[3] Lena Bressel, Dominique de Ligny, Camille Sonneville, Valérie Martinez, Vygantas Mizeikis, Ričardas Buividas, and Saulius Juodkazis. Femtosecond laser induced density changes in geo2 and sio2 glasses: fictive temperature effect. *Opt. Mater. Express*, 1(4):605–613, Aug 2011.

[4] T.M. Gross and M. Tomozawa. Fictive temperature of geo_2 glass: Its determination by ir method and its effects on density and refractive index. *Journal of Non-Crystalline Solids*, 353(52):4762–4766, 2007.

[5] J. S. Sanghera, L. B. Shaw, L. E. Busse, V. Q. Nguyen, P. C. Pureza, B. C. Cole, B. B. Harrison, I. D. Aggarwal, R. Mossadegh, F. Kung, D. Talley, D. Roselle, and R. Miklos. Development and infrared applications of chalcogenide glass optical fibers. *Fiber and Integrated Optics*, 19(3):251–274, 2000.

[6] Lorraine F. Francis. Chapter 3 - melt processes. In Lorraine F. Francis, editor, *Materials Processing*, pages 105–249. Academic Press, Boston, 2016.

[7] Alain Abou Khalil. *Direct Laser Writing of a new type of optical waveguides and components in silver containing glasses.* PhD thesis, Université Laval & Université de Bordeaux, 2018.

[8] Grant R. Fowels. *Introduction to Modern Optics.* New York: Dover Publications, 1975.

[9] A. E. Siegman. *Lasers.* Mill Valley, Calif. : University Science Books, 1986.

[10] Malvin Carl Teich Bahaa E. A. Saleh. *Fundamental of Photonics*. John Wiley & Sons, Inc, 1991.

[11] Franz Kärtner, E. Ippen, Steven Cundiff, and Jun Ye. Femtosecond laser development. pages 54–77, 01 2005.

[12] W. Sibbett, A. A. Lagatsky, and C. T. A. Brown. The development and application of femtosecond laser systems. *Opt. Express*, 20(7):6989–7001, Mar 2012.

[13] Robert W. Boyd. *Nonlinear Optics*. Academic Press, Inc., USA, 3rd edition, 2008.

[14] Sinisa Vukelic, Panjawat Kongsuwan, and Y. Lawrence Yao. Ultrafast laser induced structural modification of fused silica. part i: Feature formation mechanisms. *Journal of Manufacturing Science and Engineering-transactions of The Asme*, 132:061012, 2010.

[15] Arnaud Royon, Yannick Petit, Gautier Papon, Martin Richardson, and Lionel Canioni. Femtosecond laser induced photochemistry in materials tailored with photosensitive agents. *Opt. Mater. Express*, 1(5):866–882, Sep 2011.

[16] Tommaso Baldacchini, Christopher N. LaFratta, Richard A. Farrer, Malvin C. Teich, Bahaa E. A. Saleh, Michael J. Naughton, and John T. Fourkas. Acrylic-based resin with favorable properties for three-dimensional two-photon polymerization. *Journal of Applied Physics*, 95(11):6072–6076, 2004.

[17] Rafael R. Gattass and Eric Mazur. Femtosecond laser micromachining in transparent materials. *Nature Photonics*, 2(4):219–225, 2008.

[18] P. Kazansky, A. Cerkauskaite, M. Beresna, R. Drevinskas, J. Zhang A. Patel, and M. Gecevicius. Eternal 5d data storage via ultrafast-laser writing in glass. *SPIE Newsroom*, 10 March 2016.

[19] S. Gross and M. J. Withford. Ultrafast-laser-inscribed 3d integrated photonics: challenges and emerging applications. *Nanophotonics*, 4(3):332–352, 2015.

[20] Koji Sugioka. Progress in ultrafast laser processing and future prospects. *Nanophotonics*, 6(2):393–413, 2017.

[21] Koji Igarashi, Daiki Souma, Takehiro Tsuritani, and Itsuro Morita. Performance evaluation of selective mode conversion based on phase plates for a 10-mode fiber. *Opt. Express*, 22(17):20881–20893, Aug 2014.

[22] Lionel Nicole, Christel Laberty-Robert, Laurence Rozes, and Cément Sanchez. Hybrid materials science: a promised land for the integrative design of multifunctional materials. *Nanoscale*, 6:6267–6292, 2014.

[23] R. Osellame, G. Cerullo, and R. Ramponi. *Femtosecond Laser Micromachining: Photonic and Microfluidic Devices in Transparent Materials*. Topics in Applied Physics. Springer Berlin Heidelberg, 2012.

[24] M. Lancry, B. Poumellec, A. Chahid-Erraji, M. Beresna, and P. G. Kazansky. Dependence of the femtosecond laser refractive index change thresholds on the chemical composition of doped-silica glasses. *Opt. Mater. Express*, 1(4):711–723, Aug 2011.

[25] Alexander M. Streltsov and Nicholas F. Borrelli. Study of femtosecond-laser-written waveguides in glasses. *J. Opt. Soc. Am. B*, 19(10):2496–2504, Oct 2002.

[26] Shane M. Eaton, Haibin Zhang, Peter R. Herman, Fumiyo Yoshino, Lawrence Shah, James Bovatsek, and Alan Y. Arai. Heat accumulation effects in femtosecond laser-written waveguides with variable repetition rate. *Opt. Express*, 13(12):4708–4716, Jun 2005.

[27] Sören Richter, Matthias Heinrich, Felix Zimmermann, Christian Vetter, Andreas Tünnermann, and Stefan Nolte. *Progress in Nonlinear Nano-Optics - Nanogratings in Fused Silica: Structure, Formation and Applications*, pages 49–71. Springer International Publishing, Cham, 2015.

[28] S. Richter, M. Heinrich, S. Döring, A. Tünnermann, and S. Nolte. Formation of femtosecond laser-induced nanogratings at high repetition rates. *Applied Physics A*, 104:503–507, Dec 2011.

[29] Shane M. Eaton, Haibin Zhang, Mi Li Ng, Jianzhao Li, Wei-Jen Chen, Stephen Ho, and Peter R. Herman. Transition from thermal diffusion to heat accumulation in high repetition rate femtosecond laser writing of buried optical waveguides. *Opt. Express*, 16(13):9443–9458, Jun 2008.

[30] D. G. Lancaster, S. Gross, A. Fuerbach, H. Ebendorff Heidepriem, T. M. Monro, and M. J. Withford. Versatile large-mode-area femtosecond laser-written tm:zblan glass chip lasers. *Opt. Express*, 20(25):27503–27509, Dec 2012.

[31] Dezhi Tan, Zhuo Wang, Beibei Xu, and Jianrong Qiu. Photonic circuits written by femtosecond laser in glass: improved fabrication and recent progress in photonic devices. *Advanced Photonics*, 3(2):1 – 24, 2021.

[32] T. A. Birks, I. Gris-Sánchez, S. Yerolatsitis, S. G. Leon-Saval, and R. R. Thomson. The photonic lantern. *Adv. Opt. Photon.*, 7(2):107–167, Jun 2015.

[33] Jun He, Baijie Xu, Xizhen Xu, Changrui Liao, and Yiping Wang. Review of femtosecond-laser-inscribed fiber bragg gratings: Fabrication technologies and sensing applications. *Photonic Sensors*, 11(2):203–226, 2021.

[34] V. Mizrahi P.J. Lemaire, R.M. Atkins and W.A. Reed. High pressure h_2 loading as a technique for achieving ultrahigh uv photosensitivity and thermal sensitivity in geo_2 doped optical fibres. *Electronics Letters*, 29:1191–1193(2), June 1993.

[35] Maxime Royon, Emmanuel Marin, Sylvain Girard, Aziz Boukenter, Youcef Ouerdane, and Razvan Stoian. X-ray preconditioning for enhancing refractive index contrast in femtosecond laser photoinscription of embedded waveguides in pure silica. *Opt. Mater. Express*, 9(1):65–74, Jan 2019.

[36] Alexander Arriola, Simon Gross, Nemanja Jovanovic, Ned Charles, Peter G. Tuthill, Santiago M. Olaizola, Alexander Fuerbach, and Michael J. Withford. Low bend loss waveguides enable compact, efficient 3d photonic chips. *Opt. Express*, 21(3):2978–2986, Feb 2013.

[37] Jerome Lapointe, Jean-Philippe Bérubé, Samuel Pouliot, and Réal Vallée. Control and enhancement of photo-induced refractive index modifications in fused silica. *OSA Continuum*, 3(10):2851–2862, Oct 2020.

[38] R. Graf, A. Fernandez, Mykhaylo Dubov, H.J. Brueckner, B.N. Chichkov, and A. Apolonski. Pearl-chain waveguides written at megahertz repetition rate. *Applied Physics B*, 87(1):21–27, March 2007.

[39] Javier Martínez, Airán Ródenas, Toney Fernandez, Javier R. Vázquez de Aldana, Robert R. Thomson, Magdalena Aguiló, Ajoy K. Kar, Javier Solis, and Francesc Díaz. 3d laser-written silica glass step-index high-contrast waveguides for the 3.5μm mid-infrared range. *Opt. Lett.*, 40(24):5818–5821, Dec 2015.

[40] Luke B. Fletcher, Jonathan J. Witcher, Neil Troy, Signo T. Reis, Richard K. Brow, Rebeca Martinez Vazquez, Roberto Osellame, and Denise M. Krol. Femtosecond laser writing of waveguides in zinc phosphate glasses. *Opt. Mater. Express*, 1(5):845–855, Sep 2011.

[41] Théo Guérineau. *Synthèse et caractérisation de verres pour l'impression 3D par laser: verres phosphates et d'oxydes lourds á l'argent.* PhD thesis, Université de Bordeaux, 2020.

[42] Yannick Petit, Sylvain Danto, Théo Guérineau, Alain Abou Khalil, Arthur Le Camus, Evelyne Fargin, Guillaume Duchateau, Jean-Philippe Bérubé, Réal Vallée, Younès Messaddeq, Thierry Cardinal, and Lionel Canioni. On the femtosecond laser-induced photochemistry in silver-containing oxide glasses: mechanisms, related optical and physico-chemical properties, and technological applications. *Advanced Optical Technologies*, 7(5):291–309, 2018.

[43] Evgeniya Smetanina, Benoit Chimier, Yannick Petit, Nadezda Varkentina, Evelyne Fargin, Lionel Hirsch, Thierry Cardinal, Lionel Canioni, and Guillaume Duchateau. Modeling of cluster organization in metal-doped oxide glasses irradiated by a train of femtosecond laser pulses. *Phys. Rev. A*, 93:013846, Jan 2016.

[44] Kevin Bourhis, Arnaud Royon, Matthieu Bellec, Jiyeon Choi, Alexandre Fargues, Mona Treguer, Jean-Jacques Videau, David Talaga, Martin Richardson, Thierry Cardinal, and Lionel Canioni. Femtosecond laser structuring and optical properties of a silver and zinc phosphate glass. *Journal of Non-Crystalline Solids*, 356(44):2658–2665, 2010. 12th International Conference on the Physics of Non-Crystalline Solids (PNCS 12).

[45] Matthieu Bellec, Arnaud Royon, Bruno Bousquet, Kevin Bourhis, Mona Treguer, Thierry Cardinal, Martin Richardson, and Lionel Canioni. Beat the diffraction limit in 3d direct laser writing in photosensitive glass. *Opt. Express*, 17(12):10304–10318, Jun 2009.

[46] Matthieu Bellec, Arnaud Royon, Kevin Bourhis, Jiyeon Choi, Bruno Bousquet, Mona Treguer, Thierry Cardinal, Jean-Jacques Videau, Martin Richardson, and Lionel Canioni. 3d patterning at the nanoscale of fluorescent emitters in glass. *The Journal of Physical Chemistry C*, 114(37):15584–15588, Sep 2010.

[47] A. Abou Khalil, J.P. Bérubé, S. Danto, J.C. Desmoulin, T. Cardinal, Y. Petit, R. Vallée, and L. Canioni. Direct laser writing of a new type of waveguides in silver containing glasses. *Scientific Reports*, 7:2045–2322, Oct 2017.

[48] Raman Kashyap. Chapter 3 - fabrication of bragg gratings. In Raman Kashyap, editor, *Fiber Bragg Gratings (Second Edition)*, pages 53–118. Academic Press, Boston, second edition edition, 2010.

[49] Stephen J. Mihailov. 6 - femtosecond laser-inscribed fiber bragg gratings for sensing applications. In Hamid Alemohammad, editor, *Opto-Mechanical Fiber Optic Sensors*, pages 137–174. Butterworth-Heinemann, 2018.

[50] Graham D. Marshall, Martin Ams, and Michael J. Withford. Direct laser written waveguide-bragg gratings in bulk fused silica. *Opt. Lett.*, 31(18):2690–2691, Sep 2006.

[51] Haibin Zhang, Shane M. Eaton, and Peter R. Herman. Single-step writing of bragg grating waveguides in fused silica with an externally modulated femtosecond fiber laser. *Opt. Lett.*, 32(17):2559–2561, Sep 2007.

[52] Matthieu Bellec. *Nanostructuration par laser femtoseconde dans un verre photoluminescent*. PhD thesis, Université de Bordeaux 1, 2009.

[53] Ivan Divliansky. Volume bragg gratings: Fundamentals and applications in laser beam combining and beam phase transformations. In Izabela Naydenova, Dimana Nazarova, and Tsvetanka Babeva, editors, *Holographic Materials and Optical Systems*, chapter 3. IntechOpen, Rijeka, 2017.

[54] Herwig Kogelnik. Coupled wave theory for thick hologram gratings. *Bell System Technical Journal*, 48(9):2909–2947, 1969.

[55] I. Fanderlik. *Optical Properties of Glass*. Number v. 5 in Developments in Food Science. Elsevier, 1983.

[56] Rei Kitamura, Laurent Pilon, and Miroslaw Jonasz. Optical constants of silica glass from extreme ultraviolet to far infrared at near room temperature. *Appl. Opt.*, 46(33):8118–8133, Nov 2007.

[57] Koichi Kajihara. Improvement of vacuum-ultraviolet transparency of silica glass by modification of point defects. *Journal of the Ceramic Society of Japan*, 115(1338):85–91, 2007.

[58] Andrei M. Efimov and Vera G. Pogareva. Ir absorption spectra of vitreous silica and silicate glasses: The nature of bands in the 1300 to 5000 cm^{-1} region. *Chemical Geology*, 229:198–217, 2006.

[59] Lasers and laser-related equipment - test methods for laser beam widths, divergence angles and beam propagation ratios - part 2: General astigmatic beams. Standard, International Organization for Standardization, 2005.

[60] Jeff Squier and Michiel Müller. High resolution nonlinear microscopy: A review of sources and methods for achieving optimal imaging. *Review of Scientific Instruments*, 72(7):2855–2867, 2001.

[61] A. J. DeMaria, D. A. Stetser, and H. Heynau. Self mode-locking of lasers with saturable absorbers. *Applied Physics Letters*, 8(7):174–176, 1966.

[62] C. V. Shank and I. E. Ippen. Subpicosecond kilowatt pulses from a modelocked cw dye laser. *Applied Physics Letters*, 24(373), 1974.

[63] J. A. Valdmanis, R. L. Fork, and J. P. Gordon. Generation of optical pulses as short as 27 femtoseconds directly from a laser balancing self-phase modulation, group-velocity dispersion, saturable absorption, and saturable gain. *Opt. Lett.*, 10(3):131–133, Mar 1985.

[64] R. L. Fork, C. H. Brito Cruz, P. C. Becker, and C. V. Shank. Compression of optical pulses to six femtoseconds by using cubic phase compensation. *Opt. Lett.*, 12(7):483–485, Jul 1987.

[65] D. E. Spence, P. N. Kean, and W. Sibbett. 60-fsec pulse generation from a self-mode-locked ti:sapphire laser. *Opt. Lett.*, 16(1):42–44, Jan 1991.

[66] D.H. Sutter, I.D. Jung, F.X. Kartner, N. Matuschek, F. Morier-Genoud, V. Scheuer, M. Tilsch, T. Tschudi, and U. Keller. Self-starting 6.5-fs pulses from a ti:sapphire laser using a semiconductor saturable absorber and double chirped mirrors. *IEEE Journal of Selected Topics in Quantum Electronics*, 4(2):169–178, 1998.

[67] J. Aus der Au, D. Kopf, F. Morier-Genoud, M. Moser, and U. Keller. 60-fs pulses from a diode-pumped nd:glass laser. *Opt. Lett.*, 22(5):307–309, Mar 1997.

[68] C. Hönninger, F. Morier-Genoud, M. Moser, U. Keller, L. R. Brovelli, and C. Harder. Efficient and tunable diode-pumped femtosecond yb:glass lasers. *Opt. Lett.*, 23(2):126–128, Jan 1998.

[69] Simon Rivier, Xavier Mateos, Junhai Liu, Valentin Petrov, Uwe Griebner, Martin Zorn, Markus Weyers, Huaijin Zhang, Jiyang Wang, and Minhua Jiang. Passively mode-locked yb:luvo$_4$ oscillator. *Opt. Express*, 14(24):11668–11671, Nov 2006.

[70] H. Liu, J. Nees, and G. Mourou. Diode-pumped kerr-lens mode-locked yb:ky(wo4)2 laser. *Opt. Lett.*, 26(21):1723–1725, Nov 2001.

[71] Akira Yoshida, Andreas Schmidt, Valentin Petrov, Christian Fiebig, Götz Erbert, Junhai Liu, Huaijin Zhang, Jiyang Wang, and Uwe Griebner. Diode-pumped mode-locked yb:ycob laser generating 35 fs pulses. *Opt. Lett.*, 36(22):4425–4427, Nov 2011.

[72] Y. J. Chai, C. G. Leburn, A. A. Lagatsky, C. T. A. Brown, R. V. Penty, I. H. White, and W. Sibbett. 1.36-tb/s spectral slicing source based on a cr4+-yag femtosecond laser. *J. Lightwave Technol.*, 23(3):1319, Mar 2005.

[73] E. Sorokin, S. Naumov, and I.T. Sorokina. Ultrabroadband infrared solid-state lasers. *IEEE Journal of Selected Topics in Quantum Electronics*, 11(3):690–712, 2005.

[74] Simon Lefrançois, Khanh Kieu, Yujun Deng, James D. Kafka, and Frank W. Wise. Scaling of dissipative soliton fiber lasers to megawatt peak powers by use of large-area photonic crystal fiber. *Opt. Lett.*, 35(10):1569–1571, May 2010.

[75] Guoqing Chang and Zhiyi Wei. Ultrafast fiber lasers: An expanding versatile toolbox. *iScience*, 23(5):101101, 2020.

[76] L V Keldysh. Ionization in the field of a strong electromagnetic wave. *Zh. Eksperim. i Teor. Fiz.*, 47, 11 1964.

[77] Merrick J. DeWitt and Robert J. Levis. Calculating the keldysh adiabaticity parameter for atomic, diatomic, and polyatomic molecules. *The Journal of Chemical Physics*, 108(18):7739–7742, 1998.

[78] Tang Zhilie, Yang Chuping, Pei Hongjin, Liang Ruisheng, and Liu Songhao. Imaging theory and resolution improvement of two-photon confocal microscopy. *Science in China Series A: Mathematics*, 45(11):1468–1478, 2002.

[79] Warren R Zipfel, Rebecca M Williams, and Watt W Webb. Nonlinear magic: multiphoton microscopy in the biosciences. *Nature Biotechnology*, 21(11):1369–1377, 2003.

[80] B. Poumellec, M. Lancry, A. Chahid-Erraji, and P. G. Kazansky. Modification thresholds in femtosecond laser processing of pure silica: review of dependencies on laser parameters. *Opt. Mater. Express*, 1(4):766–782, Aug 2011.

[81] Sören Richter, Fei Jia, Matthias Heinrich, Sven Döring, Ulf Peschel, Andreas Tünnermann, and Stefan Nolte. The role of self-trapped excitons and defects in the formation of nanogratings in fused silica. *Opt. Lett.*, 37(4):482–484, Feb 2012.

[82] S. S. Mao, F. Quéré, S. Guizard, X. Mao, R. E. Russo, G. Petite, and P. Martin. Dynamics of femtosecond laser interactions with dielectrics. *Applied Physics A*, 79(7):1695–1709, 2004.

[83] Mark MacKenzie, Haonan Chi, Manoj Varma, Parama Pal, Ajoy Kar, and Lynn Paterson. Femtosecond laser fabrication of silver nanostructures on glass for surface enhanced raman spectroscopy. *Scientific Reports*, 9(1):17058, 2019.

[84] Huijun Wang, Yuhao Lei, Lei Wang, Masaaki Sakakura, Yanhao Yu, Gholamreza Shayeganrad, and Peter G. Kazansky. 100-layer error-free 5d optical data storage by ultrafast laser nanostructuring in glass. *Laser & Photonics Reviews*, 16(4):2100563.

[85] Feng Chen and J. R. Vázquez de Aldana. Optical waveguides in crystalline dielectric materials produced by femtosecond-laser micromachining. *Laser & Photonics Reviews*, 8(2):251–275, 2014.

[86] Mangirdas Malinauskas, Albertas Žukauskas, Satoshi Hasegawa, Yoshio Hayasaki, Vygantas Mizeikis, Ričardas Buividas, and Saulius Juodkazis. Ultrafast laser processing of materials: from science to industry. *Light: Science & Applications*, 5(8):e16133–e16133, 2016.

[87] K Hirao and K Miura. Writing waveguides and gratings in silica and related materials by a femtosecond laser. *Journal of Non-Crystalline Solids*, 239(1):91–95, 1998.

[88] J. W. Chan, T. Huser, S. Risbud, and D. M. Krol. Structural changes in fused silica after exposure to focused femtosecond laser pulses. *Opt. Lett.*, 26(21):1726–1728, Nov 2001.

[89] Hong-Bo Sun, Ying Xu, Saulius Juodkazis, Kai Sun, Mitsuru Watanabe, Shigeki Matsuo, Hiroaki Misawa, and Junji Nishii. Arbitrary-lattice photonic crystals created by multiphoton microfabrication. *Opt. Lett.*, 26(6):325–327, Mar 2001.

[90] M. J. Ventura, M. Straub, and M. Gu. Void channel microstructures in resin solids as an efficient way to infrared photonic crystals. *Applied Physics Letters*, 82(11):1649–1651, 2003.

[91] Guangyong Zhou, Michael James Ventura, Min Gu, Aaron F. Mattews, and Yuri S. Kivshar. Photonic bandgap properties of void-based body-centered-cubic photonic crystals in polymer. *Opt. Express*, 13(12):4390–4395, Jun 2005.

[92] C. B. Schaffer, J. F. Garcia, and E. Mazur. Bulk heating of transparent materials using a high repetition-rate femtosecond laser. *Appl. Phys. A*, 76:351–354, 2003.

[93] S. Nolte, M. Will, J. Burghoff, and A. Tuennermann. Femtosecond waveguide writing: a new avenue to three-dimensional integrated optics. *Applied Physics A*, 77(1):109–111, 2003.

[94] R. Osellame, S. Taccheo, M.Marangoni, R. Ramponi, P. Laporta, D. Polli, S. De Silvestri, and G. Cerullo. Femtosecond writing of active optical waveguides with astigmatically shaped beams. *J. Opt. Soc. Am. B*, 20(7):1559–1567, Jul. 2003.

[95] R. Osellame, N. Chiodo, V. Maselli, A. Yin, M. Zavelani-Rossi, G. Cerullo, P. Laporta, L. Aiello, S. De Nicola, P. Ferraro, A. Finizio, and G. Pierattini. Optical properties of waveguides written by a 26 mhz stretched cavity ti:sapphire femtosecond oscillator. *Opt. Express*, 13(2):612–620, Jan. 2005.

[96] Lawrence Shah, Alan Y. Arai, Shane M. Eaton, and Peter R. Herman. Writing waveguides in glass with a femtosecond laser. *Opt. Express*, 13(6):1999–2006, Mar. 2005.

[97] Shingo Kanehira, Kiyotaka Miura, and Kazuyuki Hirao. Ion exchange in glass using femtosecond laser irradiation. *Applied Physics Letters*, 93(2):023112, 2008.

[98] Yasuhiko Shimotsuma, Peter G. Kazansky, Jiarong Qiu, and Kazuoki Hirao. Self-organized nanogratings in glass irradiated by ultrashort light pulses. *Phys. Rev. Lett.*, 91:247405, Dec 2003.

[99] Peter G. Kazansky and Yasuhiko Shimotsuma. Self-assembled sub-wavelength structures and form birefringence created by femtosecond laser writing in glass: properties and applications. *Journal of the Ceramic Society of Japan*, 116(1358):1052–1062, 2008.

[100] Sören Richter, Matthias Heinrich, Sven Döring, Andreas Tünnermann, Stefan Nolte, and Ulf Peschel. Nanogratings in fused silica: Formation, control, and applications. *Journal of Laser Applications*, 24(4):042008, 2012.

[101] Jing Tian, Heng Yao, Maxime Cavillon, Enric Garcia-Caurel, Razvigor Ossikovski, Michel Stchakovsky, Celine Eypert, Bertrand Poumellec, and Matthieu Lancry. A comparison between nanogratings-based and stress-engineered waveplates written by femtosecond laser in silica. *Micromachines*, 11(2), 2020.

[102] Kim Lammers, Max Ehrhardt, Teodor Malendevych, Xiaoyu Xu, Christian Vetter, Alessandro Alberucci, Alexander Szameit, and Stefan Nolte. Embedded nanograting-based waveplates for polarization control in integrated photonic circuits. *Opt. Mater. Express*, 9(6):2560–2572, Jun 2019.

[103] Andrius Marcinkevičius, Saulius Juodkazis, Mitsuru Watanabe, Masafumi Miwa, Shigeki Matsuo, Hiroaki Misawa, and Junji Nishii. Femtosecond laser-assisted three-dimensional microfabrication in silica. *Opt. Lett.*, 26(5):277–279, Mar 2001.

[104] C. Hnatovsky, R. S. Taylor, E. Simova, V. R. Bhardwaj, D. M. Rayner, and P. B. Corkum. Polarization-selective etching in femtosecond laser-assisted microfluidic channel fabrication in fused silica. *Opt. Lett.*, 30(14):1867–1869, Jul 2005.

[105] C. Hnatovsky, R. S. Taylor, E. Simova, P. P. Rajeev, D. M. Rayner, V. R. Bhardwaj, and P. B. Corkum. Fabrication of microchannels in glass using focused femtosecond laser radiation and selective chemical etching. *Applied Physics A*, 84(1):47–61, 2006.

[106] Valeria Maselli, Roberto Osellame, Giulio Cerullo, Roberta Ramponi, Paolo Laporta, Luca Magagnin, and Pietro Luigi Cavallotti. Fabrication of long microchannels with circular cross section using astigmatically shaped femtosecond laser pulses and chemical etching. *Applied Physics Letters*, 88(19):191107, 2006.

[107] K. M. Davis, K. Miura, N. Sugimoto, and K. Hirao. Writing waveguides in glass with a femtosecond laser. *Opt. Lett.*, 21(21):1729–1731, Nov. 1996.

[108] Jean-Philippe Bérubé, Arthur Le Camus, Sandra Helena Messaddeq, Yannick Petit, Younès Messaddeq, Lionel Canioni, and Réal Vallée. Femtosecond laser direct inscription of mid-ir transmitting waveguides in bgg glasses. *Opt. Mater. Express*, 7(9):3124–3135, Sep 2017.

[109] Takeshi Fukuda, Shimon Ishikawa, Tomoko Fujii, Ken Sakuma, and Hideyuki Hosoya. Low-loss optical waveguides written by femtosecond laser pulses for three-dimensional photonic devices. In *Photon Processing in Microelectronics and Photonics III*, volume 5339, pages 524 – 538. International Society for Optics and Photonics, SPIE, 2004.

[110] Yusuke Nasu, Masaki Kohtoku, and Yoshinori Hibino. Low-loss waveguides written with a femtosecond laser for flexible interconnection in a planar light-wave circuit. *Opt. Lett.*, 30(7):723–725, Apr 2005.

[111] George Y Chen, Fiorina Piantedosi, Dale Otten, Yvonne Qiongyue Kang, Wen Qi Zhang, Xiaohong Zhou, Tanya M Monro, and David G Lancaster. Femtosecond-laser-written microstructured waveguides in bk7 glass. *Sci Rep*, 8(1):10377, Jul 2018.

[112] Ci-Yu Wang, Jun Gao, and Xian-Min Jin. On-chip rotated polarization directional coupler fabricated by femtosecond laser direct writing. *Opt. Lett.*, 44(1):102–105, Jan 2019.

[113] René Heilmann, Markus Gräfe, Stefan Nolte, and Alexander Szameit. Arbitrary photonic wave plate operations on chip: Realizing hadamard, pauli-x and rotation gates for polarisation qubits. *Scientific Reports*, 4(1):4118, Jan 2014.

[114] Simon Gross, Nicolas Riesen, John D. Love, and Michael J. Withford. Three-dimensional ultra-broadband integrated tapered mode multiplexers. *Laser & Photonics Reviews*, 8(5):L81–L85, 2014.

[115] Giacomo Corrielli, Simone Atzeni, Simone Piacentini, Ioannis Pitsios, Andrea Crespi, and Roberto Osellame. Symmetric polarization-insensitive directional couplers fabricated by femtosecond laser writing. *Opt. Express*, 26(12):15101–15109, Jun 2018.

[116] Nicolas Riesen, Simon Gross, John D. Love, and Michael J. Withford. Femtosecond direct-written integrated mode couplers. *Opt. Express*, 22(24):29855–29861, Dec 2014.

[117] Luís A. Fernandes, Jason R. Grenier, Peter R. Herman, J. Stewart Aitchison, and Paulo V. S. Marques. Femtosecond laser fabrication of birefringent directional couplers as polarization beam splitters in fused silica. *Opt. Express*, 19(13):11992–11999, Jun 2011.

[118] R. R. Thomson, T. A. Birks, S. G. Leon-Saval, A. K. Kar, and J. Bland-Hawthorn. Ultrafast laser inscription of an integrated photonic lantern. *Opt. Express*, 19(6):5698–5705, Mar 2011.

[119] G. Douglass, F. Dreisow, S. Gross, and M. J. Withford. Femtosecond laser written arrayed waveguide gratings with integrated photonic lanterns. *Opt. Express*, 26(2):1497–1505, Jan 2018.

[120] Barnaby R M Norris, Nick Cvetojevic, Tiphaine Lagadec, Nemanja Jovanovic, Simon Gross, Alexander Arriola, Thomas Gretzinger, Marc-Antoine Martinod, Olivier Guyon, Julien Lozi, Michael J Withford, Jon S Lawrence, and Peter Tuthill. First on-sky demonstration of an integrated-photonic nulling interferometer: the GLINT instrument. *Monthly Notices of the Royal Astronomical Society*, 491(3):4180–4193, 11 2019.

[121] Stephen C. Warren-Smith, Linh Viet Nguyen, Catherine Lang, Heike Ebendorff-Heidepriem, and Tanya M. Monro. Temperature sensing up to 1300°c using suspended-core microstructured optical fibers. *Opt. Express*, 24(4):3714–3719, Feb 2016.

[122] Jun He, Yiping Wang, Changrui Liao, Chao Wang, Shen Liu, Kaiming Yang, Ying Wang, Xiaocong Yuan, Guo Ping Wang, and Wenjing Zhang. Negative-index gratings formed by femtosecond laser overexposure and thermal regeneration. *Scientific Reports*, 6(1):23379, 2016.

[123] E. A. J. Marcatili. Bends in optical dielectric guides. *The Bell System Technical Journal*, 48(7):2103–2132, 1969.

[124] T. Erdogan R.M. Atkins, P.J. Lemaire and V. Mizrahi. Mechanisms of enhanced uv photosensitivity via hydrogen loading in germanosilicate glasses. *Electronics Letters*, 29:1234–1235(1), July 1993.

[125] M. Lancry, P. Niay, and M. Douay. Comparing the properties of various sensitization methods in h2-loaded, uv hypersensitized or oh-flooded standard germanosilicate fibers. *Opt. Express*, 13(11):4037–4043, May 2005.

[126] P. P. Rajeev, M. Gertsvolf, E. Simova, C. Hnatovsky, R. S. Taylor, V. R. Bhardwaj, D. M. Rayner, and P. B. Corkum. Memory in nonlinear ionization of transparent solids. *Phys. Rev. Lett.*, 97:253001, Dec 2006.

[127] Jiaren Liu, Zhiyi Zhang, C. Flueraru, Xingping Liu, Shoude Chang, and C.P. Grover. Waveguide shaping and writing in fused silica using a femtosecond laser. *IEEE Journal of Selected Topics in Quantum Electronics*, 10(1):169–173, 2004.

[128] E. Metwalli, M. Karabulut, D.L. Sidebottom, M.M. Morsi, and R.K. Brow. Properties and structure of copper ultraphosphate glasses. *Journal of Non-Crystalline Solids*, 344(3):128–134, 2004.

[129] G.D. Khattak, E.E. Khawaja, L.E. Wenger, David J. Thompson, M.A. Salim, A.B. Hallak, and M.A. Daous. Composition-dependent loss of phosphorus in the formation of transition-metal phosphate glasses. *Journal of Non-Crystalline Solids*, 194(1):1–12, 1996.

[130] Théo Guérineau, Laura Loi, Yannick Petit, Sylvain Danto, Alexandre Fargues, Lionel Canioni, and Thierry Cardinal. Structural influence on the femtosecond laser ability to create fluorescent patterns in silver-containing sodium-gallium phosphate glasses. *Opt. Mater. Express*, 8(12):3748–3760, Dec 2018.

[131] N. Marquestaut, Y. Petit, A. Royon, P. Mounaix, T. Cardinal, and L. Canioni. Three-dimensional silver nanoparticle formation using femtosecond laser irradiation in phosphate glasses: Analogy with photography. *Advanced Functional Materials*, 24(37):5824–5832, 2014.

[132] Pierre Bon, Guillaume Maucort, Benoit Wattellier, and Serge Monneret. Quadriwave lateral shearing interferometry for quantitative phase microscopy of living cells. *Opt. Express*, 17(15):13080–13094, Jul 2009.

[133] Alain Abou Khalil, Wendwesen Gebremichael, Yannick Petit, and Lionel Canioni. Refractive index change measurement by quantitative microscopy phase imaging for femtosecond laser written structures. *Optics Communications*, 485:126731, 2021.

[134] Alain Abou Khalil, Philippe Lalanne, Jean-Philippe Bérubé, Yannick Petit, Réal Vallée, and Lionel Canioni. Femtosecond laser writing of near-surface waveguides for refractive-index sensing. *Opt. Express*, 27(22):31130–31143, Oct 2019.

[135] Alain Abou Khalil, Jean-Philippe Bérubé, Sylvain Danto, Thierry Cardinal, Yannick Petit, Lionel Canioni, and Réal Vallée. Comparative study between the standard type i and the type a femtosecond laser induced refractive index change in silver containing glasses. *Opt. Mater. Express*, 9(6):2640–2651, Jun 2019.

[136] Jean-Charles Desmoulin, Yannick Petit, Lionel Canioni, Marc Dussauze, Michel Lahaye, Hernando Magallanes Gonzalez, Etienne Brasselet, and Thierry Cardinal. Femtosecond

laser structuring of silver-containing glass: Silver redistribution, selective etching, and surface topology engineering. *Journal of Applied Physics*, 118(21):213104, 2015.

[137] R. E. Wagner and W. J. Tomlinson. Coupling efficiency of optics in single-mode fiber components. *Appl. Opt.*, 21(15):2671–2688, Aug 1982.

[138] K. O. Hill, Y. Fujii, D. C. Johnson, and B. S. Kawasaki. Photosensitivity in optical fiber waveguides: Application to reflection filter fabrication. *Applied Physics Letters*, 32(10):647–649, 1978.

[139] Binfeng Yun, Guohua Hu, Ruohu Zhang, and Yiping Cui. Fabrication of a third-order polymer chirped waveguide bragg grating with tapered core size by contact lithography. *Appl. Opt.*, 54(3):467–471, Jan 2015.

[140] Weifeng Zhang and Jianping Yao. A fully reconfigurable waveguide bragg grating for programmable photonic signal processing. *Nature Communications*, 9(1):1396, 2018.

[141] G. Meltz, W. W. Morey, and W. H. Glenn. Formation of bragg gratings in optical fibers by a transverse holographic method. *Opt. Lett.*, 14(15):823–825, Aug 1989.

[142] K. O. Hill, B. Malo, F. Bilodeau, D. C. Johnson, and J. Albert. Bragg gratings fabricated in monomode photosensitive optical fiber by uv exposure through a phase mask. *Applied Physics Letters*, 62(10):1035–1037, 1993.

[143] Dana Z. Anderson, Victor Mizrahi, Turan Erdogan, and Alice E. White. Phase-mask method for volume manufacturing of fiber phase gratings. In *Conference on Optical Fiber Communication/International Conference on Integrated Optics and Optical Fiber Communication*, page PD16. Optica Publishing Group, 1993.

[144] A V Dostovalov, A A Wolf, and S A Babin. Long-period fibre grating writing with a slit-apertured femtosecond laser beam. *Quantum Electronics*, 45(3):235–239, mar 2015.

[145] Dmitrii V. Przhiialkovskii and Oleg V. Butov. High-precision point-by-point fiber bragg grating inscription. *Results in Physics*, 30:104902, 2021.

[146] K.C. Byron, K. Sugden, T. Bricheno, and I. Bennion. Fabrication of chirped bragg gratings in photosensitive fibre. *Electronics letters*, 29(18):1659–1660, 1993.

[147] Y. Wang, J. Grant, A. Sharma, and G. Myers. Modified talbot interferometer for fabrication of fiber-optic grating filter over a wide range of bragg wavelength and bandwidth using a single phase mask. *Journal of Lightwave Technology*, 19(10):1569–1573, 2001.

[148] Martin Becker, Joachim Bergmann, Sven Brückner, Marco Franke, Eric Lindner, Manfred W. Rothhardt, and Hartmut Bartelt. Fiber bragg grating inscription combining duv sub-picosecond laser pulses and two-beam interferometry. *Opt. Express*, 16(23):19169–19178, Nov 2008.

[149] Oscar Eduardo Martinez. Pulse distortions in tilted pulse schemes for ultrashort pulses. *Optics Communications*, 59(3):229–232, 1986.

[150] Zsolt Bor, Bela Racz, Gabor Szabo, Margit Hilbert, and H. A. Hazim. Femtosecond pulse front tilt caused by angular dispersion. *Optical Engineering*, 32(10):2501 – 2504, 1993.

[151] Nurmemet Abdukerim, Dan Grobnic, Rune Lausten, Cyril Hnatovsky, and Stephen J. Mihailov. Complex diffraction and dispersion effects in femtosecond laser writing of fiber bragg gratings using the phase mask technique. *Opt. Express*, 27(22):32536–32555, 2019.

[152] Stephen J. Mihailov, Christopher W. Smelser, Ping Lu, Robert B. Walker, Dan Grobnic, Huimin Ding, George Henderson, and James Unruh. Fiber bragg gratings made with a phase mask and 800-nm femtosecond radiation. *Opt. Lett.*, 28(12):995–997, Jun 2003.

[153] Graham D. Marshall, Robert J. Williams, Nemanja Jovanovic, M. J. Steel, and Michael J. Withford. Point-by-point written fiber-bragg gratings and their application in complex grating designs. *Opt. Express*, 18(19):19844–19859, Sep 2010.

[154] Jörg Burgmeier, Christian Waltermann, Günter Flachenecker, and Wolfgang Schade. Point-by-point inscription of phase-shifted fiber bragg gratings with electro-optic amplitude modulated femtosecond laser pulses. *Opt. Lett.*, 39(3):540–543, Feb 2014.

[155] Sergei Antipov, Martin Ams, Robert J. Williams, Eric Magi, Michael J. Withford, and Alexander Fuerbach. Direct infrared femtosecond laser inscription of chirped fiber bragg gratings. *Opt. Express*, 24(1):30–40, Jan 2016.

[156] Martin Ams, Peter Dekker, Simon Gross, and Michael J. Withford. Fabricating waveguide bragg gratings (wbgs) in bulk materials using ultrashort laser pulses. *Nanophotonics*, 6(5):743–763, 2017.

[157] Nemanja Jovanovic, Jens Thomas, Robert J. Williams, M. J. Steel, Graham D. Marshall, Alexander Fuerbach, Stefan Nolte, Andreas Tünnermann, and Michael J. Withford. Polarization-dependent effects in point-by-point fiber bragg gratings enable simple, linearly polarized fiber lasers. *Opt. Express*, 17(8):6082–6095, Apr 2009.

[158] G. Zhang, G. Cheng, M. Bhuyan, C. D'Amico, and R. Stoian. Efficient point-by-point bragg gratings fabricated in embedded laser-written silica waveguides using ultrafast bessel beams. *Opt. Lett.*, 43(9):2161–2164, May 2018.

[159] Jung-Ho Chung, Yu Gu, and James G. Fujimoto. Submicron-period waveguide bragg gratings direct written by an 800-nm femtosecond oscillator. In *Conference on Lasers and Electro-Optics/Quantum Electronics and Laser Science Conference and Photonic Applications Systems Technologies*, page CThS4. Optica Publishing Group, 2007.

[160] Xin Liu, Xuewen Shu, Adenowo Gbadebo, and Lin Zhang. Generation of ultrahigh repetition rate pulse bursts using phase-modulated grating. In *Advanced Photonics 2018 (BGPP, IPR, NP, NOMA, Sensors, Networks, SPPCom, SOF)*, page JTu2A.9. Optica Publishing Group, 2018.

[161] Hongye Li, Xiaofan Zhao, Binyu Rao, Meng Wang, Baiyi Wu, and Zefeng Wang. Line position-dependent effect in line-by-line inscribed fiber bragg gratings. *Sensors*, 21(21), 2021.

[162] Hongye Li, Xiaofan Zhao, Binyu Rao, Meng Wang, Baiyi Wu, and Zefeng Wang. Fabrication and characterization of line-by-line inscribed tilted fiber bragg gratings using femtosecond laser. *Sensors (Basel)*, 21(18), Sept 2021.

[163] Haibin Zhang and Peter R. Herman. Chirped bragg grating waveguides directly written inside fused silica glass with an externally modulated ultrashort fiber laser. *IEEE Photonics Technology Letters*, 21(5):277–279, 2009.

[164] Jason R. Grenier, Luís A. Fernandes, J. Stewart Aitchison, Paulo V. S. Marques, and Peter R. Herman. Femtosecond laser fabrication of phase-shifted bragg grating waveguides in fused silica. *Opt. Lett.*, 37(12):2289–2291, Jun 2012.

[165] Jun He, Ziyong Chen, Xizhen Xu, Jia He, Baijie Xu, Bin Du, Kuikui Guo, Runxiao Chen, and Yiping Wang. Femtosecond laser line-by-line inscription of apodized fiber bragg gratings. *Opt. Lett.*, 46(22):5663–5666, Nov 2021.

[166] Christopher Miese, Michael J. Withford, and Alexander Fuerbach. Femtosecond laser direct-writing of waveguide bragg gratings in a quasi cumulative heating regime. *Opt. Express*, 19(20):19542–19550, Sep 2011.

[167] A. Yariv. Coupled-mode theory for guided-wave optics. *IEEE Journal of Quantum Electronics*, 9(9):919–933, 1973.

[168] D. Marcuse. Coupled mode theory of round optical fibers. *Bell System Technical Journal*, 52(6):817–842, 1973.

[169] H. Kogelnik. *Theory of Dielectric Waveguides*, pages 13–81. Springer Berlin Heidelberg, 1975.

[170] T. Erdogan. Fiber grating spectra. *Journal of Lightwave Technology*, 15(8):1277–1294, 1997.

[171] Sebastian Kroesen, Wolfgang Horn, Jörg Imbrock, and Cornelia Denz. Electro–optical tunable waveguide embedded multiscan bragg gratings in lithium niobate by direct femtosecond laser writing. *Opt. Express*, 22(19):23339–23348, Sep 2014.

[172] P. Dekker, M. Ams, T. Calmano, S. Gross, C. Kränkel, G. Huber, and M. J. Withford. Spectral narrowing of yb:yag waveguide lasers through hybrid integration with ultrafast laser written bragg gratings. *Opt. Express*, 23(15):20195–20202, Jul 2015.

[173] N. Vorobiev, L. Glebov, and V. Smirnov. Single-frequency-mode q-switched nd:yag and er:glass lasers controlled by volume bragg gratings. *Opt. Express*, 16(12):9199–9204, Jun 2008.

[174] Armen Sevian, Oleksiy Andrusyak, Igor Ciapurin, Vadim Smirnov, George Venus, and Leonid Glebov. Efficient power scaling of laser radiation by spectral beam combining. *Opt. Lett.*, 33(4):384–386, Feb 2008.

[175] Oliver Beyer, Ingo Nee, Frank Havermeyer, and Karsten Buse. Holographic recording of bragg gratings for wavelength division multiplexing in doped and partially polymerized poly(methyl methacrylate). *Appl. Opt.*, 42(1):30–37, Jan 2003.

[176] Daniel Ott, Ivan Divliansky, Brian Anderson, George Venus, and Leonid Glebov. Scaling the spectral beam combining channels in a multiplexed volume bragg grating. *Opt. Express*, 21(24):29620–29627, Dec 2013.

[177] Peng Chen, Yunxia Jin, Dongbing He, Junming Chen, Jiao Xu, Huifang Dai, Jingyin Zhao, Fanyu Kong, and Hongbo He. Fabrication of high-precision reflective volume bragg gratings. *Appl. Opt.*, 58(10):2500–2504, Apr 2019.

Inscription femtoseconde de type A de guides d'onde à fort contraste d'indice et de réseaux de Bragg

Résumé: Direct Laser Writing (DLW) est une technique flexible et efficace pour modifier les propriétés optique des matériaux. Elle permet de realiser facilement des circuits photoniques intégrés. Malheureusement, le changement d'indice de réfraction induit reste encore modeste par rapport à celui obtenu par d'autres techniques, telles que la lithographie. Cela constitue un frein a son déploiement, en particulier pour la miniaturisation des circuits photoniques. Par conséquent, l'augmentation de la variation d'indice de réfraction produite par le DLW est un axe d'étude actuel. En 2017, il a été démontré une nouveau type de modification d'indice dans des verres contenant argent, basé sur la formation photoinduite d'agrégats d'ions d'argent. Cette modification a été nommée type A. L'inscription de ces structures argentique a lieu dans un régime athermique, et présente des dimensions plus petites que la limite de diffraction. Les modifications de type A ont été utilisées jusqu'à présent pour fabriquer des guides d'ondes, des coupleurs, des séparateurs de faisceau et, plus récemment, un capteur d'indice de réfraction. Le travail rapporté dans ce manuscrit a un double objectif. D'une part, accroître l'indice de réfraction et d'autre part, de concevoir et fabriquer des de réseaux de Bragg périodiques avec une grande résolution, basées sur les modifications de type A. Le premier objectif est résolu par l'adoption d'une approche multi-passages qui permet d'augmenter fortement le contraste de l'indice des guides d'ondes inscrits par plusieurs balayages laser successifs. En exploitant le régime athermique de l'inscription de type A, ce travail a démontré un changement d'indice remarquablement élevé jusqu'à 2×10^{-2}. Des guides d'ondes multi-passages ont été fabriqués dans ces verres montrant à la fois un contrôle du confinement du mode guidé et une réduction des pertes de propagation. Le deuxième objectif atteint concerne la réalisation de Waveguides Bragg Gratings (WBGs) et de Volume Bragg Gratings (VBGs) en transmission. Les WBGs de type A ont démontré des résonances de Bragg de premier ordre dans la gamme spectrale VIS-NIR avec des coefficients de couplage élevés, jusqu'à 2 ordres de grandeur plus élevés que ce qui est donné dans la littérature. Enfin, des VBGs multicouches de type A ont démontré que l'augmentation de l'efficacité de diffraction, jusqu'à 55%, est obtenue pour des réseau de seulement 20 μm d'épaisseur. Les résultats reportés dans ce manuscrit démontrent qu'un changement d'indice très élevé est accessible avec des modifications de type A et permet d'obtenir de fortes résonances de Bragg de premier ordre dans la gamme VIS-NIR. Par conséquent, ces résultats prometteurs mettent en évidence tout l'interêt des modifications de type A pour la conception de circuit photonique par DLW.

Mots clés: Direct Laser Writing, laser femtosecondes, verres contenant argents, agrégats d'argents, modifications de Type A, modifications d'indice éléve, guide d'ondes, reseaux volumique de Bragg, guides d'onde de Bragg.

Femtosecond laser inscription of type A-based high refractive index contrast waveguides and Bragg gratings

Abstract: Direct Laser Writing (DLW) is a flexible and efficient technique to modify the optical properties of media. It allows for easily fabricating Photonics Integrated Circuits (PICs). However, the induced refractive index change is still small if compared to what is achieved in other techniques, such as lithography. This constitutes a limitation of such a technique, especially for the miniaturization of photonics circuits. Therefore, the achieving of higher index modification is a research axis that is currently being investigated. In 2017, a new type of index modification has been demonstrated in silver-containing glasses, namely Type A, which is based on the photoinduced clustering of the silver ions. The inscription of silver-sustained structures occurs in an athermal regime and shows dimensions overcoming the diffraction limit. Type A modifications have been exploited to fabricate waveguides, couplers, beam splitters and, more recently, a refractive index sensor. The work reported in this manuscript has a twofold goal. On the one hand, the achievement of high Type A refractive index change, on the other hand, the conception and fabrication of high-resolution Bragg gratings. The first objective was achieved by adopting a multiscan approach, which allows for strongly increasing the induced index change by increasing the number of consecutive laser passes. By exploiting the athermal regime of Type inscription, this work demonstrates remarkably high refractive index change up to 2×10^{-2}. Moreover, Type A multiscan waveguides show fine control of the confinement of the guided mode and reduced propagation losses. The second objective has led to the realization of Waveguides Bragg Gratings (WBGs) and transmission Volume Bragg Gratings (VBGs). Type A WBGs show first-order Bragg resonances in the VIS-NIR spectral range with coupling coefficients up to 2 orders of magnitude higher than what is reported in the literature. Finally, Type A multilayers VBGs show that high diffraction efficiency, up to 55%, is achieved for only 20 μm thick gratings. The results reported in this manuscript demonstrate that high refractive index change and strong first-order Bragg resonances in the VIS-NIR can be obtained with Type A modifications. Therefore, such promising results highlight the interest of Type A modifications for the conception of photonics circuits by DLW technique.

Keywords Direct Laser Writing, femtosecond lasers, silver-containing glasses, silver clusters, Type A modifications, high refractive index change, waveguides, Volume Bragg Gratings, Waveguides Bragg Gratings.

Unité de recherche
UMR 5107 Université, 33000 Bordeaux, France.